UNIVERSITY OF COPENHAGEN
FACULTY OF SCIENCE

Master's Thesis

Study of anomalous $t\bar{t}$ production in the di-lepton final state at FCC-ee

Shengtang Yi

Supervisor: Jørgen Beck Hansen

Submitted: May 1st 2023

Abstract

The top quark, as the most massive of all observed elementary particles, has the exclusive advantage of being the optimal candidate to reveal the mystery of physics beyond the Standard Model of particle physics (BSM). Anomalous contributions to $t\bar{t}$ production can be investigated in the framework of Standard Model Effective Field Theory (SMEFT). The potential new contributions are expected to affect the production cross-section and angular distributions of the top decay products due to changed spin configurations.

The Future Circular Collider (FCC) process e^+e^- to $t\bar{t}$ will be simulated using the FCC Innovative Detector for an Electron-positron Accelerator (IDEA) detector setup and investigated with the FCC analysis software to gauge the potential experimental sensitivity to anomalous top contributions. The project will focus on the final state with two b-jets and two charged leptons, which is expected to be very clean, albeit made difficult due to the 2 unmeasured neutrinos. The project consists of the steps: event selection to identify the collision events of interest with respect to backgrounds; event reconstruction to determine the complete kinematic configuration of each event; construct observables sensitive to anomalous contributions; and finally, determine 68% confidence regions for all anomalous couplings. As part of these steps, I will investigate potential observables (production angles, decay angles a.o.) for their sensitivity to BSM contributions and gauge the improvement by using the production cross section as additional information. The final step is to fit the anomalous gauge coupling parameters using both the kinematical observables and cross-section information. The fit for anomalous contribution is performed utilising the parabolic dependency of the observables on the anomalous couplings, else determined using event simulations with the Whizard and Pythia event generators which include the contributions from SMEFT. The final result is to determine the potential sensitivity limits of anomalous couplings at a future collider. This will help to establish the physics potential of such a collider for physics beyond the Standard Model.

Acknowledgement

I am very grateful to my supervisor Jørgen Beck Hansen, his professional guidance, and patience have brought great help to my master's study in the past two years. I would also like to thank Edis Devin Tireli for helping me with my thesis writing.

Contents

*

1 Introduction

Particle physics is a field of study that focuses on elementary particles and their interactions. It is also at the forefront of modern physics, with the potential to significantly impact our understanding of the natural world. The theoretical framework of particle physics is the Standard Model (SM), which is currently the most successful theory in this field. It is capable of describing all known forces except gravity. The 2012 discovery of the Higgs boson, the last particle predicted by the Standard Model, gave the theory little scope for predicting new physics. The Standard Model is the lowest order of effective field theory, and higher dimensions may have hints of new physics. Pursuing higher energies determines the next generation of colliders. Currently, there are two types of colliders: hadron colliders and lepton colliders. Lepton colliders have much smaller centers of mass than hadron colliders, but they use elementary particles for their collisions, which generates data that is not subject to minimum bias. Conversely, in the low pt(transverse momentum) intervals of a Hadron Collider, superfluous data swamp the desired data. As a result, a Lepton Collider enables deep exploration of discovered physics. For example, PETRA (DESY) discovered gluons in 1979, and LEP (CERN) discovered three generations of neutrinos. As for the hadron collider, since hadrons are not fundamental particles, but are composed of quarks and gluons, the particles in the low pt range are of little significance. Only high pt events have the potential to reveal new physics. However, the mass of the hadron itself determines that the center of mass of the hadron collider is much heavier than that of a lepton collider. Thus, the Hadron Collider can be used to explore new physics. For example, Tevatron (Fermilab) discovered the top quark in 1995, and the Large Hadron Collider (CERN) discovered the Higgs boson in 2012. [1] The lack of new physics discovered at the LHC, despite its high energy range of 8TeV, prompted the launch of the Next Generation Collider program. The Future Circular Collider (FCC), a new-generation collider planned to be built by CERN, is divided into two phases: FCC-ee, which will provide a precise analysis of existing physics, and FCC-hh, which aims to break through the energy frontiers of physics to uncover new traces of physics.

The Standard Model is a highly successful theoretical framework that can explain many phenomena in particle physics. However, it cannot account for certain phenomena such as neutrino mass and dark matter. Therefore, exploring new physics beyond the Standard Model is necessary. However, as there is no evidence for new physics yet, one possibility is to focus on studying the top quark, which is the heaviest particle in the Standard Model. By using high-luminosity colliders with extreme statistical precision and experimental accuracy, there is a chance of detecting small deviations from the predictions of the Standard Model.

This analysis aims to explore the sensitivity of top anomalous coupling in the experimental environment of FCC-ee. The second section provides a summary of the formulas and concepts of the Standard Model, which is the framework of quantum field theory (QFT). In the third section, the theoretical basis of EFT is introduced, along with why higher-dimensional terms should be included in the Standard Model. The fourth section describes the experimental environment and construction standards, with a focus on the construction blueprint of FCC-ee and the detector IDEA. The fifth section introduces the simulation data used in this analysis, including the exper-

imental signal (top pair production) and the corresponding backgrounds generated by the Monte Carlo generator in the collider environment. Additionally, independent coupling data were generated to explore the sensitivity of top anomalous coupling. The sixth section explains how reconstructed particles are dealt with at the detector level, from the performance of the jet algorithm to the measurement of high leptons and the calculation of neutrinos. The seventh section outlines the optimized selection cut strategy used to obtain a signal that is as pure as possible for top pair production through the screening of observables. The eighth section describes how the software package is used to optimize event reconstruction by employing kinematic fitting. The ninth section presents the results of simulation experiments through five observable angles.

2 The Standard Model

The concept of atoms was first proposed by the ancient Greek philosopher Democritus in the 5th century BCE, but it wasn't until the 19th century that scientists began to study the properties of atoms in detail. This led to the development of classical mechanics, which describes the behavior of macroscopic objects. However, in the early 20th century, experiments showed that classical mechanics was unable to explain the behavior of subatomic particles, which led to the development of quantum mechanics. Quantum mechanics describes the behavior of particles on a microscopic scale and is essential for understanding the behavior of particles in the Standard Model.

The theoretical framework of the Standard Model is quantum field theory, which combines quantum mechanics with special relativity. In 1954, Chen-Ning Yang and Robert Mills proposed the Yang-Mills theory, which laid the foundation for the development of the Standard Model. In 1960, Sheldon Glashow discovered the electroweak interaction, which describes the behavior of the electromagnetic and weak nuclear forces. In 1964, Peter Higgs proposed the Higgs mechanism, which explains how particles acquire mass. In 1967, Steven Weinberg and Abdus Salam introduced the Higgs mechanism into Glashow's electroweak theory, forming the basis of the Standard Model we know today. [1]

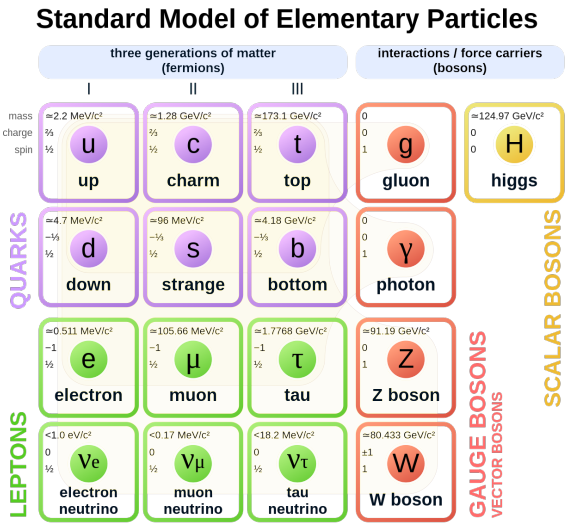

Figure 2.1: The Standard Moedel Elementary Particles: Three generations of Fermions(colume 1-3), row 1 - up type quarksu,c,t, with charge $+\frac{2}{3}$,spin $\frac{1}{2}$, row 2 - down tpye quarksd,s,b, with charge $-\frac{1}{3}$, spin $\frac{1}{2}$, row 3 - charged leptonse,μ,τ spin $\frac{1}{2}$, with charge -1, spin $\frac{1}{2}$, row 4 - zero charged leptonsν_e,ν_μ,ν_τ, spin $\frac{1}{2}$. Bosons(colume 4-5), vector bosongluon,photon,Z boson,W boson, scalar boson higgs boson. [2]

Elementary particles can be broadly classified into two categories: fermions, which make up matter, and bosons, which carry the fundamental forces. Fermions, shown in Figure 2.1, are particles with a spin of 1/2 and can be further divided into quarks and leptons. Each fermion has an antiparticle with identical mass but opposite quantum numbers. The Standard Model describes three generations of fermions, with each

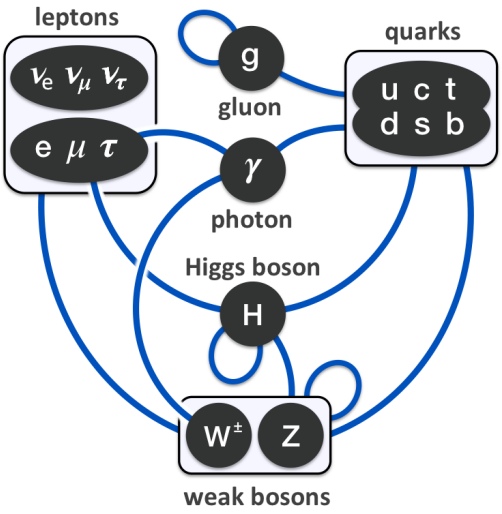

Figure 2.2: Standard Model Interactions [2]

generation containing a quark and a lepton of increasing mass, except for neutrinos, for where only the mass gap between two generations is known. Bosons can be divided into vector and scalar types. Photons, with a spin of 1, are vector bosons that carry the electromagnetic force and only interact with charged fermions. W and Z bosons, also with a spin of 1, carry the weak force, and all fermions participate in this interaction. Gluons, with a spin of 1, carry the strong force and only interact with colored fermions. The Higgs boson, a scalar boson with a spin of 0, endows particles with mass through the Higgs mechanism, with the strength of interaction proportional to the particles' mass.

The Standard Model is based on gauge theory and can be expressed mathematically as $SU(3)_c \times SU(2)_L \times U(1)_Y$.

2.1 Quantum Electrodynamics

Quantum field theory originated from classical field theory. Unlike quantum mechanics, in classical field theory, $\mathcal{L}$ Lagrangian is used to describe the motion of objects instead of $\mathcal{H}$ Hamiltonian, because Lagrangian is Lorentz invariant. The Lagrange can be defined as $\mathcal{L} = T - V$, where T is kinetic energy and V is potential energy.

Quantum Electrodynamics (QED) is a quantum field theory that describes the interactions of charged particles with the electromagnetic force. It is based on the principle of gauge invariance and is one of the most well-established theories in particle physics. QED is gauge invariant under $U(1)$ transformation, and we can write the QED Lagrangian as follows:

$$\mathcal{L}_{QED} = \bar{\psi}(i\gamma^\mu \partial_\mu - m_e)\psi + e\bar{\psi}\gamma^\mu \psi A_\mu - \frac{1}{4}F_{\mu\nu}F^{\mu\nu}, \tag{2.1}$$

where the first term describes the free charged fermion. By bringing it into the Euler-Lagrange equation, we obtain the free charged fermion Dirac quation. The second

term describes the interaction between the charged fermion and the photon field, and the third term describes the photon field itself from Maxwell's equations. Spinor fields and photon fields transform as follows:

$$\psi(x) \to e^{i\alpha(x)}\psi(x), \quad A_\mu \to A_\mu(x) - \partial_\mu \alpha(x). \tag{2.2}$$

The Lagrangian for QED sums up the entire electromagnetism and can be written as follows:

$$\mathcal{L}_{QED} = -\bar{\psi}(i\not{D} + m_e)\psi - \frac{1}{4}F_{\mu\nu}F^{\mu\nu}, \tag{2.3}$$

where D_μ is the gauge covariant derivative of electromagnetic interaction defined as follows:

$$D_\mu = \partial_\mu - ieA_\mu(x), \tag{2.4}$$

and the slash notation is defined as $\not{a} \equiv \gamma^\mu a_\mu$. Similarly, the weak interaction can be extended to the $SU(2)$ group. The $SU(2)$ group has three generators that define a non-Abelian Lie algebra, and we can see that these three generators correspond to three weak gauge bosons. The covariant derivative of charged weak current is defined as follows:

$$D_\mu = \partial_\mu + ig_W \mathbf{T} \cdot \mathbf{W}_\mu(x), \tag{2.5}$$

where g_W is the coupling of the weak boson, $\mathbf{T}$ is the three generators of the group, and $\mathbf{W}$ are the three fields corresponding to the $SU(2)$ group.

2.2 Electroweak unification

The Electroweak theory describes the unification of the electromagnetic and weak nuclear forces and is based on the gauge group $SU(2)_L \times U(1)_Y$. The theory is described by the following Lagrangian:

$$\mathcal{L}_{EW} = -\frac{1}{4}F_{\mu\nu}F^{\mu\nu} + (D_\mu\phi)^\dagger(D^\mu\phi) + \bar{\psi}(i\not{D} - m)\psi - V(\phi) \tag{2.6}$$

where $F_{\mu\nu}$ is the electromagnetic field tensor, ψ is the Dirac field that describes the electron and neutrino, D_μ is the covariant derivative that describes the interaction of the electron and neutrino with the electromagnetic and weak nuclear forces, and ϕ is the Higgs field. The last term in the Lagrangian is the Higgs potential, which gives mass to the weak gauge bosons and fermions.

In addition to the Lagrangian, the Electroweak theory introduces two important quantum numbers: weak hypercharge and weak isospin. Weak isospin is a quantum number that relates to the weak interaction, analogous to strong interaction isospin. Weak hypercharge is a quantum number that relates the electric charge and the third component of weak isospin. These quantum numbers are essential to understanding the behaviour of elementary particles in the Electroweak theory, particularly in the context of the Higgs mechanism that gives mass to the weak gauge bosons and fermions. By introducing these quantum numbers, the Electroweak theory provides a powerful framework for understanding the behaviour of elementary particles at the most fundamental level. Details are shown in Figure 2.3.

Fermion family	Left-chiral fermions				Right-chiral fermions			
		Electric charge Q	Weak isospin T_3	Weak hyper-charge Y_W		Electric charge Q	Weak isospin T_3	Weak hyper-charge Y_W
Leptons	ν_e, ν_μ, ν_τ	0	$+\frac{1}{2}$	−1	ν_R May not exist	0	0	0
	e^-, μ^-, τ^-	−1	$-\frac{1}{2}$	−1	e_R^-, μ_R^-, τ_R^-	−1	0	−2
Quarks	u, c, t	$+\frac{2}{3}$	$+\frac{1}{2}$	$+\frac{1}{3}$	u_R, c_R, t_R	$+\frac{2}{3}$	0	$+\frac{4}{3}$
	d, s, b	$-\frac{1}{3}$	$-\frac{1}{2}$	$+\frac{1}{3}$	d_R, s_R, b_R	$-\frac{1}{3}$	0	$-\frac{2}{3}$

Figure 2.3: The Left-handed Fermions and Right-handed Fermions [3]

In the structure of Electroweak unification, the physical W^+ and W^- gauge bosons can be written as a linear combination of the $SU(2)$ generators $W^{(1)}$ and $W^{(2)}$:

$$W^{\pm} = \frac{1}{\sqrt{2}}(W^{(1)} \pm W^{(2)}) \tag{2.7}$$

The photon and Z boson can be written as linear combinations of W^3 and the B field:

$$A = +B\cos\theta_W + W^{(3)}\sin\theta_W \tag{2.8}$$

$$Z = -B\sin\theta_W + W^{(3)}\cos\theta_W \tag{2.9}$$

The B field is from $U(1)_Y$, where Y is the hypercharge, which is different from electric charge, but they are connected by:

$$Y = 2Q - 2I_W^3 \tag{2.10}$$

The hypercharge connects the electromagnetic interaction and weak interaction, following the relationship:

$$e = g_W \sin\theta_W = g' \cos\theta_W \tag{2.11}$$

where e is electric charge, g_W is the coupling strength in interactions involving weak isospin, and g' is the coupling strength involving weak hypercharge.
Weak interactions W^+ and W^- can only interact with left-handed particles and right-handed antiparticles, while Z can interact with both right-handed particles and left-handed antiparticles. Due to the different weak isospin values, the left and right coupling strengths are different:

$$C_L = I_W^3 - Q\sin^2\theta_W \tag{2.12}$$

$$C_R = -Q\sin^2\theta_W \tag{2.13}$$

In terms of the V-A (vector minus axial-vector) components, we have:

$$C_V = C_L + C_R \tag{2.14}$$

$$C_A = C_L - C_R \tag{2.15}$$

2.3 Quantum Chromodynamics

Quantum Chromodynamics (QCD) is a component of the Standard Model that describes the strong interaction. Only particles that carry the colour charge can experience strong interaction, namely quarks and gluons. QCD is gauge invariant under the local gauge transformation of $SU(3)_C$, which is formed by 3×3 matrices, and has 8 generators, each corresponding to 8 different gluons. Similar to QED, the QCD covariant derivative can be written as

$$D\mu = \partial_\mu + ig_S \mathbf{G}\mu \cdot \mathbf{T}, \tag{2.16}$$

where $\mathbf{G}$ are the 8 generators. The $SU(3)$ group provides a field transformation as follows:

$$G^k\mu(x) \rightarrow G^k_\mu(x) - \partial_\mu \alpha_k(x) - g_S f_{ijk} \alpha_i(x) G^j_\mu(x), \tag{2.17}$$

where f_{ijk} are the structure constants and follow the commutation relation $[T_i, T_j] = if_{ijk}T_k$. The QCD Lagrangian can be written as follows:

$$\mathcal{L}_{QCD} = \bar{\psi}_i (i\gamma^\mu (D_\mu)_{ij} - m\delta_{ij})\psi_j - \frac{1}{4} G^\alpha_{\mu\nu} G^{\mu\nu}_\alpha, \tag{2.18}$$

where the last term is similar to QED but for the gluon field and also describes gluon self-interaction.

Although QCD is not directly related to the main analysis in this article, there is a phenomenon worth mentioning, which is the running of the strong coupling. The interaction cross-section is determined by the coupling strength, which exhibits asymptotic freedom in strong interaction, as shown in Figure 2.4. The QCD coupling can be divided into two regimes. At high energy, the running coupling converges, making perturbation theory applicable. This is also mentioned in the CKM(Cabibbo-Kobayashi-Maskawa) matrix shown in Figure 2.5, where the top quark's main decay product is the bottom quark, making b-tagging important. At low energy, quarks cannot exist as free particles. Virtual gluons can interact with each other to force quarks to form colour-neutral hadrons or mesons, a phenomenon known as quark confinement. When quarks move away from each other, the colour charge creates a colour field. If the field has enough energy, it will produce a new pair of particles while remaining colour-neutral, until the energy is no longer sufficient to do so. This process is known as hadronization. This phenomenon can explain the observation in high-energy physics that quarks and gluons can form jets.

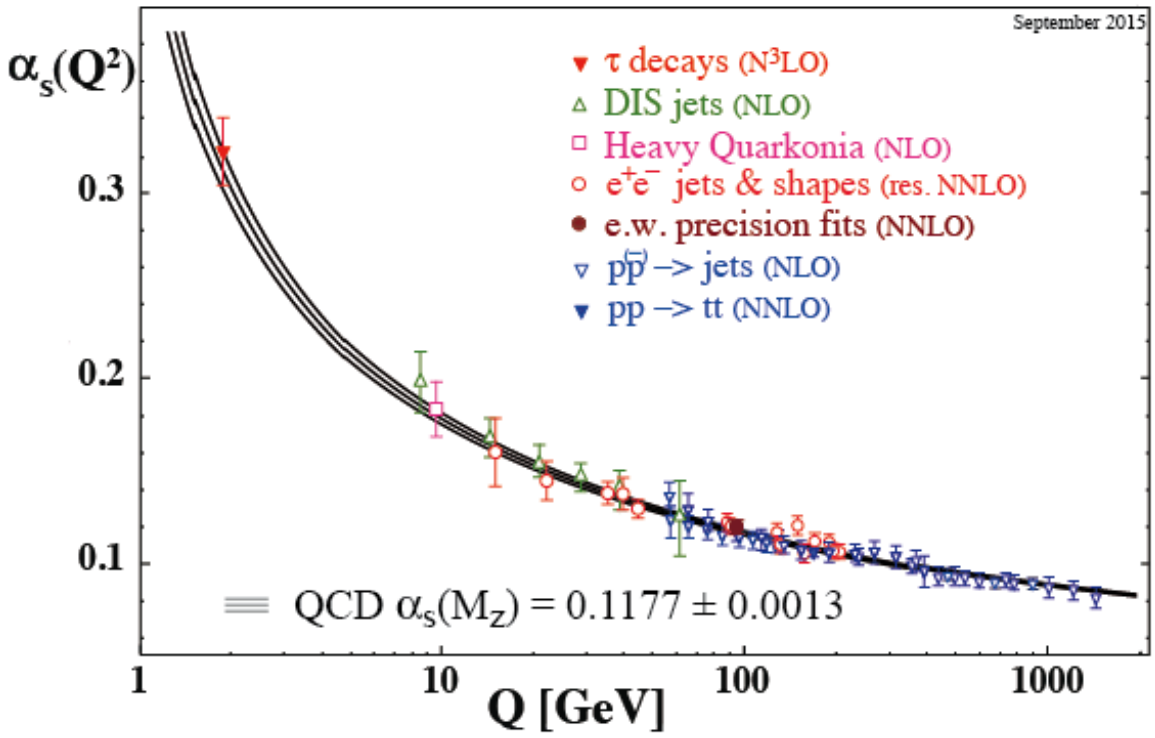

Figure 2.4: LHC 2015 running coupling results [4]

$$V_{\mathrm{CKM}} = \begin{pmatrix} 0.97428 \pm 0.00015 & 0.2253 \pm 0.0007 & 0.00347^{+0.00016}_{-0.00012} \\ 0.2252 \pm 0.0007 & 0.97345^{+0.00015}_{-0.00016} & 0.0410^{+0.0011}_{-0.0007} \\ 0.00862^{+0.00026}_{-0.00020} & 0.0403^{+0.0011}_{-0.0007} & 0.999152^{+0.000030}_{-0.000045} \end{pmatrix}$$

Figure 2.5: The CKM matrix, indicates the probability of heavy quarks decay modes. V_{33} is the probability of top quark decaying into bottom quark. [5]

2.4 Higgs Mechanism

The QFT formalism describes the interaction between bosons and fermions. However, the Lagrangian itself cannot give particles mass without violating local gauge invariance. Photons and gluons are massless particles, which does not pose a problem for the standard model. However, weak gauge bosons are massive, and forcefully introducing mass terms into the Lagrangian would make the standard model not renormalizable. [6] The Higgs mechanism can give mass to particles through interaction. The vacuum represents the lowest energy state, and since the Higgs vacuum state has a non-zero value, the Higgs field will slow down particles, which can be seen as giving mass.

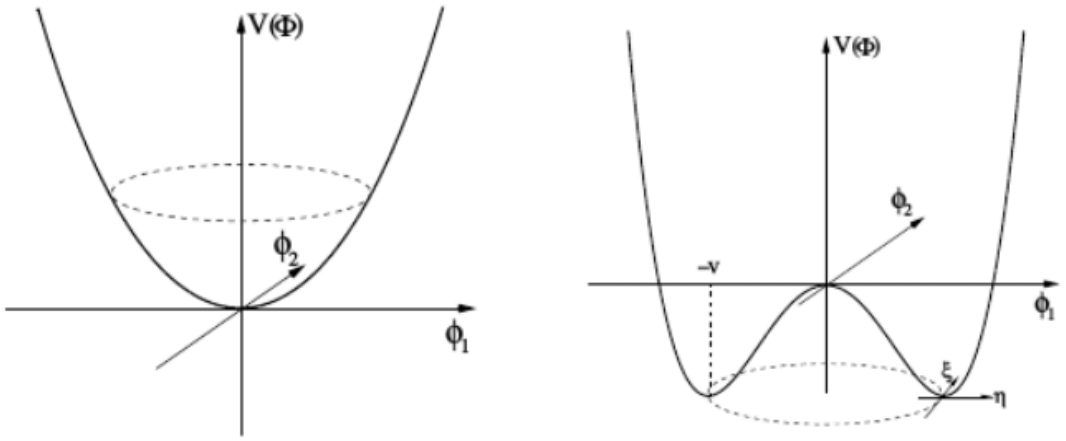

Figure 2.6: Higgs potential $\mu^2 > 0$ left and $\mu^2 < 0$ right [6]

The simplest Higgs model consists of two complex scalar fields placed in a weak isospin doublet

$$\phi = \begin{pmatrix} \phi^+ \\ \phi^0 \end{pmatrix} = \frac{1}{\sqrt{2}} \begin{pmatrix} \phi_1 + i\phi_2 \\ \phi_3 + i\phi_4 \end{pmatrix} \tag{2.19}$$

[lecture-15 page 19] The Lagrangian in $SU(2) \times U(1)$ is given by

$$\mathcal{L} = (D_\mu \phi)^\dagger (D^\mu \phi) - V(\phi) \tag{2.20}$$

where the covariant derivative is defined as

$$D_\mu = \partial_\mu + i g_W \mathbf{T} \cdot \mathbf{W}_\mu(x) + i g' \frac{Y}{2} B_\mu \tag{2.21}$$

The Higgs potential can be seen from Figure 2.6. When $\mu^2 < 0$, it takes the shape of a Mexican hat, and can be defined as

$$V(\phi) = \mu^2 \phi^\dagger \phi + \lambda (\phi^\dagger \phi)^2 \tag{2.22}$$

The point $\phi = 0$ is not a minimum of the potential. Instead, an infinite number of degenerate minima form a ring. The Vacuum Expectation Value (VEV) is defined as

$$v = \sqrt{\frac{-\mu^2}{\lambda}} \tag{2.23}$$

The choice of vacuum state breaks the symmetry of the system, and this process is called Spontaneous Symmetry Breaking (SSB).

In the unitary gauge, the Higgs doublet can be written as

$$\phi(x) = \frac{1}{\sqrt{2}} \begin{pmatrix} 0 \\ v + h(x) \end{pmatrix} \tag{2.24}$$

The kinematic term of the $SU(2) \times U(1)$ Lagrangian is given by

$$(D_\mu \phi)^\dagger (D^\mu \phi) = \frac{1}{2}(\partial_\mu h)(\partial^\mu h) + \frac{1}{8} g_W^2 (W^{(1)}\mu + iW\mu^{(2)})(W^{(1)\mu} - iW^{(2)\mu})(v+h)^2 \tag{2.25}$$

$$+ \frac{1}{8}(g_W W^{(3)}\mu - g' B\mu)(g_W W^{(3)\mu} - g' B^\mu)(v+h)^2 \tag{2.26}$$

The mass of the gauge bosons can be obtained as

$$m_W = \frac{1}{2} g_W v \tag{2.27}$$

$$m_Z = \frac{1}{2} v \sqrt{g_W^2 + g'^2} = \frac{1}{2} \frac{g_W}{\cos\theta_W} \tag{2.28}$$

whereas the Higgs boson mass is given by

$$m_H = \sqrt{2\lambda} v. \tag{2.29}$$

Direct fermion mass terms are not allowed in the Lagrangian. For all Dirac fermions, gauge-invariant mass terms can be constructed as

$$\mathcal{L} = -g_f[\bar{L}\phi R + (\bar{L}\phi R)^\dagger], \tag{2.30}$$

$$\mathcal{L} = g_f[\bar{L}\phi_c R + (\bar{L}\phi_c R)^\dagger], \tag{2.31}$$

where the mass is given by

$$m_f = \frac{1}{\sqrt{2}} g_f v \tag{2.32}$$

and the conjugate doublet is constructed from $\phi_c = -i\sigma_2 \phi^*$, L is the doublet for left-handed fermion fields with $\bar{L} = L^\dagger \gamma^0$, and R is the singlet for right-handed fermion fields. The Lagrangians above also show interactions between the fermion and the Higgs, which lead to both bosonic and fermionic decay modes of the Higgs boson. [6]

3 Anomalous Couplings

The Standard Model Effective Field Theory (SMEFT) is a theoretical framework that extends the Standard Model of particle physics by adding higher-dimensional operators that describe the interactions of particles beyond those predicted by the Standard Model. It can be seen as an analogy to the Taylor expansion. We perform a Taylor expansion on the real physical rules, and we can obtain an infinite sequence, where the first few terms of this sequence are often related to the energy regime we are currently in, and we call it the characteristic length scale Λ. The Standard Model is the first term in this sequence, and it has been able to describe all the experimental data to date. However, when the energy continues to rise, the second term will begin to show influence, and the results of experiments are likely to start to deviate from the prediction of the SM, which is what this analysis will describe.

The Standard Model is based on quantum field theory and has a minimum dimension of 4. [7] For higher dimensions, the inclusion of dim-5 operators can lead to unphysical or inconsistent predictions in the SMEFT, such as negative decay rates or non-unitary scattering amplitudes. Therefore, it is more practical and consistent to neglect the dim-5 operators in the SMEFT, we will look at dim-6. The SMEFT Lagrangian can be written as

$$\mathcal{L}_{SMEFT} = \mathcal{L}_{SM} + \sum_i \frac{c_i^{(6)}}{\Lambda^2} O_i^{(6)} + \sum_i \frac{c_i^{(8)}}{\Lambda^4} O_i^{(8)} + \cdots \tag{3.1}$$

The following sections will be based on the research in [14].

In dim-6, there are 14 contributions to top electroweak anomalous couplings, but only 7 will be investigated in this analysis, as they contribute to Wtb, $Zt\bar{t}$ and $\gamma t\bar{t}$. [8]

$$\begin{aligned}
O_{\phi q}^{(3)} &= i(\phi^\dagger \tau^I D_\mu \phi)(\bar{q}_L \gamma^\mu \tau^I q_L) \\
O_{\phi q}^{(1)} &= i(\phi^\dagger D_\mu \phi)(\bar{q}_L \gamma^\mu q_L) \\
O_{\phi\phi} &= i(\tilde{\phi}^\dagger D_\mu \phi)(\bar{t}_R \gamma^\mu b_R) \\
O_{\phi t} &= i(\phi^\dagger D_\mu \phi)(\bar{t}_R \gamma^\mu t_R) \\
O_{tW} &= (\bar{q}_L \sigma^{\mu\nu} \tau^I t_R)\tilde{\phi} W_{\mu\nu}^I \\
O_{bW} &= (\bar{q}_L \sigma^{\mu\nu} \tau^I b_R)\phi W_{\mu\nu}^I \\
O_{tB\phi} &= (\bar{q}_L \sigma^{\mu\nu} t_R)\tilde{\phi} B_{\mu\nu}
\end{aligned} \tag{3.2}$$

where quark weak interaction eigenstates

$$q_L = \begin{pmatrix} t_L \\ b_L \end{pmatrix}, \quad t_R, \quad b_R \tag{3.3}$$

The covariant derivative is

$$D_\mu = \partial_\mu + i g_s \frac{\lambda^a}{2} G_\mu^a + i g \frac{\tau^I}{2} W_\mu^I + i g' Y B_\mu \tag{3.4}$$

where G_μ^a, W_μ^I, and B_μ are the gauge fields for $SU(3)_C$, $SU(2)_L$, and $U(1)_Y$. λ^a are the Gell-Mann matrices with $a = 1, \cdots, 8$, τ^I is Pauli matrices for $I = 1, 2, 3$ and Y is the hyper charge.

3.1 Wtb Vertex

The effective Wtb vertex including SM contributions and those form dim-6 operators can be parameterised as

$$\mathcal{L}_{Wtb} = -\frac{8}{\sqrt{2}}\bar{b}\gamma^{\mu}(V_L P_L + V_R P_R)tW^{-}_{\mu} - \frac{8}{\sqrt{2}}\bar{b}\frac{i\sigma^{\mu\nu}q_{\nu}}{M_W}(g_L P_L + g_R P_R)tW^{-}_{\mu} + h.c. \quad (3.5)$$

within the SM, V_L equals the CKM matrix element $V_{tb} \simeq 1$ while the rest of coupling V_R,g_L, and g_R vanish at the tree level. The dim-6 new physics on Wtb vertex can be written as

$$\begin{aligned} \delta V_L &= C^{(3)*}_{\phi q}\frac{v^2}{\Lambda^2} \qquad \delta g_L = \sqrt{2}C^{*}_{bW}\frac{v^2}{\Lambda^2} \\ \delta V_R &= \frac{1}{2}C_{\phi\phi}\frac{v^2}{\Lambda^2} \qquad \delta g_L = \sqrt{2}C_{tW}\frac{v^2}{\Lambda^2} \end{aligned} \quad (3.6)$$

where v is vacuum expectation value

3.2 Ztt Vertex

The effective Ztt vertex including SM contributions and those form dim-6 operators can be parameterised as

$$\mathcal{L}_{Ztt} = -\frac{g}{2c_W}\bar{t}\gamma^{\mu}(X^L_{tt}P_L + X^R_{tt}P_R - 2s^2_W Q_t)tZ_{\mu} - \frac{8}{2c_W}\bar{t}\frac{i\sigma^{\mu\nu}q_{\nu}}{M_Z}(d^Z_V + id^Z_A\gamma_5)tZ_{\mu} + h.c. \quad (3.7)$$

in SM $X^L_{tt} = 2T_3(t_L) = 1, X^R_{tt} = 2T_3(t_R) = 0$ (T_3 is third component of isospin) and $d^Z_A = d^Z_V = 0$ at the tree level. The dim-6 new physics on Ztt vertex can be written as

$$\begin{aligned} \delta X^L_{tt} &= Re[C^{(3)}_{\phi q} - C^{(1)}_{\phi q}]\frac{v^2}{\Lambda^2} \quad \delta d^Z_V = \sqrt{2}Re[c_W C_{tW} - s_W C_{tb\phi}]\frac{v^2}{\Lambda^2} \\ \delta X^R_{tt} &= -ReC_{\phi t}\frac{v^2}{\Lambda^2} \quad \delta d^Z_A = \sqrt{2}Im[c_W C_{tW} - s_W C_{tb\phi}]\frac{v^2}{\Lambda^2} \end{aligned} \quad (3.8)$$

s_W, c_W are sine and cosine value of weak angle θ_W

3.3 γtt Vertex

The effective γtt vertex including SM contributions and those form dim-6 operators can be parameterised as

$$\mathcal{L}_{\gamma tt} = -eQ_t\bar{t}\gamma^{\mu}A_{\mu} - e\bar{t}\frac{i\sigma^{\mu\nu}q_v}{m_t}(d^{\gamma}_V + id^{\gamma}_A\gamma_5)tA_{\mu} + h.c. \quad (3.9)$$

The dim-6 new physics on Ztt vertex can be written as

$$\begin{aligned} \delta d^{\gamma}_V &= \frac{\sqrt{2}}{e}Re[c_W C_{tB\phi} + s_W C_{tW}]\frac{vm_t}{\Lambda^2} \\ \delta d^{\gamma}_A &= \frac{\sqrt{2}}{e}Im[c_W C_{tB\phi} + s_W C_{tW}]\frac{vm_t}{\Lambda^2} \end{aligned} \quad (3.10)$$

3.4 Anomalous Contribution to $t\bar{t}$

Figure 3.1 shows the process of $t\bar{t}$ production, where the highlighted 3 points correspond to the 3 vertexes mentioned above, the red corresponds to Ztt and γtt vertex, and the blue represents Wtb vertex. These vertexes correspond to the dim-6 Lagrangian mentioned in section 3.1. The characteristic length scale Λ is related to the energy, so we expected the FCC-ee environment to reveal dim-6 effect. The dim-6 Lagrangian will affect the cross-section of the event, and the γ^5 operator of Lagrangian will have an impact on angular distribution.

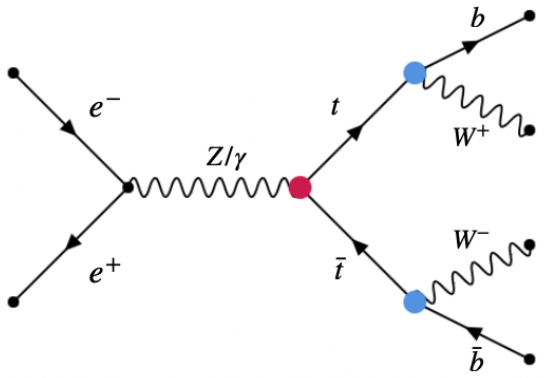

Figure 3.1: the $t\bar{t}$ production Feynman diagram, three relevant vertexes are highlighted

As mentioned above, the Lagrangian and cross-section are inherently related. By introducing the influence of dim-6 into the matrix element, we can modify SM matrix element as follows:

$$\mathbf{M} = \mathbf{M}_{SM} + c_i \mathbf{M}_{dim-6} \tag{3.11}$$

As a result, the cross-section is modified and expected to have a quadratic polynomial form.

$$|\mathbf{M}|^2 = |\mathbf{M}_{SM} + c_i \mathbf{M}_{dim-6}|^2 \tag{3.12}$$

$$= |\mathbf{M}_{SM}|^2 + c_i(\mathbf{M}^*_{SM}\mathbf{M}_{dim-6} + \mathbf{M}_{SM}\mathbf{M}^*_{dim-6}) + c_i^2 |\mathbf{M}_{dim-6}|^2 \tag{3.13}$$

This quadratic polynomial form allows us to investigate anomalous effects in an efficient way.

4 FCC-ee Experiment

4.1 FCC-ee

Since the discovery of the Higgs boson at the Large Hadron Collider (LHC) in 2012, there has been a growing interest in exploring the fundamental nature of particles and their interactions. One way to achieve this is through lepton colliders, where electrons and positrons collide to produce a range of particles for study. Among the lepton collider projects under development, the Future Circular Collider electron-positron (FCC-ee) experiment is one of the most promising. Hosted by the European Organization for Nuclear Research (CERN), the FCC-ee is a proposed circular collider with a center of mass energy ranging from 90 to 365 GeV. Compared to other lepton colliders, the FCC-ee offers several advantages, including its high energy and high luminosity, which enables researchers to study rare processes that would be difficult to observe elsewhere.

The FCC-ee project is divided into two phases. The first phase will focus on precision measurements of the electroweak sector, including the Higgs boson and the W and Z bosons. In contrast, the second phase will explore the properties of the top quark and other heavy particles.

Currently, the FCC-ee is in the design phase, with researchers working to develop an efficient and effective collider that can deliver high-quality data on a range of particles. The FCC-ee is expected to start in 2040, and the center of mass weight will be set at the Z pole of 91 GeV for the first four years, then at the WW mass for the next two years, and finally at the Higgs factory (240 GeV) for three years. Afterwards, the $t\bar{t}$ threshold will be set at 340 GeV, then increased to 365 GeV. [9]

The FCC project is consists of two parts: the FCC-ee and the FCC-hh. The FCC-ee is focused on exploring the nature of particles on the smallest scales, with high sensitivity to signs of new physics, such as small deviations from the Standard Model, and the discovery of new particles or forbidden decay processes. The FCC-hh, on the other hand, is designed to collide protons at extremely high energies, which could lead to the discovery of new particles and new physics beyond the Standard Model.

For collider physics, only two main parameters are interested, one is Beam energy, and another is luminosity. As shown in Figure 4.1, the integrated luminosity varies in different modes during the 15 years of FCC-ee operation. luminosity can be determined by parameters, such as bunches, beam size, and beam crossing angle. The full set of parameters is shown in Figure 4.2. At the $t\bar{t}$ threshold, there will be an average spacing of 48 bunches with a period of 3396 ns, and a population of $2.3 \cdot 10^4$ bunches. At this threshold, synchrotron radiation results in the highest energy loss, at 9.2 GeV per turn. In addition to maintaining a constant 2 T magnetic field, the magnet's scaling takes energy losses into account. The high brightness range of FCC-ee is further enhanced by a top-up injection scheme where the beam is refilled during operation. Without top-up injection, the integrated luminosity is expected to be lower than the planned value.

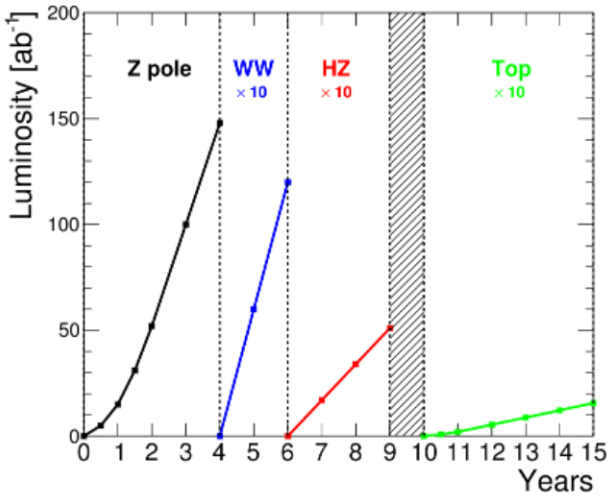

Figure 4.1: FCC-ee integrated luminosities [9]

FCC-ee parameters		Z	W^+W^-	ZH	ttbar	
Beam energy	**GeV**	**45.6**	**80**	**120**	**175**	**182.5**
Luminosity / IP	**10^{34} cm^{-2} s^{-1}**	**230**	**28**	**8.5**	**1.8**	**1.55**
Beam current	mA	1390	147	29	6.4	5.4
Bunches per beam	#	16640	2000	328	59	48
Average bunch spacing	ns	19.6	163	994	2763	3396
Bunch population	10^{11}	1.7	1.5	1.8	2.2	2.3
Horizontal emittance ε_x Vertical emittance ε_y	nm pm	0.27 1.0	0.84 1.7	0.63 1.3	1.34 2.7	1.46 2.9
β_x^* / β_y^*	**m / mm**	**0.15 / 0.8**	**0.2 / 1.0**	**0.3 / 1.0**	**1.0 / 1.6**	
beam size at IP: σ_x^* / σ_y^*	µm / nm	6.4 / 28	13 / 41	13.7 / 36	36.7 / 66	38.2/68
Energy spread: SR / total (w BS)	%	0.038 / 0.132	0.066 / 0.131	0.099 / 0.165	0.144 / 0.196	0.15 / 0.192
Bunch length: SR / total	mm	3.5 / 12.1	3 / 6.0	3.15 / 5.3	2.75 / 3.82	1.97 / 2.54
Energy loss per turn	**GeV**	**0.036**	**0.34**	**1.72**	**7.8**	**9.2**
RF Voltage /station	GV	0.1	0.75	2.0	4/5.4	4/6.9
Longitudinal damping time	turns	1273	236	70.3	23.1	20.4
Acceptance RF / energy (DA)	%	1.9 / ±1.3	2.3 / ±1.3	2.3 / ±1.7	3.5/ (-2.8; +2.4)	3.36 / (-2.8; +2.4)
Rad. Bhabha/ actual Beamstr. Lifetime	min	68 / > 200	59 / >200	38 / 18	37/ 24	40 / 18
Beam-beam parameter ξ_x / ξ_y		0.004 / 0.133	0.01 / 0.141	0.016 / 0.118	0.088 / 0.148	0.099 / 0.126
Interaction region length	mm	0.42	0.85	0.9	1.8	1.8

Figure 4.2: The summary of FCC-ee parameters [9]

The main structure of FCC consists of a circular tunnel with a diameter of 5.5 m and a circumference of 97.75 km, featuring two interaction points (IPs) as shown in Figure 4.3. In addition, an 8 km bypass tunnel with 18 shafts, 14 large caverns, and 12 surface sites is included. Moreover, this tunnel has the potential to be upgraded to a 100 TeV hadron collider as FCC-hh.

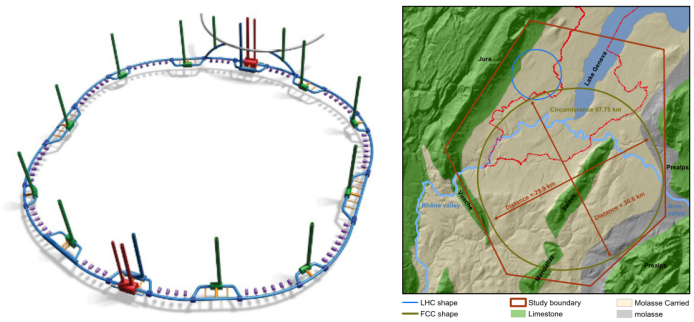

Figure 4.3: The layout of FCC and geological structures. [9]

4.2 IDEA Detector

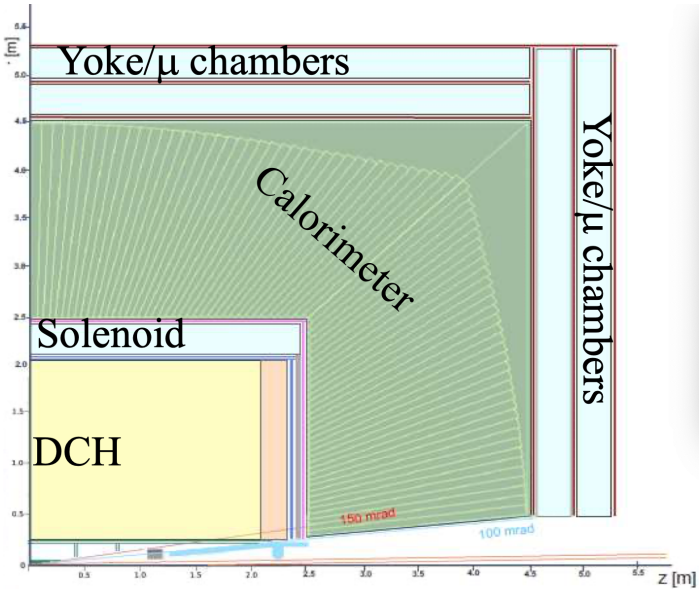

Figure 4.4: The schematic layout of the IDEA detector [10]

The IDEA detector is a multi-purpose detector employed in FCC-ee. As illustrated in Figure 4.4, this detector comprises several subdetectors. The first subdetector is the Silicon pixel strip detectors. The second subdetector is the 2 m outer radius large drift chamber, which provides more than 100 measurements for each charged particle and has excellent particle identification ability. The third subdetector is the vertex detector, which offers extremely high-precision charged particle tracking, and the innermost layer of 3 μm can reconstruct secondary vertices from heavy flavor quarks. The central tracker is enveloped by a 2 T solenoidal magnet, which is followed by the preshower. The preshower measures the resolution of 60 to 70 µm before the electromagnetic shower reaches the calorimeter. The dual-readout calorimeter simultaneously measures the electromagnetic and hadronic components, with a precision of 30% $\sqrt{E}$ for hadronic jets and 10% $\sqrt{E}$ for electromagnetic energy. The last subdetector is the muon detector, which is divided into three stations for better detection. Each muon station provides a spatial accuracy of 400 μm. The three combined can track charged particles at a distance of 5-6 meters from the vertex, enabling the iden-

tification of secondary vertices from long-lived particles. More parameters are shown in Figure 4.5. [11]

Parameters	
vertex technology	silicon
vertex inner/outer radius (cm)	1.7/34
tracker technology	drift chamber and silicon wrapper
tracker half length (m)	2.0
tracker outer radius (m)	2.0
solenoid field (T)	2.0
solenoid bore radius/half length (m)	2.1/3.0
preshower absorber	lead
preshower R_{min}/R_{max} (m)	2.4/2.5
DR calorimeter absorber	copper
DR calorimeter R_{min}/R_{max} (m)	2.5/4.5
overall height/length (m)	11/13

Figure 4.5: The main parameters of the IDEA concept detector [10]

4.3 Simulation and Reconstruction with IDEA Detector

FCC-ee is currently in the design phase, and we need to do a feasibility study, so the data from the simulation will be used in this analysis. DELPHES is a fast and flexible detector simulation package that is used to model the behaviour of particles as they pass through the detector. DELPHES uses a modular approach, allowing users to configure the simulation to include different detector components and to customize the simulation parameters. DELPHES created a simulator for the IDEA detector at FCC-ee by incorporating IDEA's specific parameters [12]. DELPHES IDEA collects a series of data such as electrons, muon, and missing energy for later analysis, and saves Monte Carlo data for checking. Those simulated data will be discussed in more depth in the next section.

5 Monte Carlo Samples

This analysis is based on a simulation generated by the Future Circular Collider Software [13], which is a powerful tool for simulating the behaviour of particles in future particle colliders. The simulation framework consists of three main components: DELPHES, Pythia8, and EDM4HEP, which are part of the Key4HEP structure.

Pythia8 is a Monte Carlo event generator that is used to simulate the initial state of the particles before they interact with the detector. EDM4HEP is a data model that is used to represent the simulated data in a format that is easily analyzed.

Key4HEP is a Turnkey Software Stack that provides all necessary components from simulation to analysis. It was developed and used in the linear collider projects ILC and CLIC as part of a common software stack, iLCSoft. This software stack covers most of the future linear and circular machines that will collide electrons, muons, and hadrons. By using established packages such as ROOT, Geant4, DD4hep, Gaudi, and others, this software stack maximizes the reuse of code, ensures coherency, and maintains program efficiency to avoid duplicating work.

To generate the signal sample and backgrounds, the DelphesPythia8_EDM4HEP command, along with the Pythia command and IDEA card, were used. The Pythia command specifies all initial conditions and event numbers, and at the Monte Carlo level, it takes care of parton showers and their hadronization process. The two tcl files tell the DELPHES program the order of data flow between modules and the collider conditions of this simulation.

Follow the development plan of FCC-ee, and start the plan of $t\bar{t}$ after completing the plan of Z, W, and Higgs. In the first year of the $t\bar{t}$ program, the luminosity was 0.2 ab, which was later increased to 0.34 ab luminosity per year and continued for four years, resulting in a total luminosity of 1.5 ab over five years of operation. In this Monte Carlo simulation, the signal and background events can be predicted by the following equation:

$$N_{expected} = \mathcal{L} \cdot \sigma \tag{5.1}$$

where $\mathcal{L}$ is the integrated luminosity and σ is the event cross-section. Table 5.1 shows the number of events for each process signal and backgrounds.

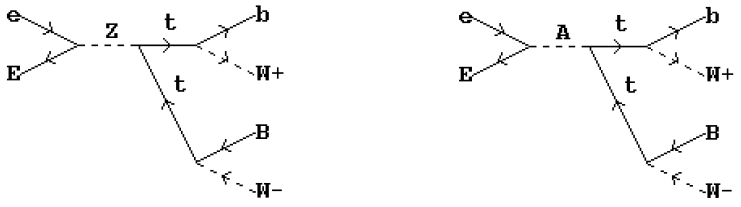

((a)) ((b))

Figure 5.1: Feynman diagrams for $t\bar{t}$ before any cuts. Diagrams are generated by CompHep. [16, 17]

Process	$\sigma[pb]$	$N_{expected}$
$t\bar{t}$	0.452 ± 0.001	687,000
$b\bar{b}$	4.063 ± 0.008	6,094,500
$\Sigma_{q=u,d,s,c} q\bar{q}$	17.034 ± 0.029	25,551,000
$\tau^+\tau^-$	1.901 ± 0.003	2,851,500
W^+W^-	11.203 ± 0.013	16,804,500
ZH	0.13 ± 0.0002	195,000
$ZZ/Z\gamma$	0.856 ± 0.0009	1,284,000
ZW^+W^-	$1.592 \times 10^{-2} \pm 0.007 \times 10^{-2}$	24,000
ZZZ	$7.633 \times 10^{-4} \pm 0.01 \times 10^{-4}$	1,500
Single_top	$2.116 \times 10^{-3} \pm 0.006 \times 10^{-3}$	3,000

Table 5.1: Expected statistics at $\sqrt{s} = 365$GeV with $\mathcal{L} = 1.5ab^{-1}$ [14, 15]

5.1 Signal

The first part of the analysis focuses on the signal of the $t\bar{t}$ production shown in Figure 5.1. The top quark (t) decays quickly, and the CKM matrix describes its decay path. Almost all top quarks decay into a bottom quark and produce a W^+ boson. The W^+ boson has two decay modes: hadronic and leptonic. The probability of each decay mode can be obtained from the branching ratio table of W boson. In this study, we focus on the di-leptonic events, which only account for about 10% of the $t\bar{t}$ pair production [6]. For this target event, we ideally acquire two b-jets and two high-energy charged leptons (e or μ). Due to the mass of the τ lepton, it decays into lighter leptons before being detected by the detector. Data and cross-sections are obtained from Pythia, and there are no restrictions on the decay of the W boson. Later chapters will demonstrate how to obtain di-leptonic data.

5.2 Backgrounds

For $t\bar{t}$ production di-leptonic channel, two high energy lepton with opposite charge, 2 b-jets are the key characteristic, for ee collision, other processes will also produce this characteristic. Simulation of other processes is also necessary for this analysis. The next step is to analyze the background. By calculating the cross-sections, we can estimate the amount of background data. Among them, W^+W^- events and

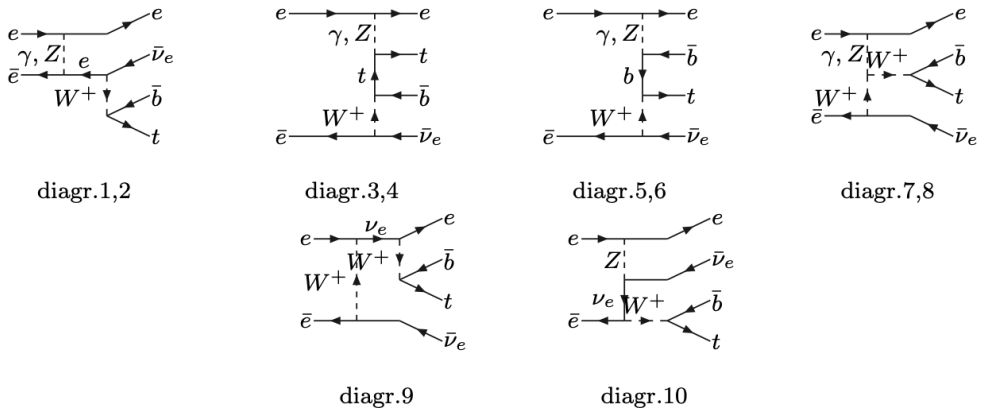

((a))

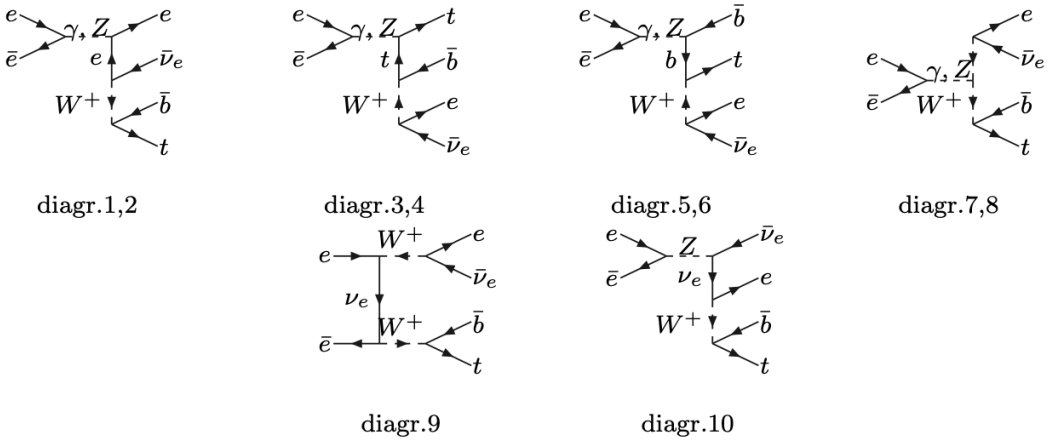

((b))

Figure 5.2: Feynman diagram for single top events. note: second diagram on downside overlap signal events. [20]

light $q\bar{q}$ events account for the most. The events $b\bar{b}$, $ZZ/Z\gamma$, W^+W^-, ZZ, ZH, and $\tau^+\tau^-$ are all generated by Pythia8. The ZWW and ZZZ events are generated by the Whizard Les Houches Event file and then imported into the Pythia command card and made by Pythia8. For single top events, the $e^+e^- \to e^-\bar{\mu_e}t\bar{b}$ Feynman diagram overlaps with $t\bar{t}$, $b\bar{b}$, and W^+W^-, as can be seen in Figure 5.2. Pythia8 avoids creating higher mass particles when dealing with $b\bar{b}$ and W^+W^-, so we only need to manually remove Feynman diagrams that overlap with $t\bar{t}$. Because MadGraph5 has a special code \$\$t to avoid on-shell t, it can produce the data we need. However, due to the removal of Feynman diagrams, errors may occur. Nevertheless, the cross-section of the affected events is low, so it is not expected to cause significant issues [18]. It is important to note that $\mu\mu$ events are not included in the background analysis because they are particles that can be detected by the detector. Furthermore, studies of their properties have shown that the probability of these events surviving the subsequent event selection process is infinitesimally close to zero. [14, 15, 19]

5.3 Anomalous Couplings In Top Production

For the analysis of anomalous top production, we used Whizard to generate data, following a similar process to the previous steps. However, in this case, we modified the model from SM to SM_top_anom. There are ten parameters associated with the ten couplings mentioned in the previous section. Based on research conducted in [21], we fixed three parameters to ensure gauge invariance. We used Whizard to generate seven corresponding files, with only one parameter being modified at a time for a later one-coupling fit. We also performed a two-coupling fit by modifying two couplings at once, combining one-coupling data. The changed and fixed parameters are displayed in Table 5.2 below.

Parameter	Coupling	Gauge freedom
ta_ttA	δd_A^γ	Free
tv_ttA	δd_V^γ	Free
ta_ttZ	δd_A^Z	Fixed
tv_ttZ	δd_V^Z	Fixed
vl_ttZ	δX_{tt}^L	Fixed
vr_ttZ	δX_{tt}^R	Free
tl_tbW_Re	δg_L	Free
tr_tbW_Re	δg_R	Free
vl_tbW_Re	δV_L	Free
vr_tbW_Re	δV_R	Free

Table 5.2: Model parameters and corresponding couplings

5.4 Initial-State Radiation

The different processing methods used by Monte Carlo generators can have a significant impact on their cross-sections. In this analysis, the signal background BSM data is sourced from three different Monte Carlo generators. The cross-sections of Whizard and MG5 do not take into account the ISR effect, whereas for Pythia, the experimental data is generated after the inclusion of ISR data via a process called afterburner. Since the center of mass of FCC-ee is slightly higher than the energy required for $t\bar{t}$-production, after ISR, there is a higher probability that the data will fall on the resonance peak. Therefore, Pythia's cross-section is higher compared to the other Monte Carlo generators. For BSM data, Whizard provides a simple method for generating experimental data. To ensure consistency, the signal and BSM data are generated by Whizard, and the Whizard events are reweighted by comparing Pythia and Whizard SM data.

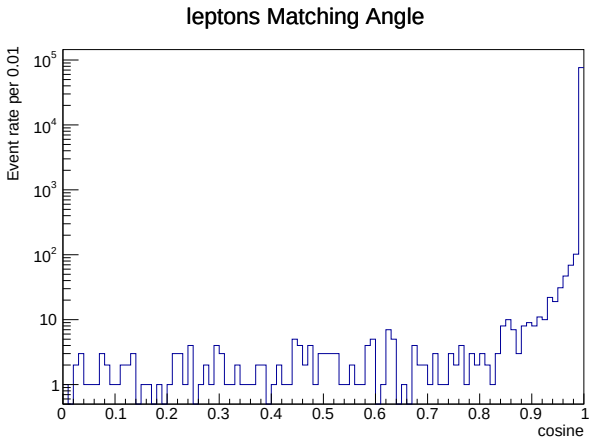

Figure 6.1: Angle matching between RC high energy leptons and MC high energy leptons

6 Reconstructed Particles

In experimental physics, real experiments and simulations play an important role. Real experiments can provide the possibility of new physics, while simulated experiments can allow us to learn more deeply about known physics. As mentioned in the previous chapters, in particle physics, we use Monte Carlo generators to generate simulation data determined by their parameters. For researchers, the output of simulated data can be roughly divided into two categories. The first category is MC truth, which represents real data, and the second category is Reconstructed Particles, which represent what can be observed by detectors. In this section, we will mainly discuss RC data. Among them, two high-energy leptons, two b-jets, and two unobservable neutrinos will be reconstructed from the RC data.

6.1 High Energy Leptons

In the di-leptonic channel, we expect to observe two oppositely charged leptons. Figures 6.1 and 6.2 show the matching angle and energy between the reconstructed (RC) level and Monte Carlo (MC) level. The plots are presented in a logarithmic scale, which clearly shows that the values for both the angle and energy are close to 1, indicating a high degree of agreement between RC and MC levels.

6.2 Jets

In particle physics experiments, quarks carry a color charge and cannot exist in free form due to QCD confinement. As a result, only colorless particles can be found in experiments. When a color-charged particle travels through the detector, it will decay and produce many colorless particles to obey confinement, and those particles will form a jet. Jet definitions are not unique and depend on the jet algorithm used.

A jet algorithm is a computational technique used to group particles produced from a high-energy collision event into a jet. There are several different jet algorithms, such as the Durham, k_T, Cambridge-Aachen (C/A), ee-anti-k_T, and Valencia algorithms,

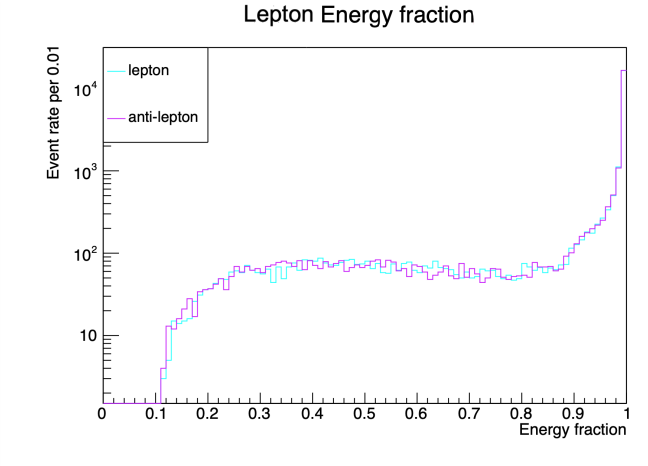

Figure 6.2: Energy matching between RC high energy leptons and MC high energy leptons

which all differ in how they group particles into jets.

Jets are essential to the study of high-energy particle collisions as they provide a way to measure the properties of quarks and gluons. Jet properties, such as the jet energy, jet mass, and jet substructure, can be used to infer the properties of the quark or gluon that produced the jet.

Jet substructure refers to the internal structure of a jet, which can reveal information about the substructure of the particle that produced the jet. Techniques such as jet grooming and jet pruning can be used to remove unwanted contributions from soft radiation, pile-up, or other sources, allowing for a cleaner and more precise measurement of the jet properties.

6.2.1 Jet Algorithms

In particle physics experiments, quarks, which carry a colour charge, cannot exist in free form due to QCD confinement. Therefore, only colourless particles can be found. When a colour-charged particle travels through the detector, it will decay and produce many colourless particles in order to obey confinement, and those particles will form a jet. Jet definitions are not unique and depend on the jet algorithm.

The first type of algorithm is cone algorithms, which were first used in the Tevatron back in the 1980s. Cone algorithms assume that particles in jets will be found within conical regions, resulting in jets with rigid circular boundaries. However, when two jets are close enough, the cones start to overlap, and some particles can be found in multiple jets, making this algorithm no longer collinear safe or infrared safe.

The second type of algorithm is the sequential clustering algorithm. During the "golden era" of jets in the 1990s, several sequential clustering algorithms were proposed. These algorithms assume that jet particles have small differences in transverse momenta, and the algorithm is no longer based on conical regions in $(\eta - \phi)$ space.

All sequential clustering algorithms have a similar method of merging the two closest particles into a pseudo-particle and repeating until the criteria (the minimum distance between two particles is larger than the distance between the beam axis and the detected particle) is met. If this process is repeated until all particles are included, then it is called inclusive clustering. If the process is repeated until a desired number of jets is found, then it is called exclusive clustering. This type of algorithm is preferred by theorists since it is collinear-safe and infrared-safe. However, until the introduction of the FastJet program, experimentalists preferred cone algorithms. [22]

In this analysis, 6 sequential clustering algorithms are demonstrated, those jet algorithms are available through FastJet package [23], some of them are native, and some of them are through the plugin.

"Sequential recombination algorithm
1.Find smallest of d_ij, d_iB
2.If ij, recombine them
3.if iB, call i a jet and remove from list of particles
4.repeat from step 1 until no particles left" [24]
where d_ij depends on algorithms.

Jade Algorithm the distance is defined as

$$d_ij = 2E_iE_j(1 - \cos\theta_{ij}) \tag{6.1}$$

Durham Algorithm the distance is defined as

$$d_ij = \min(E_i^2, E_j^2)(1 - \cos\theta_{ij}) \tag{6.2}$$

k_T **Algorithm** the distance is defined as

$$d_ij = \min(p_{ti}^2, p_{tj}^2)\frac{\Delta R_{ij}^2}{R^2} \tag{6.3}$$

where $\Delta R_{ij}^2 = (y_i + y_j)^2 + (\phi_i + \phi_j)^2$ y is rapidity and ϕ is azimuthal angle.

e^+e^- **Cambridge/Aachen Algorithm** the distance is defined as

$$d_ij = \min(E_i, E_j)\frac{1 - \cos\theta_{ij}}{1 - \cos R} \tag{6.4}$$

e^+e^- **anti-k_T Algorithm** the distance is defined as

$$d_ij = \min(E_i^{-2}, E_j^{-2})\frac{1 - \cos\theta_{ij}}{1 - \cos R} \tag{6.5}$$

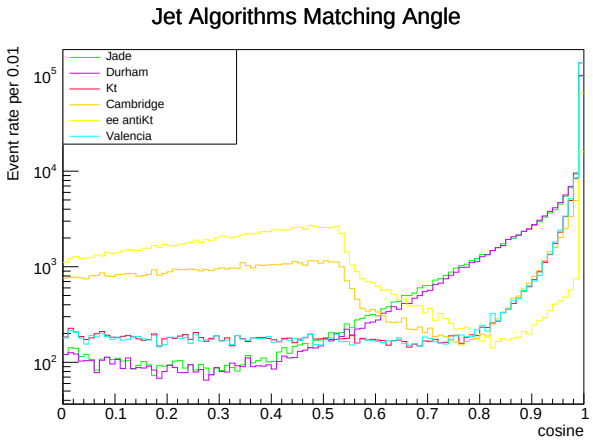

Figure 6.3: Matching angle between RC b-jets and MC b-quarks with six algorithms

Valencia Algorithm the distance is defined as

$$d_i j = \min(E_i^{2\beta}, E_j^{2\beta}) \frac{1 - \cos\theta_{ij}}{1 - \cos R} \tag{6.6}$$

To achieve optimal performance for di-leptonic events, we will compare six different algorithms. To carry out this comparison, we will use data that is simulated by the Whizard program and reconstructed by DELPHES. Since di-leptonic events require only two jets, both of which are b-jets, the production environment is less complicated than in the semileptonic and hadronic channels. However, the presence of two unobservable neutrinos makes the solutions for two neutrinos highly sensitive to the energy and momentum of the jets. Therefore, finding the optimal jet algorithm is significant. The comparison will focus on the matching angle between the RC (reconstructed) level and the MC (Monte Carlo) level, with cosine values of MC b-quarks and RC b-jets selected for the comparison.
Figure 6.3 shows that all six jet algorithms exhibit the highest peaks in the interval where the cosine value is close to 1. However, each algorithm displays some unique characteristics. The ee-antik_T and Cambridge algorithms share similarities in that they both exhibit a second peak in the interval where the cosine value is 0.5. Additionally, there is a relatively large fraction of jets that have a larger matching angle, which may be due to these algorithms occasionally combining two large-angle pseudo-jets. The Durham and Jade algorithms are very similar and exhibit a closely matched trend in the figure. Compared to the Valencia algorithm, Durham and Jade algorithms exhibit a smaller fraction of large-angle jets (cosine close to 1). However, in the interval close to cosine equal to 1, Valencia is more inclined to generate jets that are closer to the direction of the b-quark.
The energy fraction comparison also highlights differences between the various algorithms, as demonstrated in Figure 6.4. The x-axis shows the energy of the b-quark at the MC level, and the y-coordinate represents the fraction between jets and quarks. In the energy range of approximately 50GeV to 95GeV, the energy matching fractions of Jade, Durham, k_T, and Valencia are very similar, while the Cambridge algorithm exhibits an average fraction of 39%, and ee-antik_T only 12%. These results indicate

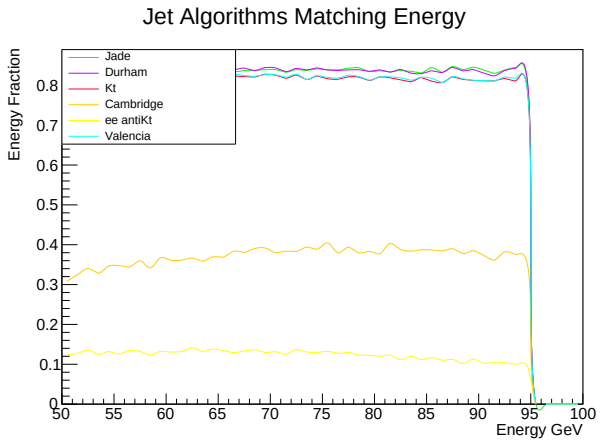

Figure 6.4: Energy matching between RC b-jets and MC b-quarks with six algorithms

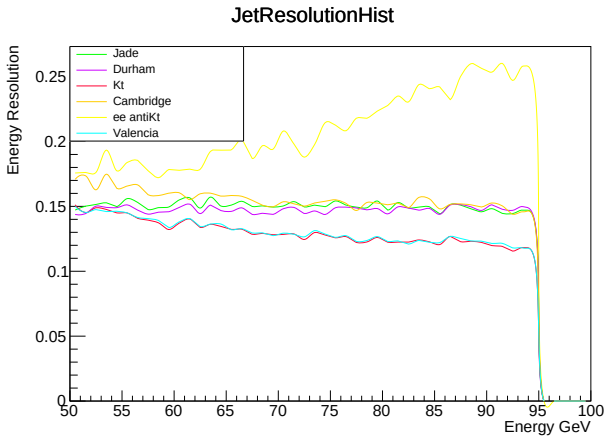

Figure 6.5: Energy resolution of six algorithms

that the Cambridge and ee-antik_T algorithms may not be suitable for use in di-leptonic events.

To provide data support, we have compared the energy resolution of different jet algorithms to determine their sensitivity to energy. We define the energy resolution as:

$$\frac{E_{RC_b-jet} - E_{MC\_b-quark}}{E_{MC\_b-quark}} \tag{6.7}$$

As shown in Figure 6.5, after excluding the ee-antik_T and Cambridge algorithms, we compared the remaining four algorithms and found that, in a di-leptonic environment, the k_T and Valencia algorithms are more sensitive to energy. Based on these results, we have reason to believe that the Valencia and k_T algorithms are more reliable for jet reconstruction under di-leptonic simulation conditions.

6.2.2 Recombination Schemes

After selecting the reconstructed particles using the algorithm, the way in which particles are combined into a pseudo-particle is determined by recombination schemes.

In this analysis, we will compare three recombination schemes: the E-scheme, E0-scheme, and p-scheme.

E-scheme

Parton i and j are replaced by a parton jet k with four-momentum

$$\mathbf{p}_k = \mathbf{p}_i + \mathbf{p}_j \tag{6.8}$$

This scheme is Lorentz invariant, it conserves both energy and momentum. however, the parton jet k has a non-zero mass value, which cannot consistently be accounted for in the QCD calculations.[29]

E0-scheme

The combined parton four-momentum is calculated as

$$E_k = E_i + E_j \tag{6.9}$$

$$\vec{p_k} = \frac{E_k}{|\vec{p_i} + \vec{p_j}|} \cdot (\vec{p_i} + \vec{p_j}) \tag{6.10}$$

the equations show the energy of combined parton are conserved, the mass of parton is set to be zero, momentum is modified to fit parton energy.

p-scheme

The combined parton four-momentum is calculated as

$$\vec{p_k} = \vec{p_i} + \vec{p_j} \tag{6.11}$$

$$E_k = |\vec{p_k}| \tag{6.12}$$

similar to E0-scheme, p-scheme choose p to be conserved value, modify parton energy to fit parton momentum.

Similar to the comparison of jet algorithms, we have compared the influence of different recombination schemes on the matching angle, jet energy, and energy resolution. Figure 6.6 shows the results for the matching angle, Figure 6.7 for jet energy, and Figure 6.8 for energy resolution. All three combination schemes showed similar performance, with no scheme outperforming the others. However, since neutrino calculations are extremely sensitive to the hadronic system, we prioritized the Lorentz invariant property. Therefore, Valencia with E-scheme has been chosen for this analysis.

6.2.3 Jet Clustering and Jet Tagging in FCCAnalyses

The FastJet library, written in C++, provides a user-friendly interface for performing jet clustering using various algorithms. It includes several algorithms designed for clustering particles into jets, such as the k_T algorithm, the Cambridge/Aachen algorithm, and the ee-anti-k_T algorithm. Although FastJet was developed in the hadron collider era, it supports both native jet algorithms and recombination schemes, as well as plugins for ee jet algorithms, such as Valencia, Jade, and Cambridge/Aachen. Jet clustering and tagging utilities have been developed by pioneers in the FCCAnalyses project, and this analysis will use those tools to investigate particle phenomena.

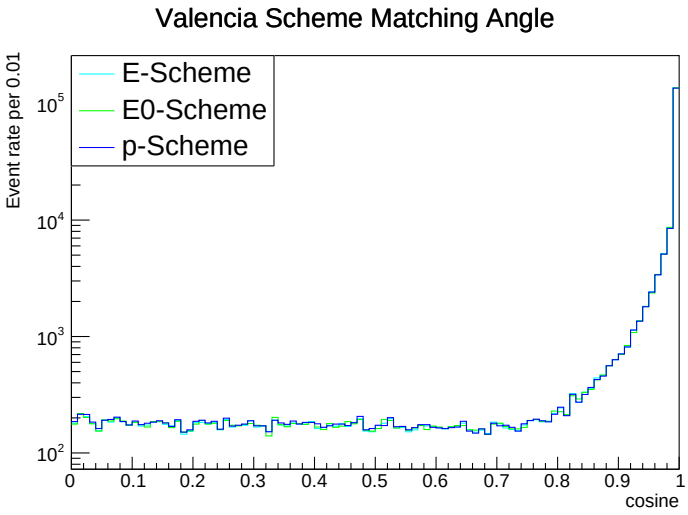

Figure 6.6: Matching angle between RC b-jets and MC b-quarks in Valencia with three recombination schemes

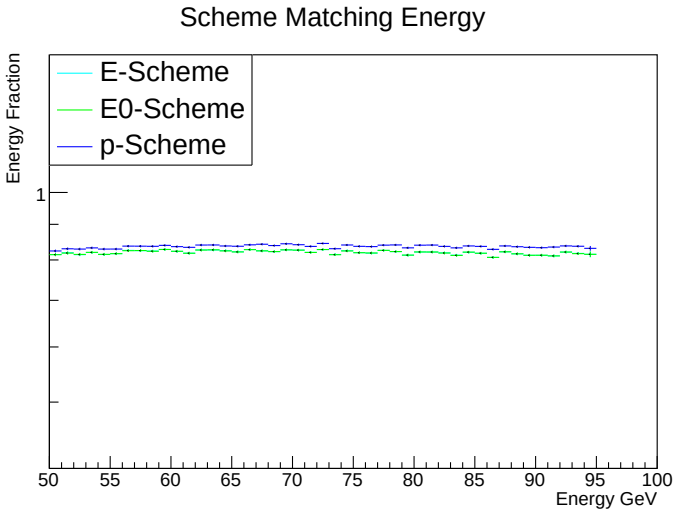

Figure 6.7: Energy matching between RC b-jets and MC b-quarks in Valencia with three recombination schemes

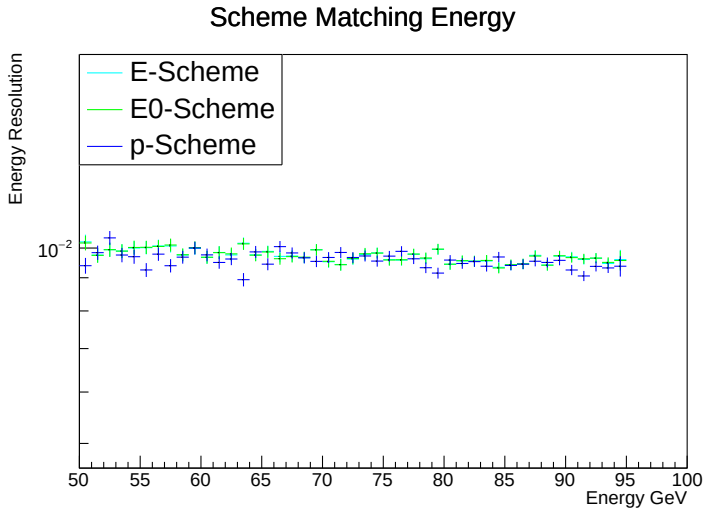

Figure 6.8: Energy resolution of Valencia with three recombination schemes

The FCCAnalyses software uses ROOT dataframe to produce root files, which can be further analyzed using Python or C++. An example of Clustering can be seen in Appendix A.

For most of algorithms, clustering consisted of 5 input parameters, Valencia algorithm needs β, γ value to be extra parameters, which relates to Valencia algorithm distance definition.

The Jet Tagging Utilities were built to check whether a jet originated from a b quark decay. This piece of code can be seen as an extension of clustering. The logic of the code involves checking if the reconstructed jets and Monte Carlo parton match with a small angle. Since the di-leptonic channel consists of only 2 jets, both from b quark decay, jet tagging is useful to distinguish signal events from background. In the IDEA detector environment, the efficiency for b tagging is set to 80%. This is because if some reconstructed particles fly in a direction not covered by the detector, the direction of the "b jet" will shift, and it will no longer be identified as a b-jet.

6.3 Neutrinos

Neutrinos are almost invisible in collider environments because they only experience weak interactions. Therefore, any phenomena raised by neutrinos can only be observed indirectly. Missing energy or missing momentum in particular are likely caused by neutrinos, but they could also be due to detector blind spots. In the di-leptonic channel, two neutrinos originate from two W decay, so the value of missing energy should be large, as shown in Figure 6.9.
Two leptons originating from W decay naturally have high energy. Since muons (μ) and electrons (e) are well-measured particles, we can easily extract those high-energy oppositely charged leptons from the reconstructed particle list. In an ideal scenario, all daughter particles originating from b-quarks are also well-measured, so the sum of the 4-momentum of the hadronic system will be close to the sum of the 4-momentum

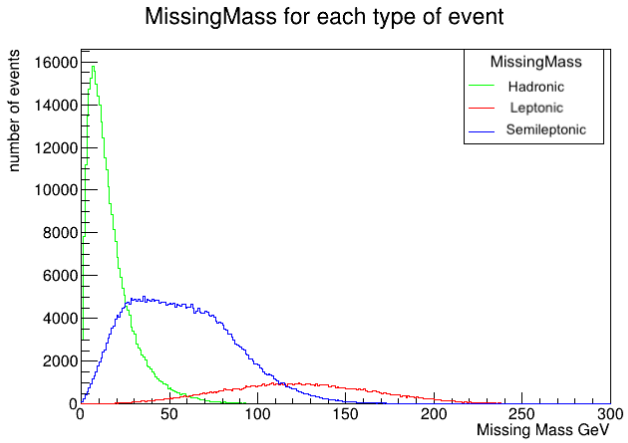

Figure 6.9: In signal events three channels missing mass comparison

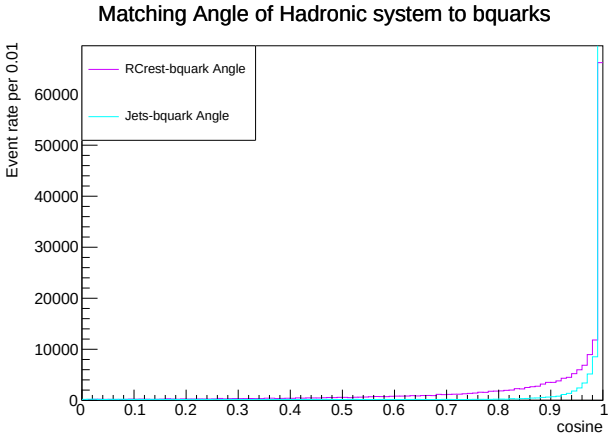

Figure 6.10: Angle matching between RCrest and the sum of two MC b-quarks

of the b-quark pair. RCrest is the way to define this scenario, RCrest is the sum of all RC particles excluding selected leptons. Figure 6.10 illustrates the angle matching comparison, while Figure 6.11 shows the energy matching. Compared to the jets, RCrest is more efficient in defining the total hadronic system. We care about the hadronic system because our di-lepton events involve a 6-particle kinematics problem ($t\bar{t}$ events). By removing the well-defined hadronic system, this problem degenerates to a 4-particle problem (WW-like events), allowing us to calculate neutrino solutions. [25] A General Lorentz Transformation Matrix can be written as

$$\begin{bmatrix} \gamma & -\gamma\beta_x & -\gamma\beta_y & -\gamma\beta_z \\ -\gamma\beta_x & 1+(\gamma-1)\frac{\beta_x^2}{\beta^2} & (\gamma-1)\frac{\beta_x\beta_y}{\beta^2} & (\gamma-1)\frac{\beta_x\beta_z}{\beta^2} \\ -\gamma\beta_y & (\gamma-1)\frac{\beta_x\beta_y}{\beta^2} & 1+(\gamma-1)\frac{\beta_y^2}{\beta^2} & (\gamma-1)\frac{\beta_y\beta_z}{\beta^2} \\ -\gamma\beta_z & (\gamma-1)\frac{\beta_x\beta_z}{\beta^2} & (\gamma-1)\frac{\beta_z\beta_y}{\beta^2} & 1+(\gamma-1)\frac{\beta_z^2}{\beta^2} \end{bmatrix} \tag{6.13}$$

where $\gamma = \frac{1}{\sqrt{1-\beta^2}}$ and $\beta = \frac{v}{c}$.

After obtaining the four-dimensional momentum of the hadronic system, we can reconstruct the back-to-back WW decay event through Lorentz transformations.

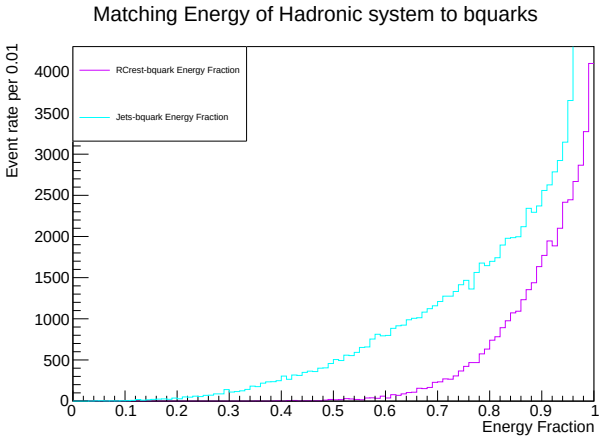

Figure 6.11: Energy matching between RCrest and the sum of two MC b-quarks

We start with the first constraint the W^- energy conservation:

$$p^0_{\bar{v}} = p^0_{W^-} - p^0_l \tag{6.14}$$

for $l\bar{v}$ decay product, which is equivalent with ($m_\mu = 0$ for SM)

$$\vec{p_{\bar{v}}}^{\,2} = (p^0_{W^-} - p^0_l)^2 \tag{6.15}$$

and similar for W^+,

$$\vec{p_v}^{\,2} = (p^0_{W^+} - p^0_{\bar{l}})^2 \tag{6.16}$$

The second constraint, total momentum conservation for the whole events

$$\vec{p_v} = -(\vec{p_{\bar{v}}} + \vec{p_l} + \vec{p_{\bar{l}}}) \tag{6.17}$$

insert Equation 6.17 to Equation 6.16, it leads to

$$(\vec{p_l} + \vec{p_{\bar{l}}}) \cdot \vec{p_{\bar{b}}} = p^0_{W^+}(p^0_{\bar{l}} + p^0_l) - (p^0_l)^2 - \vec{p_l} \cdot \vec{p_{\bar{l}}} + \frac{1}{2}(m_l + m^2_{\bar{l}}) \tag{6.18}$$

The third constraint is that the invariant mass of lepton-antineutrino system must equal the W^- mass

$$(p_l + p_{\bar{v}})^2 = m^2_W \tag{6.19}$$

and leads to

$$\vec{p_l} \cdot \vec{p_{\bar{v}}} = p^0_{W^+} p^0_l - (p^0_l)^2 - \frac{1}{2}m^2_W + \frac{1}{2}m^2_l \tag{6.20}$$

and

$$\vec{p_{\bar{l}}} \cdot \vec{p_{\bar{v}}} = -p^0_{W^+} p^0_{\bar{l}} - \vec{p_l} \cdot \vec{p_{\bar{l}}} + \frac{1}{2}m^2_W + \frac{1}{2}m^2_{\bar{l}} \tag{6.21}$$

where the lepton and anti-lepton momentum are unlikely to be parallel, so $\vec{p_l}$,$\vec{p_{\bar{l}}}$,$\vec{p_l} \times \vec{p_{\bar{l}}}$ could form a basis in the momenta space. Therefore neutrino momentum can be expressed as

$$\vec{p_{\bar{v}}} = a\vec{p_l} + b\vec{p_{\bar{l}}} + c(\vec{p_l} \times \vec{p_{\bar{l}}}) \tag{6.22}$$

at the last, by collecting all infomation, a, b, and c parameter can be expressed as

$$\begin{pmatrix} a \\ b \end{pmatrix} = \frac{1}{\vec{p_l}^2\vec{p_{\bar{l}}}^2 - (\vec{p_l}\vec{p_{\bar{l}}})^2} \begin{pmatrix} \vec{p_{\bar{l}}}^2 & -\vec{p_l}\cdot\vec{p_{\bar{l}}} \\ -\vec{p_l}\cdot\vec{p_{\bar{l}}} & \vec{p_l}^2 \end{pmatrix} \begin{pmatrix} p^0_{W^+}p^0_l - (p^0_l)^2 - \frac{1}{2}m^2_W + \frac{1}{2}m^2_l \\ -p^0_{W^+}p^0_{\bar{l}} - \vec{p_l}\cdot\vec{p_{\bar{l}}} + \frac{1}{2}m^2_W + \frac{1}{2}m^2_{\bar{l}} \end{pmatrix} \quad (6.23)$$

$$c^2 = \frac{1}{|\vec{p_l}\times\vec{p_{\bar{l}}}|^2}(p^0_{W^+} - p^0_l)^2 - a^2\vec{p_l}^2 - b^2\vec{p_{\bar{l}}}^2 - 2ab\vec{p_l}\cdot\vec{p_{\bar{l}}} \quad (6.24)$$

due to the restrictions, the sign of c cannot be determined, and we have a twofold discrete ambiguity.

After calculating the two neutrino solutions, we need to apply another Lorentz transformation to translate them back to the lab frame. Figure 6.12(a) and Figure 6.12(b) show the neutrino solutions with respect to MC level. Since neutrino solutions are sensitive to the measurements of the leptons and the hadronic system, the blurring of the neutrino momentum is expected.

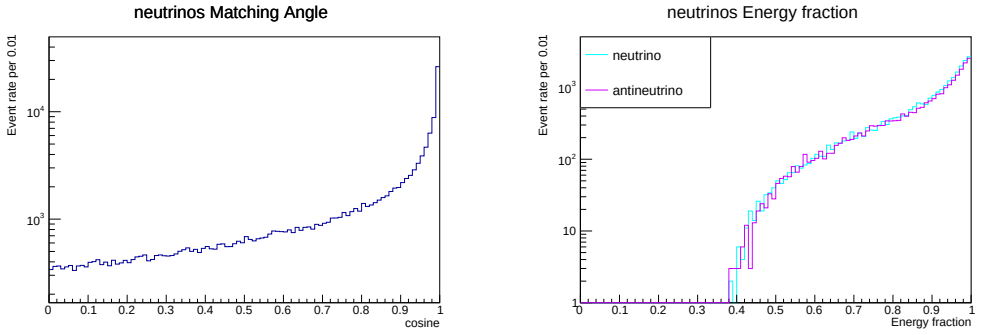

(a) (b)

Figure 6.12: The angle matching between calculated neutrinos and MC neutrinos is on the left, and the energy matching between calculated neutrinos and MC neutrinos is on the right

7 Event Selection

The definition of the signal and backgrounds has been provided in Section 5. In this section, we will discuss the optimal methods for recovering the signal from backgrounds. This will be done in two parts: the first part will focus on object identification, while the second part will determine the signal region through event selection.

7.1 Object Identification

In order to understand the motivation behind different selection criteria, we start with the characteristics of $t\bar{t}$ production. From the CKM matrix mentioned in section 2, almost all of the top quarks will decay into bottom quarks and generate a W boson. Among them, the bottom quark will eventually form a b-jet that will be detected, while the W boson will continue to decay to produce a high-energy lepton and a neutrino, with a branching ratio of approximately 33.3%. Alternatively, the W boson can decay through hadronization to form two jets, with a branching ratio of 66.6%. The final product of dileptonic events is relatively simple compared to other processes: two high-energy leptons, a large missing transverse momentum, and two b-jets. For neutrino missing momenta, there is no unambiguous solution through the kinematics shown in section 6, so this issue will be elaborated on in later chapters.

In collider physics, leptons, especially electrons and muons, provide clear signals and are easily identified. Tau leptons (1.777 GeV) have much higher mass than electrons (0.511 MeV) and muons (0.106 GeV), and since particle lifetime depends on mass ($\tau \propto \frac{1}{m^5}$), taus will decay inside the detector, with only decay products seen. The research of taus needs to be revisited in future works. From the data on tau branching ratio, (17.4% $\tau^- \to \mu^- \bar{\nu}_\mu \nu_\tau$) and (17.8% $\tau^- \to e^- \bar{\nu}_e \nu_\tau$) [26], hence approximately 35.2% of taus decay into lighter leptons. Meanwhile, in di-leptonic events, only 12.4% of tau events will be misidentified as lighter lepton events. In the events, more than one lepton can be seen from a hadronization process, but the lepton from the W leptonic decay is assumed to have the highest energy, due to it happening in the early stage of decay. This high-energy lepton assumption can be considered as part of the preselection. From Figure 7.1, we can see that in the process we are interested in, the highest energy lepton from the leptonic channel and the hadronic channel are shown, and roughly a 10 GeV energy cut is ideal to distinguish W leptonic decays from hadronic decays.

The di-leptonic events are accepted by searching reconstructed particles for two high-energy leptons with opposite charges. The remaining high-energy leptons are all accounted for as sub-products originally from b-quark decays. In this analysis, jets are reconstructed with FastJet, and 3 jets are used for further investigation. Two opposite charged high-energy leptons are excluded from the clustering, and the Valencia algorithm with E-scheme is used to define these 3 jets. The ability to identify b-jets has been set to 80%, which is the efficiency set in the Delphes card for the IDEA detector. However, 80% efficiency would result in a 36% mis-tagging rate, so at least 1 b-tagged event is also worth checking.

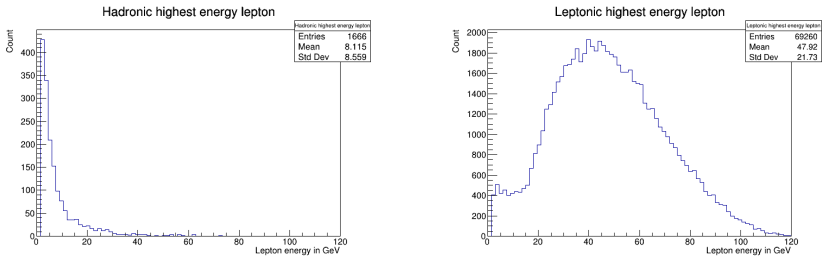

((a)) ((b))

Figure 7.1: Highest energy distribution for leptonic and hadronic channel

7.2 Signal Selection

Signal selection is crucial for picking out the desired signal from a significant number of background events, as seen from Table 5.1 where 687,000 signal events are mixed with a large number of background events. Experimentalists have developed two optimized selection cut strategies for this situation. The first strategy is based on the significance defined as:

$$\text{Significance} = \frac{sig}{\sqrt{sig + bkg}} \tag{7.1}$$

where sig represents the number of signal events left after cuts, and bkg represents the number of background events. The second strategy is based on the product of efficiency and purity (PE) and can be defined as:

$$\text{Efficiency} = \frac{\text{sig}}{\text{sig}_{\text{tot}}} \tag{7.2}$$

$$\text{Purity} = \frac{\text{sig}}{\text{sig} + \text{bkg}} \tag{7.3}$$

$$\text{PE} = \frac{\text{sig}}{\text{sig}_{\text{tot}}} * \frac{\text{sig}}{\text{sig} + \text{bkg}} \tag{7.4}$$

where sig_{tot} is the total number of signal events before the cut.
The $\varepsilon * \text{p}$ strategy is well-known and has been used for decades [27], so this analysis will be based on this strategy.

7.2.1 Pre-selection

Pre-selection is an important step in event selection as it helps to remove irrelevant events and reduces the computational burden. In this analysis of the di-leptonic channel, two pre-selections were chosen: high-energy leptons and b-jets. The high-energy lepton pre-selection requires acquiring two high-energy leptons with a threshold of 10 GeV to distinguish between hadronic and leptonic decays, thereby removing most of the irrelevant events. The b-jet pre-selection involves identifying b-jets, which are crucial for separating signal events from background events. section 4 states that b-tagging has an efficiency of 80%, which means that acquiring 2-bjets would remove 36% of signal events. However, discarding such a significant number of signal events is not ideal. Therefore, with later cuts, it is possible to preserve some events and increase the significance of the signal data. In this case, 1-bjet pre-selection is ideal.

Table 7.1 shows how many events passed the pre-selection.

Among the events that pass the pre-selection, two processes are worth discussing. The first is the $\tau^-\tau^+$ process, which survives the lepton filter but cannot form b-jets. As a result, all $\tau^-\tau^+$ events are removed by this pre-selection. The second process is the $b\bar{b}$ process, for which the b-jet filter has little impact, but the lepton filter removes almost all events.

Pre-selection	Events
all backgrounds	26,917 ± 29.7
$t\bar{t}$	26,174 ± 57.9
$b\bar{b}$	116 ± 0.2
$\Sigma_{q=u,d,s,c} q\bar{q}$	7 ± 0
$\tau^+\tau^-$	0 ± 0
W^+W^-	5 ± 0
ZH	6,291 ± 6.7
$ZZ/Z\gamma$	19,818 ± 20.8
ZW^+W^-	145 ± 0.6
ZZZ	33 ± 0
Single_top	501 ± 1.4

Table 7.1: Events passed pre-selection

7.2.2 Selection

In this section, we analyze the observables, and a list of the considered observables is shown in Table 7.2. Among them, ZH and ZZ are the most dominant backgrounds. Therefore, it is expected that two same-flavor particle pair productions will be produced on the Z resonance peak. For the two jets, the invariant mass of the two leptons, and the missing mass (neutrino), we need to consider the Z mass pole carefully. We define the distance as

$$d_{ij} = \min(E_I^2, E_j^2)\frac{1-\cos\theta_{ij}}{M_{ij}} \tag{7.5}$$

The reason for defining distance is that since the signal only consists of two b-jets, acquiring three means that two of them are likely to be close in distance. This means that we can determine the cuts by analyzing the overlapping jets. Another observable is thrust [28]. Thrust is defined as

$$T = \max\frac{\sum|\vec{p_i}|\cdot\hat{n}_T}{|\vec{p_i}|} \tag{7.6}$$

where $\hat{n}_T$ defines the direction of maximum energy flow. The T value is from 0.5 to 1, where 0.5 is more global-like ($t\bar{t}$ events), and 1 is more pencil-like ($\tau\tau$ events).

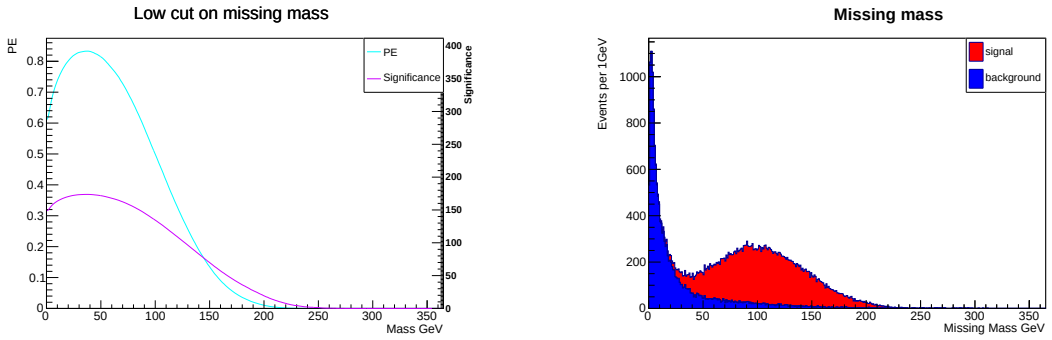

((a)) ((b))

Figure 7.2: PE plots and distribution of missing mass (discard all events with missing mass < 40GeV)

Observables
Highest energy lepton energy
Second highest energy lepton energy
Missing mass
Angle of two small energy jets
Two lepton invariant mass
All jets invariant mass
Two lepton invariant mass at Z mass pole
All jets invariant mass at Z mass pole
Two small energy jets distance
Missing mass at Z mass pole
Thrust

Table 7.2: List of observables for selection

This selection is an iterative process in which all observables (excluding one of the three Z poles) are scanned from the lower bound to the upper bound, and also from the upper bound to the lower bound. Three Z pole observables are started from the Z mass (91.2GeV) to both sides. Collect all PE values, choose the highest one as the first cut, and repeat the process, until the PE value no longer increases.

The first cut is to cut the missing mass at the lower bound, as shown in Figure 7.2. Panel (a) shows the PE value as a function of the scanned missing mass from low to high, with the significance also plotted, which has a similar shape to the PE, and in this section, event selection is based on the PE curve. Panel (b) shows the distribution of events, where the blue curve corresponds to the backgrounds and the red curve corresponds to the signal.

The remaining plots can be found in Appendix B. After removing events with missing mass < 40GeV, we iterate again and place the second cut on the lepton invariant mass around the Z pole (93.05GeV $>$ lepton invariant mass $>$ 89.35GeV). From the event distribution plots, we can see a clear peak around the Z mass. Upon cross-checking Table 7.1, we can see that the ZZ channel is the majority of backgrounds, so this cut

also significantly increases the PE value. Additionally, since the Z boson creates a lepton and its antiparticle, and the lepton flavor is well-defined in the detector, we can remove events at this cut and ensure that the lepton pair flavor is identical. The next cut is on the highest energy lepton energy, by removing events with highest lepton energy $<$ 18GeV and $>$ 106GeV, the PE value increases. The next cut is a lepton invariant mass cut on the lower side, placed at $<$ 6.0GeV. Two more cuts are placed on missing mass $>$ 256GeV and two jets minimum angle $>$ 4 degrees, respectively. For the remaining cuts, some of them do increase the PE value, but it is too small to make a significant difference. Tables 7.3 and 7.4 summarize the cut flow.

Selection	Signal	Backgrounds	ϵ_{sig}	ϵ_{bkg}	PE
Initial	26,174 ± 57.9	26,917 ± 29.7	1.00	1.00	0.49
Missing mass $<$ 40 GeV	24573 ± 54.4	3172 ± 3.5	0.94	0.12	0.83
89.35 GeV $<$ Z cut $<$ 93.05 GeV	23957 ± 53	2562 ± 2.8	0.92	0.10	0.88
Highest energy lepton $>$ 106 GeV	23808 ± 52.7	2215 ± 2.4	0.91	0.08	0.91
Highest energy lepton $<$ 18 GeV	23738 ± 52.5	2124 ± 2.3	0.91	0.08	0.92
Lepton invariant mass $<$ 6 GeV	23731 ± 52.5	2091 ± 2.3	0.91	0.08	0.92
Missing mass $>$ 256 GeV	23730 ± 52.5	2078 ± 2.3	0.91	0.08	0.92
Jets minimum angle $<$ 4.0 degree	23699 ± 52.4	2044 ± 2.3	0.91	0.08	0.92

Table 7.3: Cut flow for signal and backgrounds

Selection	$t\bar{t}$	$b\bar{b}$	$\Sigma_{q=u,d,s,c} q\bar{q}$	$\tau^+\tau^-$	W^+W^-
Missing mass < 40 GeV	24573 ± 54.4	81 ± 0.2	7 ± 0	0 ± 0	3 ± 0
89.35 GeV < Lepton invariant mass < 93.05 GeV, same flavor	23957 ± 53	81 ± 0.2	6 ± 0	0 ± 0	3 ± 0
Highest energy lepton > 106 GeV	23808 ± 52.7	77 ± 0.1	6 ± 0	0 ± 0	2± 0
Highest energy lepton < 18 GeV	23738 ± 52.5	53 ± 0.1	6± 0	0± 0	2± 0
Lepton invariant mass < 6 GeV	23731 ± 52.5	27 ± 0	2± 0	0± 0	2 ± 0
Missing mass > 256 GeV	23730 ± 52.5	21 ± 0	1± 0	0± 0	2±0
Jets minimum angle < 4.0 degree	23699 ± 52.4	21 ± 0	1±0	0±0	2±0
Selection	ZH	$ZZ/Z\gamma$	ZW^+W^-	ZZZ	Single_top
Missing mass < 40 GeV	803 ±1.2	1693±1.7	128 ±0.5	10±0	448±1.3
89.35 GeV < Lepton invariant mass < 93.05 GeV, same flavor	635±1	1278±1.3	123±0.5	2±0	434±1.2
Highest energy lepton > 106 GeV	578 ± 0.9	1030±1	108±0.4	2±0	412±1.2
Highest energy lepton < 18 GeV	560 ± 0.9	987±1	108±0.4	2±0	412±1.2
Lepton invariant mass < 6 GeV	559 ±0.9	979±1	108 ±0.4	2±0	412±1.2
Missing mass > 256 GeV	559 ±0.9	973±1	108 ±0.4	2±0	411±1.2
Jets minimum angle < 4.0 degree	559±0.9	948 ±1	108 ±0.4	2±0	411±1.2

Table 7.4: Cut flow for all process

8 Kinematic Fitting

In the words of William Blake, "To see a world in a wild flower, and a bodhi in a leaf." Experiments can be considered the leaves in the world of science. In the field of particle physics, each collision between particles has the potential to produce both desired and undesired events. In some cases, desired events are discarded while undesired ones are preserved, introducing bias into the results. While this experimental bias cannot be entirely eliminated, it can be minimized by collecting a large amount of collision data. By applying specific constraints, valid data may be discarded, but a larger amount of invalid data is also removed. This approach enables experimentalists to narrow the range of uncertainty around the parameter, bringing it closer to the true value of nature.

8.0.1 Simple Rescaling

A method to improve the measurements of reconstructed objects is setting the mass of particles to massless. The energy is assumed to be fixed, and it fulfils the condition

$$\sum_{i=1}^{4} \mathbf{p}_i = 0 \tag{8.1}$$

and the momentum is rescaled by

$$\vec{p_j} = E_j \frac{\vec{p_j}}{|\vec{p_j}|} \tag{8.2}$$

the direction of jets therefore preserved. [25]

8.1 Constrained Fit

the following section is based on [29]. The least-square methods are simple yet powerful statistical tools. The least squares principle is to minimise the sum of squares of deviations Δy_i between the model and data. The sum of squared deviations could be written in different forms:

$$S = \sum_{i=1}^{n} \Delta y_i^2 \qquad S = \sum_{i=1}^{n} (\frac{\Delta y_i}{\sigma_i})^2 \qquad S = \Delta y^T V^{-1} \Delta y \tag{8.3}$$

The principle of least squares requires to minimise the sum of squared deviations

$$S = \sum_{i=1}^{n} (y - y_i)^2 = minimum \tag{8.4}$$

and mean value of n measured value y_i

$$\hat{y} = \sum_{i=1}^{n} \frac{y_i}{n} \tag{8.5}$$

In di-leptonic events, two unmeasurable neutrinos have ambiguity in momentum, so least square methods can help to choose the best neutrino solution to satisfy constraints.

A linear or non-linear (equality) constraint could be written as

$$f_k(a =_{true}, y_{true}) = 0 \qquad k = 1, 2, \ldots, m \tag{8.6}$$

where a_{true} and y_{true} are equivalent to the expectation value if there are a large number of measurements. k represents the number of constraints.
The Method of Lagrange multipliers can be used to minimise the sum of squared

$$S(a, \Delta y) = \Delta y^T \mathbf{W} \Delta y \tag{8.7}$$

under the conditions

$$f_k(a, y + \Delta y = 0 \qquad k = 1, 2, \ldots, m) \tag{8.8}$$

where $\mathbf{W}$ is the inverted covariance matrix of the data, also called as a weight matrix. The method of Lagrange multipliers defines a new function

$$L(a, \Delta y) = S(a, \Delta y) + 2 \sum_{k=1}^{m} \lambda_k f_k(a, y + \Delta y) \tag{8.9}$$

for this equation, the necessary condition is for a local extremum with respect to all parameters (Δy, a and λ) is equivalent to the condition which minimises the sum of squared under the condition $f_k(a, y + \Delta y = 0)$.
The solution simultaneously fulfils

$$\frac{\partial L}{\partial y} = 0 \qquad \frac{\partial L}{\partial a} = 0 \qquad \frac{\partial L}{\partial \lambda} = 0 \tag{8.10}$$

In general, the problem is Non-linear, and Non-linear conditions can be linearised by Taylor-expansion[70]

$$f_k(a^n, y^n) + \sum_j \frac{\partial f_k}{\partial a_j^{n+1}} (\Delta a_j^{n+1} - \Delta a_j.) + \sum_i \frac{\partial f_k}{\partial y_i^{n+1}} (\Delta y_i^{n+1} - \Delta y_i.) \approx 0 \tag{8.11}$$

and function L for the $(n+1) - th$ iteration can be rewritten as

$$L = \Delta y^T \mathbf{V}(y)^{-1} \Delta y + 2\lambda^T (A\Delta a + B\Delta y - c) \tag{8.12}$$

and

$$c = A\Delta a^n + B\Delta y^n - f \tag{8.13}$$

where

$$A = \begin{pmatrix} \partial f_1/\partial a_1 & \partial f_1/\partial a_2 & \ldots & \partial f_1/\partial a_p \\ \partial f_2/\partial a_1 & \partial f_2/\partial a_2 & \ldots & \partial f_2/\partial a_p \\ \ldots & \ldots & \ldots & \ldots \\ \partial f_m/\partial a_1 & \partial f_m/\partial a_1 & \ldots & \partial f_m/\partial a_p \end{pmatrix} \qquad f = \begin{pmatrix} f_1(a^n, y^n) \\ f_2(a^n, y^n) \\ \ldots \\ f_m(a^n, y^n) \end{pmatrix} \tag{8.14}$$

$$B = \begin{pmatrix} \partial f_1/\partial y_1 & \partial f_1/\partial y_2 & \ldots & \partial f_1/\partial y_n \\ \partial f_2/\partial y_1 & \partial f_2/\partial y_2 & \ldots & \partial f_2/\partial y_n \\ \ldots & \ldots & \ldots & \ldots \\ \partial f_m/\partial y_1 & \partial f_m/\partial y_1 & \ldots & \partial f_m/\partial y_n \end{pmatrix} \tag{8.15}$$

the system of equations to be solved in the general case are

$$\begin{pmatrix} W & 0 & B^T \\ 0 & 0 & A^T \\ B & A & 0 \end{pmatrix} \begin{pmatrix} \Delta y \\ \Delta a \\ \lambda \end{pmatrix} = \begin{pmatrix} 0 \\ 0 \\ c \end{pmatrix} \tag{8.16}$$

and

$$\begin{pmatrix} W & 0 & B^T \\ 0 & 0 & A^T \\ B & A & 0 \end{pmatrix}^{-1} = \begin{pmatrix} C_{11} & C_{21}^T & C_{31}^T \\ C_{21} & C_{22} & C_{32}^T \\ C_{31} & C_{32} & C_{33} \end{pmatrix} \tag{8.17}$$

where

$$C_{11} = V - VB^T W_B BV + VB^T W_B A W_A^{-1} A^T W_B BV \tag{8.18}$$
$$C_{21} = -W_A^{-1} A^T W_B BV \tag{8.19}$$
$$C_{22} = W_A^{-1} \tag{8.20}$$
$$C_{31} = W_B BV - W_B A W_A^{-1} A^T W_B BV \tag{8.21}$$
$$C_{32} = W_B A W_A^{-1} \tag{8.22}$$
$$C_{33} = -W_B + W_B A W_A^{-1} A^T W_B \tag{8.23}$$

$W_B = (BVB^T)^{-1}$ and $W_A^{-1} = (A^T W_B A)^{-1}$ V for measurements in symmetric, and C_{11}, C_{22}, C_{31} and C_{33} are also symmetric so we can arrive

$$V \begin{pmatrix} \hat{y} \\ \hat{a} \\ \hat{\lambda} \end{pmatrix} = \begin{pmatrix} C_{11} & C_{21}^T & 0 \\ C_{21} & C_{22} & 0 \\ 0 & 0 & -C_{33} \end{pmatrix} \tag{8.24}$$

The covariance matrix shows that Lagrange multipliers are independent to measured and unmeasured particles.

8.2 Inclusion of Breit-Wigners

The derivations in this section are based on [25]. After including four-momentum conservation, we have an additional four constraints to the problem: mass constraints. When two t-quarks are created, they decay very quickly into 2 b-quarks and 2 W bosons, which will decay further. For one of the W bosons, its mass will be equal to the invariant mass of the neutrino and lepton, and the same applies to the other W boson. W bosons and b-jets can be reconstructed into Top quarks, allowing us to add four mass constraints. Due to the Breit-Wigners distribution, the top and W bosons do not need to be completely on the peak, so the constraints can be relaxed by the Breit-Wigners distribution. The function L can be extended accordingly.

$$L(y) = S(y) + g(x) + 2\sum_{k=1}^{m} \lambda_k f_k(a, y, x) \tag{8.25}$$

$g(x)$ only depends on the scalar, and it could be a penalty function. the measured parameters can be corrected as

$$\begin{pmatrix} y^{n+1} \\ x^{n+1} \end{pmatrix} = \begin{pmatrix} y_0 \\ x^n \end{pmatrix} - \tilde{V} \begin{pmatrix} 0 \\ \frac{1}{2}\frac{d^2 g}{dx^2}|_{x=x^n}^{-1} \end{pmatrix} + \tilde{V} B^T (B\tilde{V}B^T)^{-1} \tag{8.26}$$

$$\times[A(a^n - a_0) + B\begin{pmatrix} y^n - y_0 \\ \frac{dg}{dx}|^{-1}_{x=x^n}\frac{1}{2}\frac{d^2g}{dx^2}|_{x=x^n} \end{pmatrix} - f(a^n, y^n, x^n)] \tag{8.27}$$

and free parameters can be written as

$$a^{n+1} = a_0 + W_A^{-1}A^T W_B \times [A(a^n - a_0) + B\begin{pmatrix} y^n - y_0 \\ \frac{dg}{dx}|^{-1}_{x=x^n}\frac{1}{2}\frac{d^2g}{dx^2}|_{x=x^n} \end{pmatrix} - f(a^n, y^n, x^n)] \tag{8.28}$$

8.3 ABC-Parametrisation

In order to use constrained fit, we need to use particle momentum in a way that can be associated with Gaussian distribution, the otherwise constrained fit will be meaningless. Similar to energy resolution of the detectors, we could write reconstructed jets as

$$\vec{P_j^r} = a_j|\vec{P_j^m}|\vec{P_j^a} + b_j\vec{P_j^b} + c_j\vec{P_j^c} \tag{8.29}$$

where $\vec{P_j^m}$ is measured jet momentum $\vec{P_j^a}$, $\vec{P_j^b}$, $\vec{P_j^c}$ is defined as

$$\tag{8.30}$$

$$\vec{P_j^a} = \frac{\vec{P_j^m}}{|\vec{P_j^m}|} \tag{8.31}$$

$$\vec{P_j^b} = \frac{1}{\sqrt{P_{x,m}^2 + P_{y,m}^2}}(P_y^m, -P_x^m, 0) \tag{8.32}$$

$$\vec{P_j^c} = \frac{1}{|\vec{P_j^m}|^2\sqrt{P_{x,m}^2 + P_{y,m}^2}}(-P_x^m P_z^m, -P_y^m P_z^m, p_{x,m}^2 + P_{y,m}^2) \tag{8.33}$$

from formula, we can see the $\vec{P_j^a}$ is the direction of the original particle, and the initial parameter can be defined as $\{a_j, b_j, c_j\} = \{1, 0, 0\}$

8.4 ABCfit++ Software Package

The ABCfit++ software package was written in connection with this analysis. [30]

The following classes are used in this analysis:

Coordinate Representation: CoorRepr.h is the basic class, and it contains 4 derived classes, and they are PxPyPzE.h, PxPyPzM.h, PtEtaPhiM.h, and ABCD.h, and each class defined how representation transforms itself. Naively we know PxPyPzE, 3 momenta and energy, and PxPyPzM is just straightforward replacing energy to mass. PtEtaPhiM and ABCD are more tricky. Pt is transverse momentum, Eta the pseudorapidity, Phi the polar angle in the transverse plane, and M mass as usual. ABCD coordinates were introduced in previous section, the D again, the mass. In addition, the default expectation values of the first three representations are simply themselves, but the ABCD is {1,0,0,m}.

Particle Object: basic class for particles, to define the particle information and input coordinate representation. in addition, one extra input is provided, and only measured particles contribute to the χ^2, it provides extra information, and depends on how well particles are measured.

Constraint: this class is written for constraints setting, and there are 5 constraints derived from it, named SumP(x,y,z) Constraint.h, SumEConstraint.h, and InvMass-Constraint.h. The first 4 constraints are simply conservation of energy and momentum, the constrained particles must fulfil the condition of constraints. The InvMass-Constraint needs extra Breit-Wigners function as input, but due to the Breit-Wigner peak being similar to Gaussian, so Gaussian is used here, and due to this distribution, it allows particles to vary in mass.

CompositeConstraint: this class is used to create a linear combination of constraints, it takes a list of constraints as input and also takes a constraint value or a PDF depending on how tight the composite constraint should be defined.

Probability distribution functions: The PDF is currently used to set up Gaussian PDF, in the future it could be expanded by adding ISR, this PDF tells the constraint how tight it should be. The penalty function is calculated from the PDF by

$$g(x) = -2\ln(pdf(x)) \tag{8.34}$$

this class does not only have a calculation of those, but it also includes expectation value for the initial setting of fit.

Matrix Algebra: This class is used to calculate matrices, such as addition, multiplication, and also inverse and transpose.

ABC Fit: The class take a list of composite constraints, and also a maximum number of iterations It iterates the calculation of the parameter until reaching the maximum number of iterations or converged. It returns the number of iterations before converging, χ^2 value on how well its constrained, the number of degrees of freedom, and a list of fitted particles. Since the particle objects are passed as pointers into the constraints, a constrained fit can be applied in stages where the fit is first applied for one set of constraints followed by another set of constraints instead of requiring all constraints to be fulfilled at once. This could be relevant in cases of convergence issues. [18]

9 Analysis

9.1 Event Reconstruction of Di-leptonic $t\bar{t}$ Production

In section 8, we discussed the constrained fit which aims to improve the consistency of the output particle momentum with a perfect collision through event conditions, thereby reducing the systematic error caused by observation behavior. However, the neutrino is an unobservable quantity, and its calculation can overlap and amplify the measurement error of the jet and lepton, resulting in a relatively low resolution of the four-dimensional momentum of the neutrino. In Figure 9.1, we show the improvement of constrained fit for jets and leptons. Although it is not unique matching shown in Figure 9.1(a), it can show the improvement of constrained fit for jets momentum from a statistical point of view. For lepton (Figure 9.1(b)), since lepton is a well-measured particle, the optimization of constrained fit for lepton is not obvious. The optimization logic for these two objects will be shown in Figure 9.2.

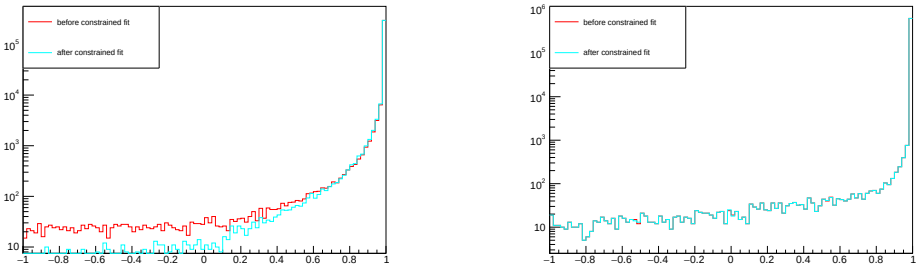

((a)) ((b))

Figure 9.1: Constrained fit to jets and leptons

For the signal events analyzed in this article, there are a total of eight constraints, with the first being the conservation of energy and the conservation of momentum, making a total of four constraints. Additionally, there are two rest masses of W and two rest masses of the t quark. Since two unobservable neutrinos have used W mass and 4-momentum conservation, the constrained fit performed after that is called a 2-constraint fit, simply because the two t quark masses have not yet been used.

In the previous section, we mentioned the issue of the neutrino ambiguous solution. The two results obtained are consistent with the WW system from the perspective of the derivation method. Therefore, for the selection of the neutrino reco level, the constraint of t quark mass is particularly important. In this analysis, we use the basic χ^2(Equation 9.1) as the basis for selecting the optimal solution.

$$\sum \frac{(m_{l\nu j} - m_{top})^2}{\sigma^2} = min \tag{9.1}$$

Since the measurements of leptons are more precise than those of other particles, particle combinations are mainly focused on neutrinos and b-jets. There is no way to distinguish the jets formed by b and $\bar{b}$, so there are ultimately four combinations. To obtain the closest true value, we select the combination with the lowest chi-squared value by calculating it for each combination. Although obtaining a weighted sum by

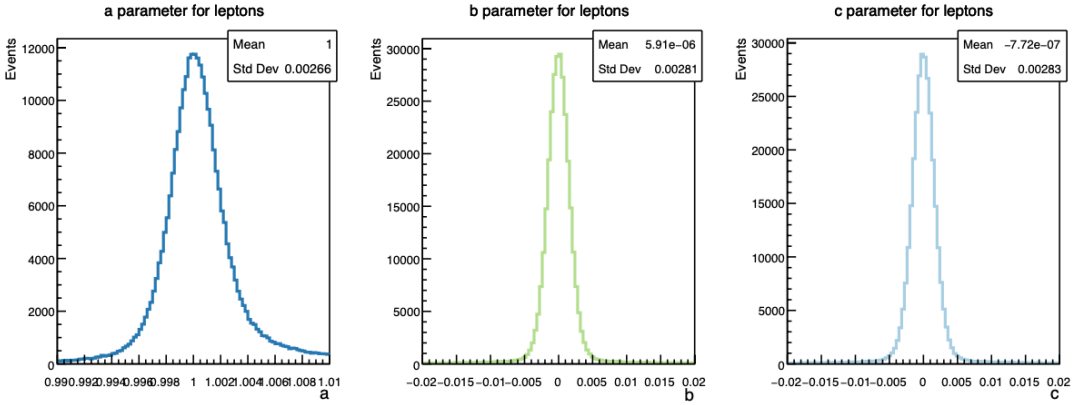

(a) a, b, and c parameter distribution for leptons

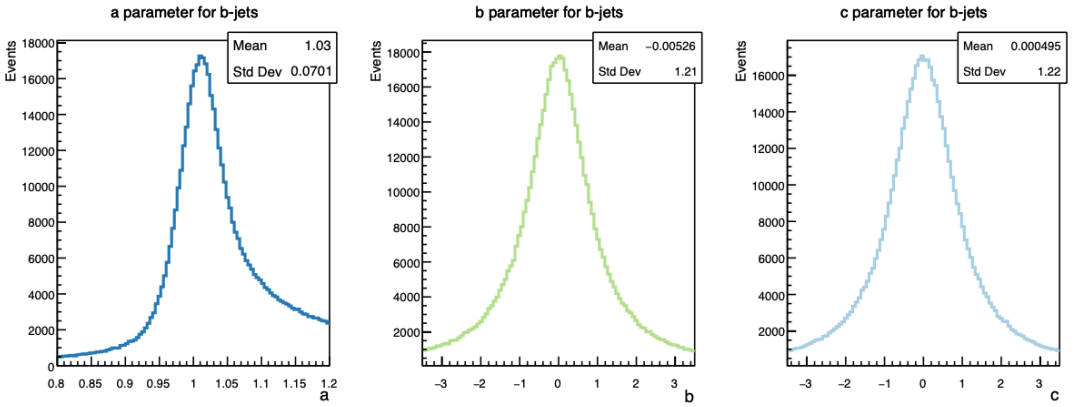

(b) a, b, and c parameter distribution for b-jets

Figure 9.2: a, b and c parameter distributions for leptons and b-jets.(Reproduced from [18]

calculating the probability of each combination is an option, in this analysis, we always choose the combination with the lowest chi-squared value to show the most likely data.

Next, we will discuss how to apply the constrained fitting technique in the case of di-lepton $t\bar{t}$ events. In section 8, we mentioned that the ABCfit++ used in this analysis is based on the contributions in reference. [30]

The process of event reconstruction involves cycling through all possible combinations and conducting a constrained fit to determine the combination that results in the lowest constraint χ^2 value, as calculated from Eq. 8.25. The fit utilizes the ABCD-parametrisation explained in the preceding section. Assuming that measurements are uncorrelated, the covariance matrix is diagonal as

$$V = \delta_{ij}\sigma_i\sigma_j \tag{9.2}$$

Figure 9.2 presents the distribution of the a, b, and c parameters for leptons and b-jets, respectively. These distributions were obtained by matching the measured leptons and jets to their corresponding true counterparts in the Monte Carlo data, with each jet matched to the quark closest in angle. The mean value of the parameter for leptons is 1, indicating that quark-level leptons and measured leptons have equal energies

on average. However, for b-jets, the mean of the parameter is 1.03, suggesting that the measured energies of b-jets are slightly lower than those of their corresponding quarks. The leptons have a resolution of 0.003 for all three parameters, while the resolutions for a, b, and c are 0.07 and 1.2, respectively, for b-jets. The covariance matrices for leptons and b-jets are provided to further characterize their distributions. The covariance matrix for leptons is given by a 4x4 matrix with diagonal elements of 0.003 and 10 in the last element. On the other hand, the covariance matrix for b-jets is a 4x4 matrix with diagonal elements of 0.07 for a and 1.2 for b and c, and 10 in the last element.

$$V_{lepton} = \begin{pmatrix} 0.003 & 0 & 0 & 0 \\ 0 & 0.003 & 0 & 0 \\ 0 & 0 & 0.003 & 0 \\ 0 & 0 & 0 & 10 \end{pmatrix}, V_{b-jet} = \begin{pmatrix} 0.07 & 0 & 0 & 0 \\ 0 & 1.2 & 0 & 0 \\ 0 & 0 & 1.2 & 0 \\ 0 & 0 & 0 & 10 \end{pmatrix} \tag{9.3}$$

The mass parameter is not used in the fit because it is fixed after scaling the energy and momentum of the input particles to have zero mass. Therefore, the mass parameter does not contribute to the fitting process. To match the mean values of the a distributions, the parametrisation function for the jets has been modified from the default $(1.0, 0.0, 0.0, m)$ to $(1.03, 0.0, 0.0, m)$. However, since the neutrino is not measured, there is no associated covariance matrix for it.

9.2 Observables

After completing the selection and processing of event samples, the next thing to analyze is the final observables, cross-section and angular distributions. There are a total of 5 angles we are interested in, the first one is the polar angle in the electron beam and the reconstructed top quark, which is given by [26]

$$\cos\theta_{et} = \frac{\mathbf{p}_e \cdot \mathbf{p}_t}{|\mathbf{p}_e|\,|\mathbf{p}_t|} \tag{9.4}$$

where $\mathbf{p}_e$ is the unit vector of the electron beam, and it naively parallels to the z-axis (0,0,1), the $\mathbf{p}_t$ is the 3-momentum of reconstructed top quark.

The next two angles are the polar angle and azimuthal angle of the top quark and its decay product. For the signal event, this decay product can be considered as a b-quark, and the three-dimensional momentum of a b-quark can be converted into the direction parallel to the top quark and vertical The direction of the top quark.

$$\mathbf{p}_{t\parallel} = (\mathbf{p}_t \cdot \mathbf{p}_b)\frac{\mathbf{p}_t}{|\mathbf{p}_t|^2} \tag{9.5}$$

$$\mathbf{p}_{t\perp} = \mathbf{p}_t - \mathbf{p}_{t\parallel} \tag{9.6}$$

when we move to the reference frame of the top quark, the parallel momentum of b quark can be transformed by Lorentz transformation.

$$\mathbf{p}^*_{t\parallel} = \gamma(\mathbf{p}_{t\parallel} - \beta E) \tag{9.7}$$

$t\bar{t}$ production	$t \to Wb$	$W \to l\nu$
θ_{et}	$\theta^*_{tb}, \phi^*_{tb}$	$\theta^*_{Wl}, \phi^*_{Wl}$

Table 9.1: Summary of the angles of interest

So the polar angle of the t-quark and the b-quark can be calculated as

$$\cos\theta^*_{tb} = \frac{\mathbf{p}^*_{t\|}}{\sqrt{(\mathbf{p}^*_{t\|})^2 + (\mathbf{p}_{t\perp})^2}} \tag{9.8}$$

At the same time, for their azimuthal angle, we can redefine the coordinate system. The z-axis, in relation to the top particle, is aligned with its direction of travel. This implies that $\hat{z}' = \frac{\mathbf{p}_t}{|\mathbf{p}_t|}$ In this same reference frame, the x'-axis can be obtained by taking the cross product between the z'-axis and the z-axis $x' = \hat{z}' \times \mathbf{p}_e$. the y'-axis can be obtained by taking the cross product of x' and z^', where it is perpendicular to both the x and z axes $y' = x' \times \hat{z}'$. From this, we can get the azimuthal angle between them as

$$\phi_{tb} = \arctan\frac{x' \cdot \mathbf{p}_b}{y' \cdot \mathbf{p}_b} \tag{9.9}$$

Similarly, we repeat the same steps for the decay of W to obtain the angle of W related to its decay products. All the angles we are interested in are summarized in table 9.1. After completing the selection and processing of event samples, the next step is to analyze the final observables, including the cross-section and angular distributions. In particular, we want to investigate the impact of event selection on the SM signal angular distribution and understand how it may affect BSM data.

The analysis uses the χ^2 test, a basic statistical test, to compare the distribution images before and after event selection. As mentioned in the observables section, we compare the distribution of five angles before and after selection. Figure 9.3 shows only one angle, and the remaining angular distributions are in Appendix C. Since event selection removes some signal events, there is a certain gap between the amplitudes of the two distributions. To better show the impact on the distribution and remove the impact on the cross-section, we rescale the before-selection histogram to the after-selection histogram.

The χ^2 test estimates the degree of relevance between two histograms by calculating the value of each degree of freedom. However, since the χ^2 test is sensitive to bin value and bin width, it can only verify the two histograms to a certain extent. For θ_{et}, the value of χ^2 is 67.889, the degree of freedom is 24, and the p-value is 4.544^{-6}. Therefore, event selection has affected this angle distribution. For θ_{tb}, the value of χ^2 is 109.325, the degree of freedom is 15, and the p-value is 2.172^{-16}, indicating that event selection has affected this angle distribution. The third angle, ϕ_{tb}, has a χ^2 value of 8.507, the degree of freedom is 31, and the p-value is 1.000. The impact of event selection on this angle can be ignored. The last two angles, θ_{Wl} and ϕ_{Wl}, have p-values of 1.422^{-246} and 3.414^{-7}, respectively, indicating that these angles are affected by event selection. The effect of event selection on these angles can also be seen from the ratio plot of Figure 9.3.

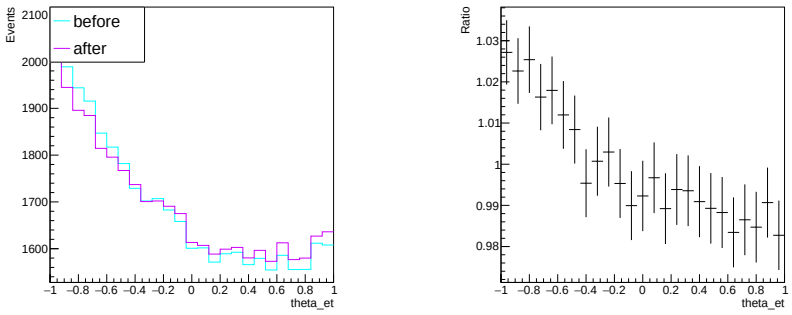

((a)) ((b))

Figure 9.3: Normalised θ_{et} angular distribution before and after event selection, and its ratio plot

As mentioned earlier, the χ^2 test is affected by the bin effect, and the impact of event selection on the angular distribution deserves a more detailed discussion.

The previous part mentioned the impact of event selection on the SM angular distribution. From Figure 9.4, we can intuitively see the impact of event selection on the BSM cross-section. Compared with the 33.22% of SM, the couplings tr_tbW_re and tl_tbW_re have a significant decline, while the efficiency of the remaining couplings is comparable to the SM.

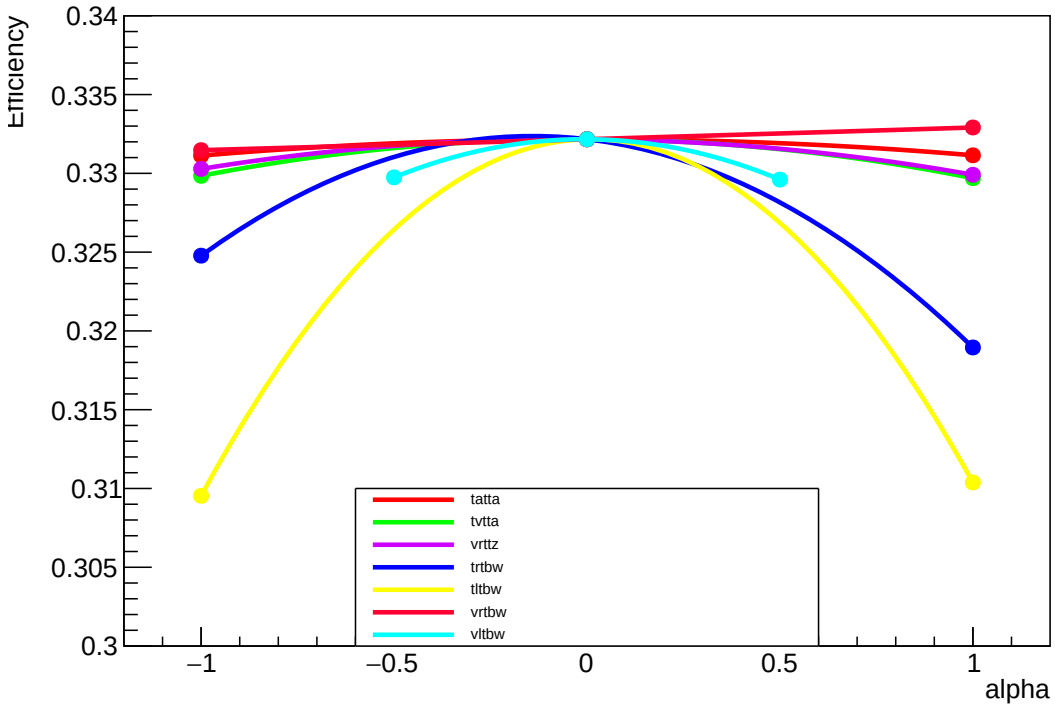

Figure 9.4: Event selction efficiency of all couplings and the SM

coupling	α	$\sigma_{tot}[pb]$
SM	0.0	0.4834
ta_ttA	+1.0	0.6505
	-1.0	0.6505
tv_ttA	+1.0	2.874
	-1.0	7.416
vr_ttZ	+1.0	0.7907
	-1.0	0.4854
tl_tbW_Re	+1.0	0.4834
	-1.0	0.4834
tr_tbW_Re	+1.0	2.591
	-1.0	4.129
vl_tbW_Re	+0.5	0.8308
	-0.5	0.4453
vr_tbW_Re	+1.0	0.4834
	-1.0	0.4834

Table 9.2: Whizard Cross-section for different couplings. Not normalized by the leptonic branching ratio.

9.3 Results

After completing all the previous steps, the next step is to determine the confidence intervals of the couplings. These intervals are a way for us to explore the sensitivity of the FCC to anomalous couplings. In section 3, we mentioned that in order to explore the influence of BSM in FCC, we first seek higher-order modifications in the SM. The BSM fit model is expected to have a quadratic polynomial form (Equation 3.11-3.13).

9.3.1 Single-Parameter Fit to 1 Dimensional Angular Distribution

Three points can determine a parabolic model, as shown in Table 9.2. For most couplings, we choose α values of -1, 0, and +1. When the coupling is zero, it corresponds to the SM. However, since vl_tbW_Re is particularly sensitive to coupling changes, we choose α values of -0.5, 0, and 0.5 in this analysis instead.

In order to describe the parabola of the BSM-included fit model, we parameterize the angular distribution.

$$f(\alpha^0) = C \tag{9.10}$$
$$f(\alpha^+) = A\alpha^2 + B\alpha + C \tag{9.11}$$
$$f(\alpha^-) = A\alpha^2 - B\alpha + C \tag{9.12}$$

it is trivial to get BSM fit model parameters

$$A = \frac{f(\alpha^+) + f(\alpha^-)}{2\alpha^2} - \frac{f(SM)}{\alpha^2} \tag{9.13}$$
$$B = \frac{f(\alpha^+) - f(\alpha^-)}{2\alpha} \tag{9.14}$$
$$C = f(SM) \tag{9.15}$$

and the BSM fit model is

$$f(x) = A \cdot x^2 + B \cdot x + C \tag{9.16}$$

where the C parameter includes signal and background events.

The confidence intervals of single coupling could be determined by the minimum χ^2 method, by scanning each bin. The χ^2 is getting from

$$\chi^2 = \sum_{i=1}^{n} \frac{(y_i - f(x_i;\alpha))^2}{y_i + \sigma^2_{f(x_i;\alpha)}} \tag{9.17}$$

The numerator in the expression for χ^2 represents the squared difference between the SM histogram and the i-th bin content of the fitted histogram. The denominator is obtained by summing the i-th bin content of the SM histogram and the square of the fitting model error.

Monte Carlo simulators generate perfect data, which are also known as Asimov datasets, and their expected values are perfectly equal to the true value. However, when generating BSM data through Whizard, the generated values are larger than the expected cross-section value. This implies that the weight of these data is less than 1. Consequently, generating more data can help reduce statistical error in the fit model. On the other hand, SM data, although generated using Monte Carlo, need to be treated as real data. Therefore, we use their standard deviation when calculating χ^2, and this is why the i-th bin content is used.

For the Minimum χ^2 Method, a 1σ confidence interval of 68% is used here, and since we are performing a one-coupling fit, the number of parameters is also 1. Therefore, as shown in Figure 9.5 (a), the upper and lower bounds of the 1σ confidence interval are limited to $\Delta\chi^2 = 1$, and the fit model can be clearly seen within 1σ confidence interval. A special example is shown in Figure 9.6, where the double minimum structure arises due to the effect of the linear term, indicating a non-trivial correlation.

Appendix D1 contains the relevant values for the remaining angles and couplings. the right side demonstrates the agreement between the fit model and the data in the signal region.

In this analysis, both the cross-section and angular distribution are important for determining anomalous top couplings. Removing the cross-section would theoretically reduce the sensitivity of the analysis. To demonstrate the impact of removing the cross-section, we normalized the fit histogram to the SM histogram. The following table presents the results with and without the cross-section.

In Table 9.3, all 70 confidence intervals are summarized, with marks indicating whether or not the cross-section is included. In general, the results are in agreement with previous predictions, and the confidence intervals have higher sensitivity when cross-section information is included. We use four significant figures for each result, as some results differ in the third significant figure. When comparing with Table 9.2, couplings that cause a significant change in the cross-section also have a significant change in

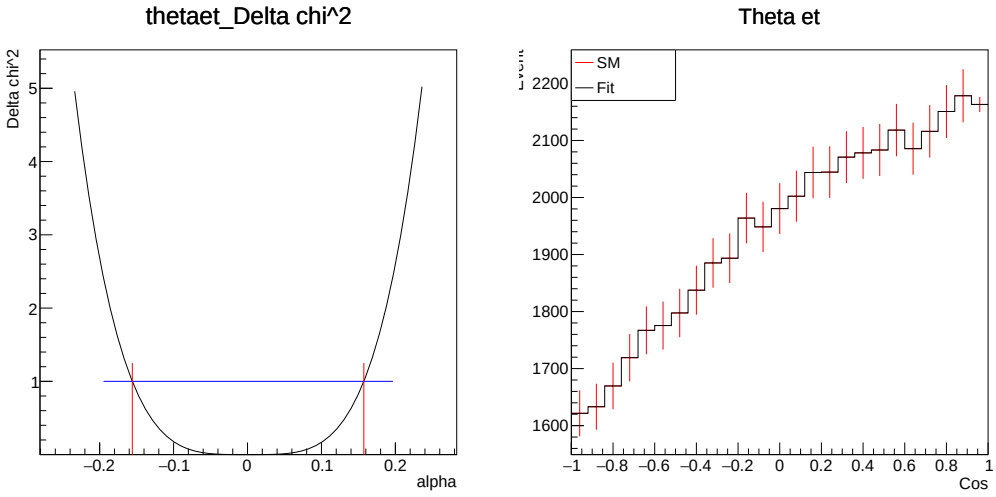

(a) (b)

Figure 9.5: θ_{et} for ta_ttA σ included

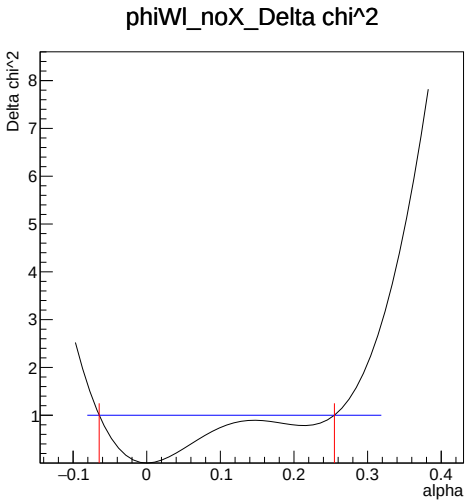

((a))

Figure 9.6: ϕ_{Wl} for tr_tbW_Re σ excluded

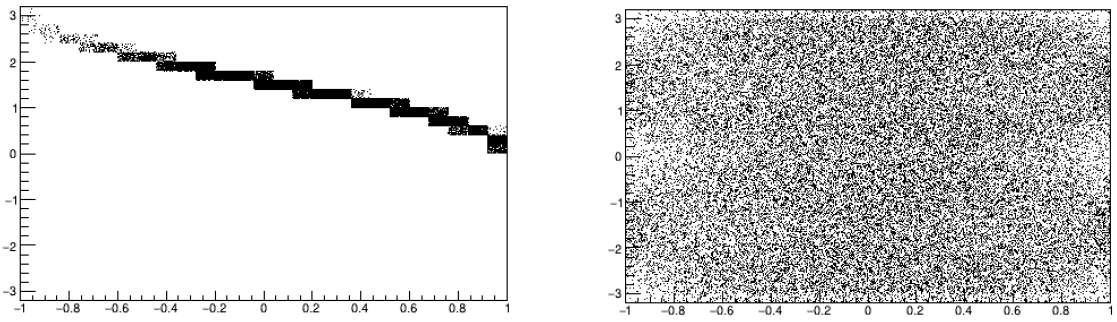

((a)) ((b))

Figure 9.7: The left is the TH2D plot of strong correlation 2 variables, the right is the TH2D plot of weak correlation 2 variables.

the confidence interval when the cross-section is removed. Among them, θ_{Wl} is less affected by cross-section compared to other angles. Overall, the coupling with the highest sensitivity for FCC-ee is tv_ttA, with a more precise value compared to other couplings. On the other hand, the coupling with the worst sensitivity for FCC-ee is vr_tbW_Re, with a larger value compared to other couplings.

9.3.2 Single-Parameter Fit to 2 Dimensional Angular Distribution

At the theoretical level, there is no fundamental difference between using 2D and the previous 1D analysis, as it simply provides more information for a specific angle to increase sensitivity. The same logic as before is applied to construct the fit model.

In this section, the five observables from the previous part are expanded to seven observables, and the *cos* part can be expressed in radians, mapping an angle from the interval [-1,1] to $[-\pi, \pi]$. While there is a strong correlation(Figure 9.7(a)) between these observables, their confidence intervals will still change due to the binning effect. However, the effect of binning on sensitivity is not significant, and meaningful variables should be weakly correlated(Figure 9.7(b)) and have a more homogeneous distribution. Except for strongly correlated observables, additional information will improve sensitivity for anomalous contributions. Figure 9.8 shows that, for the same angle, any second angle will positively contribute to the anomalous top coupling sensitivity. Similar to the 1D analysis, we can remove the cross-section effect to assess its impact on sensitivity.

Figure 9.9 shows cos(et) angle(tb) for ta_ttA, while the figures for other angles will be included in Appendix D2. On the left, we see cos(et) angle(tb) for ta_ttA$\Delta\chi^2$, with SM still at the minimum point. In this section, the upper and lower bounds of the 1σ confidence intervals are still limited to $\Delta\chi^2 = 1$. On the right, we see the agreement between the fit model and the data in the signal region of the 2D plot.

From Table 9.4 to Table 9.10, where each table is divided into lower left and upper right parts using a diagonal line. The lower left part separated by a diagonal block corresponds to the cross-section excluded confidence interval, while the upper right part is the cross-section included confidence interval. For By combining weakly corre-

coupling	σ_{tot}	θ_{et}	θ_{tb}	ϕ_{tb}	θ_{Wl}	ϕ_{Wl}
ta_ttA	Yes	-0.1558 to 0.1573	-0.1581 to 0.1573	-0.1591 to 0.1598	-0.1578 to 0.1573	-0.1592 to 0.1586
	No	-0.3097 to 0.3535	-0.3787 to 0.3663	-0.5971 to 0.6768	-0.3453 to 0.3429	-0.5924 to 0.5928
tl_tbW_Re	Yes	-0.1083 to 0.1125	-0.1060 to 0.1108	-0.1084 to 0.1126	-0.06177 to 0.06045	-0.09552 to 0.094669
	No	-0.2771 to 0.2879	-0.2110 to 0.2234	-0.3810 to 0.3260	-0.06357 to 0.06168	-0.1214 to 0.1139
tr_tbW_Re	Yes	-0.004303 to 0.004439	-0.004216 to 0.004346	-0.004259 to 0.004392	-0.004149 to 0.004275	-0.004244 to 0.004376
	No	-0.07265 to 0.1509	-0.1034 to 0.2046	-0.1459 to 0.1701	-0.02174 to 0.02514	-0.06459 to 0.2549
tv_ttA	Yes	-0.001501 to 0.001510	-0.001466 to 0.001475	-0.001480 to 0.001489	-0.001467 to 0.001476	-0.001479 to 0.001488
	No	-0.1125 to 0.07370	-0.06120 to 0.06407	-0.07532 to 0.06918	-0.05358 to 0.05213	-0.08701 to 0.07304
vl_tbW_Re	Yes	-0.007315 to 0.007249	-0.007113 to 0.007049	-0.007197 to 0.007133	-0.007117 to 0.007053	-0.007176 to 0.007112
	No	-0.1660 to 0.1908	-0.3684 to 0.09693	-0.3736 to 0.3022	-0.2311 to 0.1155	-0.4799 to 0.1508
vr_tbW_Re	Yes	-0.2758 to 0.2930	-0.2885 to 0.3121	-0.2905 to 0.3166	-0.1904 to 0.1909	-0.2697 to 0.2935
	No	-0.5055 to 0.4205	-0.6314 to 0.5742	-0.6172 to 0.6061	-0.2010 to 0.1965	-0.3854 to 0.3947
vr_ttZ	Yes	-0.01811 to 0.01773	-0.02224 to 0.02150	-0.02247 to 0.02171	-0.02225 to 0.02151	-0.02244 to 0.02169
	No	-0.03295 to 0.03283	-0.5686 to 0.3368	-0.6024 to 0.4619	-0.4956 to 0.3394	-0.7389 to 0.5650

Table 9.3: Confidence interval for every couplings. The first column denotes the name of the couplings, the second indicates the cross-section, and the rest column denotes the confidence interval of five angles of interest.

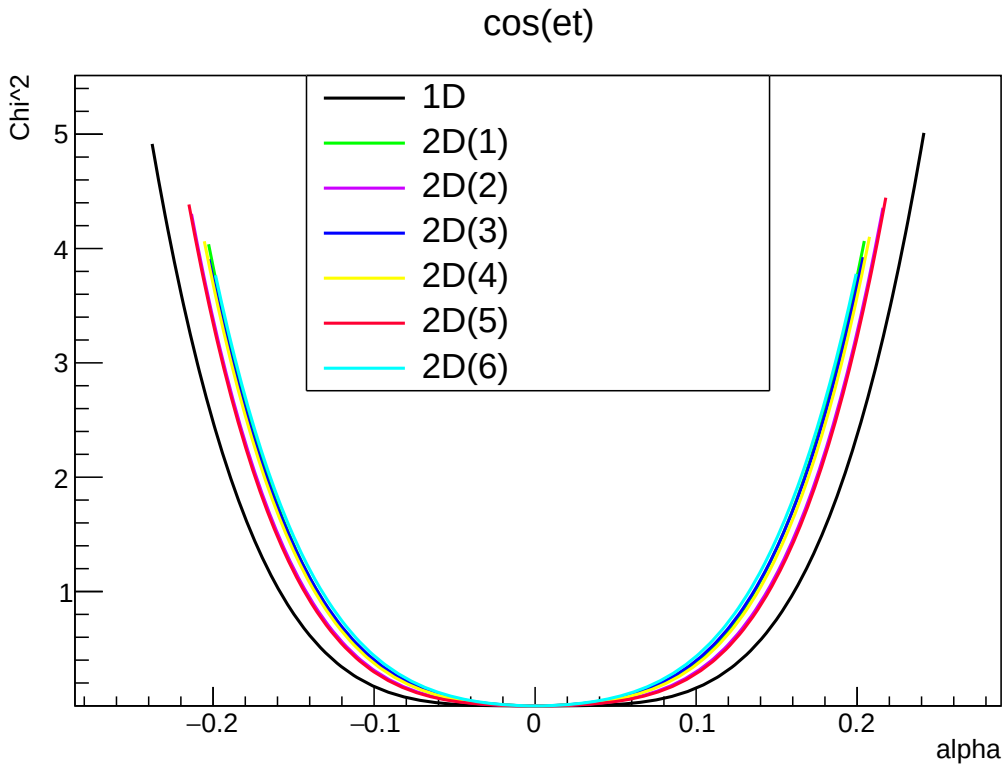

Figure 9.8: ta_ttA cos(et) is selected to be a demo, the black curve is the 1D fit, and all 2D fits are inside the black curve.

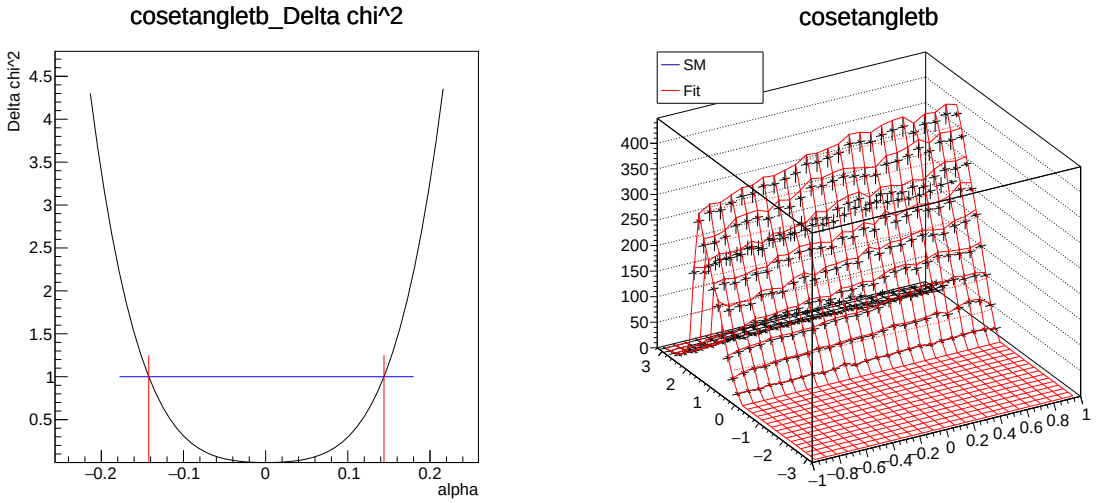

((a)) ((b))

Figure 9.9: cos(et) angle(tb) for ta_ttA

lated observables, we have raised the sensitivity of single-parameter fit to a new level. Comparing all confidence intervals, we can see that most of them have improved by around 20%. The highest sensitivity in the 1D fitting, tv_ttA, still exhibits a certain degree of improvement in the 2D fitting. Thus, in general, the sensitivity ranking of the 1D fitting is still preserved in the 2D fitting. Similarly, the change of cross-section to the confidence interval is also significant. For example, for the data of tv_ttA, removing the cross-section will increase the confidence interval of $\cos\theta_{et} - \cos\theta_{tb}$ from [-0.001411,0.001419] to [-0.01821,0.01769]. If we compare the data of 1D tv_ttA, we find that for the case where the cross-section is excluded, the 2D fitting sensitivity has significantly improved. Thus, we can draw the conclusion that for the cross-section included case, the improvement of the confidence interval is much lower than for the cross-section excluded case.

ta_ttA	$cos\theta_{et}$	$cos\theta_{tb}$	$angle\theta_{tb}$	ϕ_{tb}	$cos\theta_{Wl}$	$angle\theta_{Wl}$	ϕ_{Wl}
$cos\theta_{et}$	\ to \	-0.1351 to 0.1362	-0.1422 to 0.1440	-0.1350 to 0.1358	-0.1369 to 0.1384	-0.1433 to 0.1451	-0.1323 to 0.1329
$cos\theta_{tb}$	-0.1840 to 0.1887	\ to \	\ to \	-0.1351 to 0.1353	-0.1383 to 0.1379	-0.1453 to 0.1452	-0.1336 to 0.1340
$angle\theta_{tb}$	-0.2047 to 0.2157	\ to \	\ to \	-0.1437 to 0.1434	-0.1468 to 0.1477	-0.1509 to 0.1513	-0.1429 to 0.1420
ϕ_{tb}	-0.1819 to 0.1886	-0.1897 to 0.1934	-0.2242 to 0.2292	\ to \	-0.1344 to 0.1351	-0.1422 to 0.1417	-0.1299 to 0.1290
$cos\theta_{Wl}$	-0.1855 to 0.1927	-0.2021 to 0.2012	-0.2361 to 0.2477	-0.1824 to 0.1895	\ to \	\ to \	-0.1339 to 0.1334
$angle\theta_{Wl}$	-0.2071 to 0.2189	-0.2359 to 0.2366	-0.2612 to 0.2706	-0.2147 to 0.2177	\ to \	\ to \	-0.1422 to 0.1414
ϕ_{Wl}	-0.1748 to 0.1779	-0.1853 to 0.1883	-0.2234 to 0.2191	-0.1704 to 0.1694	-0.1823 to 0.1811	-0.2165 to 0.2132	\ to \

Table 9.4: ta_ttA 2D Confidence regions.

tl_tbW_Re	$cos\theta_{et}$	$cos\theta_{tb}$	$angle\theta_{tb}$	ϕ_{tb}	$cos\theta_{Wl}$	$angle\theta_{Wl}$	ϕ_{Wl}
$cos\theta_{et}$	\ to \	-0.09044 to 0.09485	-0.09322 to 0.09941	-0.09036 to 0.09294	-0.05634 to 0.05550	-0.05842 to 0.05737	0.08307 to 0.08339
$cos\theta_{tb}$	-0.1219 to 0.1266	\ to \	\ to \	-0.08963 to 0.09119	-0.05671 to 0.05517	-0.05864 to 0.05704	-0.08237 to 0.08131
$angle\theta_{tb}$	-0.1288 to 0.1441	\ to \	\ to \	-0.09442 to 0.09596	-0.05829 to 0.05685	-0.06006 to 0.05851	-0.08633 to 0.08498
ϕ_{tb}	-0.1243 to 0.1233	-0.1190 to 0.1152	-0.1348 to 0.1292	\ to \	-0.05659 to 0.05519	-0.05863 to 0.05738	-0.07587 to 0.07515
$cos\theta_{Wl}$	-0.05749 to 0.05624	-0.05787 to 0.05586	-0.05951 to 0.05763	-0.05774 to 0.05593	\ to \	\ to \	-0.05628 to 0.05510
$angle\theta_{Wl}$	-0.05995 to 0.05839	-0.06016 to 0.05798	-0.06166 to 0.05956	-0.06016 to 0.05842	\ to \	\ to \	-0.05808 to 0.05709
ϕ_{Wl}	-0.09592 to 0.09330	-0.09471 to 0.08974	-0.1010 to 0.09527	-0.08290 to 0.08034	-0.05738 to 0.05579	-0.05951 to 0.05804	\ to \

Table 9.5: tl_tbW_Re 2D Confidence regions.

tr_tbW_Re	$cos\theta_{et}$	$cos\theta_{tb}$	$angle\theta_{tb}$	ϕ_{tb}	$cos\theta_{Wl}$	$angle\theta_{Wl}$	ϕ_{Wl}
$cos\theta_{et}$	\ to \	-0.004033 to 0.004150	-0.004110 to 0.004232	-0.004077 to 0.004196	-0.003964 to 0.004074	-0.003981 to 0.004092	-0.004078 to 0.004197
$cos\theta_{tb}$	-0.02702 to 0.02844	\ to \	\ to \	-0.004088 to 0.004209	-0.004039 to 0.004158	-0.004052 to 0.004171	-0.004085 to 0.004206
$angle\theta_{tb}$	-0.03057 to 0.03275	\ to \	\ to \	-0.004163 to 0.004289	-0.004118 to 0.004242	-0.004129 to 0.004254	-0.004164 to 0.004290
ϕ_{tb}	-0.02992 to 0.03097	-0.03381 to 0.03477	-0.04214 to 0.04418	\ to \	-0.004084 to 0.004205	-0.004098 to 0.004220	-0.004095 to 0.004217
$cos\theta_{Wl}$	-0.01360 to 0.01401	-0.01802 to 0.01992	-0.01894 to 0.02128	-0.01881 to 0.02061	\ to \	\ to \	-0.004087 to 0.004208
$angle\theta_{Wl}$	-0.01408 to 0.01455	-0.01867 to 0.02084	-0.01948 to 0.02208	-0.01971 to 0.02188	\ to \	\ to \	-0.004104 to 0.004227
ϕ_{Wl}	-0.02750 to 0.02891	-0.03068 to 0.03247	-0.03603 to 0.03945	-0.02306 to 0.02492	-0.01846 to 0.02012	-0.01960 to 0.02172	\ to \

Table 9.6: tr_tbW_Re 2D Confidence regions.

tv_ttA	$cos\theta_{et}$	$cos\theta_{tb}$	$angle\theta_{tb}$	ϕ_{tb}	$cos\theta_{Wl}$	$angle\theta_{Wl}$	ϕ_{Wl}
$cos\theta_{et}$	\ to \	-0.001411 to 0.001419	-0.001436 to 0.001444	-0.001425 to 0.001434	-0.001432 to 0.001441	-0.001435 to 0.001444	-0.001426 to 0.001434
$cos\theta_{tb}$	-0.01821 to 0.01769	\ to \	\ to \	-0.001428 to 0.001436	-0.001434 to 0.001442	-0.001437 to 0.001446	-0.001427 to 0.001435
$angle\theta_{tb}$	-0.02133 to 0.02067	\ to \	\ to \	-0.001453 to 0.001461	-0.001461 to 0.001470	-0.001464 to 0.001473	-0.001453 to 0.001462
ϕ_{tb}	-0.01976 to 0.01883	-0.01846 to 0.01778	-0.02305 to 0.02210	\ to \	-0.001448 to 0.001457	-0.001452 to 0.001461	-0.001440 to 0.001448
$cos\theta_{Wl}$	-0.01839 to 0.01781	-0.02032 to 0.01957	-0.02549 to 0.02463	-0.01881 to 0.01809	\ to \	\ to \	-0.001450 to 0.001458
$angle\theta_{Wl}$	-0.02069 to 0.01999	-0.02397 to 0.02302	-0.02902 to 0.02801	-0.02252 to 0.02152	\ to \	\ to \	-0.001453 to 0.001462
ϕ_{Wl}	-0.01782 to 0.01719	-0.01869 to 0.01800	-0.02282 to 0.02186	-0.01576 to 0.01528	-0.01891 to 0.01822	-0.02241 to 0.02146	\ to \

Table 9.7: tv_ttA 2D Confidence regions.

vl_tbW_Re	$cos\theta_{et}$	$cos\theta_{tb}$	$angle\theta_{tb}$	ϕ_{tb}	$cos\theta_{Wl}$	$angle\theta_{Wl}$	ϕ_{Wl}
$cos\theta_{et}$	\ to \	-0.006776 to 0.006717	-0.006915 to 0.006855	-0.006887 to 0.006827	-0.006903 to 0.006843	-0.006923 to 0.006863	-0.006882 to 0.006823
$cos\theta_{tb}$	-0.05056 to 0.04739	\ to \	\ to \	-0.006901 to 0.006840	-0.006928 to 0.006866	-0.006944 to 0.006882	-0.006901 to 0.006839
$angle\theta_{tb}$	-0.05711 to 0.05304	\ to \	\ to \	-0.007041 to 0.006978	-0.007080 to 0.007017	-0.007096 to 0.007032	-0.007050 to 0.006987
ϕ_{tb}	-0.07596 to 0.06704	-0.08416 to 0.06120	-0.1064 to 0.07063	\ to \	-0.007021 to 0.006959	-0.007042 to 0.006980	-0.006989 to 0.006927
$cos\theta_{Wl}$	-0.05675 to 0.05274	-0.07840 to 0.05943	-0.09389 to 0.06725	-0.08479 to 0.06563	\ to \	\ to \	-0.007034 to 0.006972
$angle\theta_{Wl}$	-0.06120 to 0.05758	-0.08501 to 0.06290	-0.09906 to 0.06947	-0.1007 to 0.07492	\ to \	\ to \	-0.007054 to 0.006991
ϕ_{Wl}	-0.06002 to 0.05567	-0.07771 to 0.05858	-0.09279 to 0.06665	-0.07785 to 0.06291	-0.08294 to 0.06404	-0.09914 to 0.07161	\ to \

Table 9.8: vl_tbW_Re 2D Confidence regions.

vr_tbW_Re	$cos\theta_{et}$	$cos\theta_{tb}$	$angle\theta_{tb}$	ϕ_{tb}	$cos\theta_{Wl}$	$angle\theta_{Wl}$	ϕ_{Wl}
$cos\theta_{et}$	\ to \	-0.2120 to 0.2204	-0.2235 to 0.2340	-0.2027 to 0.2106	-0.1641 to 0.1626	-0.1718 to 0.1691	-0.2013 to 0.2103
$cos\theta_{tb}$	-0.2409 to 0.2408	\ to \	\ to \	-0.2060 to 0.2137	-0.1668 to 0.1693	-0.1744 to 0.1759	-0.2062 to 0.2099
$angle\theta_{tb}$	-0.2618 to 0.2625	\ to \	\ to \	-0.2288 to 0.2407	-0.1757 to 0.1778	-0.1818 to 0.1821	-0.2215 to 0.2308
ϕ_{tb}	-0.2267 to 0.2277	-0.2356 to 0.2316	-0.2807 to 0.2766	\ to \	-0.1599 to 0.1616	-0.1702 to 0.1715	-0.1818 to 0.1891
$cos\theta_{Wl}$	-0.1692 to 0.1653	-0.1727 to 0.1722	-0.1827 to 0.1815	-0.1653 to 0.1642	\ to \	\ to \	-0.1617 to 0.1621
$angle\theta_{Wl}$	-0.1785 to 0.1725	-0.1821 to 0.1797	-0.1907 to 0.1866	-0.1775 to 0.1751	\ to \	\ to \	-0.1698 to 0.1708
ϕ_{Wl}	-0.2212 to 0.2253	-0.2326 to 0.2242	-0.2585 to 0.2556	-0.1947 to 0.1970	-0.1670 to 0.1646	-0.1768 to 0.1743	\ to \

Table 9.9: vr_tbW_Re 2D Confidence regions.

vr _ttZ	$cos\theta_{et}$	$cos\theta_{tb}$	$angle\theta_{tb}$	ϕ_{tb}	$cos\theta_{Wl}$	$angle\theta_{Wl}$	ϕ_{Wl}
$cos\theta_{et}$	\ to \	-0.01758 to 0.01723	-0.01787 to 0.01751	-0.01786 to 0.01750	-0.01748 to 0.01715	-0.01753 to 0.01720	-0.01764 to 0.01730
$cos\theta_{tb}$	-0.02869 to 0.02865	\ to \	\ to \	-0.02155 to 0.02085	-0.02167 to 0.02096	-0.02175 to 0.02104	-0.02154 to 0.02085
$angle\theta_{tb}$	-0.02900 to 0.02896	\ to \	\ to \	-0.02197 to 0.02125	-0.02214 to 0.02140	-0.02220 to 0.02146	-0.02199 to 0.02127
ϕ_{tb}	-0.02937 to 0.02932	-0.2064 to 0.1507	-0.2536 to 0.1796	\ to \	-0.02189 to 0.02117	-0.02198 to 0.02126	-0.02175 to 0.02104
$cos\theta_{Wl}$	-0.02748 to 0.02746	-0.2389 to 0.1658	-0.3060 to 0.2043	-0.2100 to 0.1562	\ to \	\ to \	-0.02191 to 0.02119
$angle\theta_{Wl}$	-0.02761 to 0.02760	-0.2860 to 0.1937	-0.3470 to 0.2222	-0.2597 to 0.1862	\ to \	\ to \	-0.02199 to 0.02127
ϕ_{Wl}	-0.02837 to 0.02835	-0.2030 to 0.1525	-0.2427 to 0.1808	-0.1770 to 0.1419	-0.2038 to 0.1547	-0.2455 to 0.1828	\ to \

Table 9.10: vr_ttZ 2D Confidence regions.

9.3.3 Two-Parameter Fit to 1 Dimensional Angular Distribution

Unlike the previous section, the following discussion aims to expand on the number of parameters used in the minimum χ^2 method. As mentioned in section 3, the events we are concerned with involve a total of seven couplings. Combining them results in 21 possible arrangements. To perform a two-parameter fit, we must restructure the fit model. A generic fit model would appear as follows:

$$f(\alpha, \beta) = A \cdot \alpha^2 + B \cdot \alpha + C \cdot \beta^2 + D \cdot \beta + E \cdot \alpha\beta + F \tag{9.18}$$

To generate the fit model, we require additional data based on the previous MC data sets. Using Whizard, we set both couplings to 1 simultaneously. The specifics are outlined in Table 9.11, which encompasses 21 arrangements.
In the previous section, we utilized $f(\alpha)$ to denote angular distribution. However, in this section, we incorporate a second coupling and use $f(\alpha, \beta)$ to describe the angular distribution, where β denotes the second coupling. The entire derivation process can be expressed as follows:

$$f(\alpha^+, 0) = A \cdot \alpha^2 + B \cdot \alpha + F \tag{9.19}$$
$$f(\alpha^-, 0) = A \cdot \alpha^2 - B \cdot \alpha + F \tag{9.20}$$
$$f(0, \beta^+) = C \cdot \beta^2 + D \cdot \beta + F \tag{9.21}$$
$$f(0, \beta^-) = C \cdot \beta^2 - D \cdot \beta + F \tag{9.22}$$
$$f(\alpha^+, \beta^+) = A \cdot \alpha^2 + B \cdot \alpha + C \cdot \beta^2 + D \cdot \beta + E \cdot \alpha\beta + F \tag{9.23}$$
$$f(0, 0) = F \tag{9.24}$$
$$\tag{9.25}$$

the parameters can be easily concluded

$$A = \frac{f(\alpha^+, 0) + f(\alpha^-, 0)}{2\alpha^2} - \frac{f(0, 0)}{\alpha^2} \tag{9.26}$$
$$B = \frac{f(\alpha^+, 0) - f(\alpha^-, 0)}{2\alpha} \tag{9.27}$$
$$C = \frac{f(0, \beta^+) + f(0, \beta^-)}{2\beta^2} - \frac{f(0, 0)}{\beta^2} \tag{9.28}$$
$$D = \frac{f(0, \beta^+) - f(0, \beta^-)}{2\beta} \tag{9.29}$$
$$E = f(\alpha^+, \beta^+) - A - B - C - D - F \tag{9.30}$$
$$F = f(0, 0) \tag{9.31}$$

For a two-parameter fit, the definition of χ^2 is the same as Equation 9.17. For 1σ of 2 parameters, its upper and lower limits of confidence intervals are limited to $\Delta\chi^2 = 2.3$.

For a two-parameter fit, the logic behind χ^2 is similar to that of the previous method, but as it is a 2D fit, it can be visualized as a funnel shape. The most intuitive way to display this is through contour plots. As depicted in Figure 9.10, the two figures correspond to each other. The (0,0) position denotes the Standard Model (SM), while the red and blue lines indicate the 2D confidence interval. The couplings associated with Figure 9.10 are ta_ttA and vr_ttZ θ_{et}, and additional images can be found in Appendix D3. Similarly to the previous method, the contour plots are divided into including and excluding cross-sections. It can be observed from Appendix D3 that the cross-section has a significant impact on the shape of the contour plots.

All the confidence intervals obtained from the two-parameter fit are summarized in five Tables (Table 9.12-9.16), where each table is divided into lower left and upper right parts using a diagonal line. Each cell is also divided into upper and lower parts, where the upper part of each cell corresponds to the confidence interval of the abscissa, and the lower part corresponds to the confidence interval of the ordinate. The lower left part separated by a diagonal block corresponds to the cross-section excluded confidence interval, while the upper right part is the cross-section included confidence interval. For each set of data, there are corresponding contour plots similar to Figure 9.10 (a) in Appendix D3. For two-parameter fit contour plots, there are many different shapes, the most common of which are banana-shape and ellipse-shape. Figure

9.11 shows a more complex contour plot for the two-parameter fit.

In principle, this analysis should use minos to obtain the confidence interval [31]. However, since 2D χ^2 sometimes has a double minimum or the contour is larger than the expected range, minos fails. Therefore, in this analysis, we used a solution scanning method to this problem by scanning in the α and β ranges from -2 to 2 to get a relatively low resolution. There is no essential difference between this approach and minos, but by comparing a scanning solution with a successful minos solution, we can know how reliable its confidence interval is. We selected the confidence interval of ta_ttA vr_ttZ θ_{et} to calibrate the data, where the α and β of the minos solution are [-0.2470, 0.2674] and [-0.05057, 0.02689], respectively, while the α and β of the scanning solution are [-0.248, 0.269] and [-0.05, 0.027], respectively. By comparing these two sets of data, they are consistent in two decimal places. Since Equation 9.17 is very sensitive to the coupling value, theoretically increasing the precision of the solution scanning or changing to a more efficient algorithm can make these confidence intervals more convincing.

The choice of coupling value in this analysis is -1 and 1, so there is some ambiguity about the number greater than 1 in Table 9.12-9.16. Since the weight of each event is greater than one, it will increase the statistical error. Thus, setting a higher coupling value will become a necessary choice in future research. For the contour plots in Appendix D3, although most of the auxiliary lines can perfectly match the contour edges, there are still a small number of figures that have mismatches. This is because the fitting line does not necessarily connect every TH2D point, and the accuracy of the scan can be improved or more efficient algorithms can be used to optimize this situation.

In Table 9.12-9.16, some confidence intervals are equal to 2 or -2, which correspond to unclosed contours. For these data, we can only obtain more simulated data for research by increasing the coupling value in the future.

σ_{tot}[pb]	ta_ttA(1)	tv_ttA(1)	vr_ttZ(1)	tl_tbW_Re(1)	tr_tbW_Re(1)	vl_tbW_Re(0.5)	vr_tbW_Re(1)
ta_ttA(1)	\	3.041	0.958	0.651	2.758	0.998	0.651
tv_ttA(1)	\	\	3.764	2.874	2.381	3.804	2.874
vr_ttZ(1)	\	\	\	0.791	1.610	1.407	0.791
tl_tbW_Re(1)	\	\	\	\	2.591	0.831	0.483
tr_tbW_Re(1)	\	\	\	\	\	1.650	2.591
vl_tbW_Re(0.5)	\	\	\	\	\	\	0.831
vr_tbW_Re(1)	\	\	\	\	\	\	\

Table 9.11: Cross-section calculated by Whizard with 2 couplings, and this is not normalized by branching ratio. the bracket value denotes α value

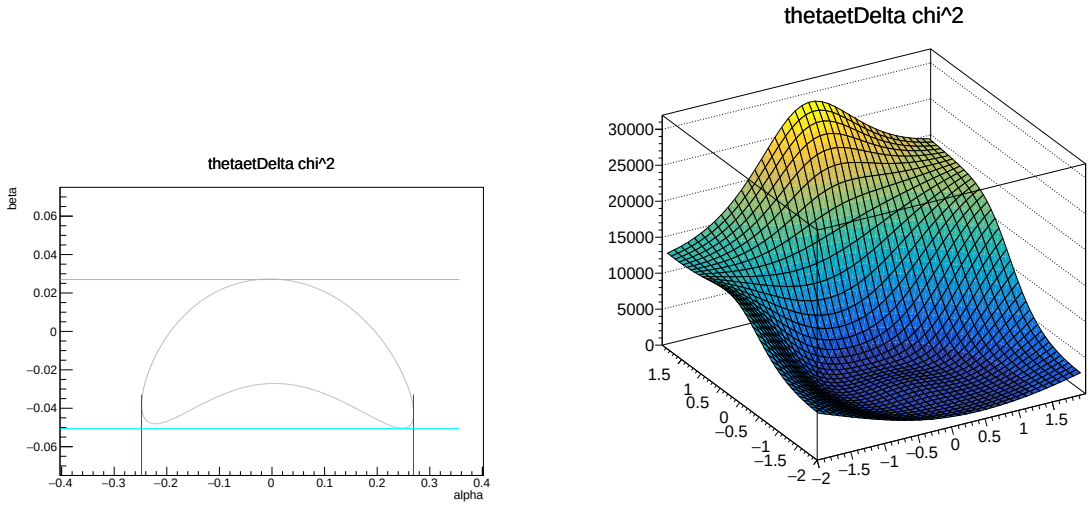

((a)) ((b))

Figure 9.10: ta_ttA and tr_ttZ, θ_{et} two-parameter fit χ^2 plots, the left is the contour plot, and the right is the surface plot.

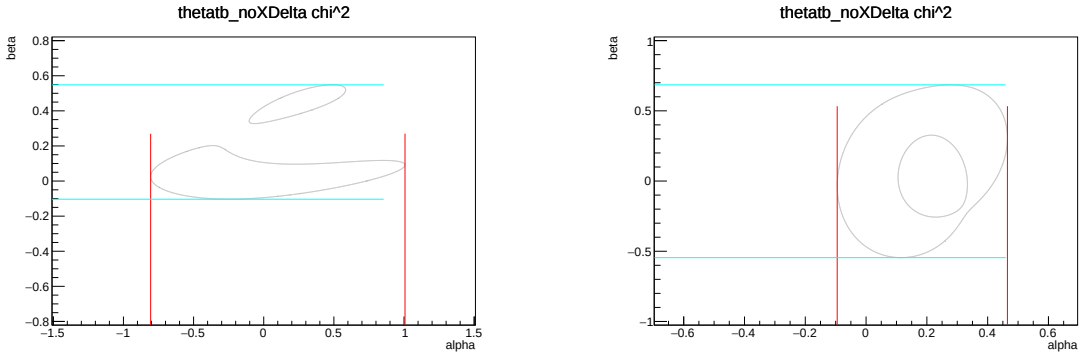

((a)) ((b))

Figure 9.11: more complicated contour plots of two-parameter fit

θ_{et}	ta_ttA	tv_ttA	vr_ttZ	tl_tbW_Re	tr_tbW_Re	vl_tbW_Re	vr_tbW_Re
ta_ttA	\	-0.368 to 0.395	-0.05 to 0.027	-0.566 to 0.621	-0.376 to 0.405	-0.341 to 0.388	-0.335 to 0.418
	\	-0.002 to 0.01	-0.248 to 0.269	-0.368 to 0.388	-0.006 to 0.034	-0.041 to 0.011	-0.666 to 0.656
tv_ttA	-0.218 to 0.105	\	-0.003 to 0.005	-0.015 to 0.003	-0.021 to 0.041	-0.029 to 0.073	-0.005 to 0.003
	-0.374 to 0.454	\	-0.047 to 0.047	-0.706 to 0.68	-0.076 to 0.18	-0.186 to 0.223	-0.571 to 0.508
vr_ttZ	-0.378 to 0.42	-0.064 to 0.051	\	-0.027 to 0.0430	-0.187 to 0.05	-0.045 to 0.046	-0.027 to 0.072
	-0.05 to 0.048	-0.207 to 0.136	\	-0.332 to 0.345	-0.011 to 0.251	-0.017 to 0.019	-0.486 to 0.633
tl_tbW_Re	-0.381 to 0.413	-0.738 to 0.806	-0.77 to 0.784	\	-0.04 to 0.305	-0.631 to 0.71	-0.304 to 0.337
	-0.772 to 0.809	-0.204 to 0.138	-0.054 to 0.048	\	-0.700 to 0.536	-0.01 to 0.064	-0.39 to 0.437
tr_tbW_Re	-0.098 to 0.179	-0.117 to 0.18	-0.263 to 0.265	-0.744 to 0.817	\	-0.147 to 0.31	-0.015 to 0.007
	-0.378 to 0.408	-0.203 to 0.111	-0.217 to 0.056	-0.212 to 0.431	\	-0.24 to 0.122	-0.579 to 0.538
vl_tbW_Re	-0.219 to 0.478	-0.248 to 0.273	-0.485 to 0.269	-0.233 to 0.289	-0.462 to 0.425	\	-0.01 to 0.027
	-0.56 to 0.551	-0.208 to 0.105	-0.193 to 0.058	-0.704 to 0.736	-0.204 to 0.898	\	-0.536 to 0.51
vr_tbW_Re	-0.704 to 0.747	-0.692 to 0.637	-0.654 to 0.67	-0.585 to 1.191	-0.757 to 0.588	-0.7 to 0.558	\
	-0.42 to 0.53	-0.206 to 0.124	-0.047 to 0.078	-0.847 to 1.645	-0.135 to 0.206	-0.51 to 0.253	\

Table 9.12: θ_{et} two-parameter fit confidence intervals

$\cos\theta_{tb}$	ta_ttA	tv_ttA	vr_ttZ	tl_tbW_Re	tr_tbW_Re	vl_tbW_Re	vr_tbW_Re
ta_ttA	\	-0.483 to 0.484	-0.466 to 0.033	-0.529 to 0.570	-0.466 to 0.492	-0.587 to 0.465	-0.39 to 0.379
	\	-0.002 to 0.015	-0.518 to 0.426	-0.336 to 0.355	-0.006 to 0.053	-0.117 to 0.011	-0.921 to 0.924
tv_ttA	-0.095 to 0.465	\	-0.019 to 0.447	-0.009 to 0.003	-0.021 to 0.206	-0.044 to 0.048	-0.009 to 0.49
	-0.545 to 0.685	\	-0.634 to 0.58	-0.509 to 0.573	-0.156 to 0.227	-0.347 to 0.167	-0.757 to 0.677
vr_ttZ	-0.547 to 0.464	-0.804 to 0.616	\	-0.034 to 0.137	-0.713 to 0.666	-0.312 to 0.449	-0.034 to 0.107
	-0.742 to 0.479	-0.1 to 0.449	\	-0.549 to 0.515	-0.15 to 0.124	-0.128 to 0.118	-0.625 to 0.76
tl_tbW_Re	-1.118 to 2.0	-0.711 to 0.609	-0.559 to 0.58	\	-0.029 to 0.295	-0.528 to 0.553	-0.308 to 0.337
	-0.904 to 1.747	-0.137 to 0.427	-0.834 to 0.67	\	-0.469 to 0.623	-0.01 to 0.045	-0.416 to 0.458
tr_tbW_Re	-0.142 to 0.244	-0.167 to 0.364	-0.225 to 0.363	-0.604 to 0.634	\	-0.097 to 0.335	-0.028 to 0.283
	-0.471 to 0.5	-0.095 to 0.569	-0.756 to 0.822	-0.356 to 0.53	\	-0.159 to 0.373	-0.841 to 0.632
vl_tbW_Re	-0.472 to 0.142	-0.494 to 0.197	-0.458 to 0.137	-0.511 to 0.179	-0.511 to 0.409	\	-0.01 to 0.035
	-0.626 to 0.468	-0.112 to 0.423	-0.731 to 0.469	-0.537 to 0.563	-0.233 to 0.439	\	-0.622 to 0.728
vr_tbW_Re	-1.134 to 1.24	-0.806 to 1.007	-2.0 to 0.914	-2.0 to 2.0	-1.024 to 0.885	-1.492 to 0.769	\
	-0.626 to 0.771	-0.103 to 0.548	-2.0 to 0.629	-2.0 to 2.0	-0.405 to 0.484	-0.75 to 0.173	\

Table 9.13: θ_{tb} two-parameter fit confidence intervals

ϕ_{tb}	ta_ttA	tv_ttA	vr_ttZ	tl_tbW_Re	tr_tbW_Re	vl_tbW_Re	vr_tbW_Re
ta_ttA	\	-0.751 to 0.964	-0.519 to 0.033	-0.762 to 0.878	-0.636 to 0.649	-0.674 to 0.7	-0.354 to 0.382
	\	-0.002 to 0.064	-0.529 to 0.635	-0.471 to 0.537	-0.006 to 0.284	-0.162 to 0.011	-0.721 to 0.796
tv_ttA	-0.119 to 0.2	\	-0.019 to 0.116	-0.022 to 0.003	-0.021 to 0.194	-0.044 to 0.163	-0.008 to 0.003
		\	-0.678 to 0.657	-0.853 to 0.733	-0.156 to 0.291	-0.349 to 0.32	-0.72 to 0.709
vr_ttZ	-0.785 to 0.927	-0.83 to 0.689	\	-0.034 to 0.24	-0.576 to 0.782	-0.5 to 0.474	-0.034 to 0.122
	-0.745 to 0.654	-0.12 to 0.17	\	-0.707 to 0.837	-0.119 to 0.484	-0.135 to 0.217	-0.666 to 0.753
tl_tbW_Re	-0.829 to 1.179	-0.995 to 1.086	-1.053 to 0.931	\	-0.047 to 0.301	-0.776 to 0.846	-0.309 to 0.338
	-1.005 to 1.137	-0.121 to 0.161	-0.795 to 0.703	\	-0.768 to 0.78	-0.01 to 0.096	-0.418 to 0.465
tr_tbW_Re	-0.24 to 0.591	-0.261 to 1.096	-0.232 to 0.726	-1.087 to 0.829	\	-0.125 to 0.331	-0.023 to 0.284
	-0.77 to 0.995	-0.126 to 0.946	-0.744 to 0.928	-0.253 to 0.333	\	-0.205 to 0.343	-0.723 to 0.716
vl_tbW_Re	-0.498 to 0.475	-0.545 to 0.445	-0.523 to 0.455	-0.558 to 0.614	-0.559 to 0.428	\	-0.01 to 0.048
	-0.774 to 0.982	-0.122 to 0.18	-0.747 to 0.665	-1.097 to 1.163	-0.268 to 0.382	\	-0.727 to 0.748
vr_tbW_Re	-0.784 to 0.886	-0.848 to 0.908	-0.85 to 0.8	-1.999 to 2.0	-0.773 to 0.805	-0.768 to 0.81	\
	-0.801 to 1.077	-0.119 to 0.224	-0.769 to 0.673	-2.0 to 2.0	-0.238 to 0.543	-0.51 to 0.481	\

Table 9.14: ϕ_{tb} two-parameter fit confidence intervals

$\cos\theta_{Wl}$	ta_ttA	tv_ttA	vr_ttZ	tl_tbW_Re	tr_tbW_Re	vl_tbW_Re	vr_tbW_Re
ta_ttA	\	-0.439 to 0.44	-0.287 to 0.033	-0.188 to 0.180	-0.343 to 0.356	-0.471 to 0.417	-0.216 to 0.225
	\	-0.002 to 0.013	-0.462 to 0.404	-0.22 to 0.229	-0.006 to 0.025	-0.072 to 0.011	-0.256 to 0.252
tv_ttA	-0.083 to 0.212	\	-0.018 to 0.46	-0.002 to 0.003	-0.01 to 0.012	-0.035 to 0.044	-0.002 to 0.492
	-0.495 to 0.542	\	-0.522 to 0.663	-0.152 to 0.154	-0.028 to 0.037	-0.242 to 0.157	-0.244 to 0.245
vr_ttZ	-0.469 to 0.426	-0.858 to 0.686	\	-0.034 to 0.037	-0.202 to 0.165	-0.362 to 0.414	-0.034 to 0.039
	-0.608 to 0.465	-0.084 to 0.516	\	-0.161 to 0.151	-0.039 to 0.032	-0.119 to 0.141	-0.252 to 0.241
tl_tbW_Re	-0.425 to 0.427	-0.708 to 0.319	-0.244 to 0.289	\	-0.007 to 0.007	-0.157 to 0.153	-0.202 to 0.201
	-0.197 to 0.189	-0.088 to 0.492	-0.616 to 0.449	\	-0.153 to 0.169	-0.01 to 0.012	-0.308 to 0.309
tr_tbW_Re	-0.033 to 0.041	-0.047 to 0.27	-0.123 to 0.051	-0.462 to 0.265	\	-0.12 to 0.032	-0.007 to 0.007
	-0.434 to 0.429	-0.112 to 0.587	-0.916 to 0.46	-0.053 to 0.089	\	-0.196 to 0.054	-0.244 to 0.274
vl_tbW_Re	-0.389 to 0.166	-0.516 to 0.164	-0.36 to 0.162	-0.371 to 0.184	-0.419 to 0.184	\	-0.01 to 0.013
	-0.491 to 0.425	-0.083 to 0.198	-0.607 to 0.451	-0.188 to 0.156	-0.204 to 0.204	\	-0.248 to 0.245
vr_tbW_Re	-0.257 to 0.252	-0.765 to 0.33	-0.283 to 0.31	-0.337 to 0.323	-0.482 to 0.454	-0.253 to 0.275	\
	-0.429 to 0.433	-0.093 to 0.5	-0.615 to 0.45	-0.216 to 0.207	-0.071 to -0.059	-0.365 to 0.199	\

Table 9.15: θ_{Wl} two-parameter fit confidence intervals

ϕ_{Wl}	ta_ttA	tv_ttA	vr_ttZ	tl_tbW_Re	tr_tbW_Re	vl_tbW_Re	vr_tbW_Re
ta_ttA	\	-0.718 to 0.728	-0.72 to 0.033	-0.363 to 0.341	-0.689 to 0.647	-0.772 to 0.647	-0.367 to 0.369
	\	-0.002 to 0.034	-0.54 to 0.569	-0.311 to 0.333	-0.006 to 0.287	-0.231 to 0.011	-0.536 to 0.554
tv_ttA	-0.147 to 0.112	\	-0.019 to 0.115	-0.003 to 0.003	-0.021 to 0.044	-0.05 to 0.054	-0.004 to 0.003
	-0.786 to 0.782	\	-0.874 to 0.656	-0.285 to 0.284	-0.08 to 0.302	-0.467 to 0.182	-0.459 to 0.492
vr_ttZ	-0.907 to 1.241	-1.044 to 0.807	\	-0.034 to 0.059	-0.927 to 0.74	-0.434 to 0.591	-0.034 to 0.078
	-1.075 to 1.195	-0.147 to 0.138	\	-0.315 to 0.273	-0.123 to 0.472	-0.164 to 0.178	-0.503 to 0.476
tl_tbW_Re	-0.929 to 1.014	-0.603 to 0.632	-0.503 to 0.485	\	-0.011 to 0.288	-0.305 to 0.283	-0.285 to 0.305
	-0.402 to 0.396	-0.147 to 0.112	-1.005 to 0.953	\	-0.278 to 0.324	-0.01 to 0.019	-0.405 to 0.454
tr_tbW_Re	-0.092 to 0.304	-0.095 to 0.307	-0.127 to 0.522	-0.84 to 0.759	\	-0.141 to 0.303	-0.017 to 0.287
	-0.859 to 0.909	-0.147 to 0.112	-1.037 to 1.037	-0.261 to 0.431	\	-0.23 to 0.175	-0.45 to 0.597
vl_tbW_Re	-0.618 to 0.22	-0.591 to 0.212	-0.671 to 0.21	-2.0 to 1.128	-0.65 to 0.521	\	-0.01 to 0.025
	-0.999 to 0.807	-0.147 to 0.114	-1.056 to 0.783	-1.161 to 0.846	-0.275 to 1.206	\	-0.494 to 0.496
vr_tbW_Re	-0.551 to 0.577	-0.684 to 0.741	-0.592 to 0.572	-0.691 to 0.737	-1.046 to 1.105	-1.014 to 2.0	\
	-0.916 to 1.159	-0.147 to 0.112	-1.006 to 1.039	-0.423 to 0.432	-0.259 to 0.564	-1.126 to 1.556	\

Table 9.16: ϕ_{Wl} two-parameter fit confidence intervals

9.3.4 Multi-Parameter Fit to Higher Dimensional Angular Distribution

Multivariate analysis is a powerful technique for improving the sensitivity of anomalous coupling studies. In the single-parameter fit, we only considered the change in confidence interval for one and two-variable analyses. However, in theory, including more independent variables can improve sensitivity more effectively. For the observables used in this analysis, there are five weakly correlated variables that are worth discussing. Therefore, for future studies, a multivariate analysis can be performed to include all variables in the single-parameter fit.

For a two-parameter fit, the same logic can be applied, but the data must be processed more carefully because more couplings are involved. Similarly, in future studies, multivariate analysis can be performed for multi-parameter fits. By including all relevant variables, we can improve the sensitivity of anomalous coupling studies and gain a better understanding of the physics at play.

10 Conclusion

The results of the sensitivity analysis of top anomalous couplings at FCC-ee have been presented in Section 9.3, where multi-variate techniques and multi-parameter analysis were employed to provide different perspectives, and the confidence interval shows the optimistic coupling in new physics to be probed in FCC-ee data. The simulated datasets used in this study were generated in the experimental setting of the IDEA detector at the FCC-ee with a center-of-mass energy of $\sqrt{s} = 365GeV$ in the leptonic channel for top pair production events. The single-parameter and two-parameter fits were performed using the minimum χ^2 method to determine the 1σ confidence interval. Five observables were selected, and the angular distribution was also analyzed to determine the inclusion of cross-section and pure distribution to obtain different results.

In the future, the data collected by the FCC-ee can be used to probe beyond the Standard Model physics using the method shown in this analysis. Even if the data collected by the FCC-ee is not enough to support anomalous top couplings, it does not necessarily mean that their effect does not exist. The method used in this analysis can still be applied to colliders with even higher energies in the future.

The analysis presented in this study demonstrated the use of FCCSoftware for Monte Carlo simulation, event selection, and event reconstruction. The reconstruction of jets is crucial for reconstructing events, and research on jets has revealed the need for further improvement in the FCC-ee project. The effectiveness of various jet definitions is influenced by experimental circumstances, so refining the selection of jet definitions might require additional investigations in the future. The constrained fit provided by ABCfit++ improves the accuracy of events and the sensitivity of anomalous top couplings.

While this analysis provides valuable insights, there are several potential points for further investigation. Future research could focus on ISR to the cross-section, higher angular analysis dimensions, or analysis of all seven couplings combinations. As science and technology continue to improve, there is also room for optimization of the tools used in this analysis. Better algorithms can provide more accurate data and more efficient calculations, which can bring higher sensitivity to this analysis. With the progress of FCC-ee feasibility, further research on processes and channels will bring more optimization to this study and obtain more accurate results.

A The Jet Clustering Example

Struct clustering {
    clustering(
        float arg_radius,
        int arg_exclusive,
        float arg_cut,
        int arg_sorted,
        int arg_recombination
        ...
    ):
}

arg_radius refers to Jet cone radius

arg_exclusive Clustering options
    0 → inclusive clustering
    1 → exclusive clustering with dcut
    2 → exclusive clustering to exactly njets
    3 → exclusive clustering up to exactly njets
    4 → exclusive clustering with ycut

arg_cut refers to cut value
    arg_exclusive = 0 → p_t cut value
    arg_exclusive = 1 → dcut value
    arg_exclusive = 2 → njets value
    arg_exclusive = 3 → njets value
    arg_exclusive = 4 → ycut value

arg_sorted refers to returned jets ordering
    0 → sorted by p_t
    1 → sorted by E

arg_recombination refers to recombination schemes
    0 → E-scheme
    1 → p_t-scheme
    2 → p_t^2-scheme
    3 → E_t-scheme
    4 → E_t^2-scheme
    5 → Boost-invariant p_t-scheme
    6 → Boost-invariant p_t^2-scheme
    10 → E0-scheme
    11 → p-scheme

B Figures for Event Selection

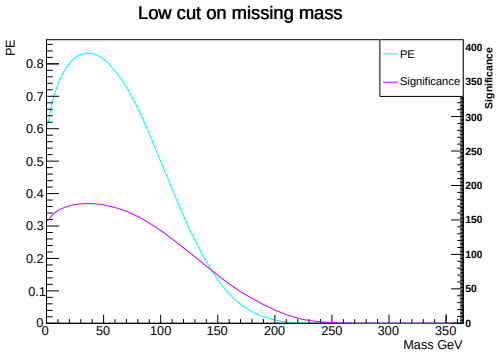

(a) PE and significance of cuts

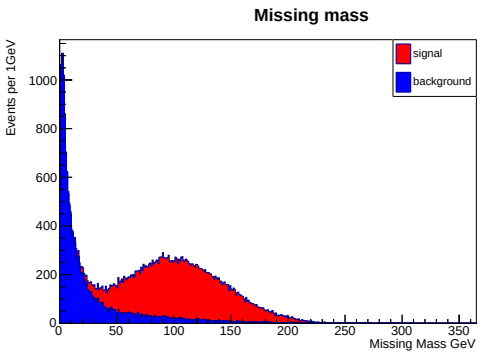

(b) The corresponding distribution plot of signal and backgrounds

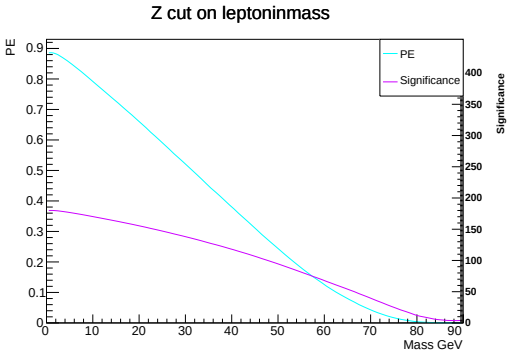

(a) PE and significance of cuts

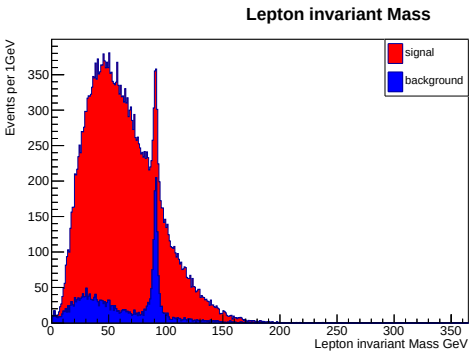

(b) The corresponding distribution plot of signal and backgrounds

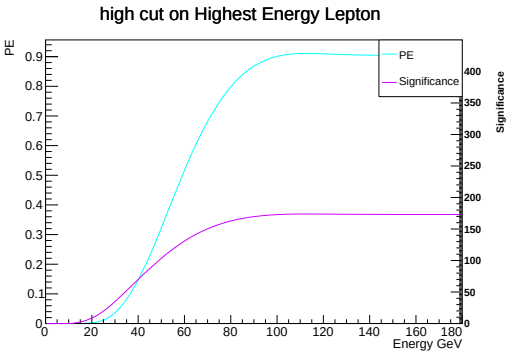

(a) PE and significance of cuts

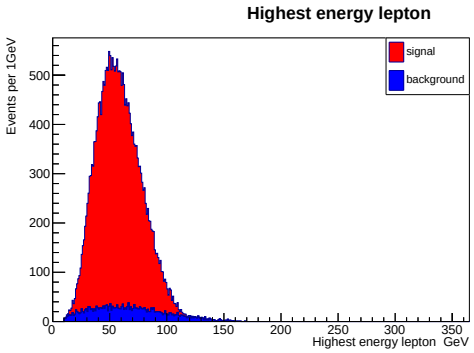

(b) The corresponding distribution plot of signal and backgrounds

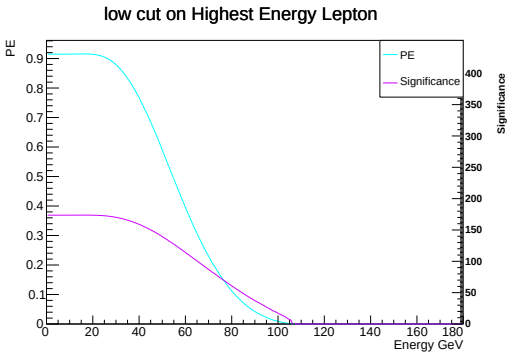

(a) PE and significance of cuts

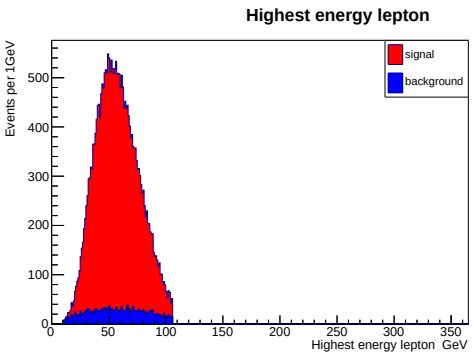

(b) The corresponding distribution plot of signal and backgrounds

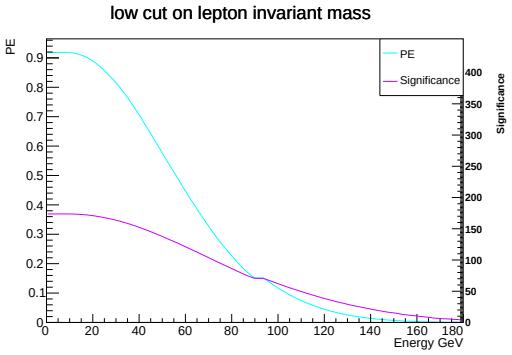

(a) PE and significance of cuts

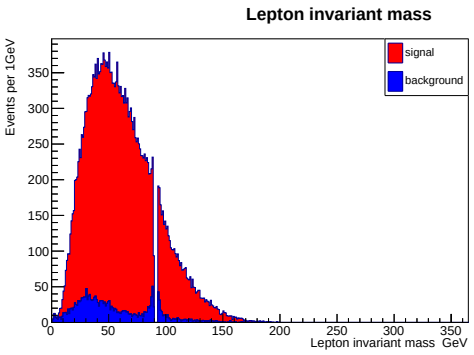

(b) The corresponding distribution plot of signal and backgrounds

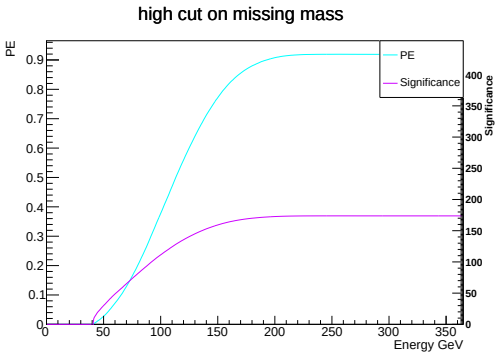

(a) PE and significance of cuts

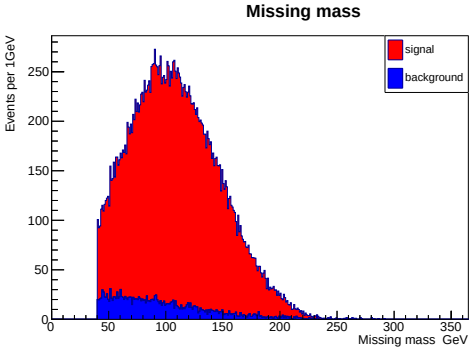

(b) The corresponding distribution plot of signal and backgrounds

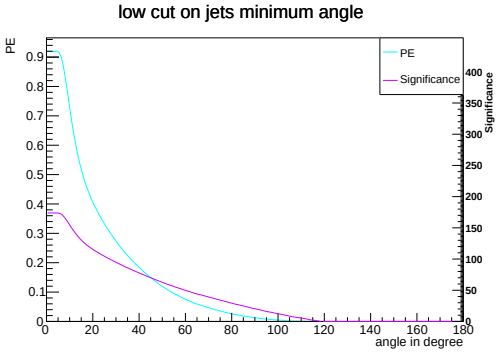

(a) PE and significance of cuts

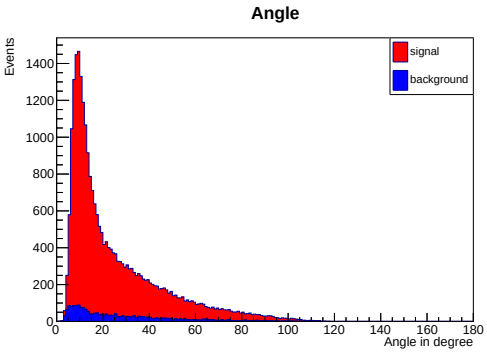

(b) The corresponding distribution plot of signal and backgrounds

Figure B.1: Sums of all event selection plots, and the order of figures follow the cut flow(Table 7.3-7.4). the left side of the figure is PE and the significance of cuts, and the right side is their distribution plots.

C Figures for χ^2 test

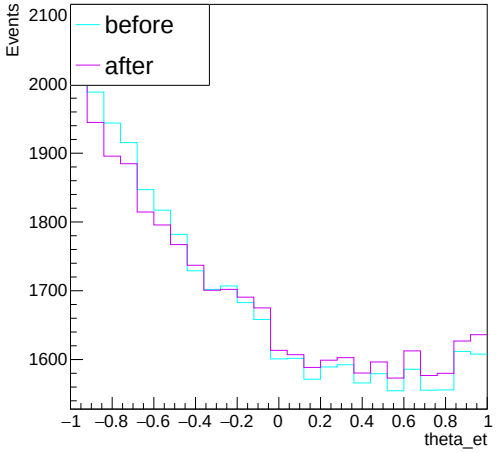

(a) The angular distribution before and after event selection

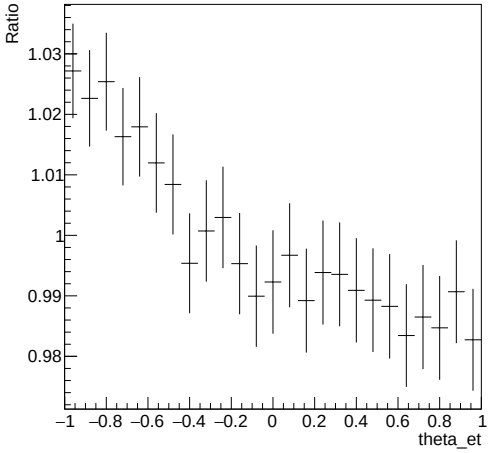

(b) The corresponding ratio plot

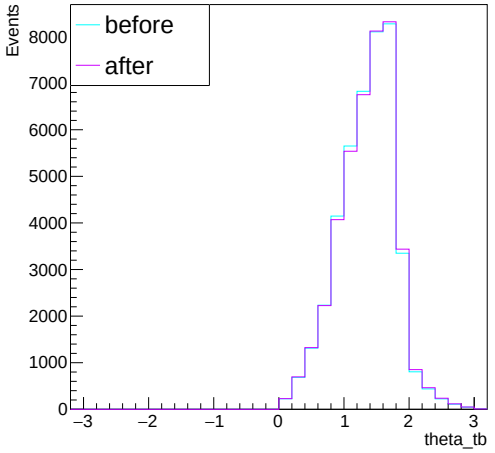

(a) The angular distribution before and after event selection

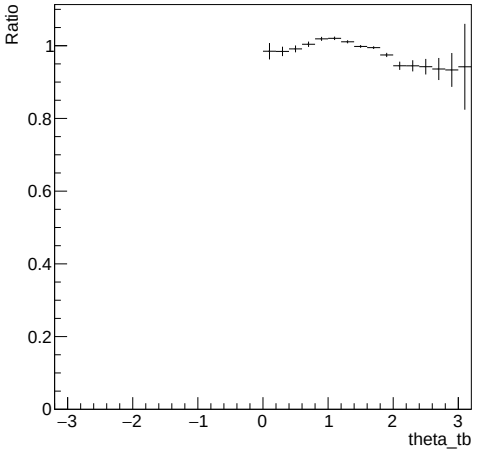

(b) The corresponding ratio plot

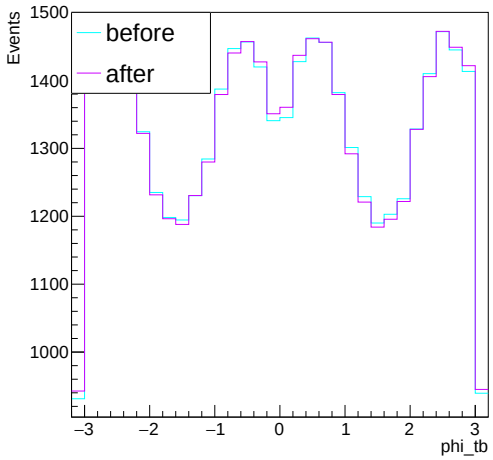

(a) The angular distribution before and after event selection

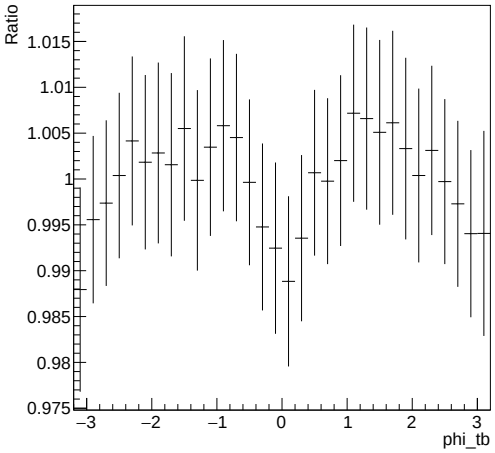

(b) The corresponding ratio plot

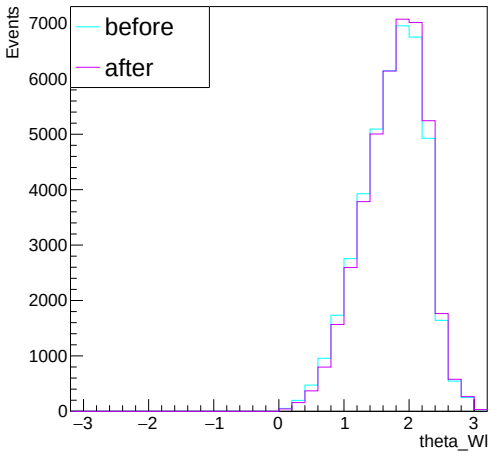

(a) The angular distribution before and after event selection

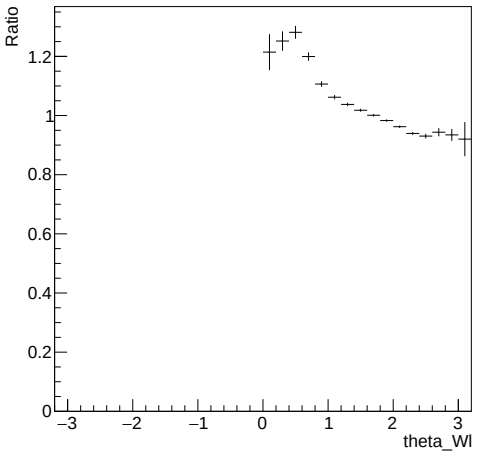

(b) The corresponding ratio plot

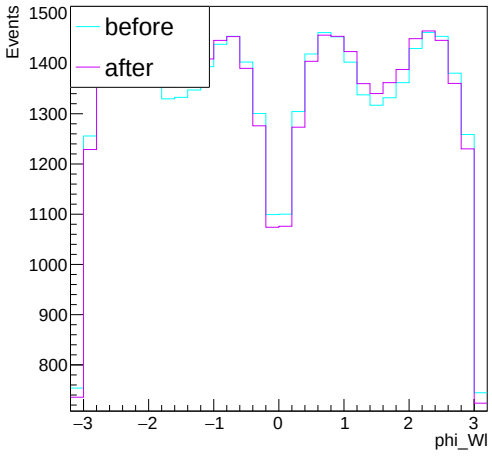

(a) The angular distribution before and after event selection

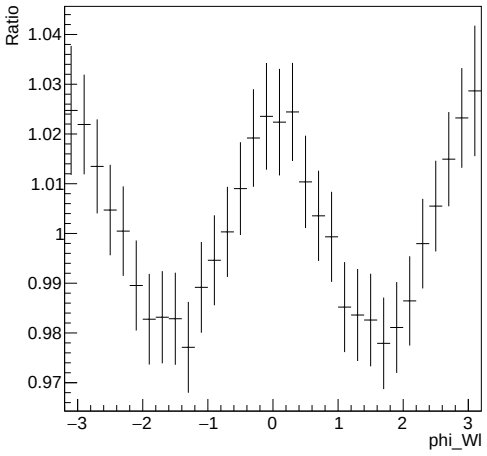

(b) The corresponding ratio plot

Figure C.1: Five angular distributions plots before and after event selection are on the left side, and ratio plots on the right side, and the order of plots θ_{et}, θ_{tb}, ϕ_{tb}, θ_{Wl}, ϕ_{Wl} is followed by Table 9.1

D Figures for Results

D.1 Single-Parameter 1 Dimensional Angular Distribution

ta_ttA σ included

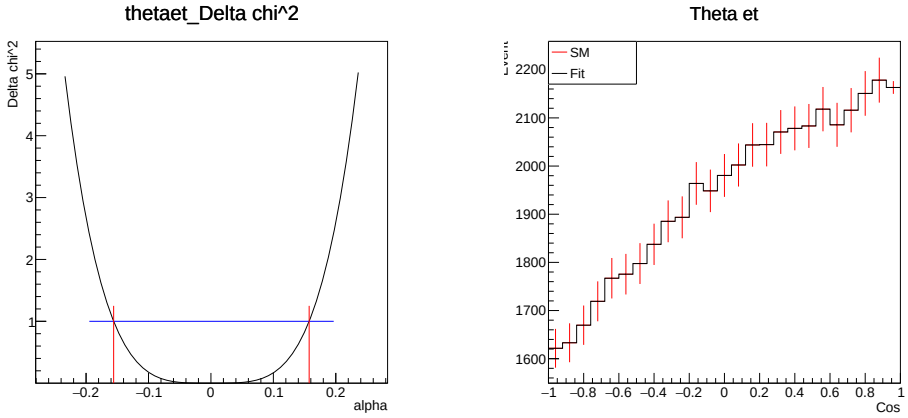

(a) χ^2 of θ_{et} (b) fit of θ_{et}

Figure D.1: θ_{et} for ta_ttA

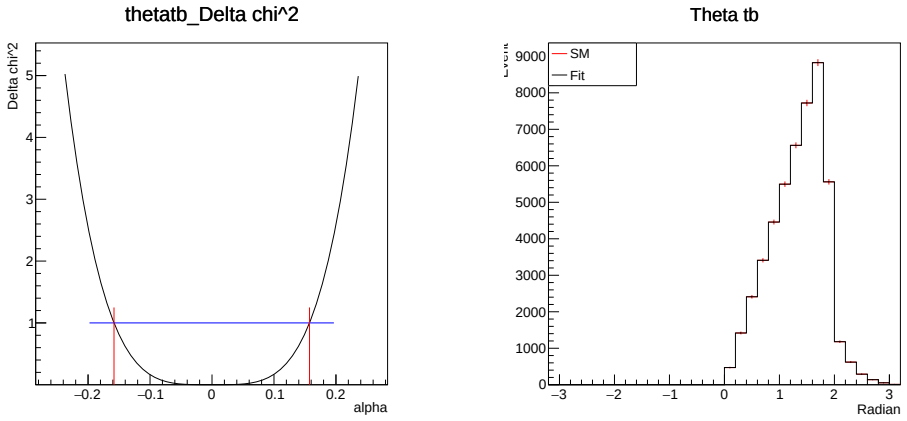

(a) χ^2 of θ_{tb} (b) fit of θ_{tb}

Figure D.2: θ_{tb} for ta_ttA

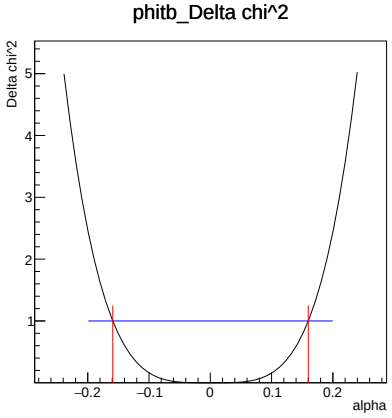

(a) χ^2 of ϕ_{tb}

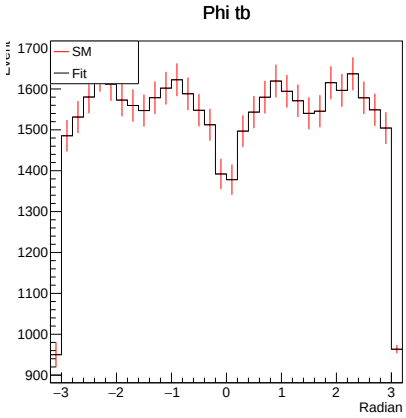

(b) fit of ϕ_{tb}

Figure D.3: ϕ_{tb} for ta_ttA

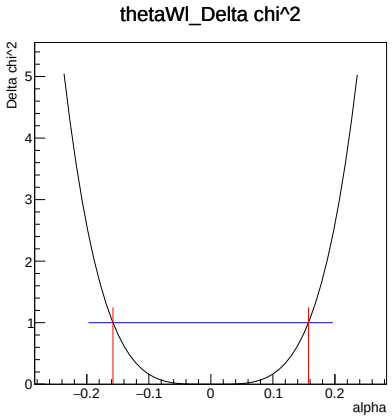

(a) χ^2 of θ_{Wl}

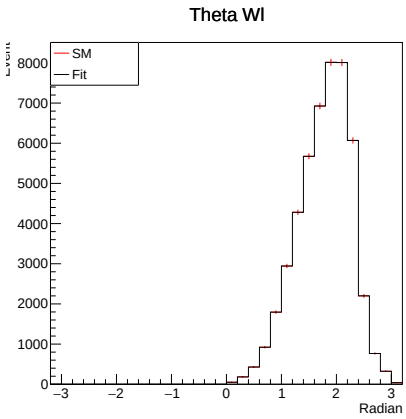

(b) fit of θ_{Wl}

Figure D.4: θ_{Wl} for ta_ttA

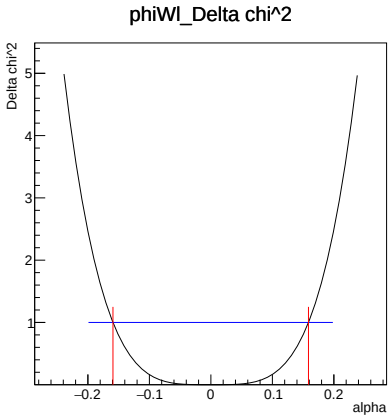

(a) χ^2 of ϕ_{Wl}

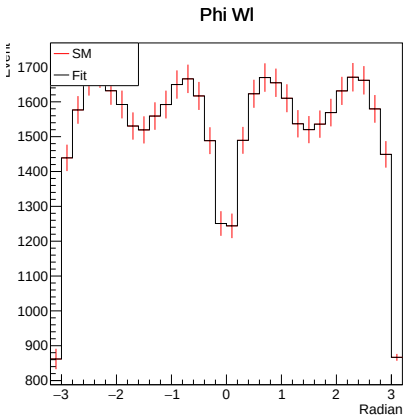

(b) fit of ϕ_{Wl}

Figure D.5: ϕ_{Wl} for ta_ttA

ta_ttA σ excluded

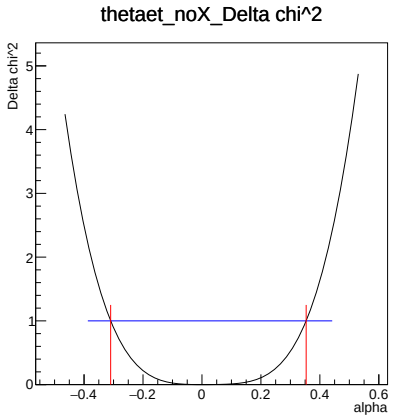

(a) χ^2 of θ_{et}

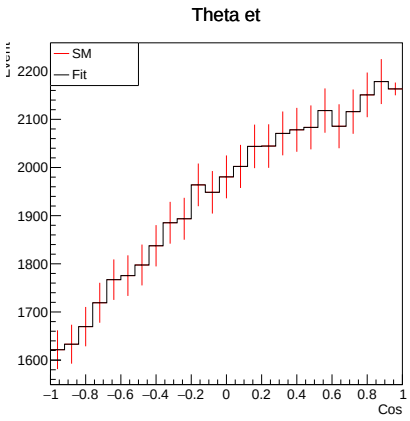

(b) fit of θ_{et}

Figure D.6: θ_{et} for ta_ttA

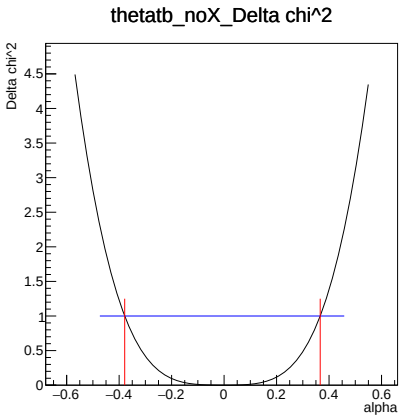

(a) χ^2 of θ_{tb}

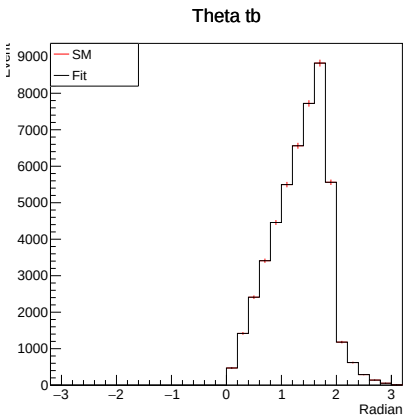

(b) fit of θ_{tb}

Figure D.7: θ_{tb} for ta_ttA

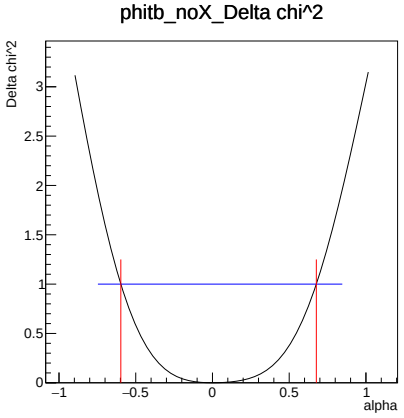

(a) χ^2 of ϕ_{tb}

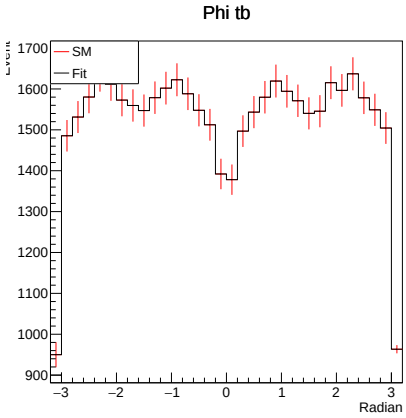

(b) fit of ϕ_{tb}

Figure D.8: ϕ_{tb} for ta_ttA

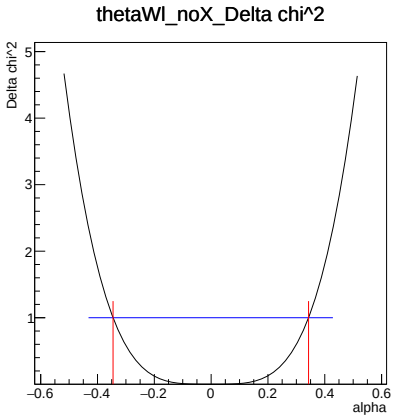

(a) χ^2 of θ_{Wl}

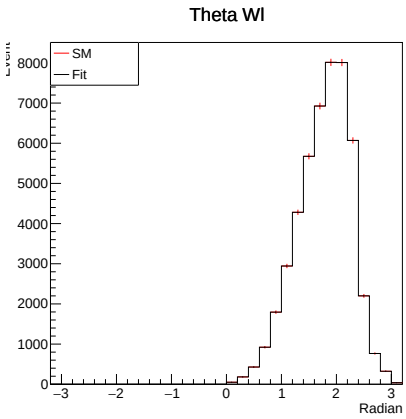

(b) fit of θ_{Wl}

Figure D.9: θ_{Wl} for ta_ttA

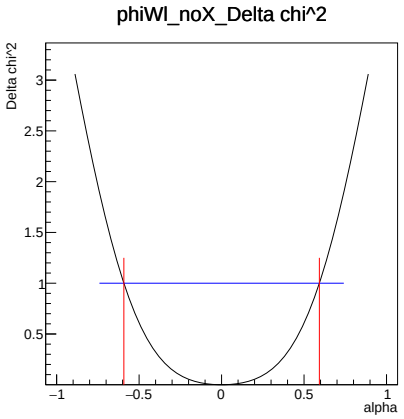

(a) χ^2 of ϕ_{Wl}

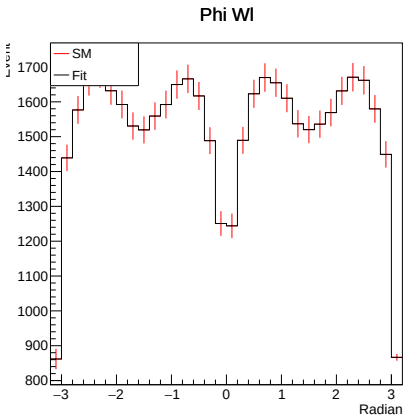

(b) fit of ϕ_{Wl}

Figure D.10: ϕ_{Wl} for ta_ttA

tv_ttA σ included

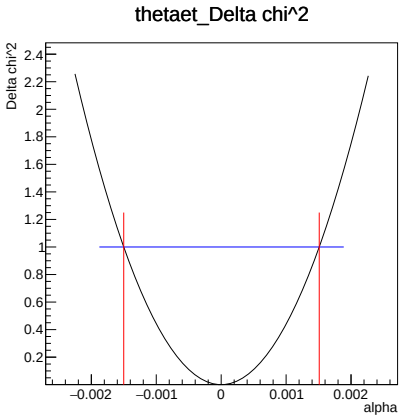

(a) χ^2 of θ_{et}

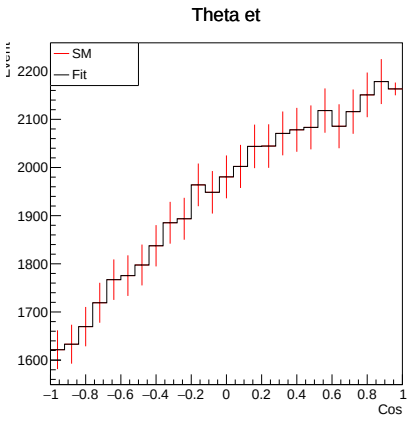

(b) fit of θ_{et}

Figure D.11: θ_{et} for tv_ttA

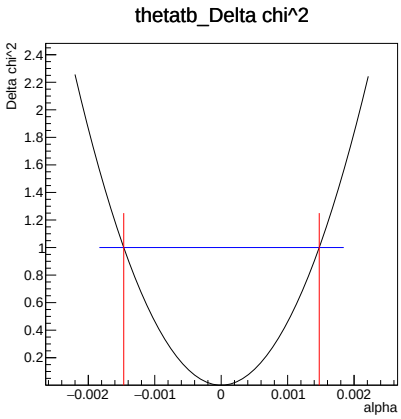

(a) χ^2 of θ_{tb}

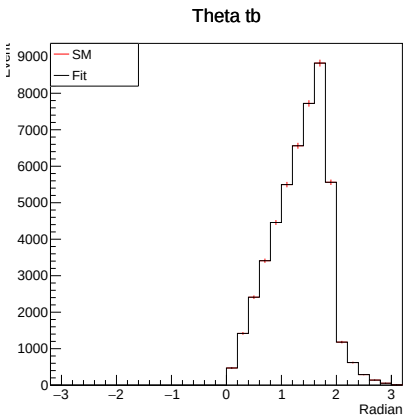

(b) fit of θ_{tb}

Figure D.12: θ_{tb} for tv_ttA

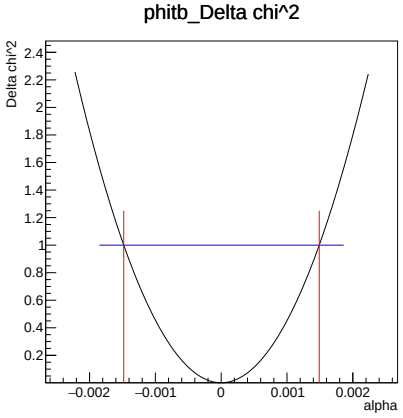

(a) χ^2 of ϕ_{tb}

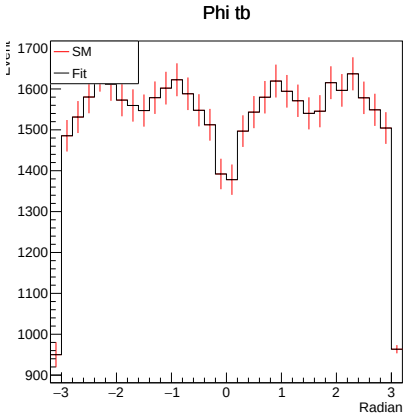

(b) fit of ϕ_{tb}

Figure D.13: ϕ_{tb} for tv_ttA

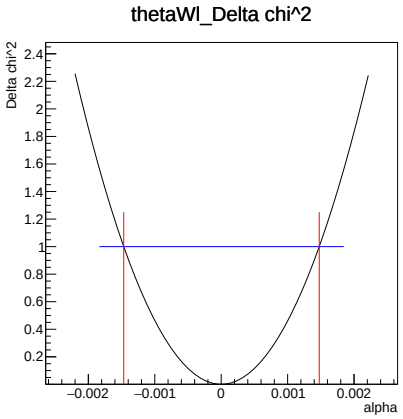

(a) χ^2 of θ_{Wl}

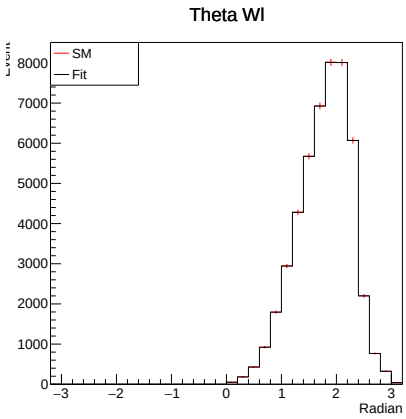

(b) fit of θ_{Wl}

Figure D.14: θ_{Wl} for tv_ttA

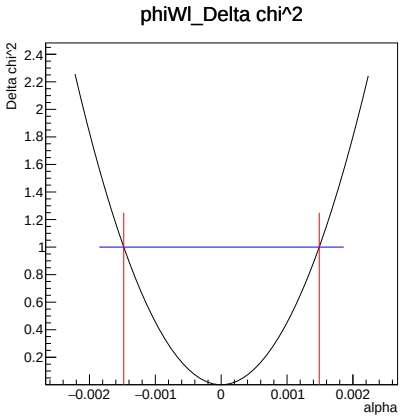

(a) χ^2 of ϕ_{Wl}

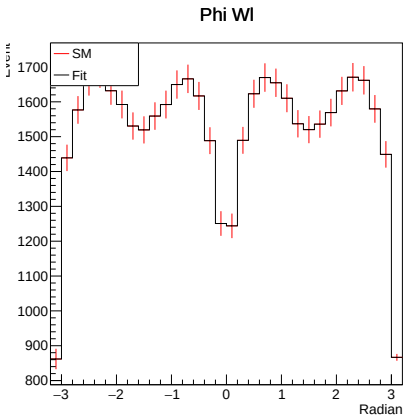

(b) fit of ϕ_{Wl}

Figure D.15: ϕ_{Wl} for tv_ttA

tv_ttA σ excluded

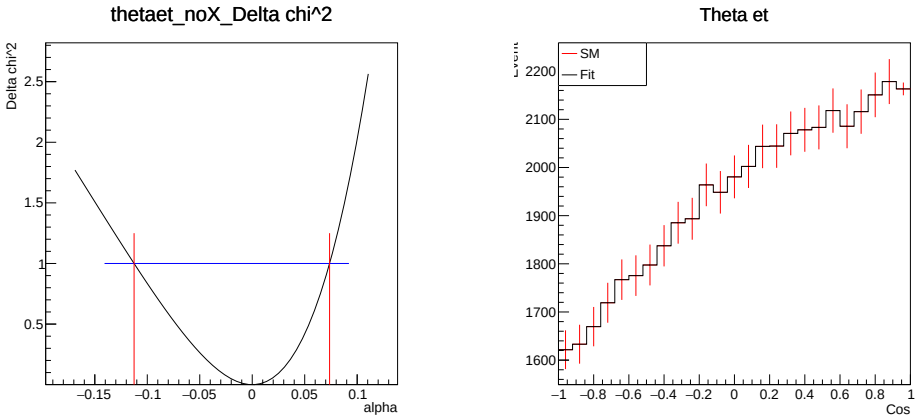

(a) χ^2 of θ_{et} (b) fit of θ_{et}

Figure D.16: θ_{et} for tv_ttA

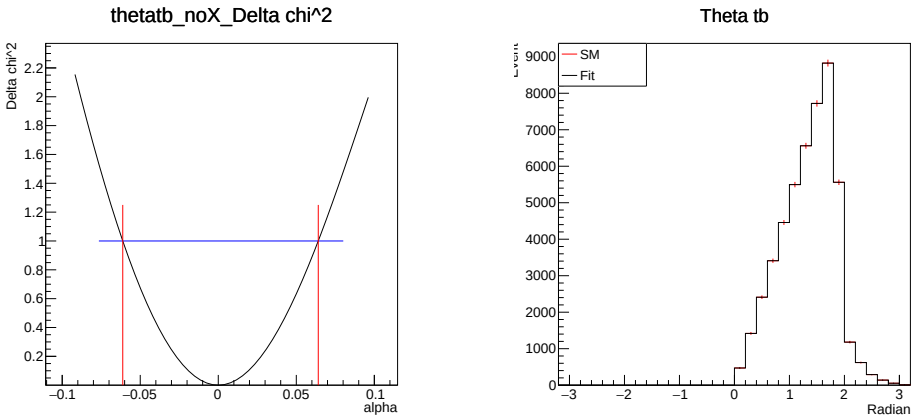

(a) χ^2 of θ_{tb} (b) fit of θ_{tb}

Figure D.17: θ_{tb} for tv_ttA

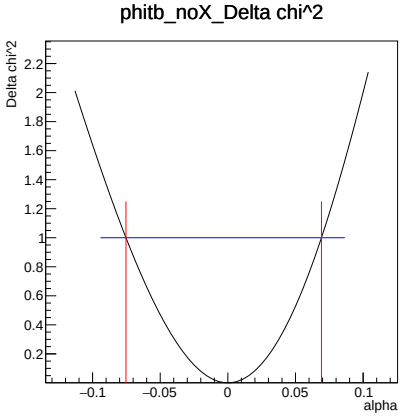

(a) χ^2 of ϕ_{tb}

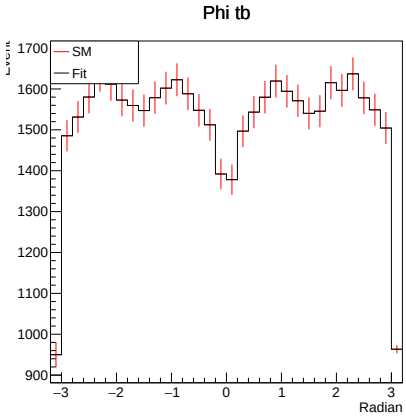

(b) fit of ϕ_{tb}

Figure D.18: ϕ_{tb} for tv_ttA

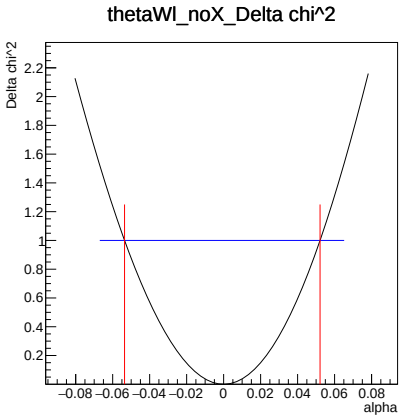

(a) χ^2 of θ_{Wl}

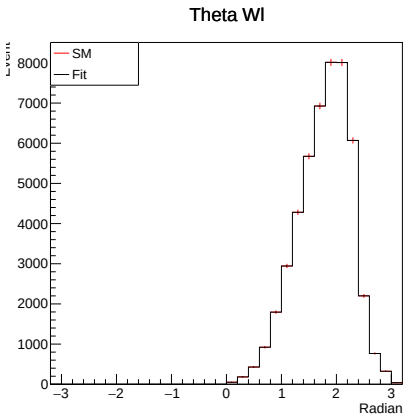

(b) fit of θ_{Wl}

Figure D.19: θ_{Wl} for tv_ttA

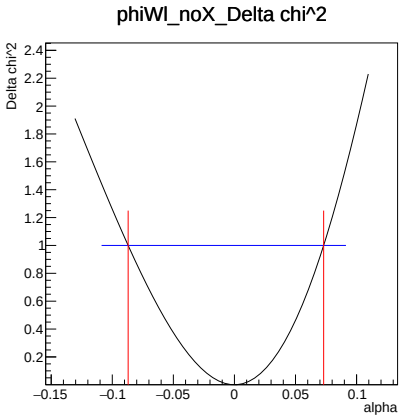

(a) χ^2 of ϕ_{Wl}

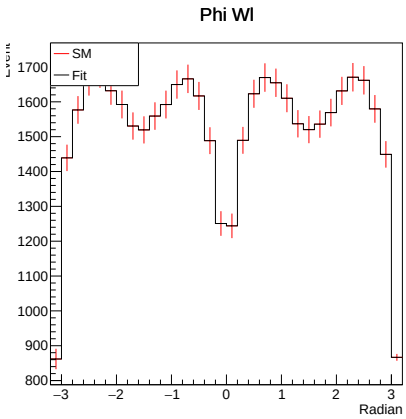

(b) fit of ϕ_{Wl}

Figure D.20: ϕ_{Wl} for tv_ttA

vr_ttZ σ included

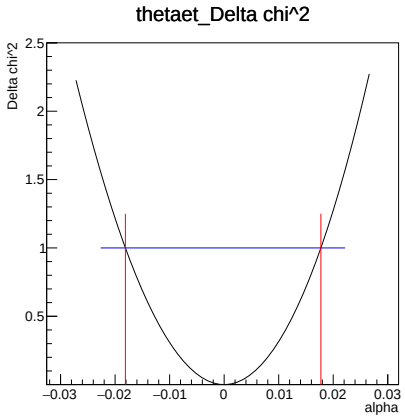

(a) χ^2 of θ_{et}

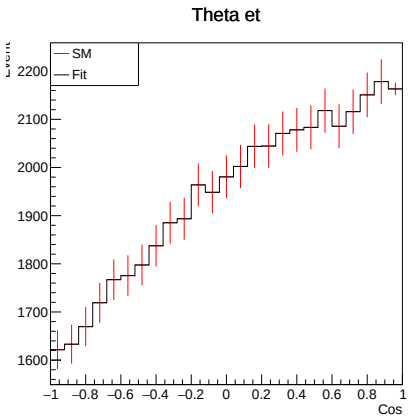

(b) fit of θ_{et}

Figure D.21: θ_{et} for vr_ttZ

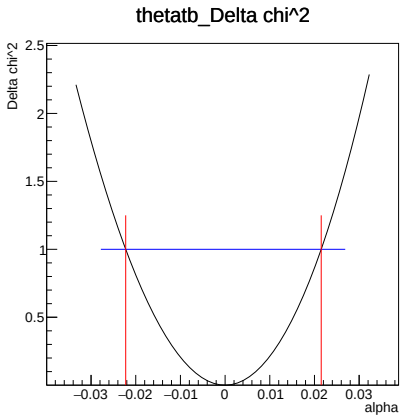

(a) χ^2 of θ_{tb}

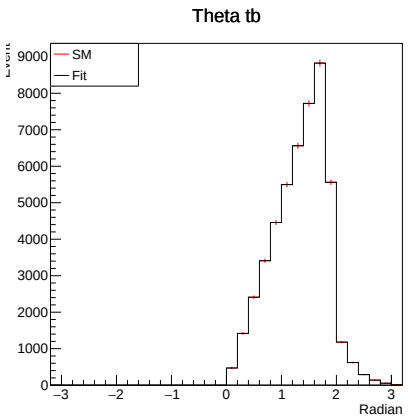

(b) fit of θ_{tb}

Figure D.22: θ_{tb} for vr_ttZ

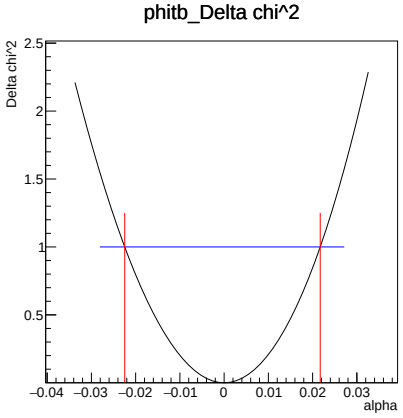

(a) χ^2 of ϕ_{tb}

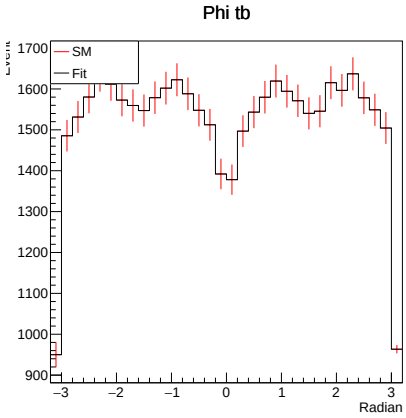

(b) fit of ϕ_{tb}

Figure D.23: ϕ_{tb} for vr_ttZ

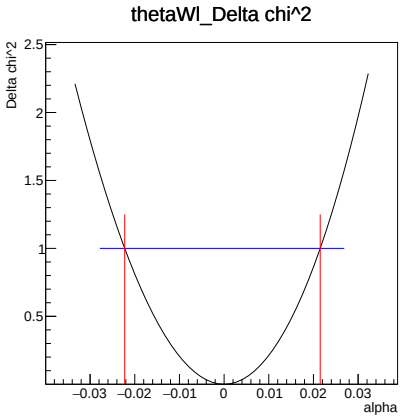

(a) χ^2 of θ_{Wl}

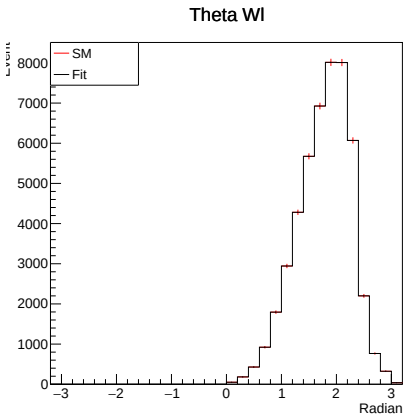

(b) fit of θ_{Wl}

Figure D.24: θ_{Wl} for vr_ttZ

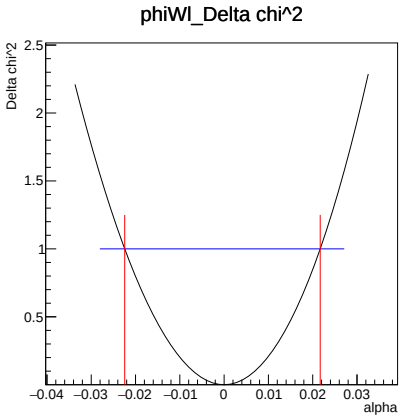

(a) χ^2 of ϕ_{Wl}

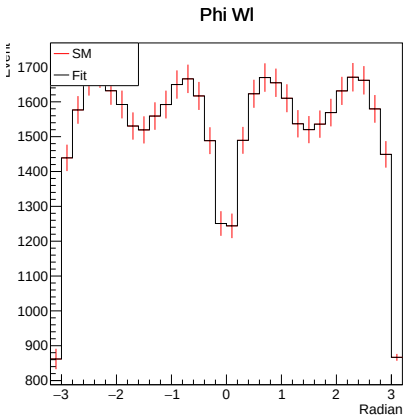

(b) fit of ϕ_{Wl}

Figure D.25: ϕ_{Wl} for vr_ttZ

vr_ttZ σ excluded

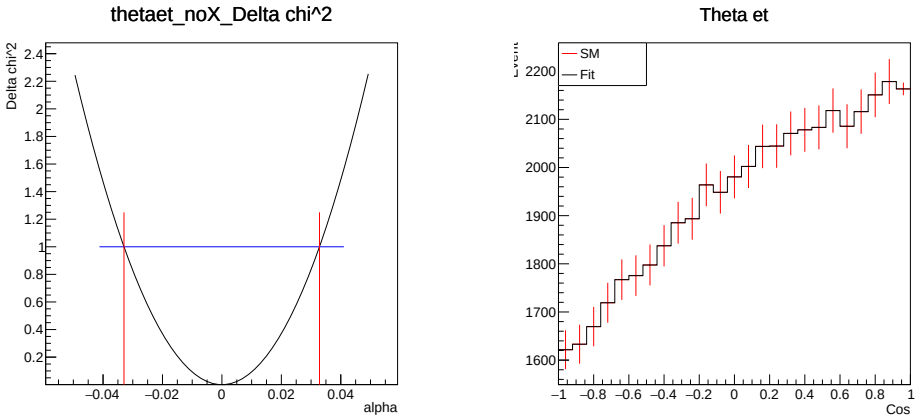

(a) χ^2 of θ_{et} (b) fit of θ_{et}

Figure D.26: θ_{et} for vr_ttZ

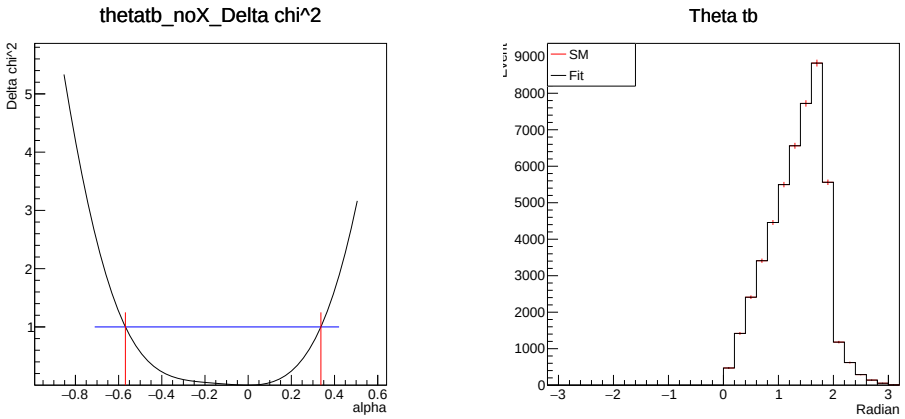

(a) χ^2 of θ_{tb} (b) fit of θ_{tb}

Figure D.27: θ_{tb} for vr_ttZ

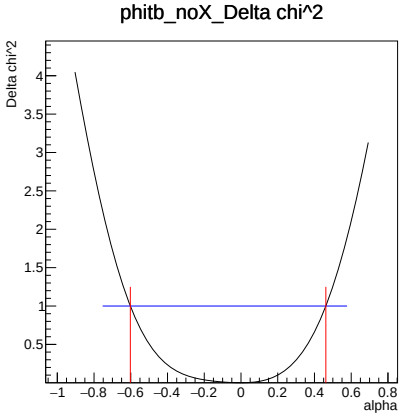

(a) χ^2 of ϕ_{tb}

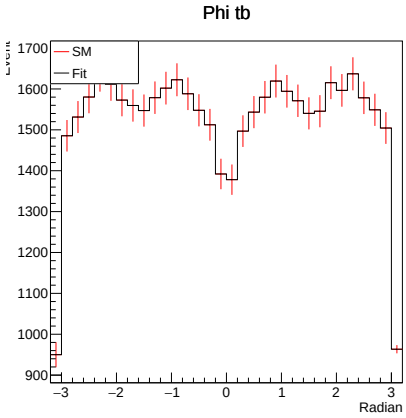

(b) fit of ϕ_{tb}

Figure D.28: ϕ_{tb} for vr_ttZ

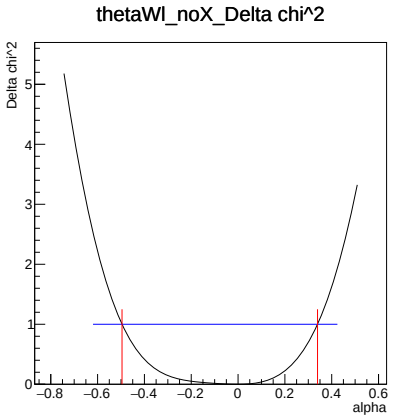

(a) χ^2 of θ_{Wl}

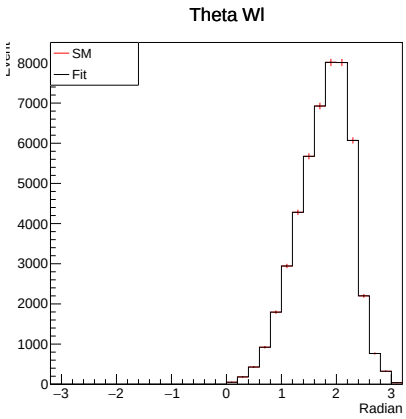

(b) fit of θ_{Wl}

Figure D.29: θ_{Wl} for vr_ttZ

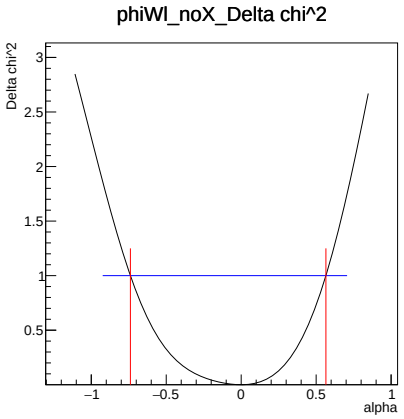

(a) χ^2 of ϕ_{Wl}

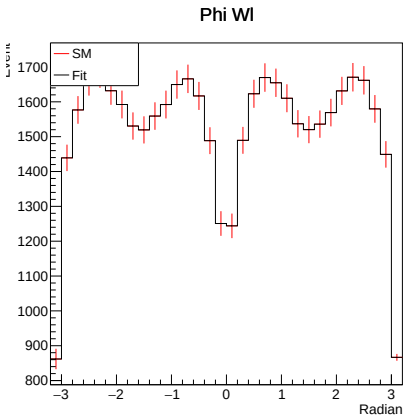

(b) fit of ϕ_{Wl}

Figure D.30: ϕ_{Wl} for vr_ttZ

tl_tbW_Re σ included

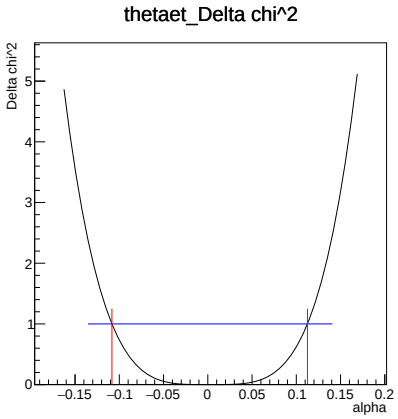

(a) χ^2 of θ_{et}

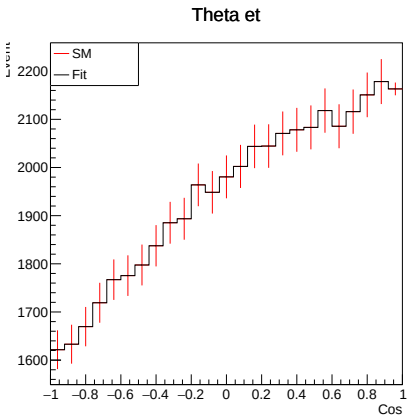

(b) fit of θ_{et}

Figure D.31: θ_{et} for tl_tbW_Re

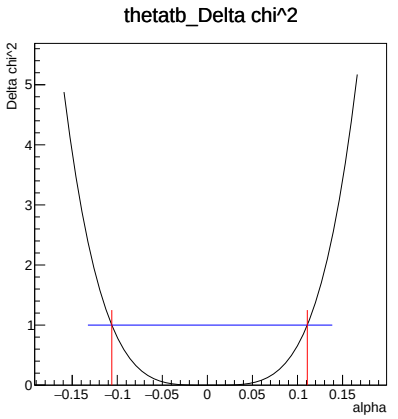

(a) χ^2 of θ_{tb}

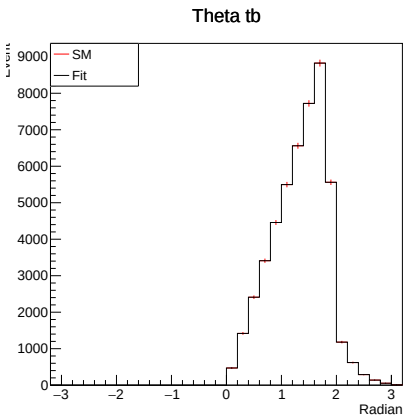

(b) fit of θ_{tb}

Figure D.32: θ_{tb} for tl_tbW_Re

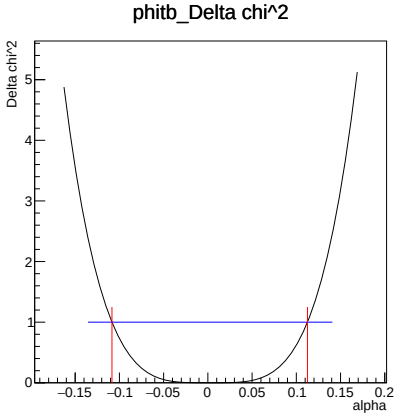

(a) χ^2 of ϕ_{tb}

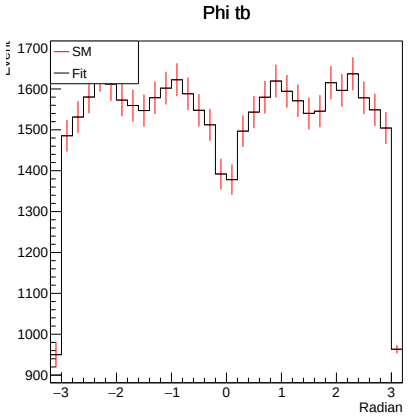

(b) fit of ϕ_{tb}

Figure D.33: ϕ_{tb} for tl_tbW_Re

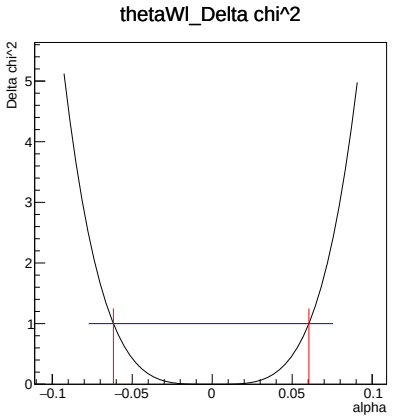

(a) χ^2 of θ_{Wl}

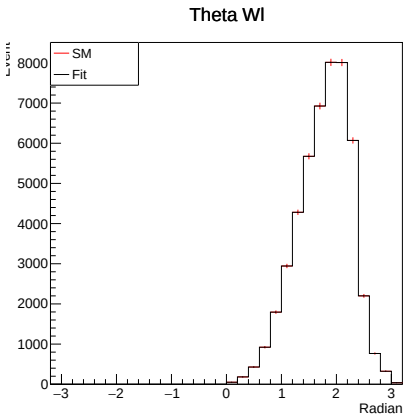

(b) fit of θ_{Wl}

Figure D.34: θ_{Wl} for tl_tbW_Re

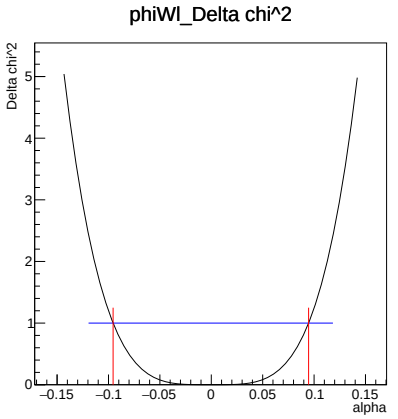

(a) χ^2 of ϕ_{Wl}

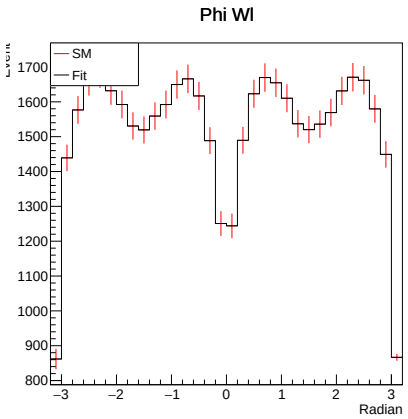

(b) fit of ϕ_{Wl}

Figure D.35: ϕ_{Wl} for tl_tbW_Re

tl_tbW_Re σ excluded

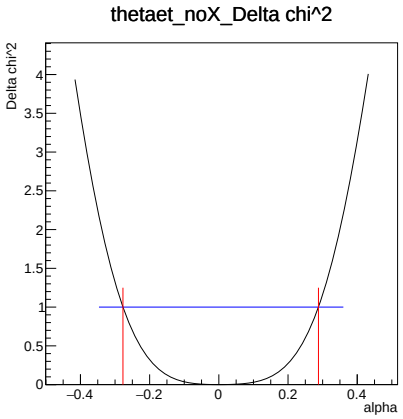

(a) χ^2 of θ_{et}

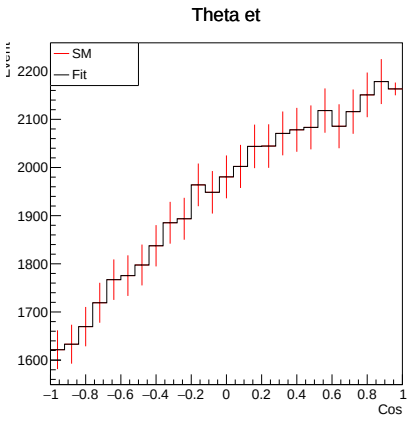

(b) fit of θ_{et}

Figure D.36: θ_{et} for tl_tbW_Re

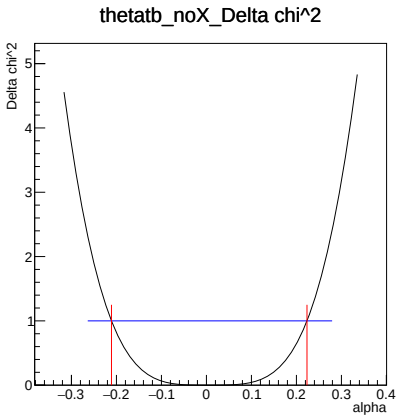

(a) χ^2 of θ_{tb}

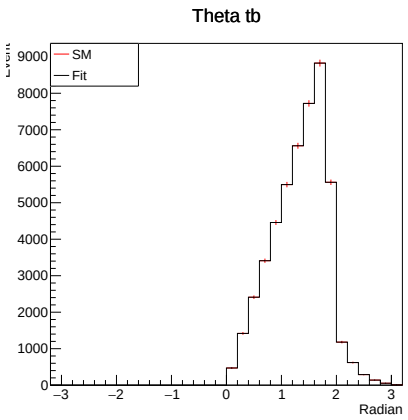

(b) fit of θ_{tb}

Figure D.37: θ_{tb} for tl_tbW_Re

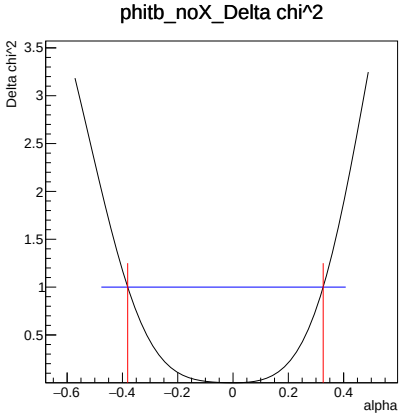

(a) χ^2 of ϕ_{tb}

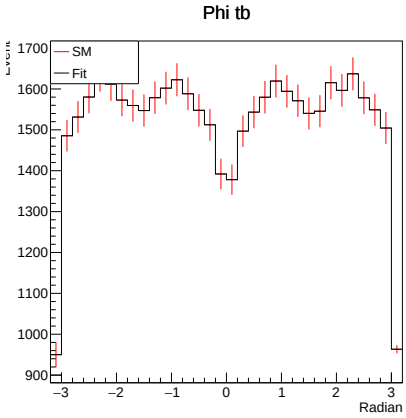

(b) fit of ϕ_{tb}

Figure D.38: ϕ_{tb} for tl_tbW_Re

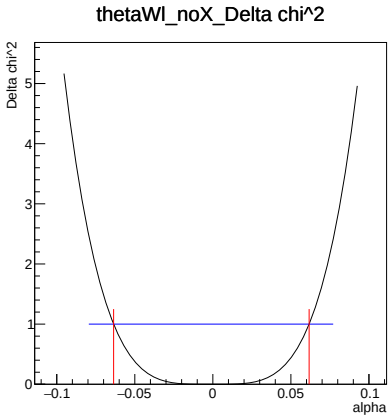

(a) χ^2 of θ_{Wl}

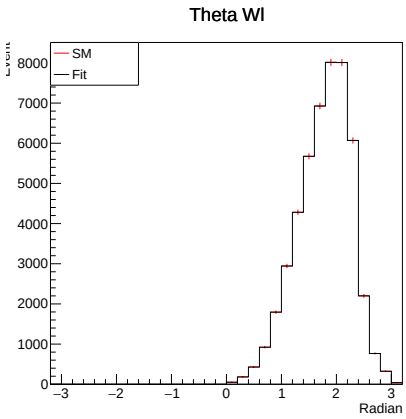

(b) fit of θ_{Wl}

Figure D.39: θ_{Wl} for tl_tbW_Re

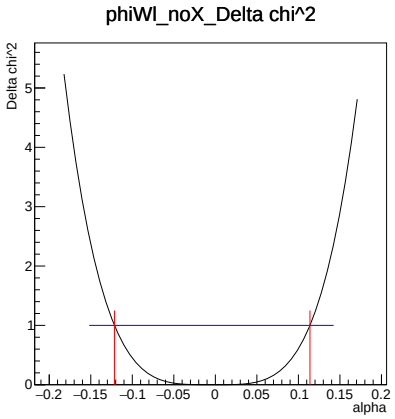

(a) χ^2 of ϕ_{Wl}

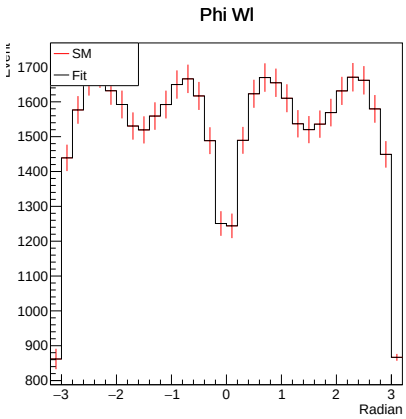

(b) fit of ϕ_{Wl}

Figure D.40: ϕ_{Wl} for tl_tbW_Re

tr_tbW_Re σ included

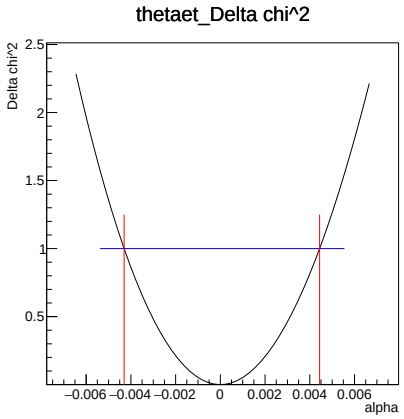

(a) χ^2 of θ_{et}

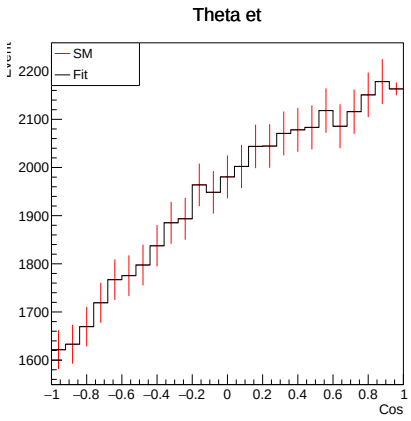

(b) fit of θ_{et}

Figure D.41: θ_{et} for tr_tbW_Re

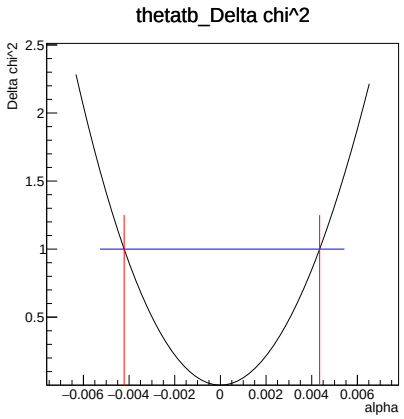

(a) χ^2 of θ_{tb}

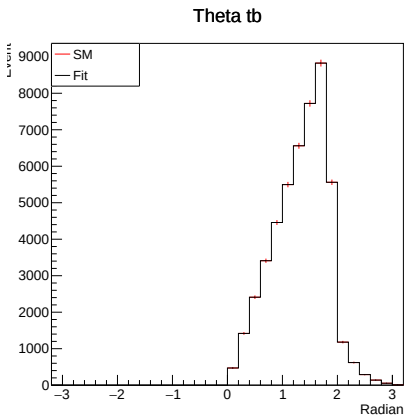

(b) fit of θ_{tb}

Figure D.42: θ_{tb} for tr_tbW_Re

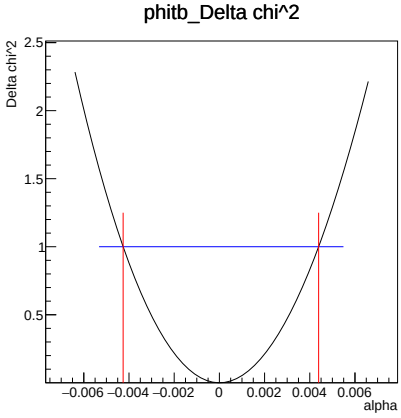

(a) χ^2 of ϕ_{tb}

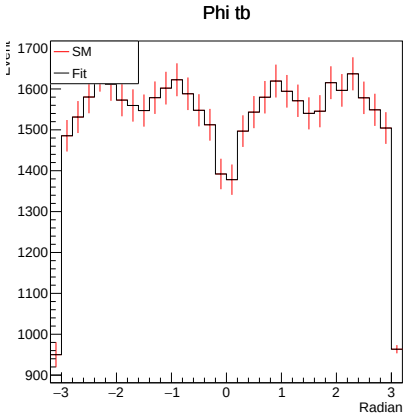

(b) fit of ϕ_{tb}

Figure D.43: ϕ_{tb} for tr_tbW_Re

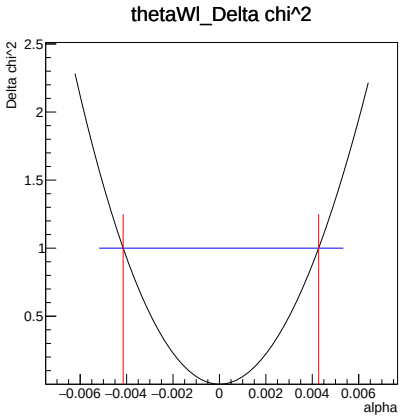

(a) χ^2 of θ_{Wl}

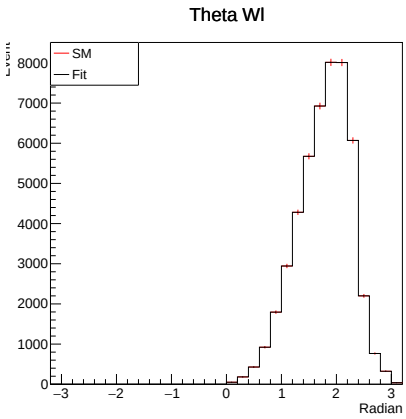

(b) fit of θ_{Wl}

Figure D.44: θ_{Wl} for tr_tbW_Re

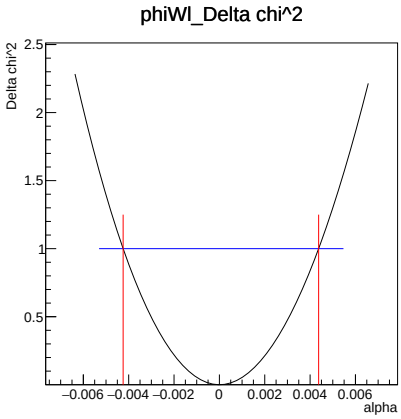

(a) χ^2 of ϕ_{Wl}

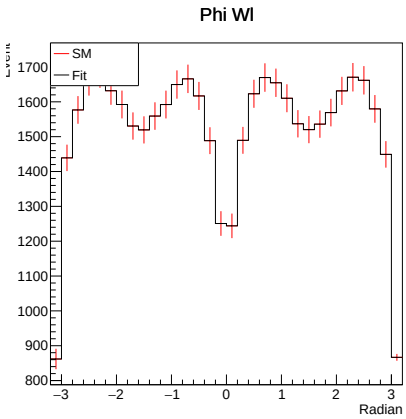

(b) fit of ϕ_{Wl}

Figure D.45: ϕ_{Wl} for tr_tbW_Re

tr_tbW_Re σ excluded

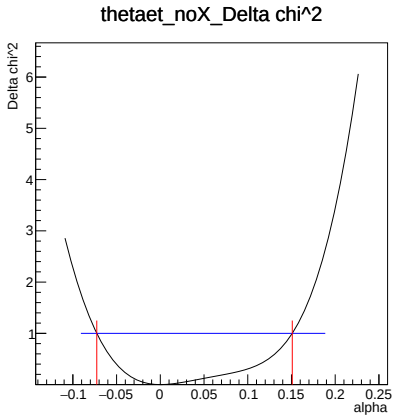

(a) χ^2 of θ_{et}

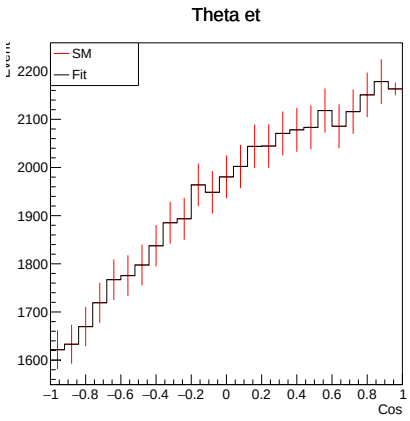

(b) fit of θ_{et}

Figure D.46: θ_{et} for tr_tbW_Re

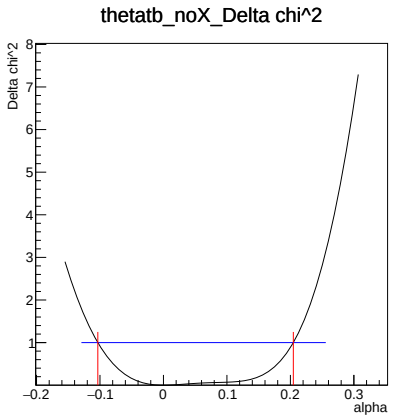

(a) χ^2 of θ_{tb}

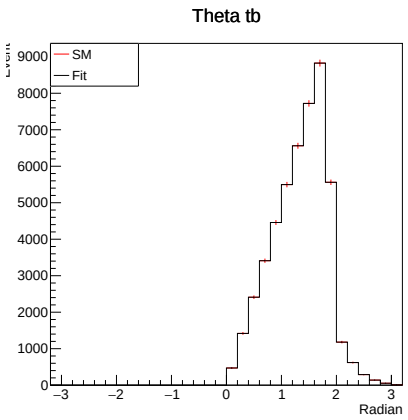

(b) fit of θ_{tb}

Figure D.47: θ_{tb} for tr_tbW_Re

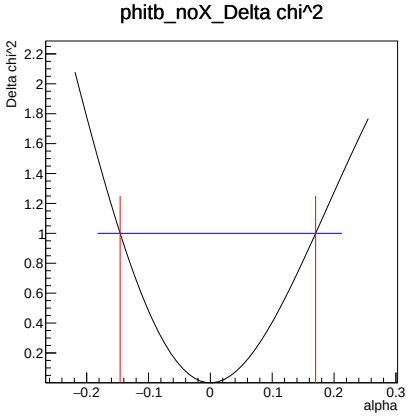

(a) χ^2 of ϕ_{tb}

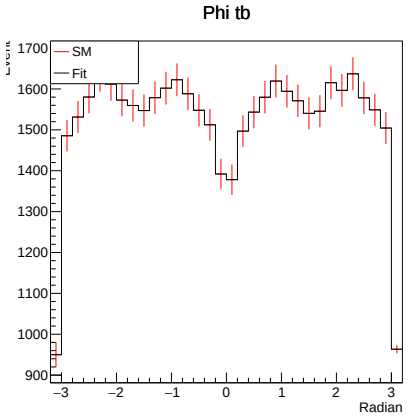

(b) fit of ϕ_{tb}

Figure D.48: ϕ_{tb} for tr_tbW_Re

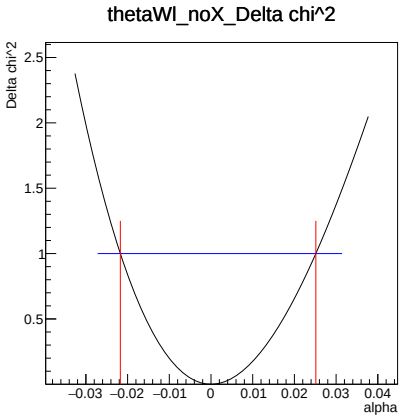

(a) χ^2 of θ_{Wl}

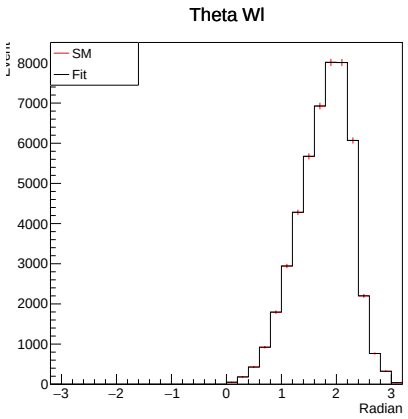

(b) fit of θ_{Wl}

Figure D.49: θ_{Wl} for tr_tbW_Re

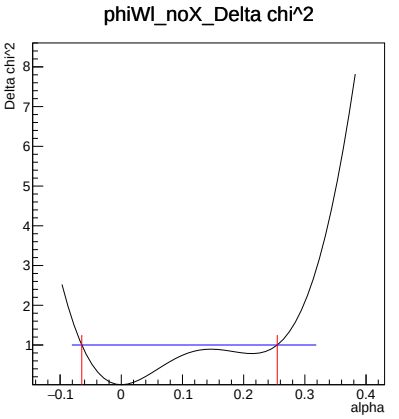

(a) χ^2 of ϕ_{Wl}

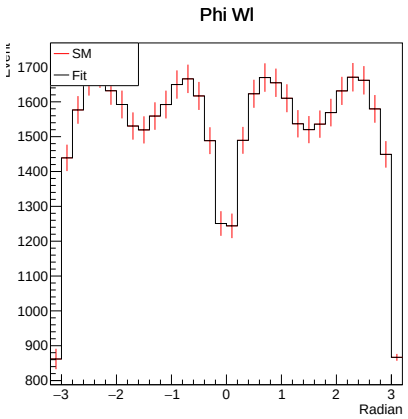

(b) fit of ϕ_{Wl}

Figure D.50: ϕ_{Wl} for tr_tbW_Re

vl_tbW_Re σ included

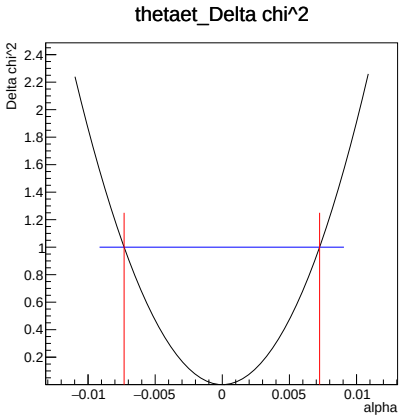

(a) χ^2 of θ_{et}

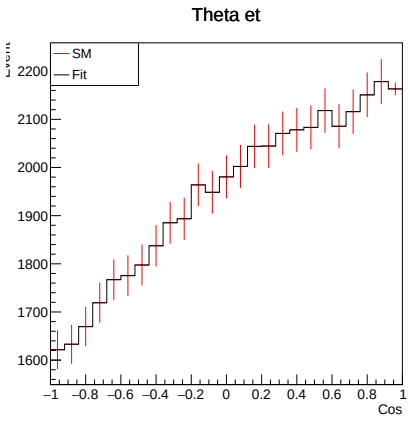

(b) fit of θ_{et}

Figure D.51: θ_{et} for vl_tbW_Re

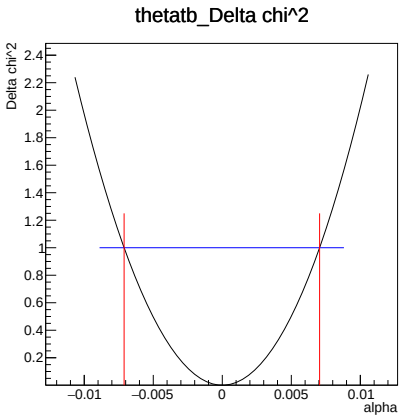

(a) χ^2 of θ_{tb}

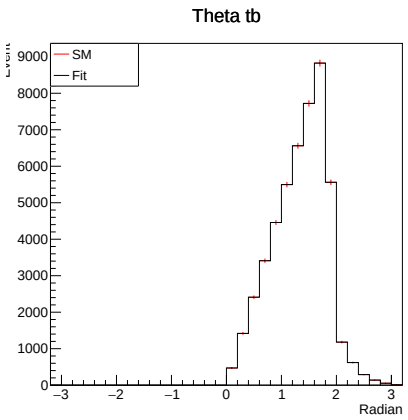

(b) fit of θ_{tb}

Figure D.52: θ_{tb} for vl_tbW_Re

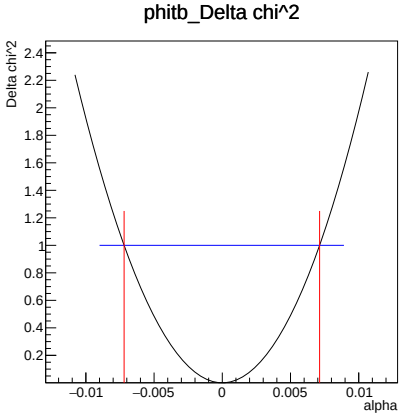

(a) χ^2 of ϕ_{tb}

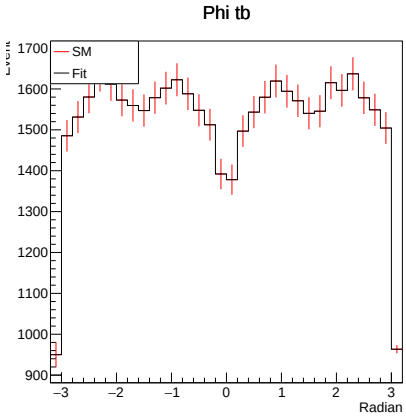

(b) fit of ϕ_{tb}

Figure D.53: ϕ_{tb} for vl_tbW_Re

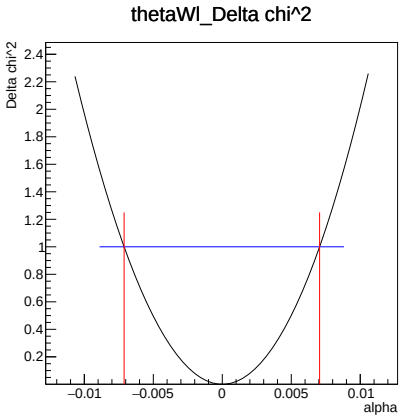

(a) χ^2 of θ_{Wl}

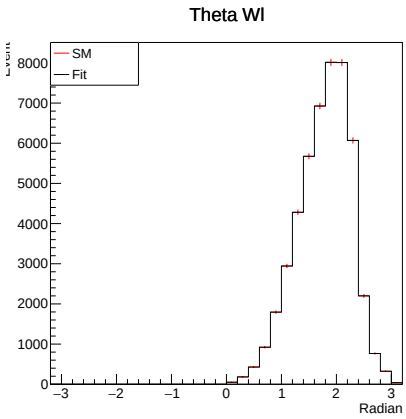

(b) fit of θ_{Wl}

Figure D.54: θ_{Wl} for vl_tbW_Re

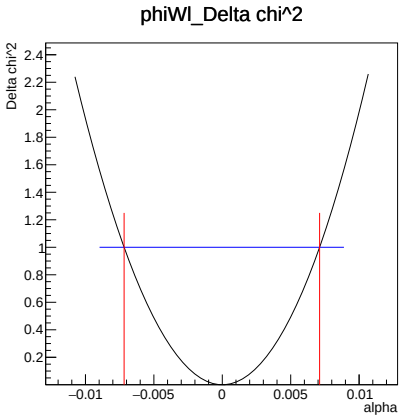

(a) χ^2 of ϕ_{Wl}

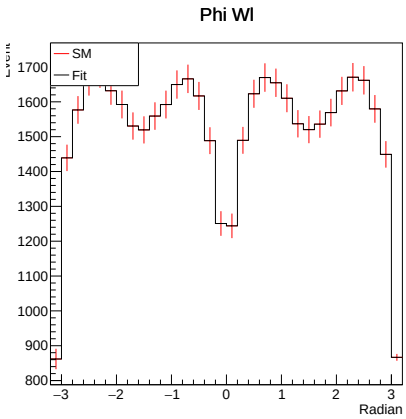

(b) fit of ϕ_{Wl}

Figure D.55: ϕ_{Wl} for vl_tbW_Re

vl_tbW_Re σ excluded

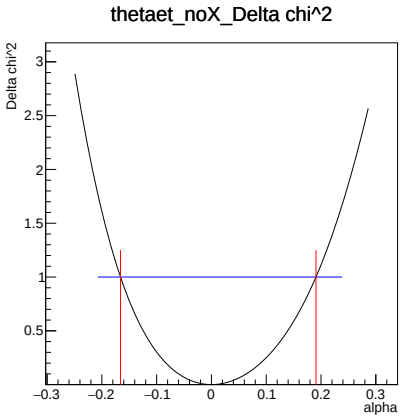

(a) χ^2 of θ_{et}

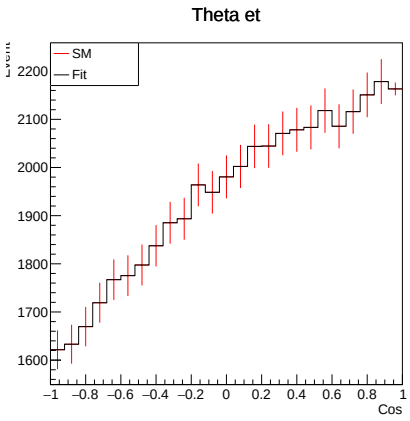

(b) fit of θ_{et}

Figure D.56: θ_{et} for vl_tbW_Re

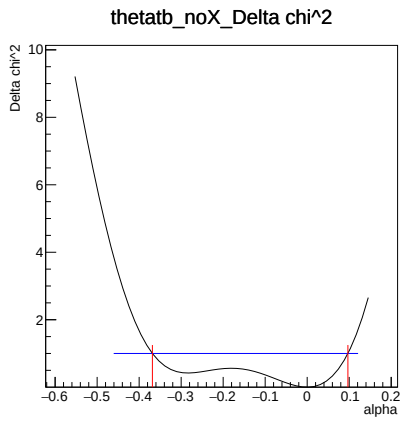

(a) χ^2 of θ_{tb}

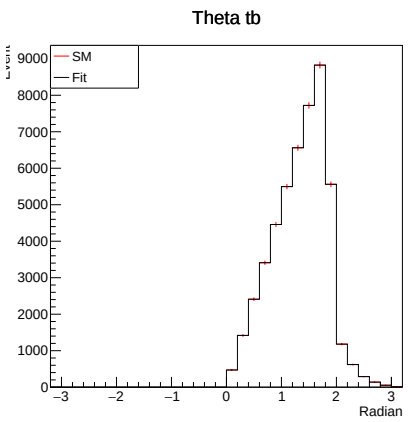

(b) fit of θ_{tb}

Figure D.57: θ_{tb} for vl_tbW_Re

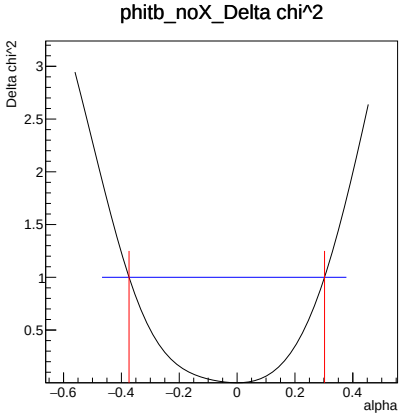

(a) χ^2 of ϕ_{tb}

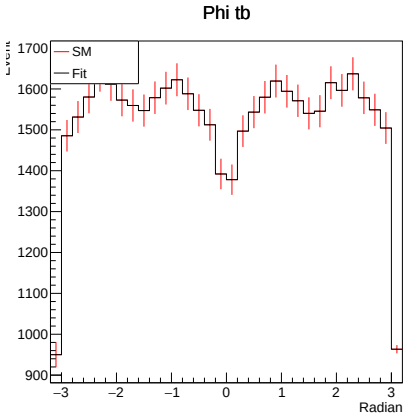

(b) fit of ϕ_{tb}

Figure D.58: ϕ_{tb} for vl_tbW_Re

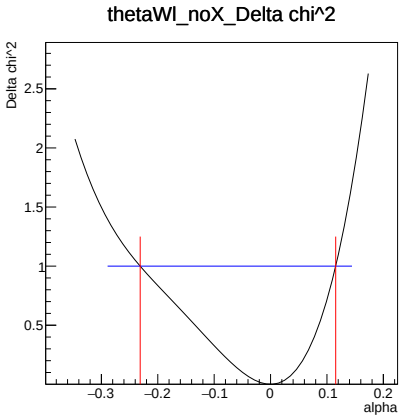

(a) χ^2 of θ_{Wl}

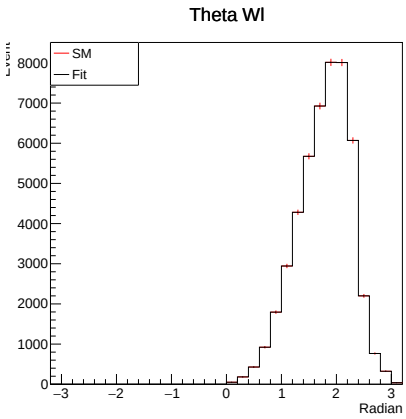

(b) fit of θ_{Wl}

Figure D.59: θ_{Wl} for vl_tbW_Re

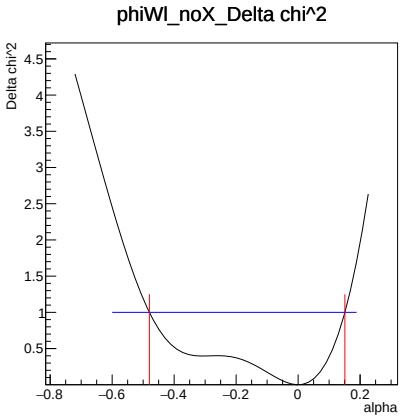

(a) χ^2 of ϕ_{Wl}

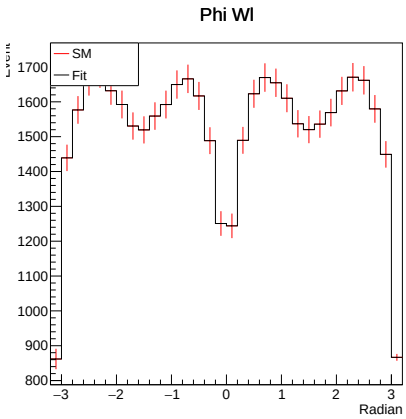

(b) fit of ϕ_{Wl}

Figure D.60: ϕ_{Wl} for vl_tbW_Re

vr_tbW_Re σ included

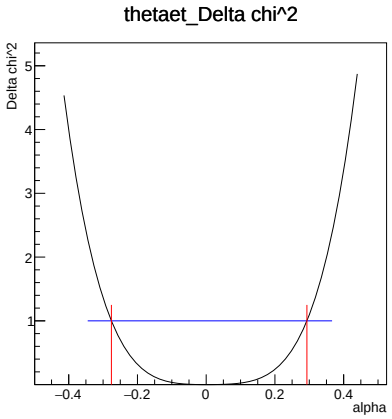

(a) χ^2 of θ_{et}

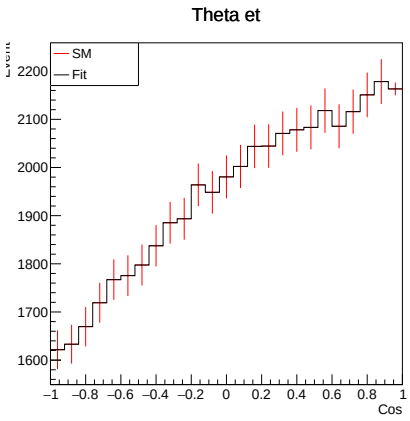

(b) fit of θ_{et}

Figure D.61: θ_{et} for vr_tbW_Re

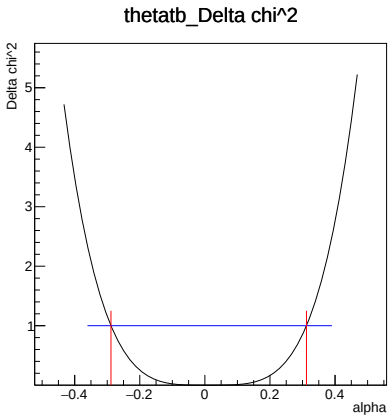

(a) χ^2 of θ_{tb}

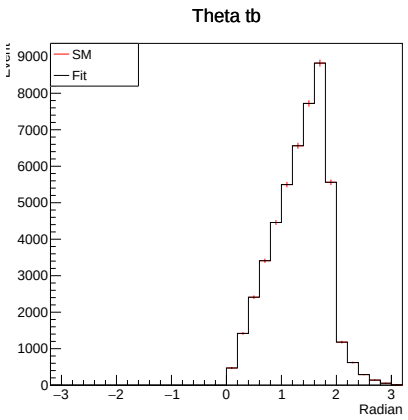

(b) fit of θ_{tb}

Figure D.62: θ_{tb} for vr_tbW_Re

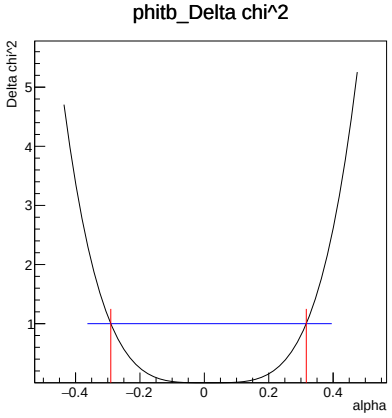

(a) χ^2 of ϕ_{tb}

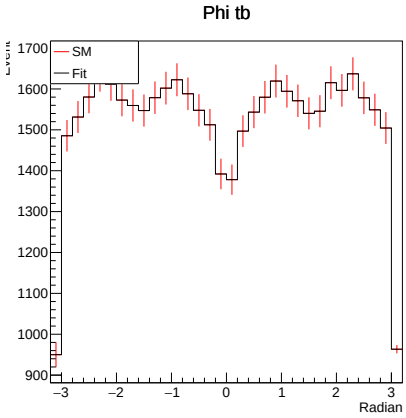

(b) fit of ϕ_{tb}

Figure D.63: ϕ_{tb} for vr_tbW_Re

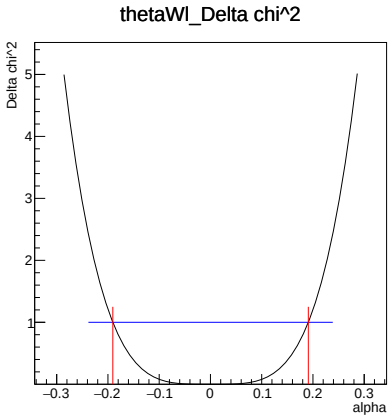

(a) χ^2 of θ_{Wl}

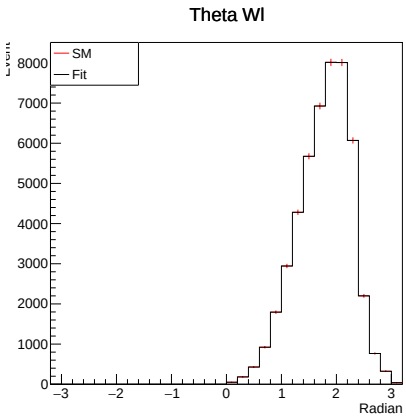

(b) fit of θ_{Wl}

Figure D.64: θ_{Wl} for vr_tbW_Re

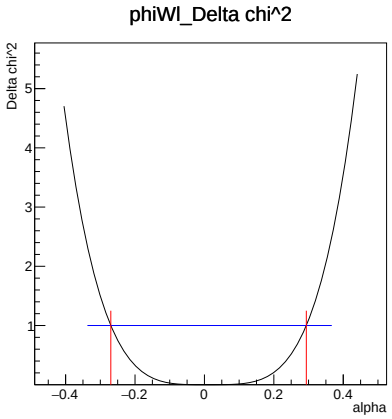

(a) χ^2 of ϕ_{Wl}

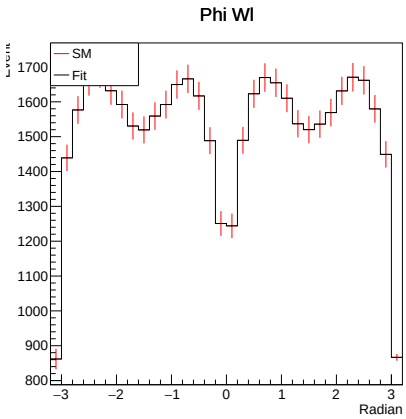

(b) fit of ϕ_{Wl}

Figure D.65: ϕ_{Wl} for vr_tbW_Re

vr_tbW_Re σ excluded

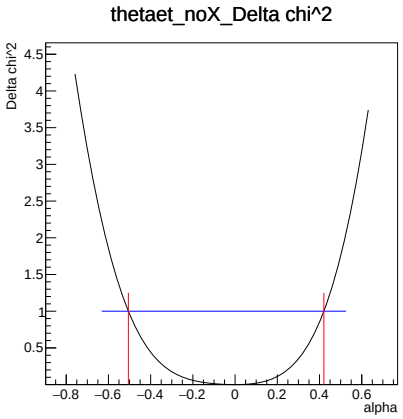

(a) χ^2 of θ_{et}

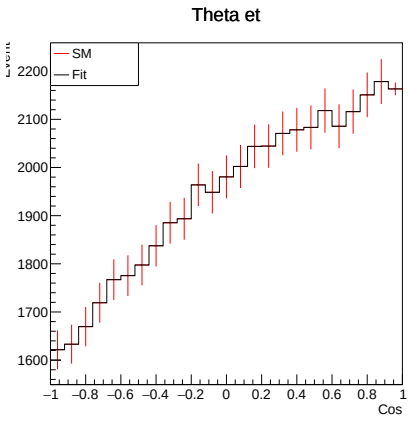

(b) fit of θ_{et}

Figure D.66: θ_{et} for vr_tbW_Re

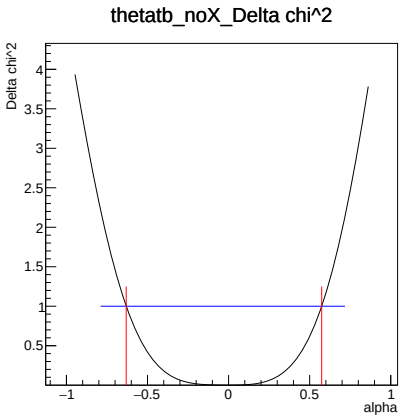

(a) χ^2 of θ_{tb}

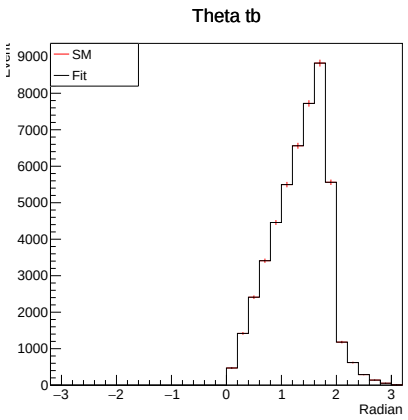

(b) fit of θ_{tb}

Figure D.67: θ_{tb} for vr_tbW_Re

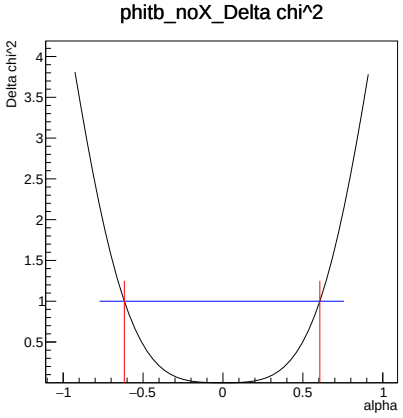

(a) χ^2 of ϕ_{tb}

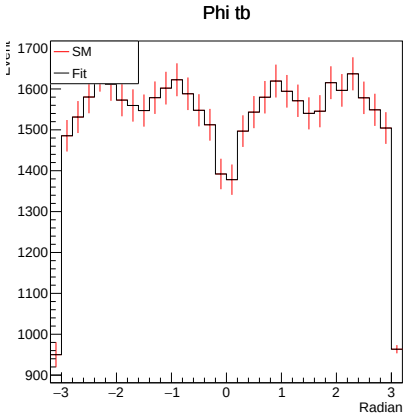

(b) fit of ϕ_{tb}

Figure D.68: ϕ_{tb} for vr_tbW_Re

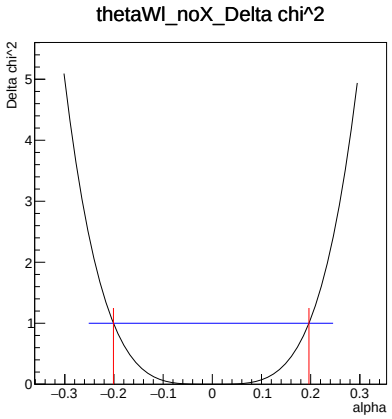

(a) χ^2 of θ_{Wl}

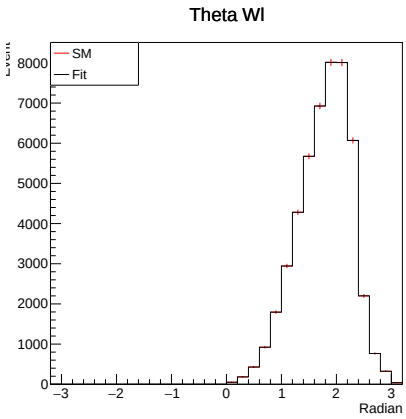

(b) fit of θ_{Wl}

Figure D.69: θ_{Wl} for vr_tbW_Re

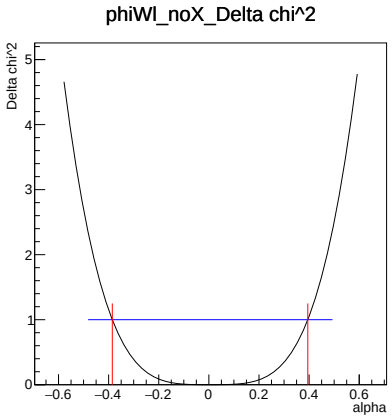

(a) χ^2 of ϕ_{Wl}

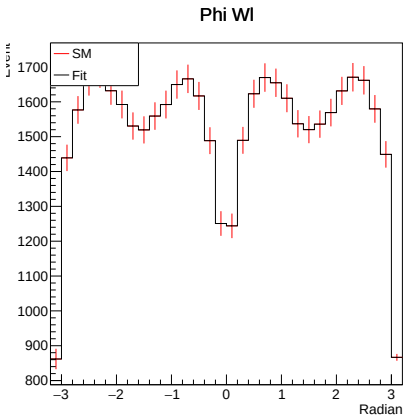

(b) fit of ϕ_{Wl}

Figure D.70: ϕ_{Wl} for vr_tbW_Re

D.2 Single-Parameter 2 Dimensional Angular Distribution

tattA-2D σ included

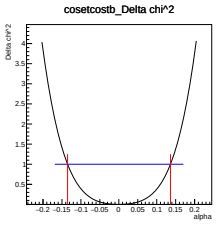

(a) $\cos\theta_{et} - \cos\theta_{tb}$

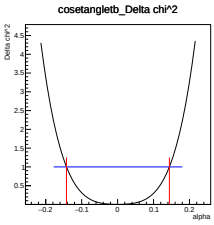

(b) $\cos\theta_{et} - \theta_{tb}$

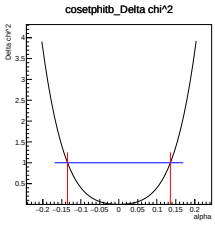

(c) $\cos\theta_{et} - \phi_{tb}$

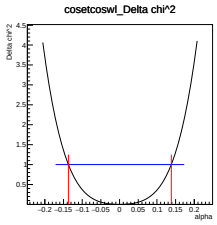

(d) $\cos\theta_{et} - \cos\theta_{Wl}$

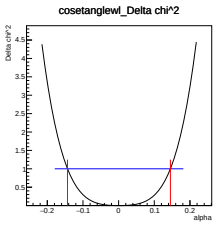

(e) $\cos\theta_{et} - \theta_{Wl}$

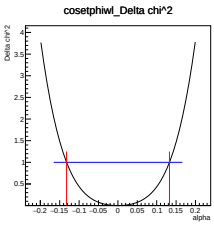

(f) $\cos\theta_{et} - \phi_{Wl}$

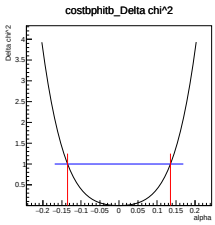

(g) $\cos\theta_{tb} - \phi_{tb}$

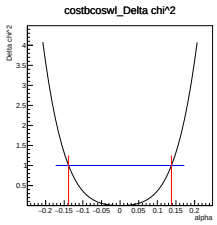

(h) $\cos\theta_{tb} - \cos\theta_{Wl}$

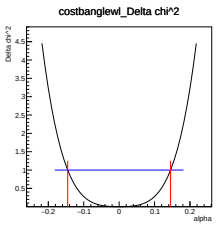

(i) $\cos\theta_{tb} - \theta_{Wl}$

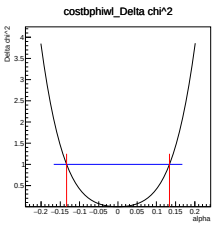

(j) $\cos\theta_{tb} - \phi_{Wl}$

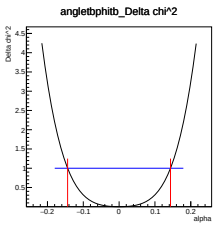

(k) $\theta_{tb} - \phi_{tb}$

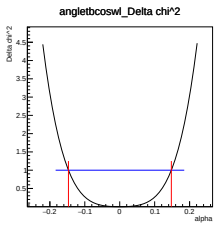

(l) $\theta_{tb} - \cos\theta_{Wl}$

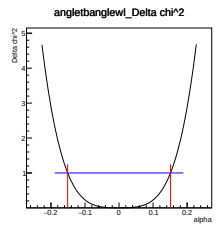

(m) $\theta_{tb} - \theta_{Wl}$

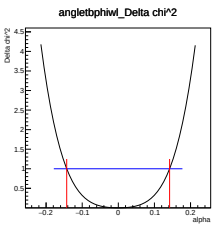

(n) $\theta_{tb} - \phi_{Wl}$

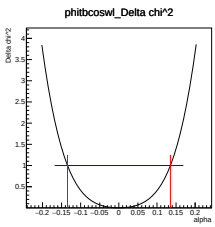

(o) $\phi_{tb} - \cos\theta_{Wl}$

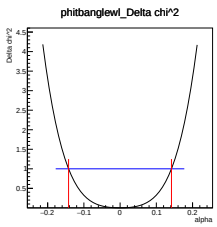

(p) $\phi_{tb} - \theta_{Wl}$

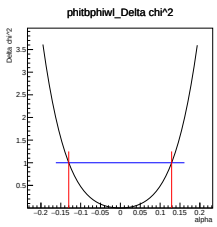

(q) $\phi_{tb} - \phi_{Wl}$

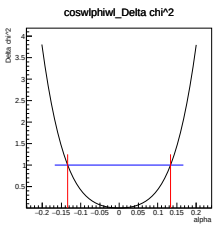

(r) $\cos\theta_{Wl} - \phi_{Wl}$

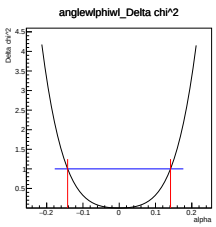

(s) $\theta_{Wl} - \phi_{Wl}$

Figure D.71: χ^2 of tattA 2 Dimensional Angular Distribution

tattA-2D σ excluded

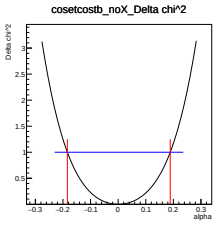

(a) $\cos\theta_{et} - \cos\theta_{tb}$

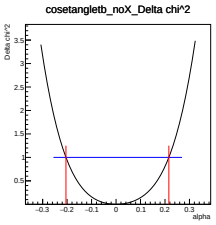

(b) $\cos\theta_{et} - \theta_{tb}$

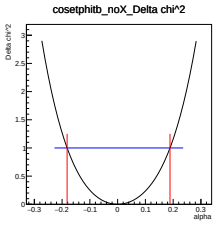

(c) $\cos\theta_{et} - \phi_{tb}$

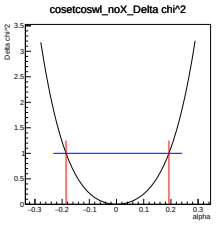

(d) $\cos\theta_{et} - \cos\theta_{Wl}$

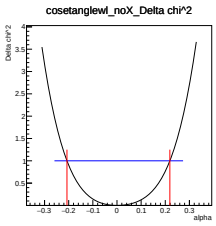

(e) $\cos\theta_{et} - \theta_{Wl}$

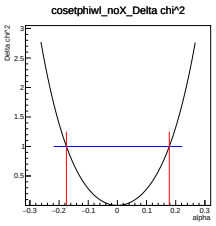

(f) $\cos\theta_{et} - \phi_{Wl}$

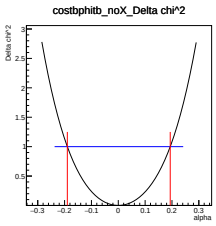

(g) $\cos\theta_{tb} - \phi_{tb}$

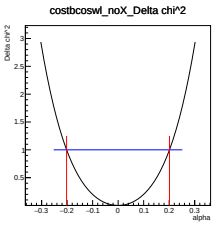

(h) $\cos\theta_{tb} - \cos\theta_{Wl}$

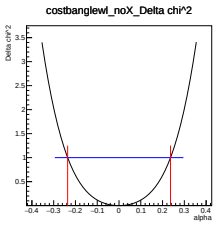

(i) $\cos\theta_{tb} - \theta_{Wl}$

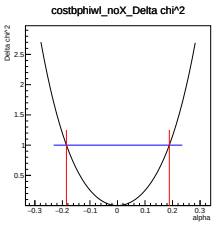

(j) $\cos\theta_{tb} - \phi_{Wl}$

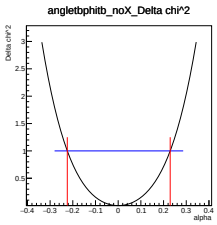

(k) $\theta_{tb} - \phi_{tb}$

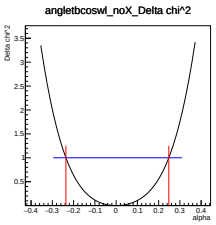

(l) $\theta_{tb} - \cos\theta_{Wl}$

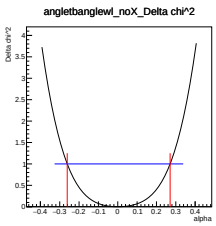

(m) $\theta_{tb} - \theta_{Wl}$

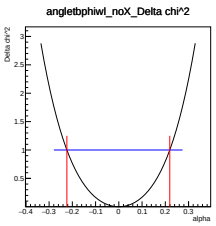

(n) $\theta_{tb} - \phi_{Wl}$

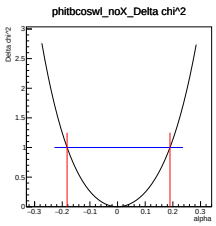

(o) $\phi_{tb} - \cos\theta_{Wl}$

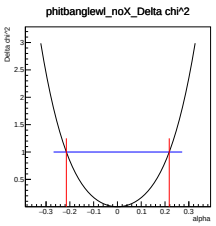

(p) $\phi_{tb} - \theta_{Wl}$

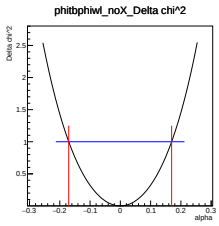

(q) $\phi_{tb} - \phi_{Wl}$

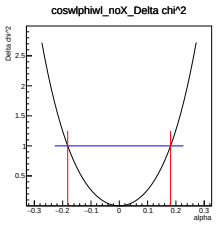

(r) $\cos\theta_{Wl} - \phi_{Wl}$

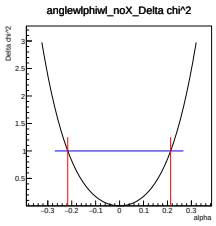

(s) $\theta_{Wl} - \phi_{Wl}$

Figure D.72: χ^2 of tattA 2 Dimensional Angular Distribution

tvttA-2D σ included

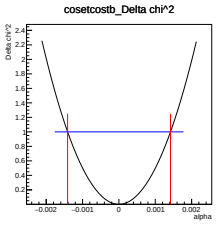

(a) $\cos\theta_{et} - \cos\theta_{tb}$

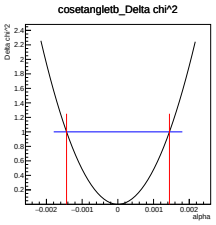

(b) $\cos\theta_{et} - \theta_{tb}$

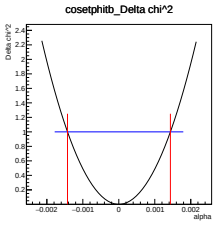

(c) $\cos\theta_{et} - \phi_{tb}$

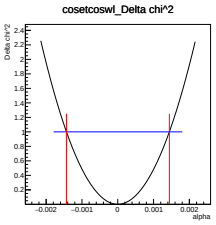

(d) $\cos\theta_{et} - \cos\theta_{Wl}$

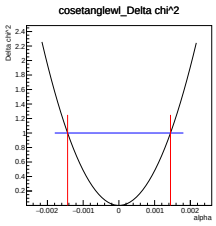

(e) $\cos\theta_{et} - \theta_{Wl}$

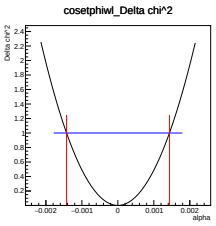

(f) $\cos\theta_{et} - \phi_{Wl}$

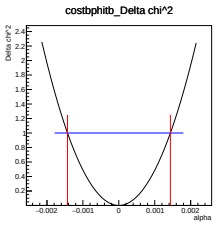

(g) $\cos\theta_{tb} - \phi_{tb}$

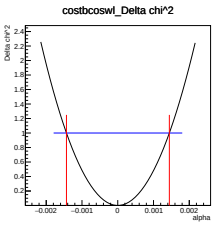

(h) $\cos\theta_{tb} - \cos\theta_{Wl}$

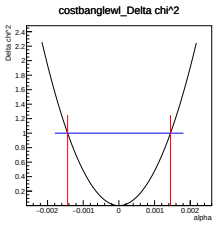

(i) $\cos\theta_{tb} - \theta_{Wl}$

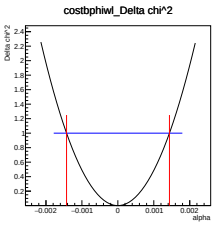

(j) $\cos\theta_{tb} - \phi_{Wl}$

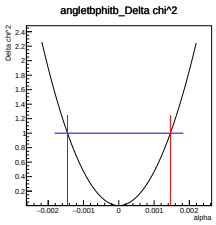

(k) $\theta_{tb} - \phi_{tb}$

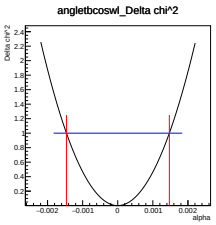

(l) $\theta_{tb} - \cos\theta_{Wl}$

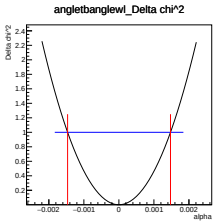

(m) $\theta_{tb} - \theta_{Wl}$

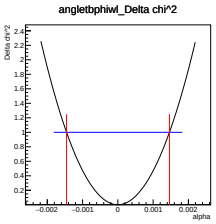

(n) $\theta_{tb} - \phi_{Wl}$

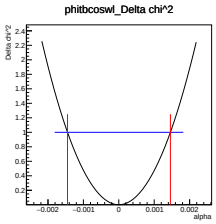

(o) $\phi_{tb} - \cos\theta_{Wl}$

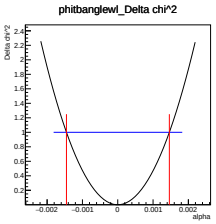

(p) $\phi_{tb} - \theta_{Wl}$

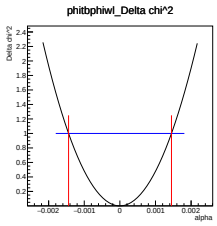

(q) $\phi_{tb} - \phi_{Wl}$

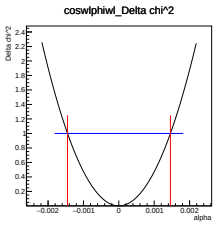

(r) $\cos\theta_{Wl} - \phi_{Wl}$

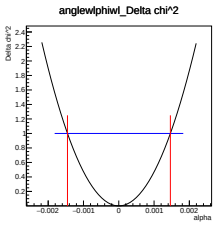

(s) $\theta_{Wl} - \phi_{Wl}$

Figure D.73: χ^2 of tvttA 2 Dimensional Angular Distribution

tvttA-2D σ excluded

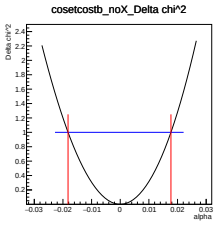

(a) $\cos\theta_{et} - \cos\theta_{tb}$

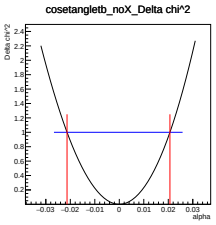

(b) $\cos\theta_{et} - \theta_{tb}$

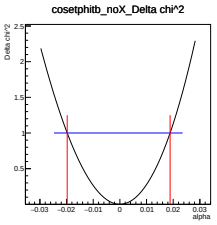

(c) $\cos\theta_{et} - \phi_{tb}$

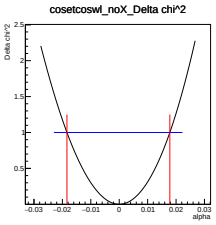

(d) $\cos\theta_{et} - \cos\theta_{Wl}$

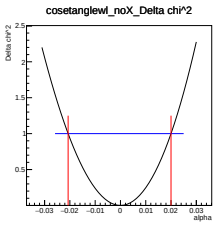

(e) $\cos\theta_{et} - \theta_{Wl}$

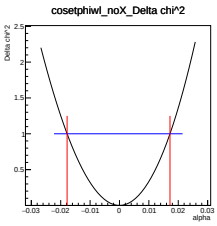

(f) $\cos\theta_{et} - \phi_{Wl}$

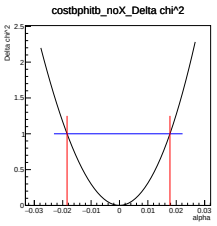

(g) $\cos\theta_{tb} - \phi_{tb}$

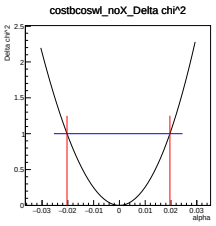

(h) $\cos\theta_{tb} - \cos\theta_{Wl}$

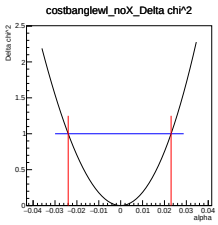

(i) $\cos\theta_{tb} - \theta_{Wl}$

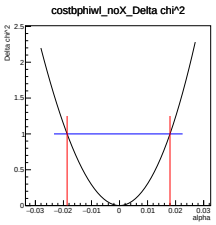

(j) $\cos\theta_{tb} - \phi_{Wl}$

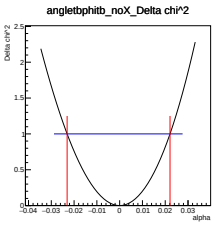

(k) $\theta_{tb} - \phi_{tb}$

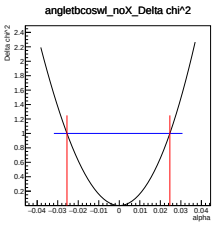

(l) $\theta_{tb} - \cos\theta_{Wl}$

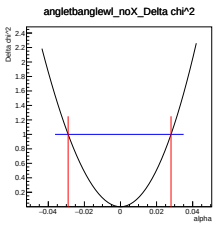

(m) $\theta_{tb} - \theta_{Wl}$

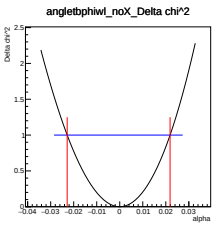

(n) $\theta_{tb} - \phi_{Wl}$

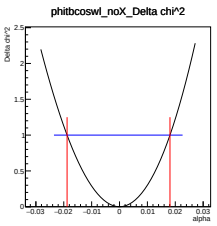

(o) $\phi_{tb} - \cos\theta_{Wl}$

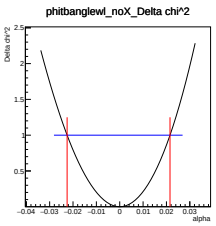

(p) $\phi_{tb} - \theta_{Wl}$

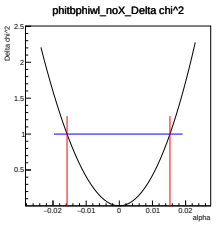

(q) $\phi_{tb} - \phi_{Wl}$

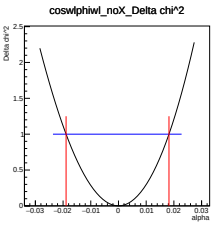

(r) $\cos\theta_{Wl} - \phi_{Wl}$

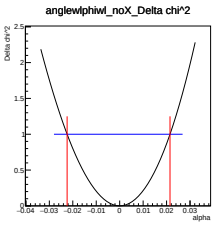

(s) $\theta_{Wl} - \phi_{Wl}$

Figure D.74: χ^2 of tvttA 2 Dimensional Angular Distribution

vrttZ-2D σ included

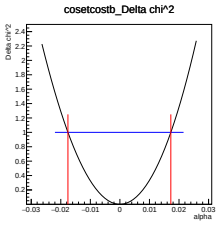

(a) $\cos\theta_{et} - \cos\theta_{tb}$

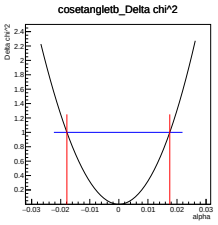

(b) $\cos\theta_{et} - \theta_{tb}$

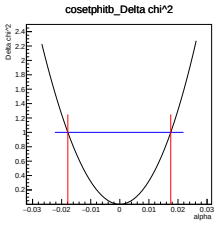

(c) $\cos\theta_{et} - \phi_{tb}$

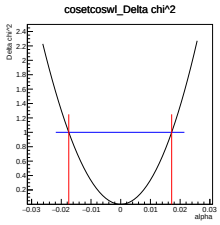

(d) $\cos\theta_{et} - \cos\theta_{Wl}$

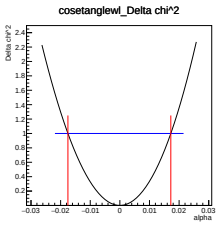

(e) $\cos\theta_{et} - \theta_{Wl}$

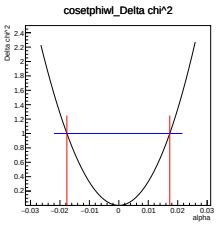

(f) $\cos\theta_{et} - \phi_{Wl}$

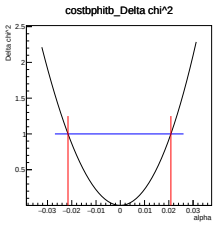

(g) $\cos\theta_{tb} - \phi_{tb}$

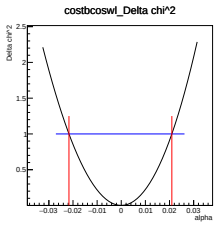

(h) $\cos\theta_{tb} - \cos\theta_{Wl}$

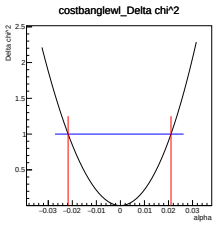

(i) $\cos\theta_{tb} - \theta_{Wl}$

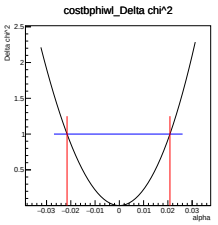

(j) $\cos\theta_{tb} - \phi_{Wl}$

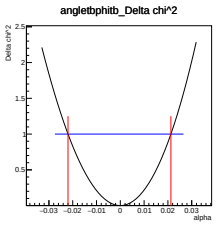

(k) $\theta_{tb} - \phi_{tb}$

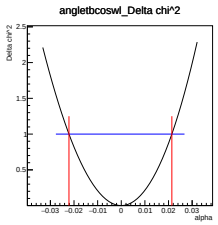

(l) $\theta_{tb} - \cos\theta_{Wl}$

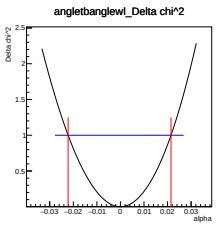

(m) $\theta_{tb} - \theta_{Wl}$

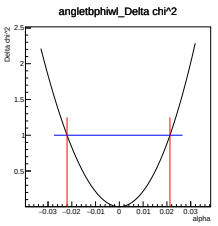

(n) $\theta_{tb} - \phi_{Wl}$

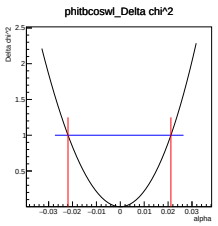

(o) $\phi_{tb} - \cos\theta_{Wl}$

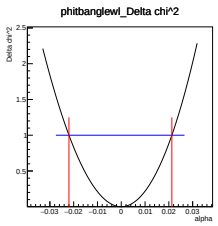

(p) $\phi_{tb} - \theta_{Wl}$

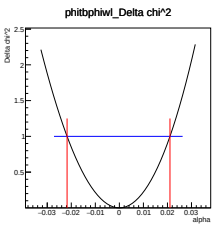

(q) $\phi_{tb} - \phi_{Wl}$

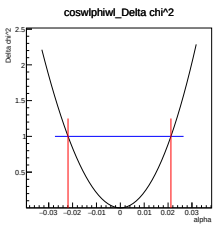

(r) $\cos\theta_{Wl} - \phi_{Wl}$

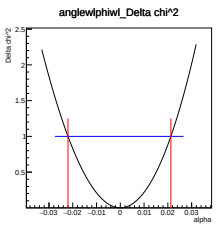

(s) $\theta_{Wl} - \phi_{Wl}$

Figure D.75: χ^2 of vrttZ 2 Dimensional Angular Distribution

vrttZ-2D σ excluded

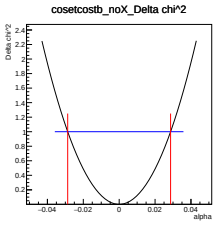

(a) $\cos\theta_{et} - \cos\theta_{tb}$

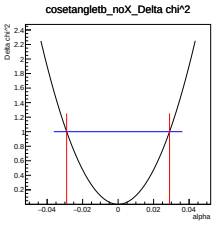

(b) $\cos\theta_{et} - \theta_{tb}$

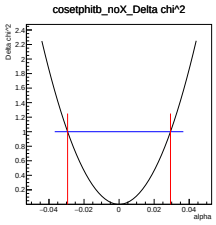

(c) $\cos\theta_{et} - \phi_{tb}$

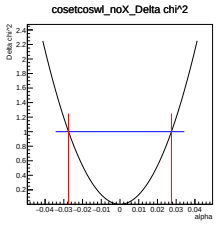

(d) $\cos\theta_{et} - \cos\theta_{Wl}$

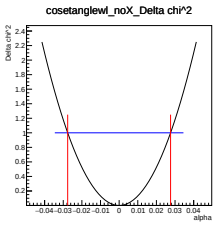

(e) $\cos\theta_{et} - \theta_{Wl}$

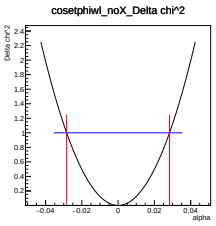

(f) $\cos\theta_{et} - \phi_{Wl}$

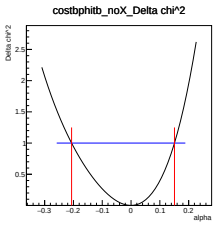

(g) $\cos\theta_{tb} - \phi_{tb}$

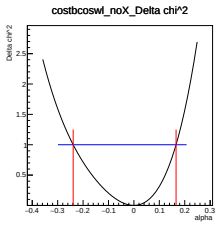

(h) $\cos\theta_{tb} - \cos\theta_{Wl}$

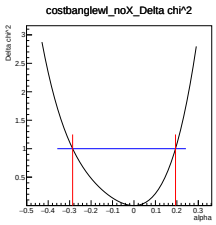

(i) $\cos\theta_{tb} - \theta_{Wl}$

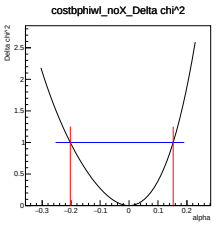

(j) $\cos\theta_{tb} - \phi_{Wl}$

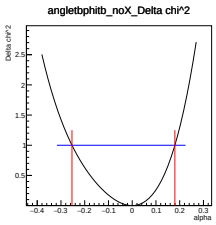

(k) $\theta_{tb} - \phi_{tb}$

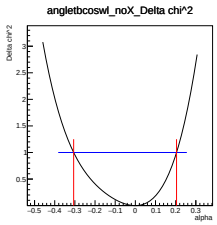

(l) $\theta_{tb} - \cos\theta_{Wl}$

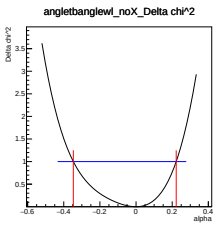

(m) $\theta_{tb} - \theta_{Wl}$

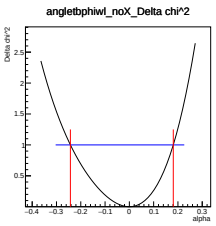

(n) $\theta_{tb} - \phi_{Wl}$

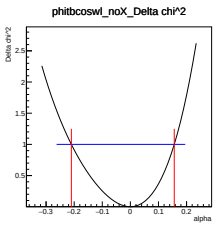

(o) $\phi_{tb} - \cos\theta_{Wl}$

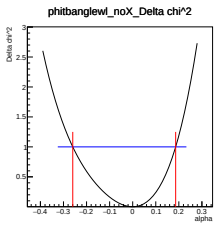

(p) $\phi_{tb} - \theta_{Wl}$

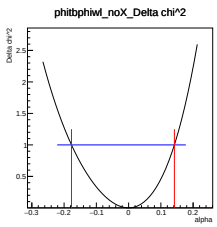

(q) $\phi_{tb} - \phi_{Wl}$

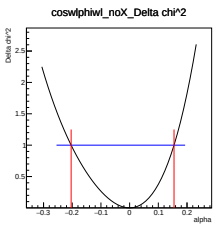

(r) $\cos\theta_{Wl} - \phi_{Wl}$

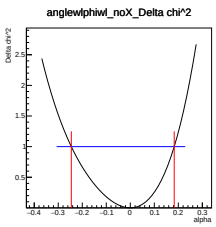

(s) $\theta_{Wl} - \phi_{Wl}$

Figure D.76: χ^2 of vrttZ 2 Dimensional Angular Distribution

tl_tbW_Re-2D σ included

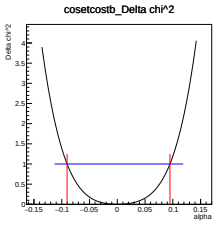

(a) $\cos\theta_{et} - \cos\theta_{tb}$

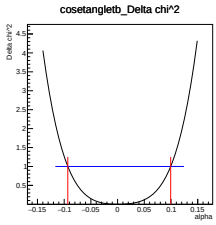

(b) $\cos\theta_{et} - \theta_{tb}$

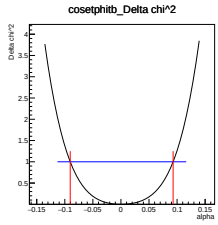

(c) $\cos\theta_{et} - \phi_{tb}$

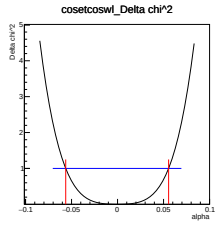

(d) $\cos\theta_{et} - \cos\theta_{Wl}$

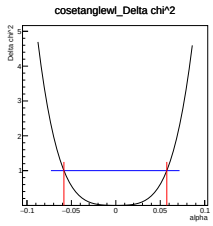

(e) $\cos\theta_{et} - \theta_{Wl}$

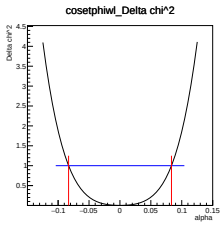

(f) $\cos\theta_{et} - \phi_{Wl}$

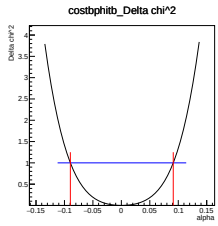

(g) $\cos\theta_{tb} - \phi_{tb}$

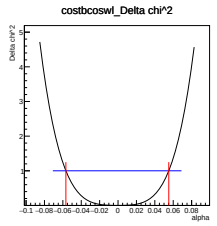

(h) $\cos\theta_{tb} - \cos\theta_{Wl}$

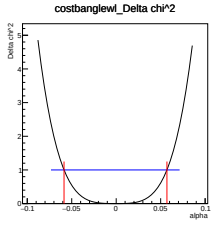

(i) $\cos\theta_{tb} - \theta_{Wl}$

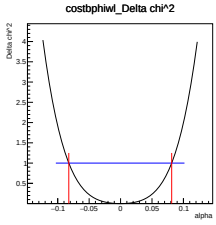

(j) $\cos\theta_{tb} - \phi_{Wl}$

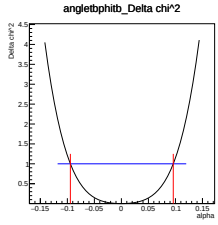

(k) $\theta_{tb} - \phi_{tb}$

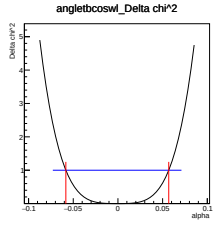

(l) $\theta_{tb} - \cos\theta_{Wl}$

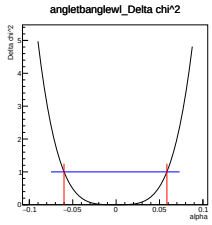

(m) $\theta_{tb} - \theta_{Wl}$

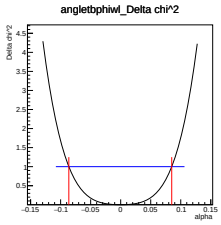

(n) $\theta_{tb} - \phi_{Wl}$

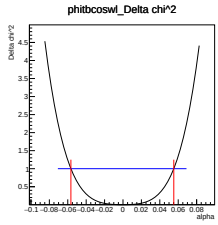

(o) $\phi_{tb} - \cos\theta_{Wl}$

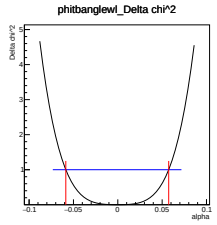

(p) $\phi_{tb} - \theta_{Wl}$

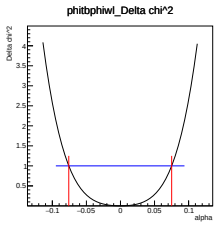

(q) $\phi_{tb} - \phi_{Wl}$

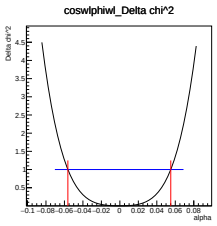

(r) $\cos\theta_{Wl} - \phi_{Wl}$

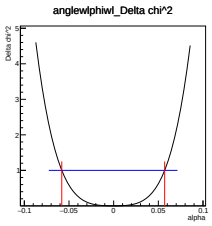

(s) $\theta_{Wl} - \phi_{Wl}$

Figure D.77: χ^2 of tl_tbW_Re 2 Dimensional Angular Distribution

tl_tbW_Re-2D σ excluded

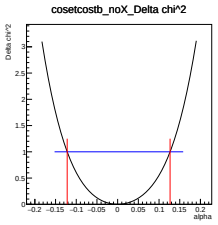

(a) $\cos\theta_{et} - \cos\theta_{tb}$

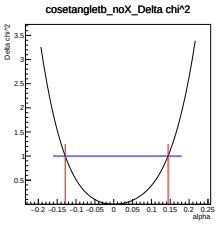

(b) $\cos\theta_{et} - \theta_{tb}$

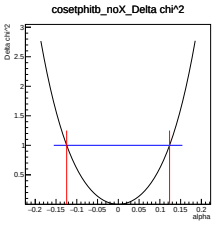

(c) $\cos\theta_{et} - \phi_{tb}$

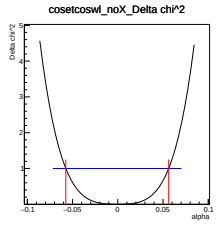

(d) $\cos\theta_{et} - \cos\theta_{Wl}$

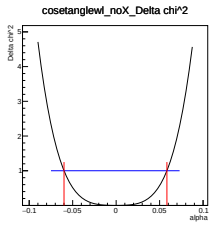

(e) $\cos\theta_{et} - \theta_{Wl}$

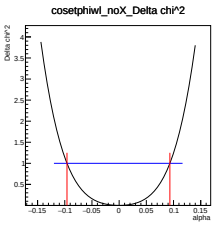

(f) $\cos\theta_{et} - \phi_{Wl}$

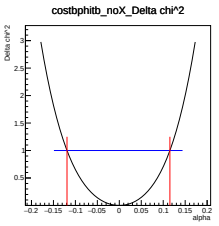

(g) $\cos\theta_{tb} - \phi_{tb}$

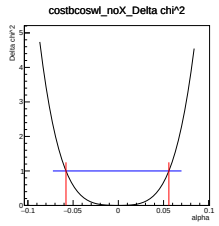

(h) $\cos\theta_{tb} - \cos\theta_{Wl}$

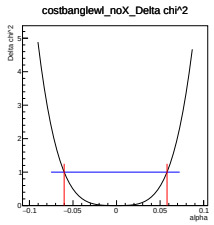

(i) $\cos\theta_{tb} - \theta_{Wl}$

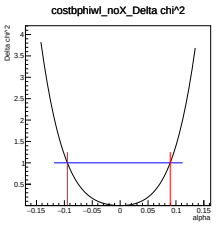

(j) $\cos\theta_{tb} - \phi_{Wl}$

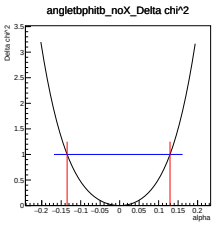

(k) $\theta_{tb} - \phi_{tb}$

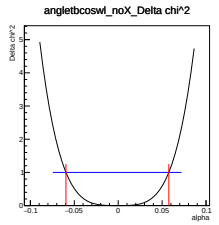

(l) $\theta_{tb} - \cos\theta_{Wl}$

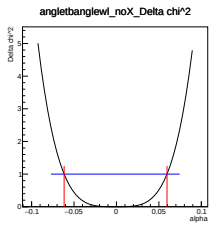

(m) $\theta_{tb} - \theta_{Wl}$

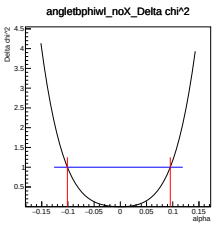

(n) $\theta_{tb} - \phi_{Wl}$

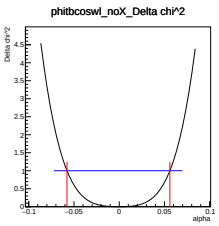

(o) $\phi_{tb} - \cos\theta_{Wl}$

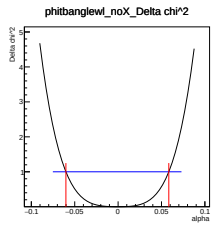

(p) $\phi_{tb} - \theta_{Wl}$

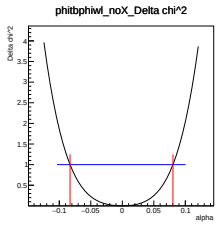

(q) $\phi_{tb} - \phi_{Wl}$

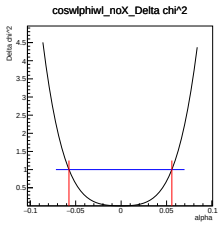

(r) $\cos\theta_{Wl} - \phi_{Wl}$

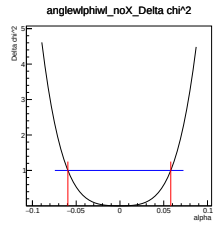

(s) $\theta_{Wl} - \phi_{Wl}$

Figure D.78: χ^2 of tl_tbW_Re 2 Dimensional Angular Distribution

tr_tbW_Re-2D σ included

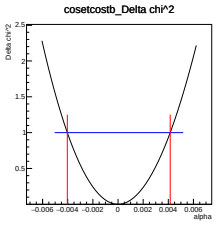

(a) $\cos\theta_{et} - \cos\theta_{tb}$

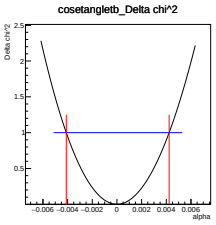

(b) $\cos\theta_{et} - \theta_{tb}$

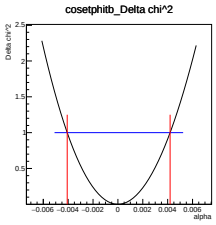

(c) $\cos\theta_{et} - \phi_{tb}$

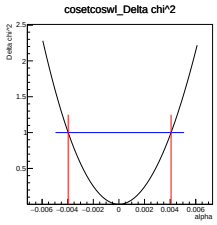

(d) $\cos\theta_{et} - \cos\theta_{Wl}$

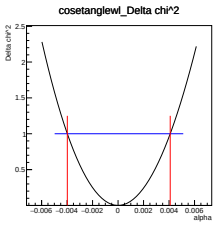

(e) $\cos\theta_{et} - \theta_{Wl}$

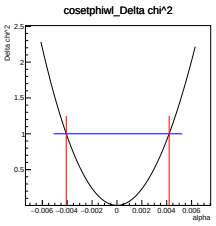

(f) $\cos\theta_{et} - \phi_{Wl}$

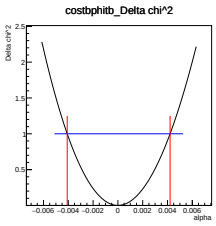

(g) $\cos\theta_{tb} - \phi_{tb}$

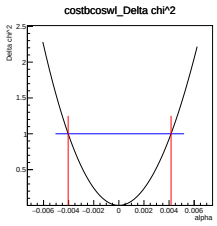

(h) $\cos\theta_{tb} - \cos\theta_{Wl}$

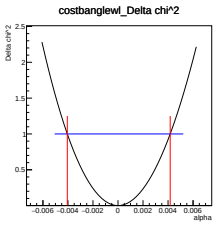

(i) $\cos\theta_{tb} - \theta_{Wl}$

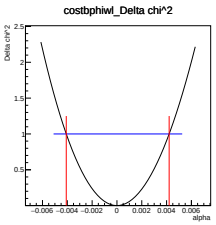

(j) $\cos\theta_{tb} - \phi_{Wl}$

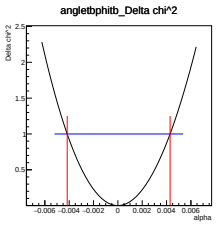

(k) $\theta_{tb} - \phi_{tb}$

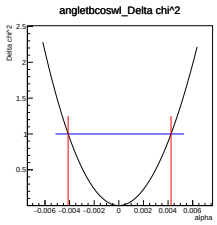

(l) $\theta_{tb} - \cos\theta_{Wl}$

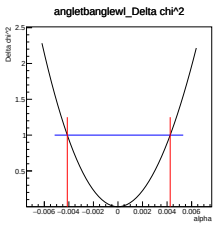

(m) $\theta_{tb} - \theta_{Wl}$

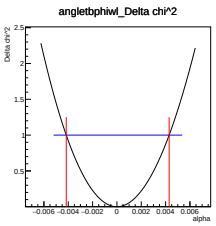

(n) $\theta_{tb} - \phi_{Wl}$

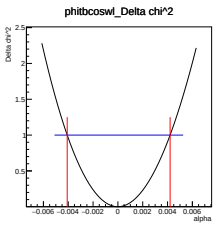

(o) $\phi_{tb} - \cos\theta_{Wl}$

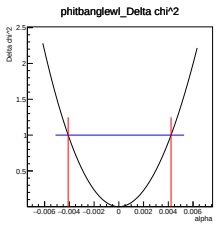

(p) $\phi_{tb} - \theta_{Wl}$

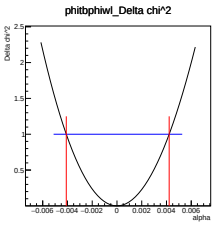

(q) $\phi_{tb} - \phi_{Wl}$

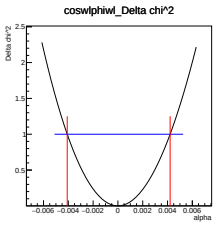

(r) $\cos\theta_{Wl} - \phi_{Wl}$

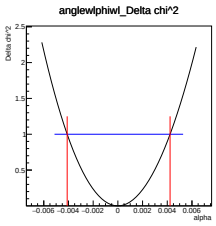

(s) $\theta_{Wl} - \phi_{Wl}$

Figure D.79: χ^2 of tr_tbW_Re 2 Dimensional Angular Distribution

tr_tbW_Re-2D σ excluded

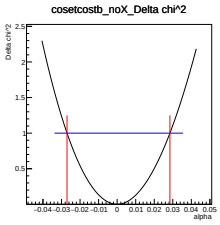

(a) $\cos\theta_{et} - \cos\theta_{tb}$

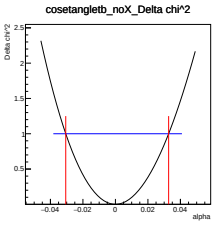

(b) $\cos\theta_{et} - \theta_{tb}$

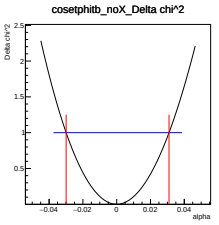

(c) $\cos\theta_{et} - \phi_{tb}$

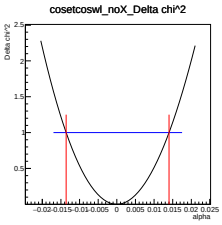

(d) $\cos\theta_{et} - \cos\theta_{Wl}$

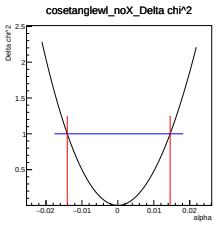

(e) $\cos\theta_{et} - \theta_{Wl}$

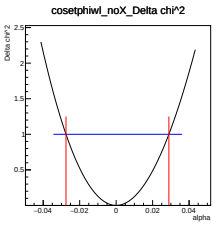

(f) $\cos\theta_{et} - \phi_{Wl}$

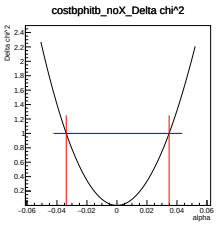

(g) $\cos\theta_{tb} - \phi_{tb}$

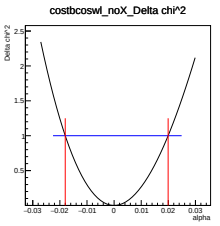

(h) $\cos\theta_{tb} - \cos\theta_{Wl}$

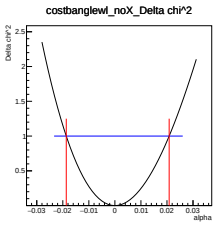

(i) $\cos\theta_{tb} - \theta_{Wl}$

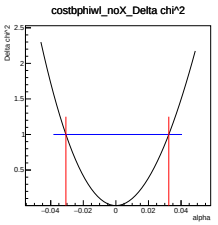

(j) $\cos\theta_{tb} - \phi_{Wl}$

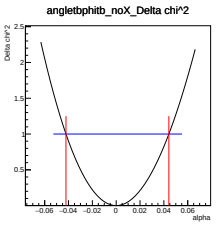

(k) $\theta_{tb} - \phi_{tb}$

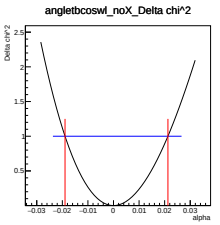

(l) $\theta_{tb} - \cos\theta_{Wl}$

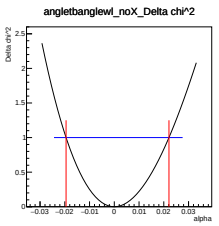

(m) $\theta_{tb} - \theta_{Wl}$

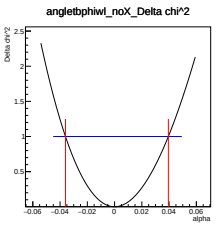

(n) $\theta_{tb} - \phi_{Wl}$

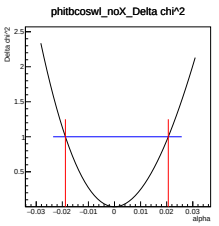

(o) $\phi_{tb} - \cos\theta_{Wl}$

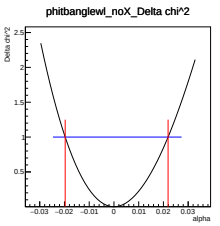

(p) $\phi_{tb} - \theta_{Wl}$

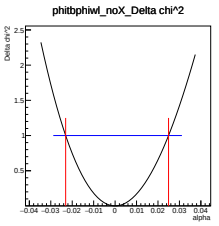

(q) $\phi_{tb} - \phi_{Wl}$

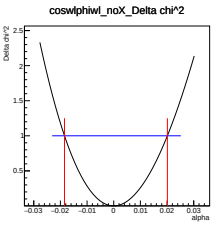

(r) $\cos\theta_{Wl} - \phi_{Wl}$

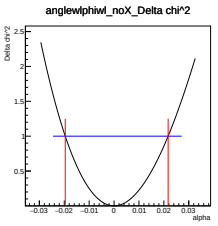

(s) $\theta_{Wl} - \phi_{Wl}$

Figure D.80: χ^2 of tr_tbW_Re 2 Dimensional Angular Distribution

vl_tbW_Re-2D σ included

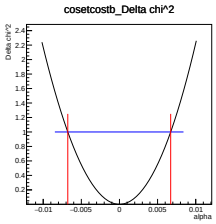

(a) $\cos\theta_{et} - \cos\theta_{tb}$

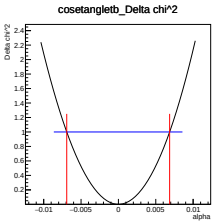

(b) $\cos\theta_{et} - \theta_{tb}$

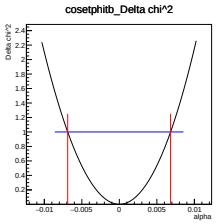

(c) $\cos\theta_{et} - \phi_{tb}$

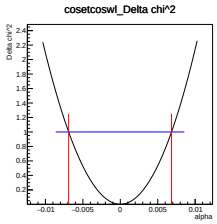

(d) $\cos\theta_{et} - \cos\theta_{Wl}$

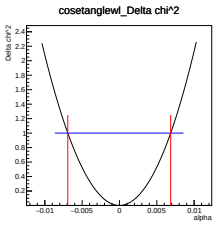

(e) $\cos\theta_{et} - \theta_{Wl}$

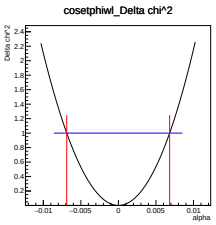

(f) $\cos\theta_{et} - \phi_{Wl}$

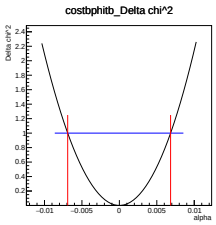

(g) $\cos\theta_{tb} - \phi_{tb}$

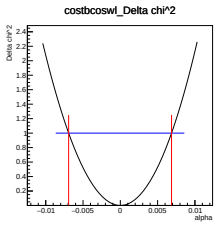

(h) $\cos\theta_{tb} - \cos\theta_{Wl}$

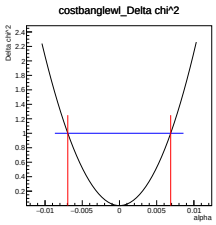

(i) $\cos\theta_{tb} - \theta_{Wl}$

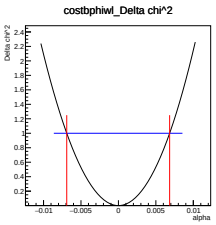

(j) $\cos\theta_{tb} - \phi_{Wl}$

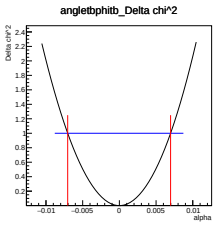

(k) $\theta_{tb} - \phi_{tb}$

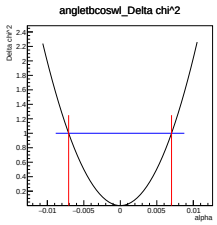

(l) $\theta_{tb} - \cos\theta_{Wl}$

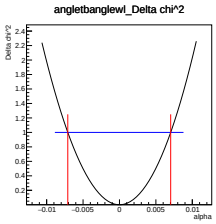

(m) $\theta_{tb} - \theta_{Wl}$

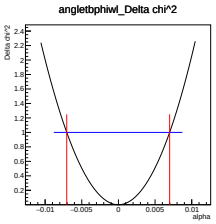

(n) $\theta_{tb} - \phi_{Wl}$

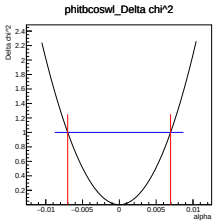

(o) $\phi_{tb} - \cos\theta_{Wl}$

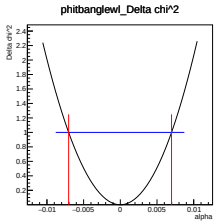

(p) $\phi_{tb} - \theta_{Wl}$

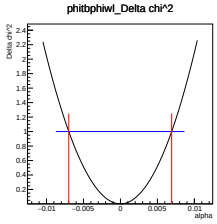

(q) $\phi_{tb} - \phi_{Wl}$

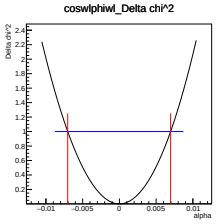

(r) $\cos\theta_{Wl} - \phi_{Wl}$

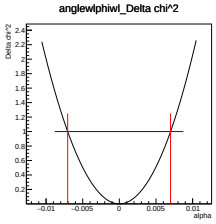

(s) $\theta_{Wl} - \phi_{Wl}$

Figure D.81: χ^2 of vl_tbW_Re 2 Dimensional Angular Distribution

vl_tbW_Re-2D σ excluded

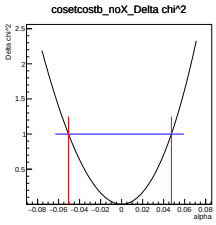

(a) $\cos\theta_{et} - \cos\theta_{tb}$

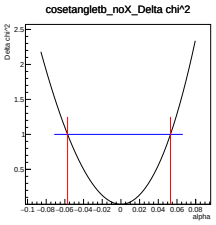

(b) $\cos\theta_{et} - \theta_{tb}$

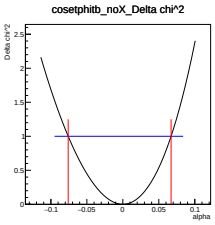

(c) $\cos\theta_{et} - \phi_{tb}$

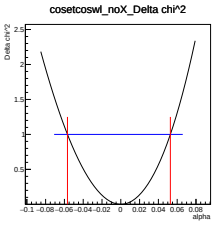

(d) $\cos\theta_{et} - \cos\theta_{Wl}$

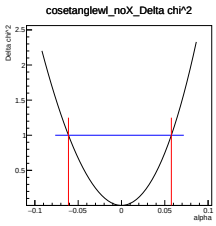

(e) $\cos\theta_{et} - \theta_{Wl}$

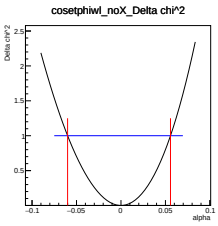

(f) $\cos\theta_{et} - \phi_{Wl}$

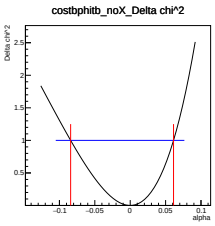

(g) $\cos\theta_{tb} - \phi_{tb}$

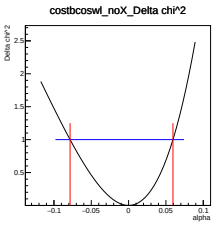

(h) $\cos\theta_{tb} - \cos\theta_{Wl}$

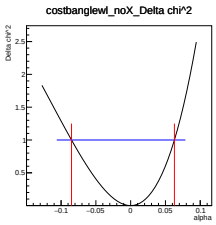

(i) $\cos\theta_{tb} - \theta_{Wl}$

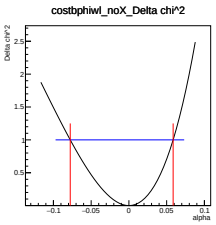

(j) $\cos\theta_{tb} - \phi_{Wl}$

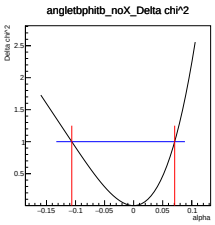

(k) $\theta_{tb} - \phi_{tb}$

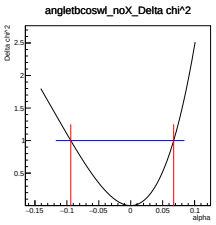

(l) $\theta_{tb} - \cos\theta_{Wl}$

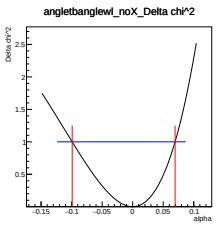

(m) $\theta_{tb} - \theta_{Wl}$

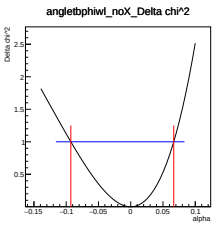

(n) $\theta_{tb} - \phi_{Wl}$

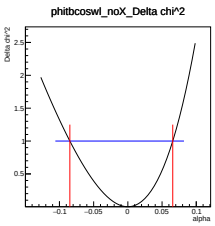

(o) $\phi_{tb} - \cos\theta_{Wl}$

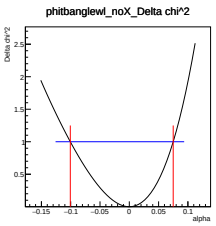

(p) $\phi_{tb} - \theta_{Wl}$

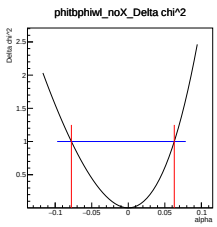

(q) $\phi_{tb} - \phi_{Wl}$

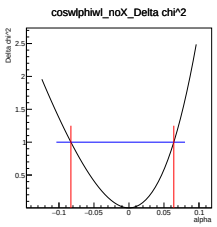

(r) $\cos\theta_{Wl} - \phi_{Wl}$

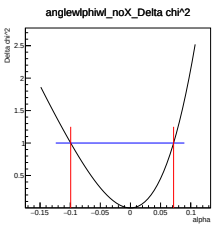

(s) $\theta_{Wl} - \phi_{Wl}$

Figure D.82: χ^2 of vl_tbW_Re 2 Dimensional Angular Distribution

vr_tbW_Re-2D σ included

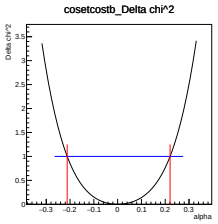

(a) $\cos\theta_{et} - \cos\theta_{tb}$

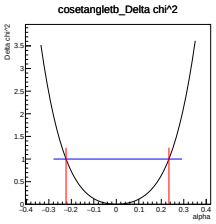

(b) $\cos\theta_{et} - \theta_{tb}$

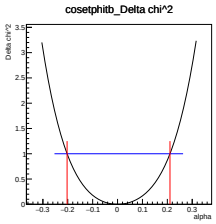

(c) $\cos\theta_{et} - \phi_{tb}$

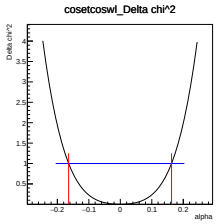

(d) $\cos\theta_{et} - \cos\theta_{Wl}$

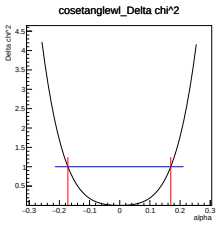

(e) $\cos\theta_{et} - \theta_{Wl}$

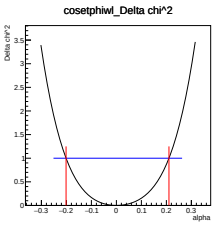

(f) $\cos\theta_{et} - \phi_{Wl}$

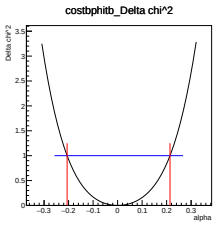

(g) $\cos\theta_{tb} - \phi_{tb}$

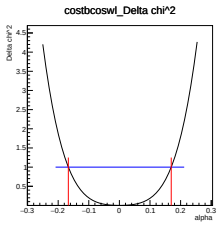

(h) $\cos\theta_{tb} - \cos\theta_{Wl}$

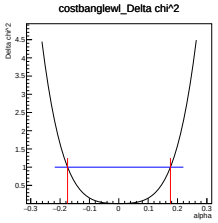

(i) $\cos\theta_{tb} - \theta_{Wl}$

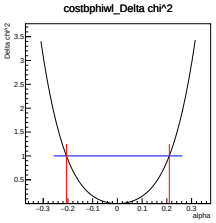

(j) $\cos\theta_{tb} - \phi_{Wl}$

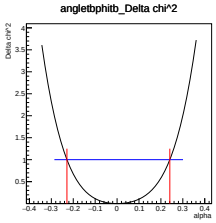

(k) $\theta_{tb} - \phi_{tb}$

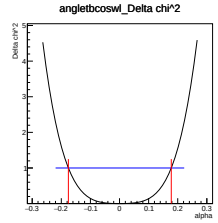

(l) $\theta_{tb} - \cos\theta_{Wl}$

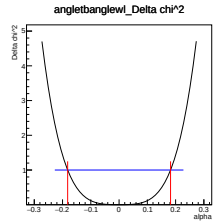

(m) $\theta_{tb} - \theta_{Wl}$

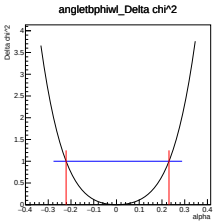

(n) $\theta_{tb} - \phi_{Wl}$

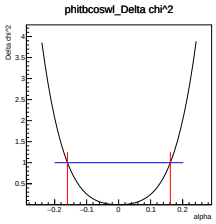

(o) $\phi_{tb} - \cos\theta_{Wl}$

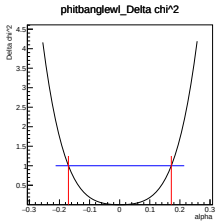

(p) $\phi_{tb} - \theta_{Wl}$

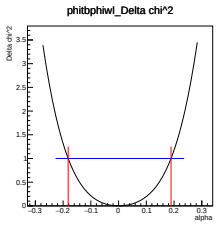

(q) $\phi_{tb} - \phi_{Wl}$

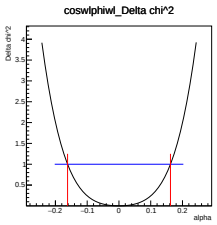

(r) $\cos\theta_{Wl} - \phi_{Wl}$

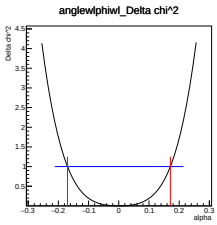

(s) $\theta_{Wl} - \phi_{Wl}$

Figure D.83: χ^2 of vr_tbW_Re 2 Dimensional Angular Distribution

vr_tbW_Re-2D σ excluded

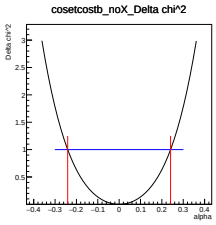

(a) $\cos\theta_{et} - \cos\theta_{tb}$

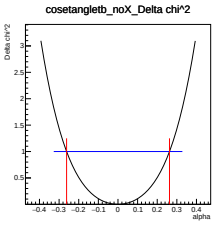

(b) $\cos\theta_{et} - \theta_{tb}$

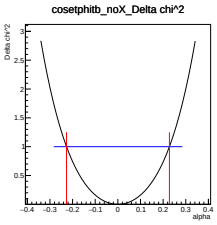

(c) $\cos\theta_{et} - \phi_{tb}$

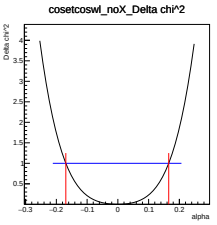

(d) $\cos\theta_{et} - \cos\theta_{Wl}$

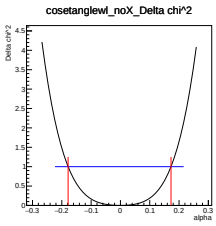

(e) $\cos\theta_{et} - \theta_{Wl}$

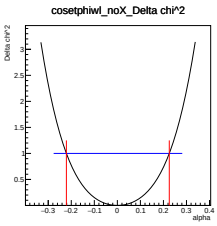

(f) $\cos\theta_{et} - \phi_{Wl}$

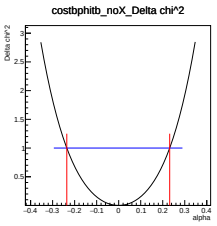

(g) $\cos\theta_{tb} - \phi_{tb}$

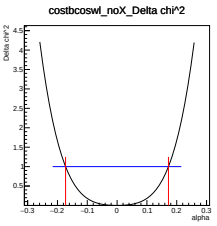

(h) $\cos\theta_{tb} - \cos\theta_{Wl}$

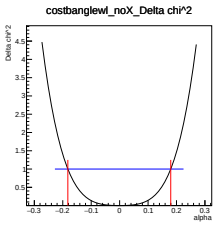

(i) $\cos\theta_{tb} - \theta_{Wl}$

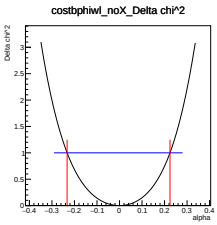

(j) $\cos\theta_{tb} - \phi_{Wl}$

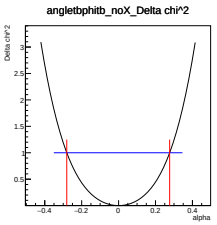

(k) $\theta_{tb} - \phi_{tb}$

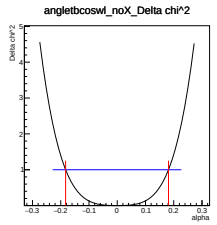

(l) $\theta_{tb} - \cos\theta_{Wl}$

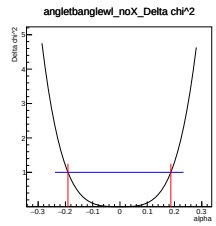

(m) $\theta_{tb} - \theta_{Wl}$

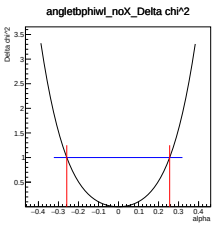

(n) $\theta_{tb} - \phi_{Wl}$

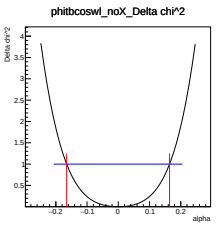

(o) $\phi_{tb} - \cos\theta_{Wl}$

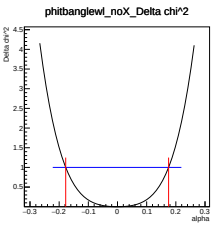

(p) $\phi_{tb} - \theta_{Wl}$

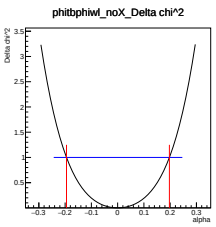

(q) $\phi_{tb} - \phi_{Wl}$

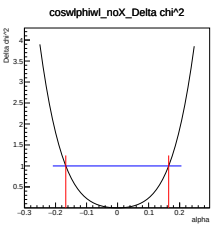

(r) $\cos\theta_{Wl} - \phi_{Wl}$

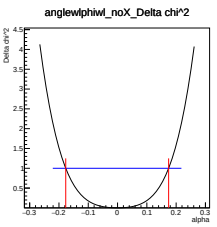

(s) $\theta_{Wl} - \phi_{Wl}$

Figure D.84: χ^2 of vr_tbW_Re 2 Dimensional Angular Distribution

D.3 Two-Parameter 1 Dimensional Angular Distribution

ta_ttA-vr_ttZ σ included

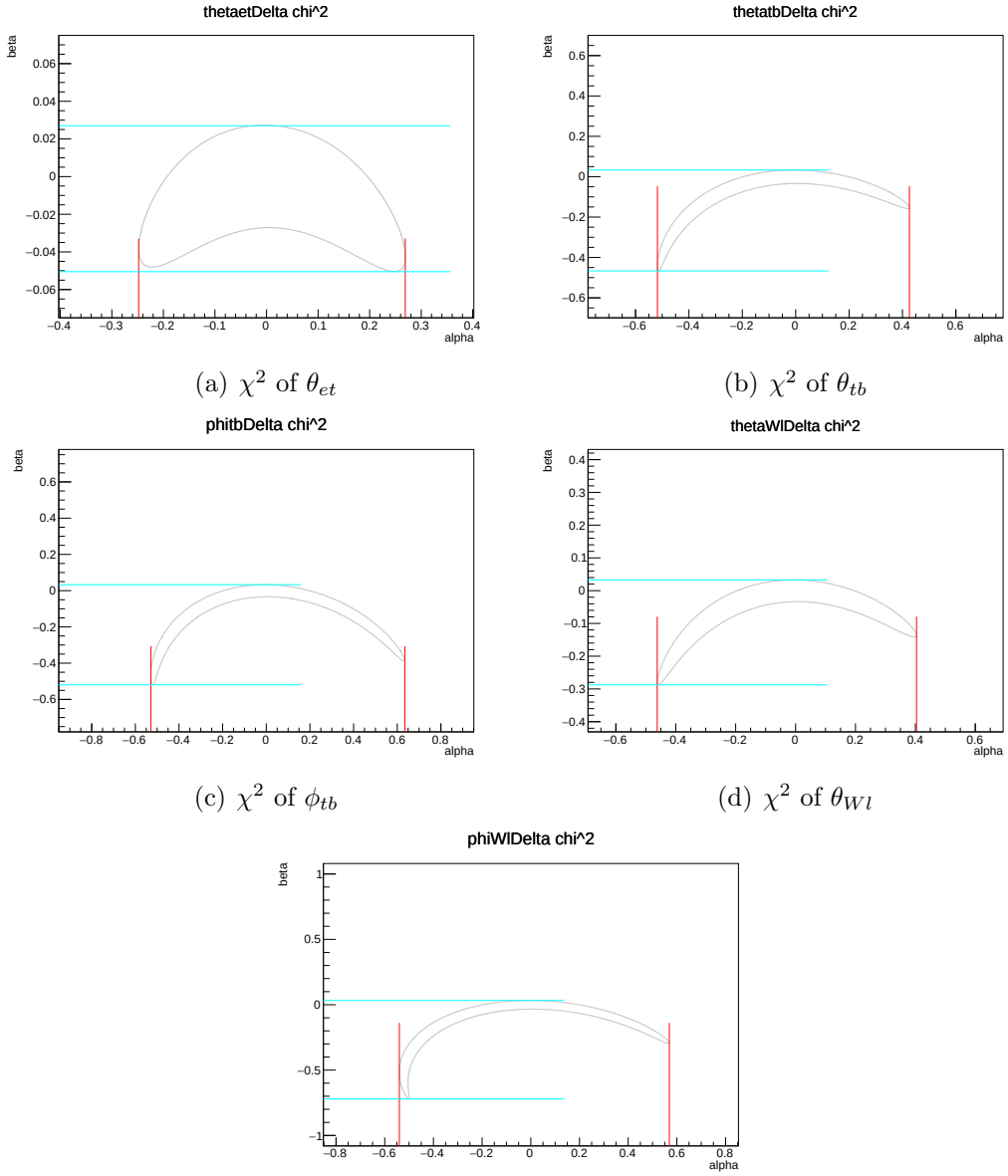

(a) χ^2 of θ_{et}

(b) χ^2 of θ_{tb}

(c) χ^2 of ϕ_{tb}

(d) χ^2 of θ_{Wl}

(e) χ^2 of ϕ_{Wl}

Figure D.85: χ^2 of ta_ttA-vr_ttZ 1 Dimensional Angular Distribution

ta_ttA-vr_ttZ σ excluded

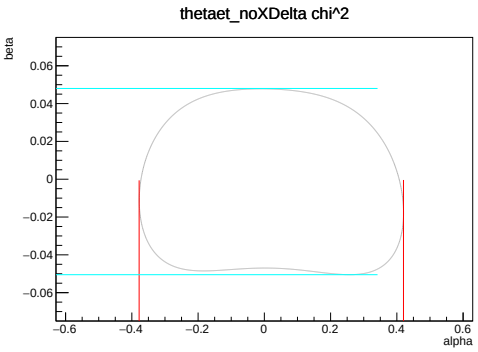

(a) χ^2 of θ_{et}

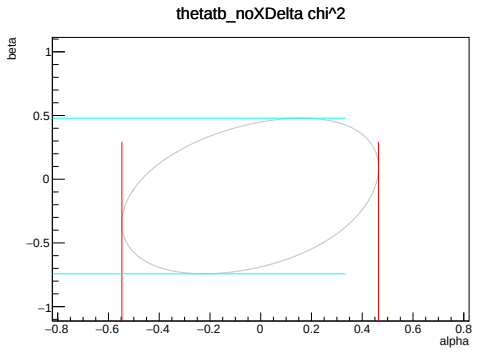

(b) χ^2 of θ_{tb}

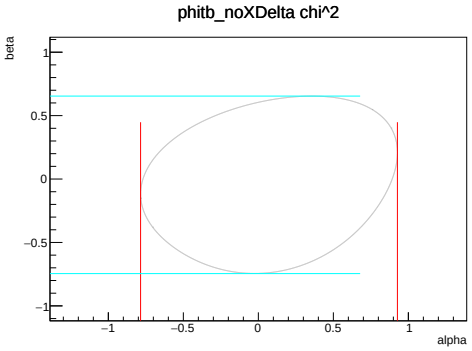

(c) χ^2 of ϕ_{tb}

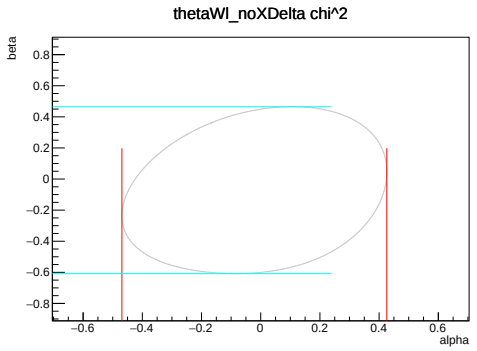

(d) χ^2 of θ_{Wl}

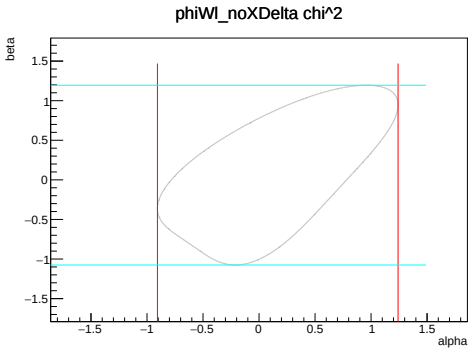

(e) χ^2 of ϕ_{Wl}

Figure D.86: χ^2 of ta_ttA-vr_ttZ 1 Dimensional Angular Distribution

tl_tbW_Re-ta_ttA σ included

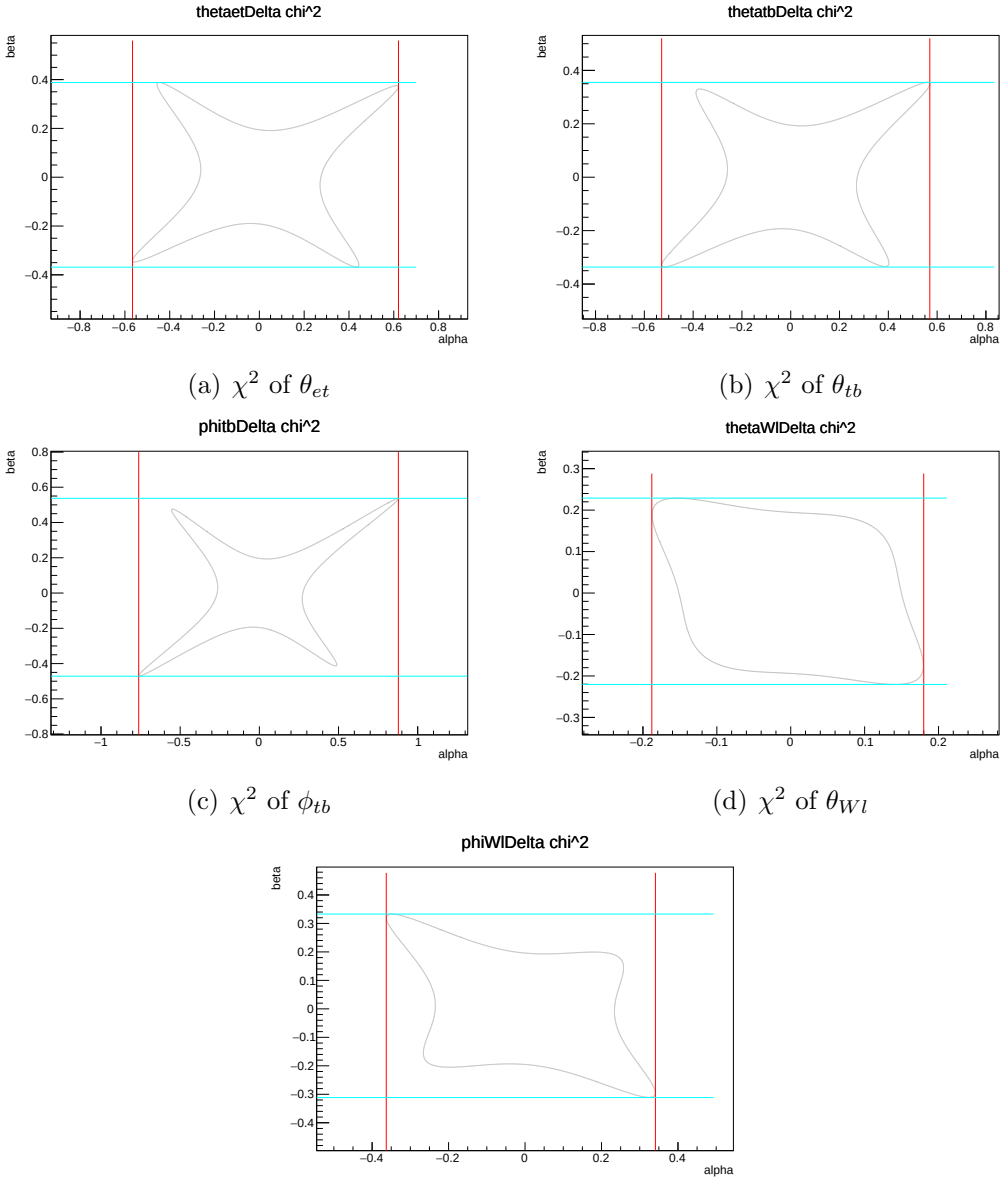

(a) χ^2 of θ_{et}

(b) χ^2 of θ_{tb}

(c) χ^2 of ϕ_{tb}

(d) χ^2 of θ_{Wl}

(e) χ^2 of ϕ_{Wl}

Figure D.87: χ^2 of tl_tbW_Re-ta_ttA 1 Dimensional Angular Distribution

tl_tbW_Re-ta_ttA σ excluded

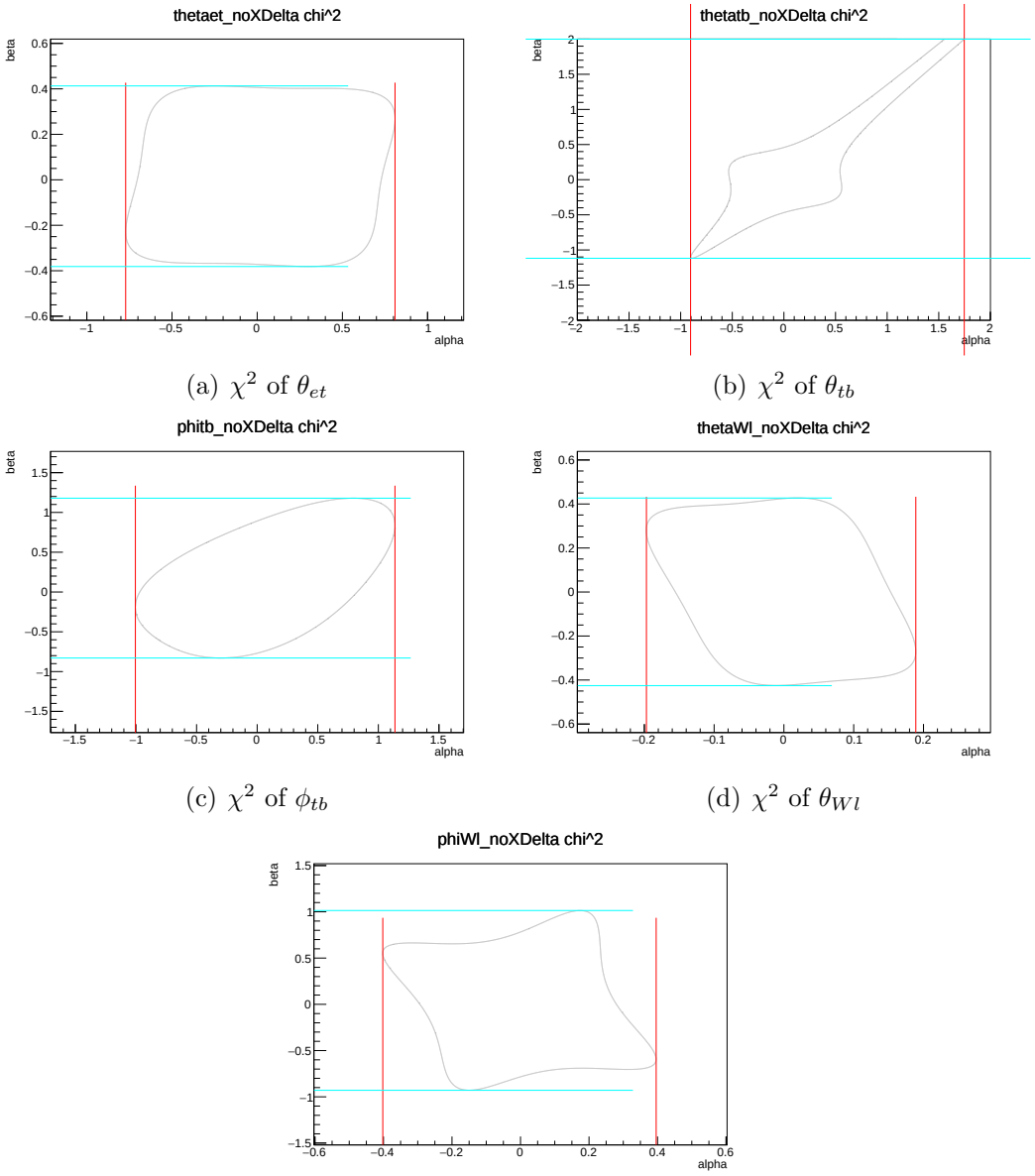

(a) χ^2 of θ_{et}

(b) χ^2 of θ_{tb}

(c) χ^2 of ϕ_{tb}

(d) χ^2 of θ_{Wl}

(e) χ^2 of ϕ_{Wl}

Figure D.88: χ^2 of tl_tbW_Re-ta_ttA 1 Dimensional Angular Distribution

tl_tbW_Re-tr_tbW_Re σ included

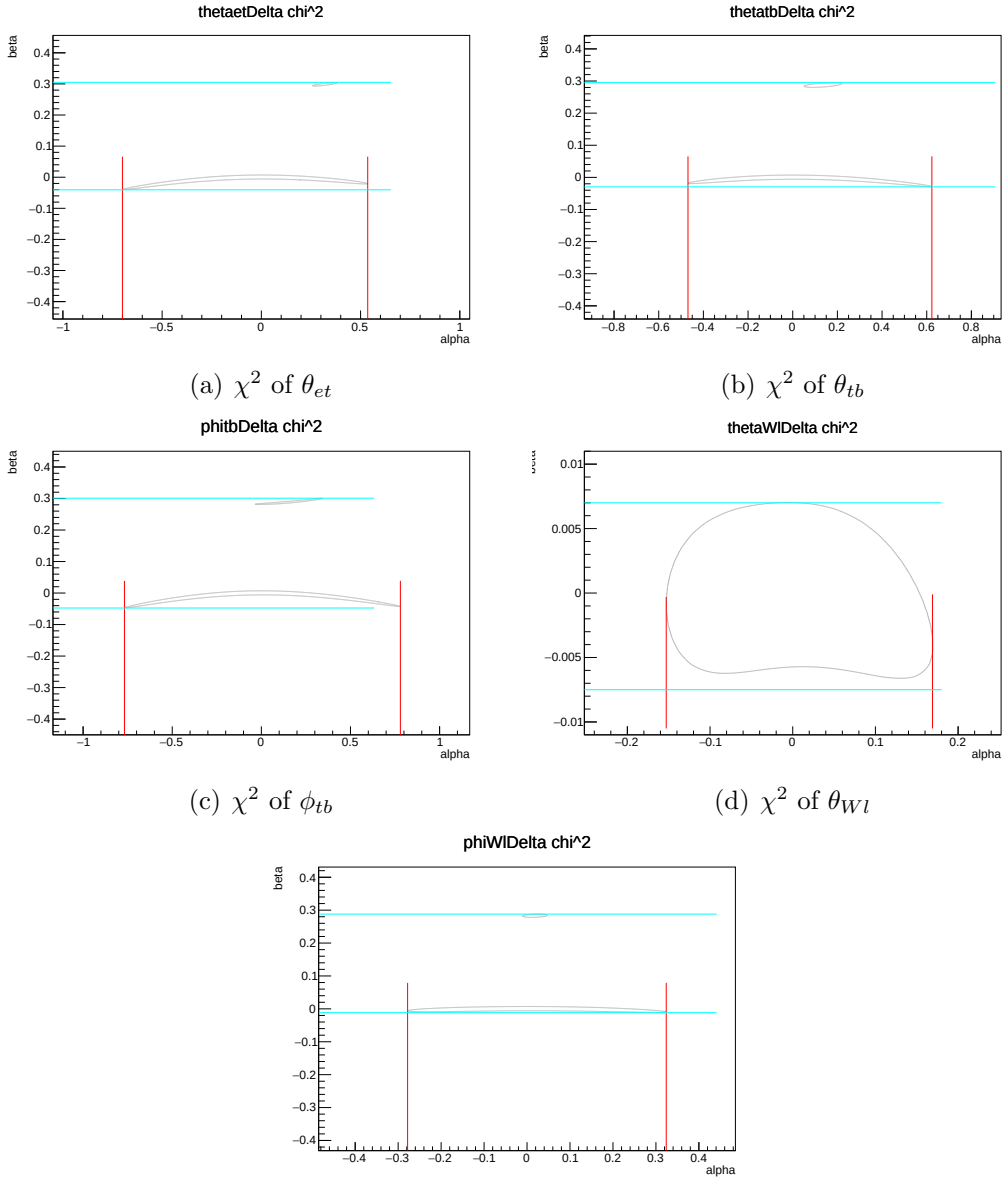

(a) χ^2 of θ_{et}

(b) χ^2 of θ_{tb}

(c) χ^2 of ϕ_{tb}

(d) χ^2 of θ_{Wl}

(e) χ^2 of ϕ_{Wl}

Figure D.89: χ^2 of tl_tbW_Re-tr_tbW_Re 1 Dimensional Angular Distribution

tl_tbW_Re-tr_tbW_Re σ excluded

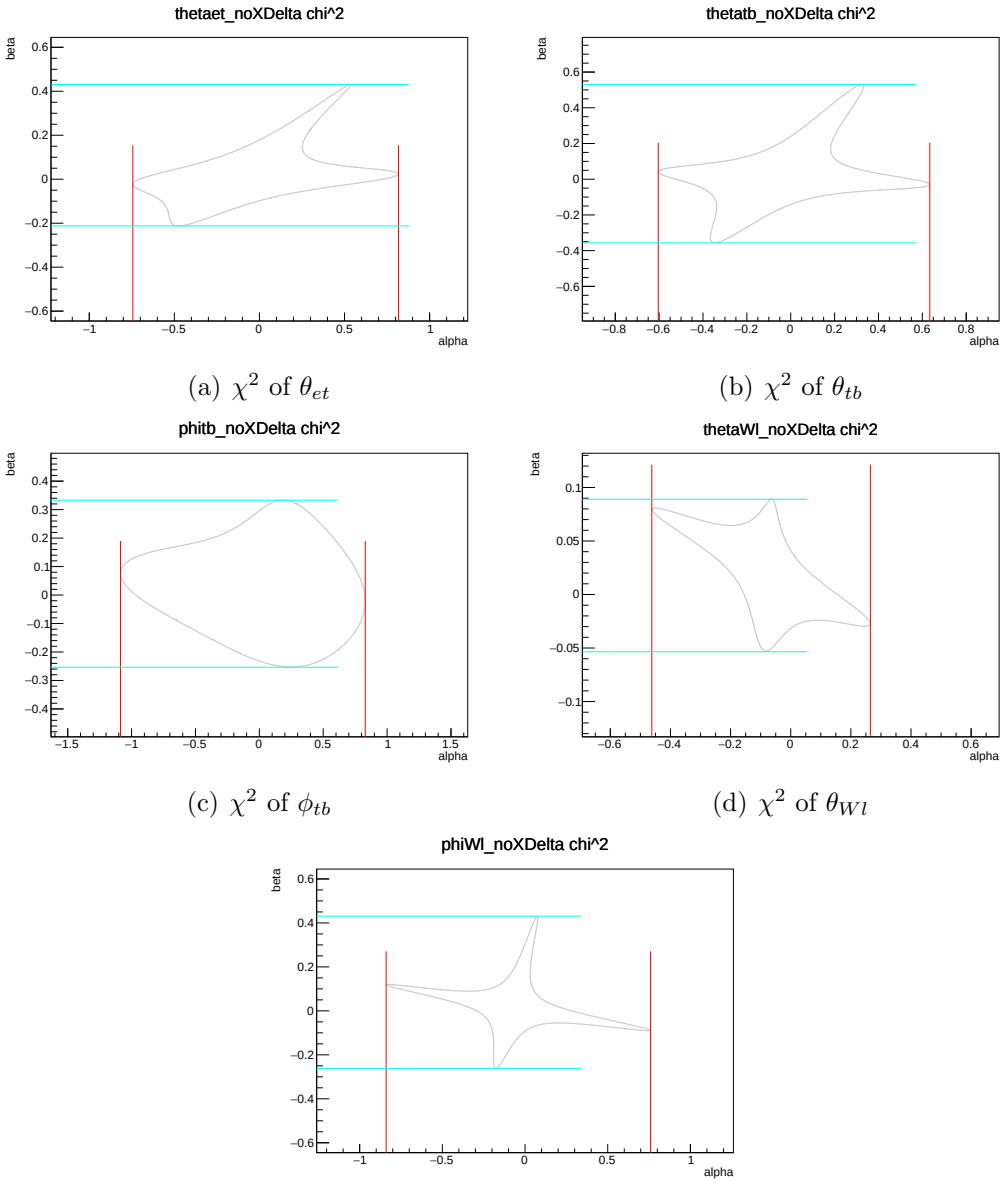

(a) χ^2 of θ_{et}

(b) χ^2 of θ_{tb}

(c) χ^2 of ϕ_{tb}

(d) χ^2 of θ_{Wl}

(e) χ^2 of ϕ_{Wl}

Figure D.90: χ^2 of tl_tbW_Re-tr_tbW_Re 1 Dimensional Angular Distribution

tl_tbW_Re-tv_ttA σ included

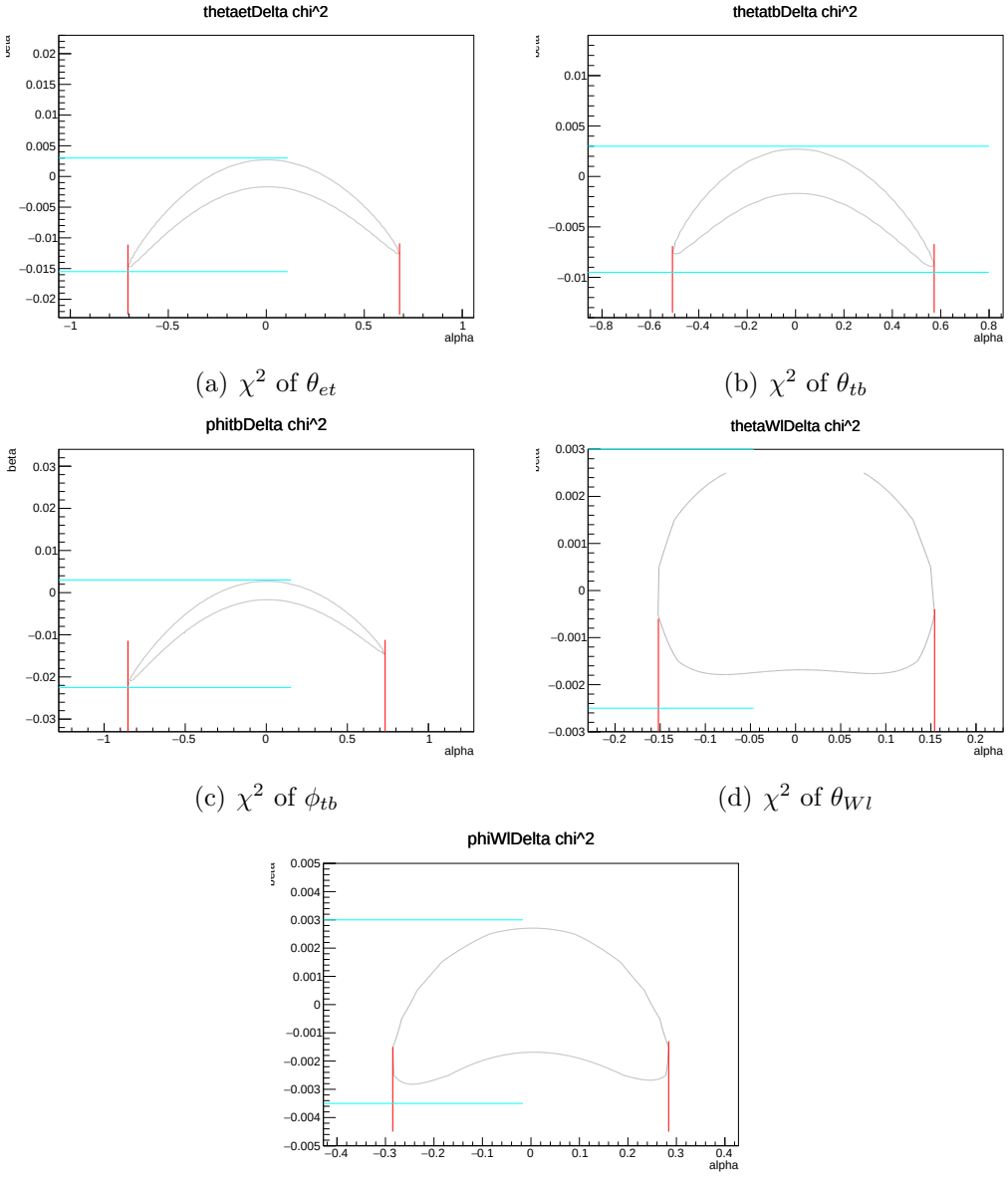

(a) χ^2 of θ_{et}

(b) χ^2 of θ_{tb}

(c) χ^2 of ϕ_{tb}

(d) χ^2 of θ_{Wl}

(e) χ^2 of ϕ_{Wl}

Figure D.91: χ^2 of tl_tbW_Re-tv_ttA 1 Dimensional Angular Distribution

tl_tbW_Re-tv_ttA σ excluded

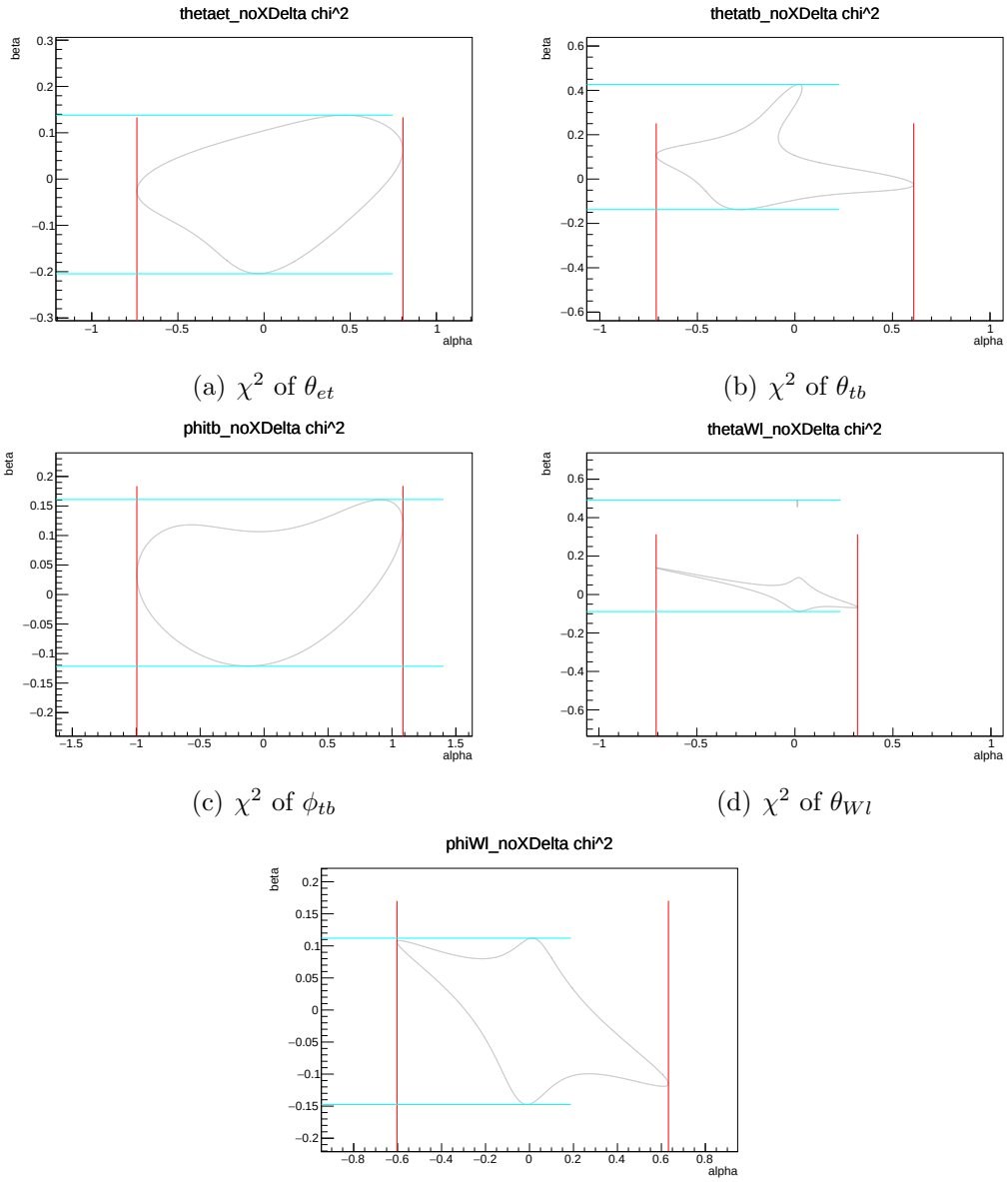

(a) χ^2 of θ_{et}

(b) χ^2 of θ_{tb}

(c) χ^2 of ϕ_{tb}

(d) χ^2 of θ_{Wl}

(e) χ^2 of ϕ_{Wl}

Figure D.92: χ^2 of tl_tbW_Re-tv_ttA 1 Dimensional Angular Distribution

tl_tbW_Re-vr_ttZ σ included

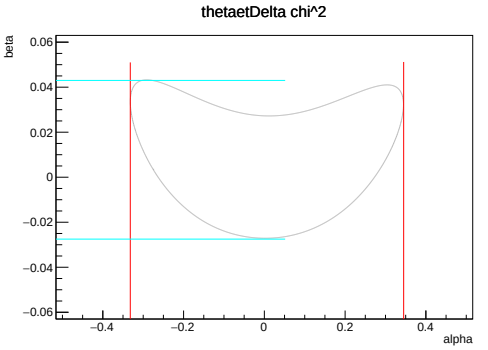

(a) χ^2 of θ_{et}

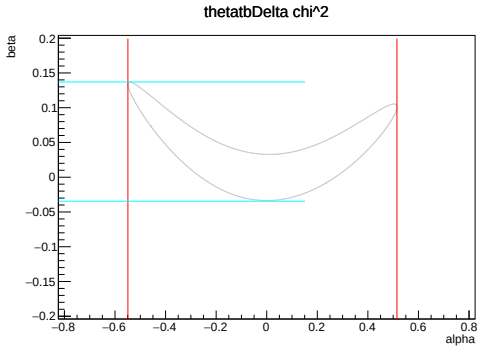

(b) χ^2 of θ_{tb}

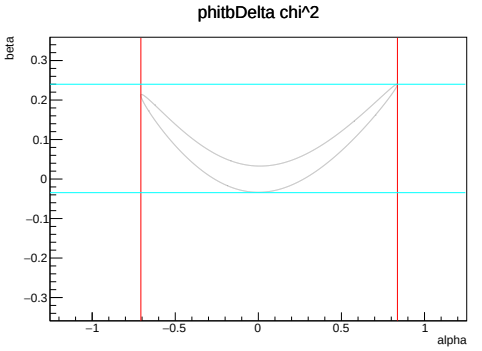

(c) χ^2 of ϕ_{tb}

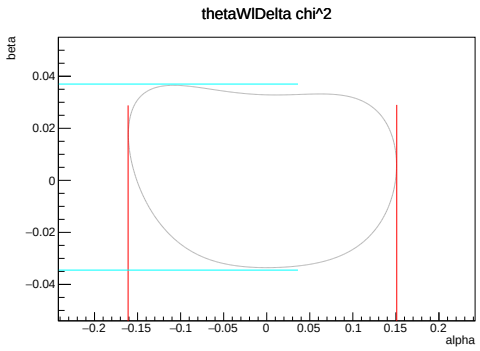

(d) χ^2 of θ_{Wl}

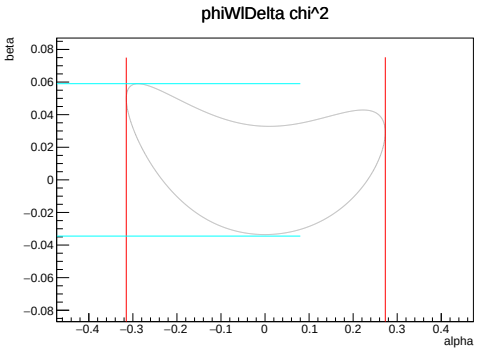

(e) χ^2 of ϕ_{Wl}

Figure D.93: χ^2 of tl_tbW_Re-vr_ttZ 1 Dimensional Angular Distribution

tl_tbW_Re-vr_ttZ σ excluded

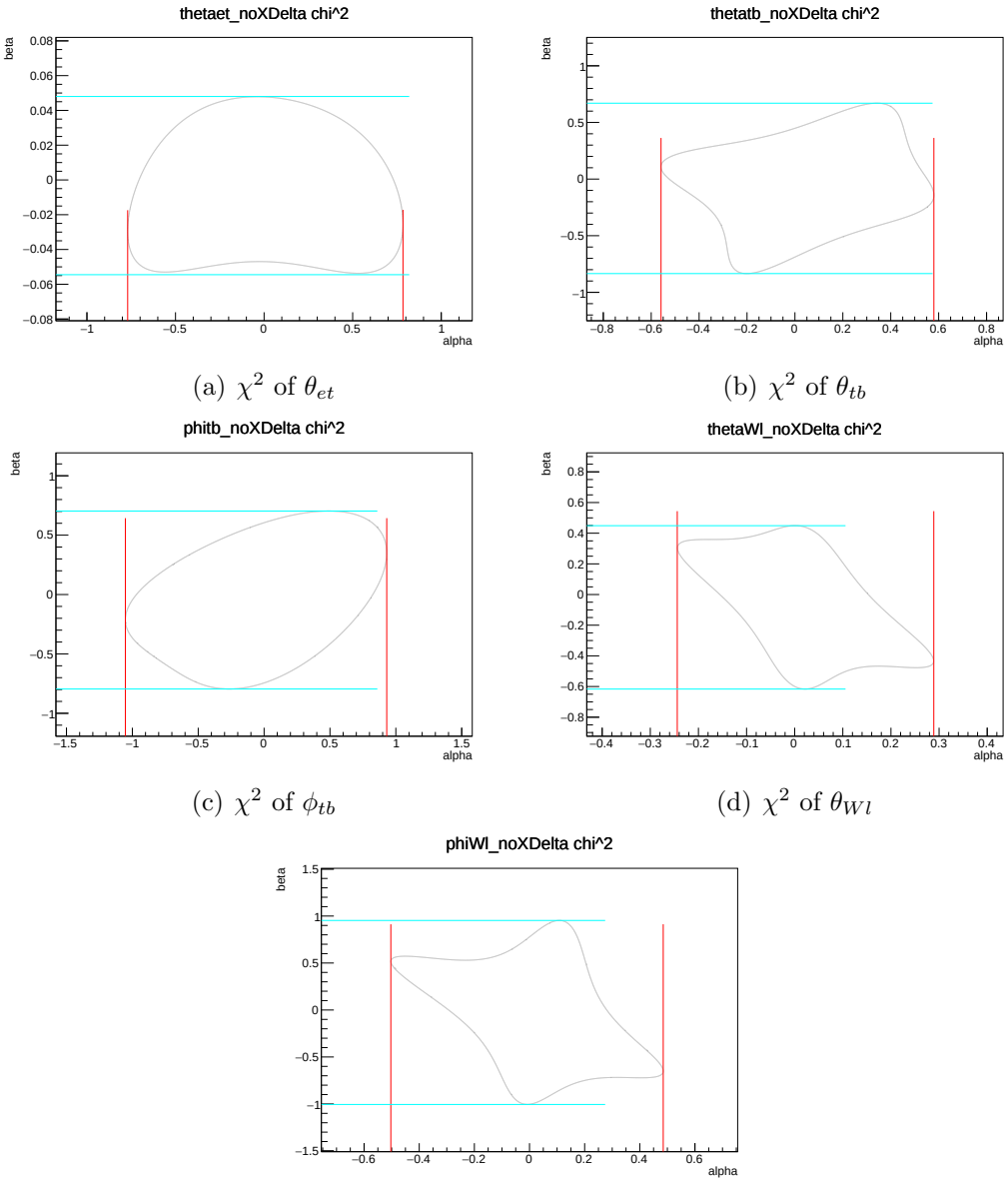

(a) χ^2 of θ_{et}

(b) χ^2 of θ_{tb}

(c) χ^2 of ϕ_{tb}

(d) χ^2 of θ_{Wl}

(e) χ^2 of ϕ_{Wl}

Figure D.94: χ^2 of tl_tbW_Re-vr_ttZ 1 Dimensional Angular Distribution

tr_tbW_Re-ta_ttA σ included

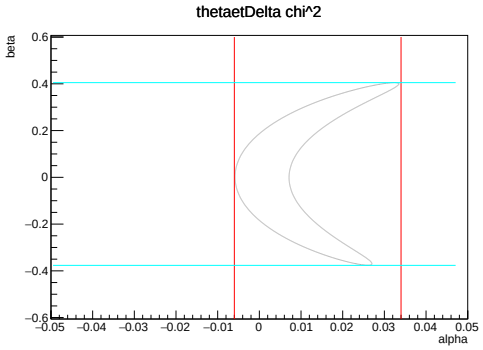

(a) χ^2 of θ_{et}

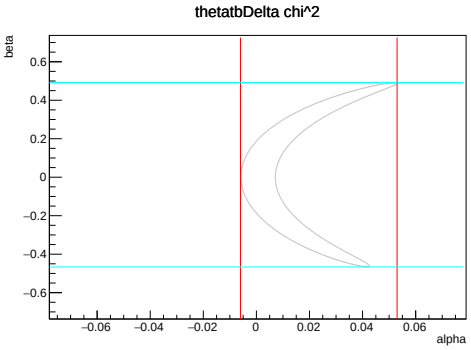

(b) χ^2 of θ_{tb}

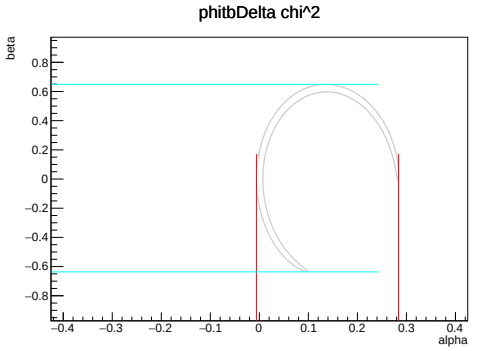

(c) χ^2 of ϕ_{tb}

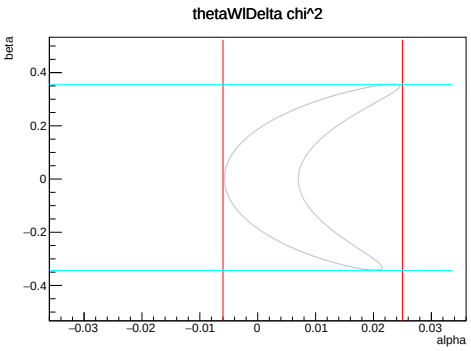

(d) χ^2 of θ_{Wl}

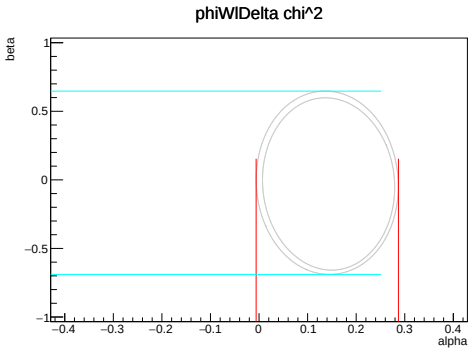

(e) χ^2 of ϕ_{Wl}

Figure D.95: χ^2 of tr_tbW_Re-ta_ttA 1 Dimensional Angular Distribution

tr_tbW_Re-ta_ttA σ excluded

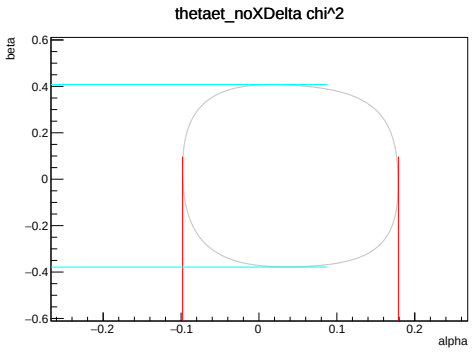

(a) χ^2 of θ_{et}

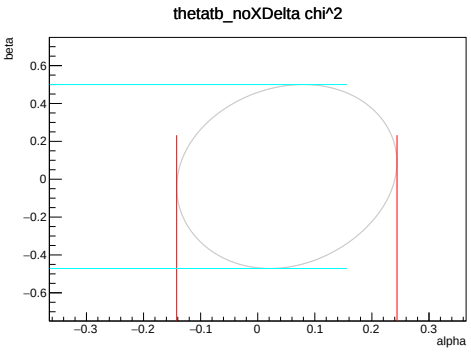

(b) χ^2 of θ_{tb}

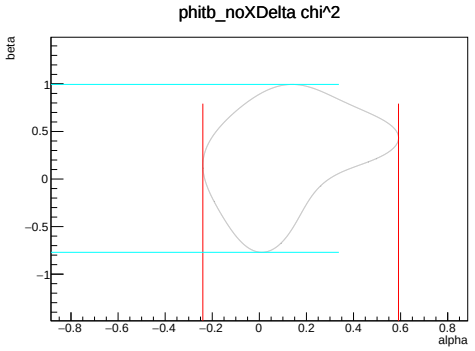

(c) χ^2 of ϕ_{tb}

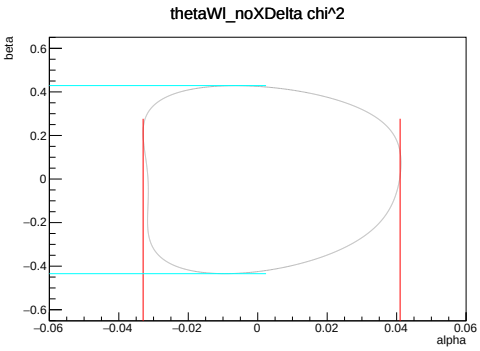

(d) χ^2 of θ_{Wl}

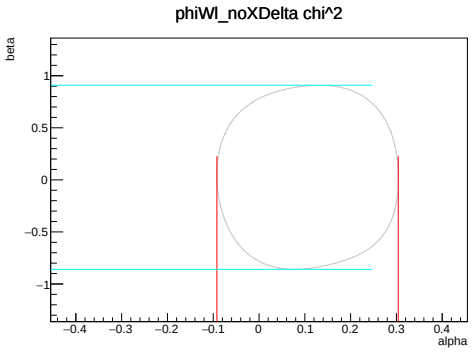

(e) χ^2 of ϕ_{Wl}

Figure D.96: χ^2 of tr_tbW_Re-ta_ttA 1 Dimensional Angular Distribution

tr_tbW_Re-tv_ttA σ included

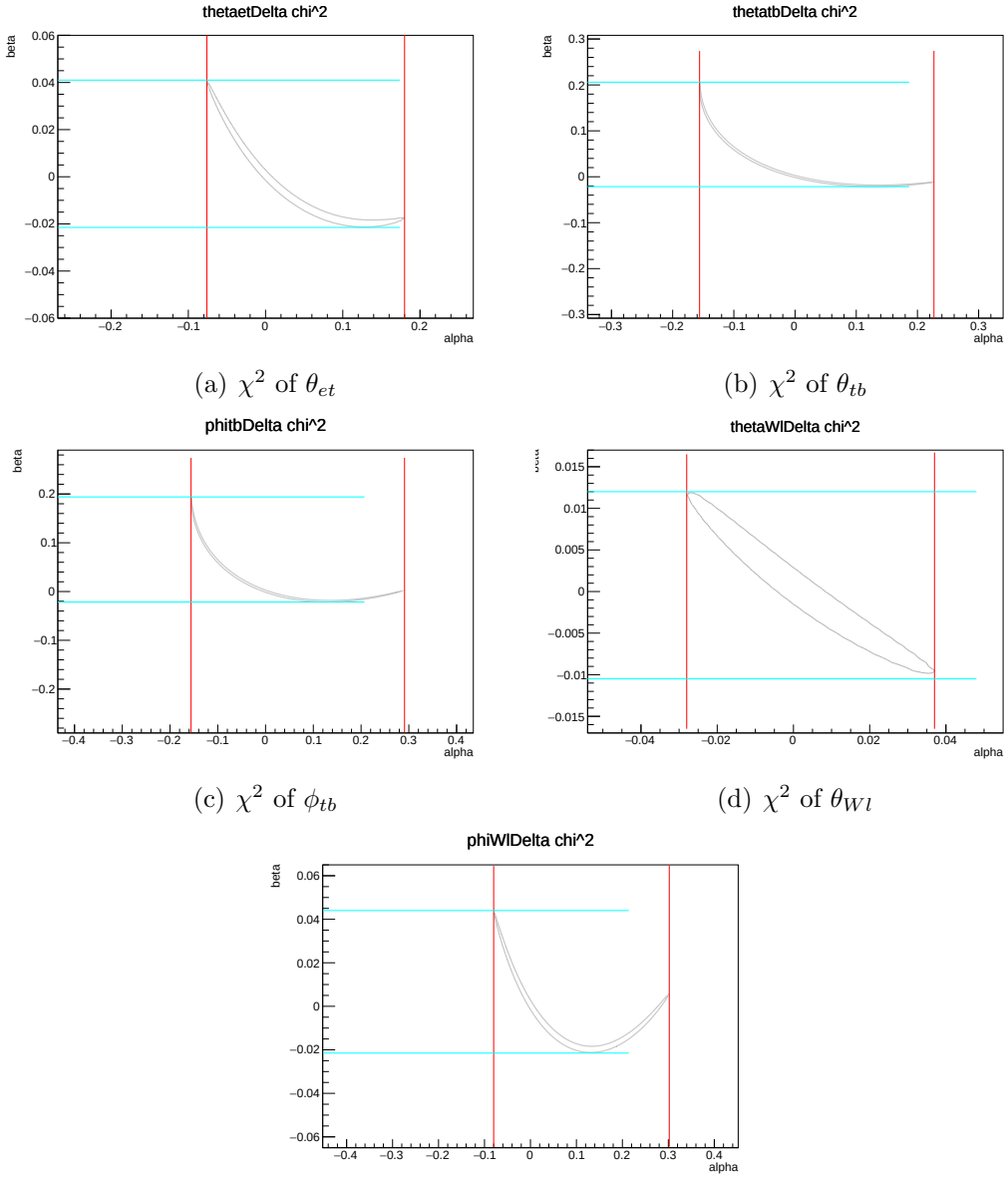

(a) χ^2 of θ_{et}

(b) χ^2 of θ_{tb}

(c) χ^2 of ϕ_{tb}

(d) χ^2 of θ_{Wl}

(e) χ^2 of ϕ_{Wl}

Figure D.97: χ^2 of tr_tbW_Re-tv_ttA 1 Dimensional Angular Distribution

tr_tbW_Re-tv_ttA σ excluded

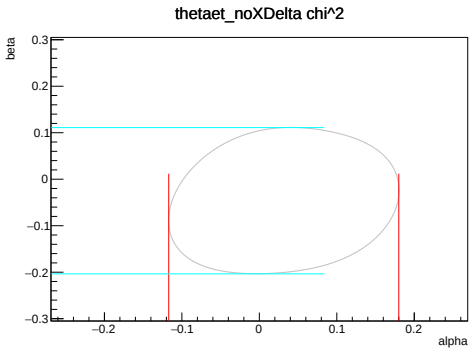

(a) χ^2 of θ_{et}

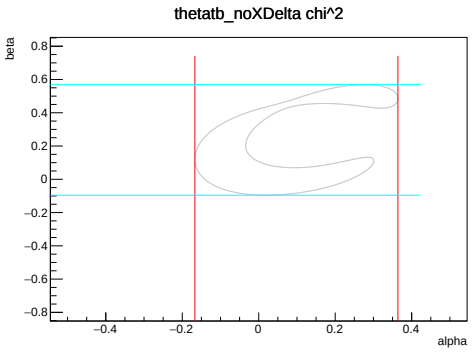

(b) χ^2 of θ_{tb}

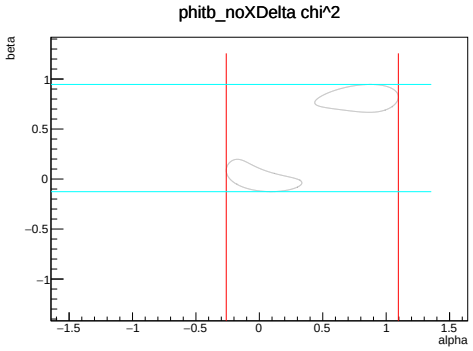

(c) χ^2 of ϕ_{tb}

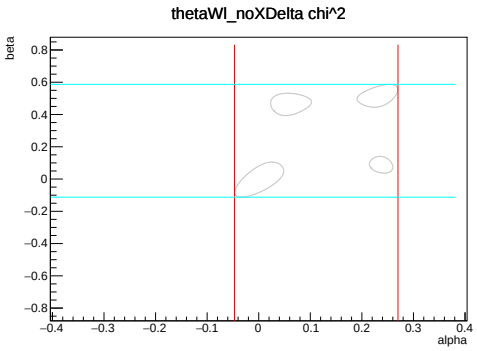

(d) χ^2 of θ_{Wl}

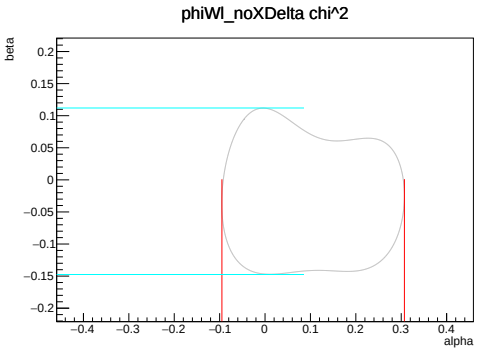

(e) χ^2 of ϕ_{Wl}

Figure D.98: χ^2 of tr_tbW_Re-tv_ttA 1 Dimensional Angular Distribution

tr_tbW_Re-vr_ttZ σ included

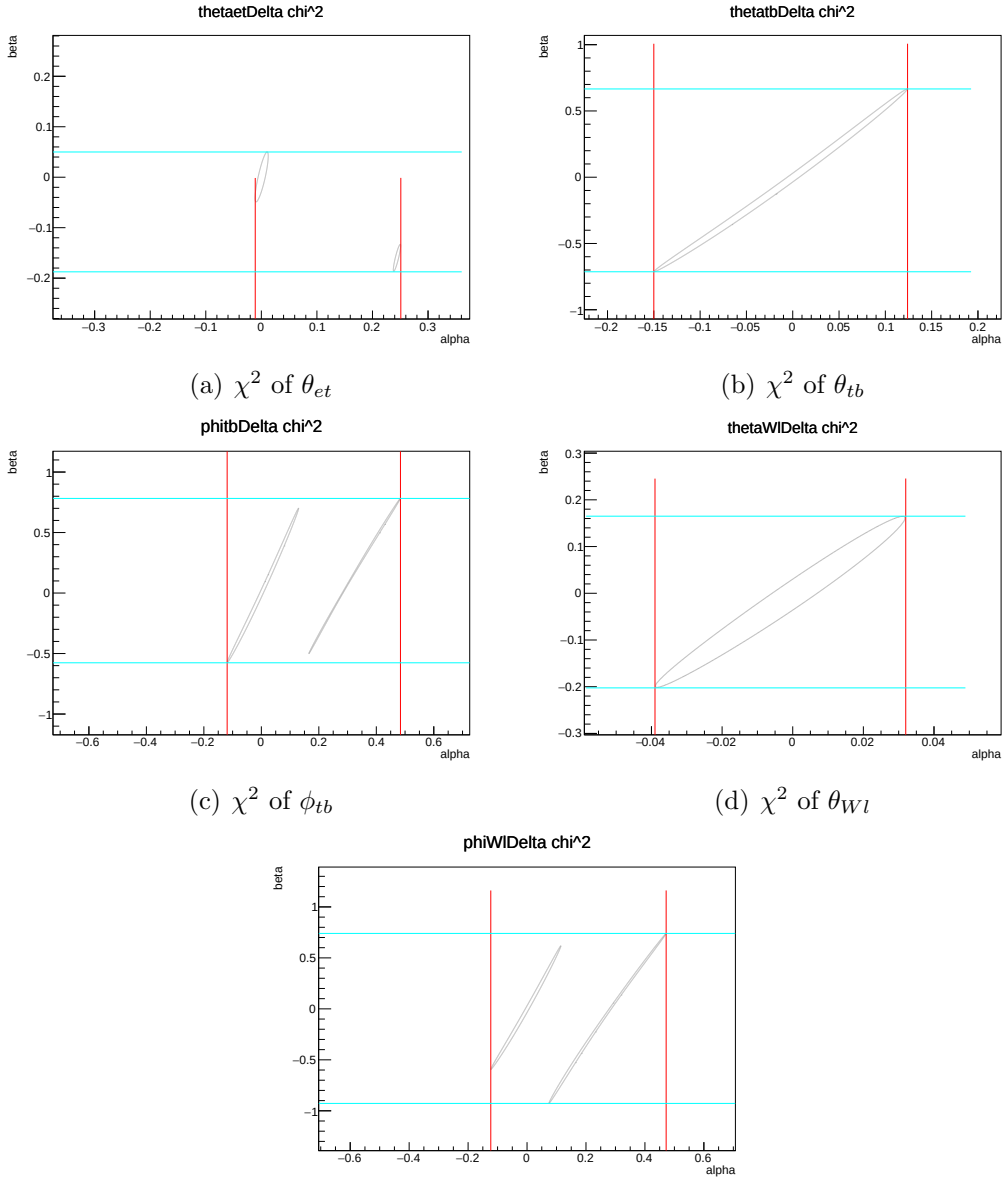

(a) χ^2 of θ_{et}

(b) χ^2 of θ_{tb}

(c) χ^2 of ϕ_{tb}

(d) χ^2 of θ_{Wl}

(e) χ^2 of ϕ_{Wl}

Figure D.99: χ^2 of tr_tbW_Re-vr_ttZ 1 Dimensional Angular Distribution

tr_tbW_Re-vr_ttZ σ excluded

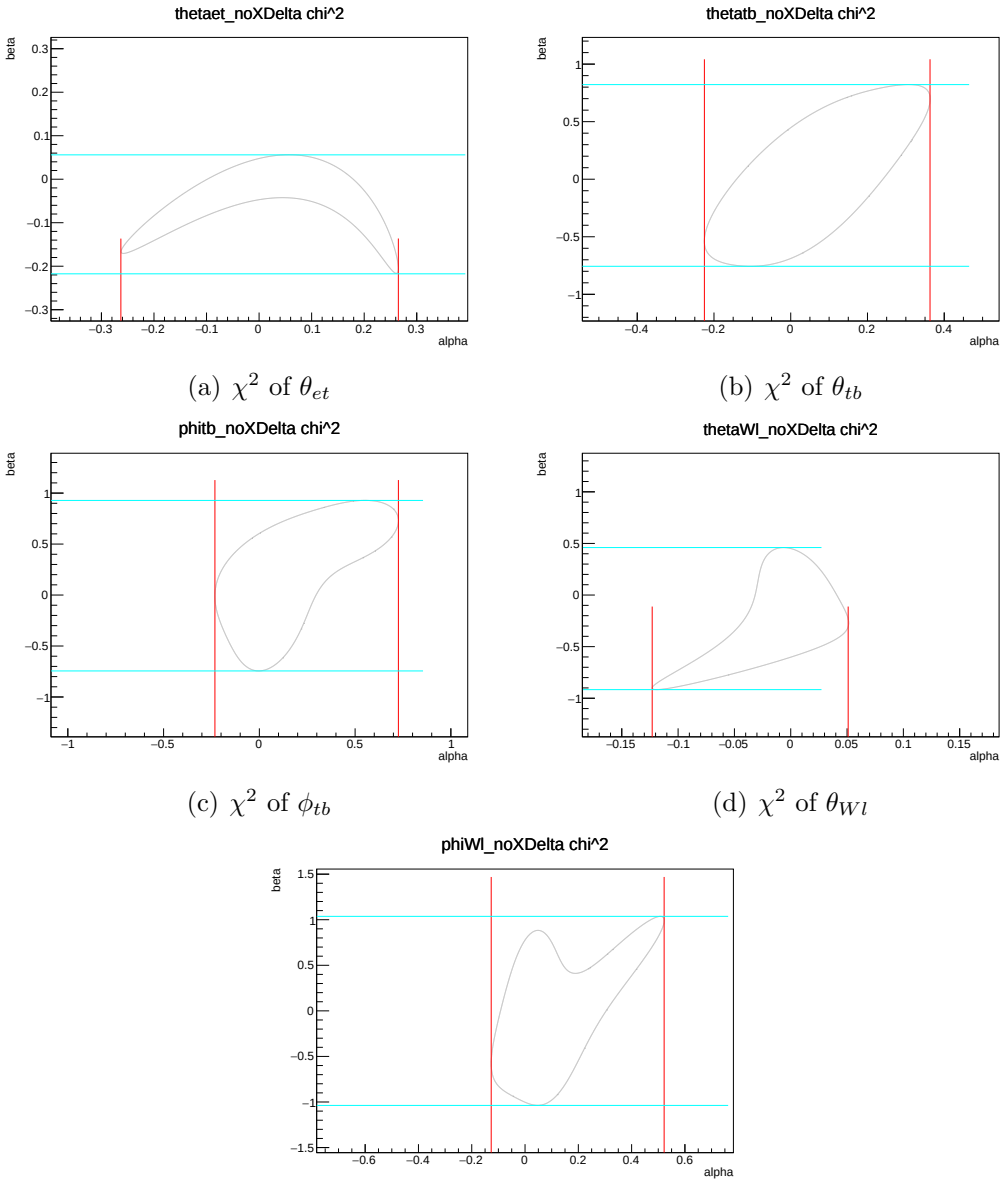

(a) χ^2 of θ_{et}

(b) χ^2 of θ_{tb}

(c) χ^2 of ϕ_{tb}

(d) χ^2 of θ_{Wl}

(e) χ^2 of ϕ_{Wl}

Figure D.100: χ^2 of tr_tbW_Re-vr_ttZ 1 Dimensional Angular Distribution

tv_ttA-ta_ttA σ included

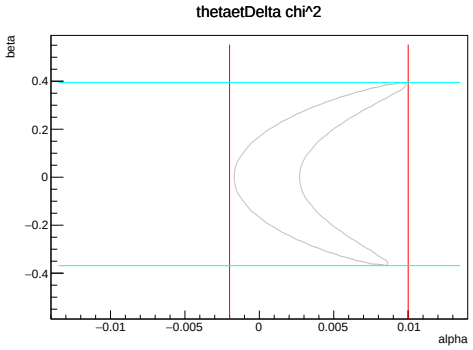

(a) χ^2 of θ_{et}

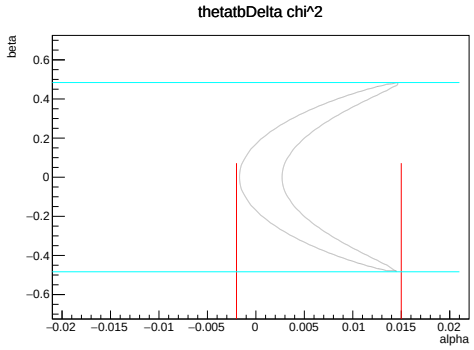

(b) χ^2 of θ_{tb}

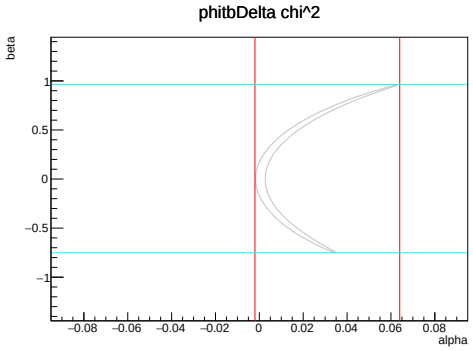

(c) χ^2 of ϕ_{tb}

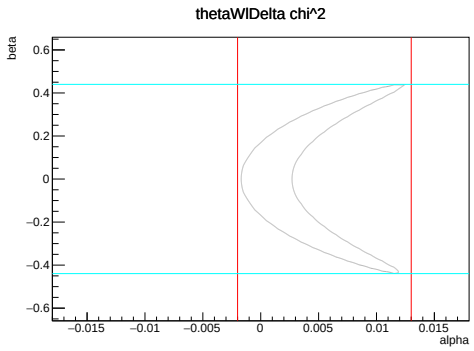

(d) χ^2 of θ_{Wl}

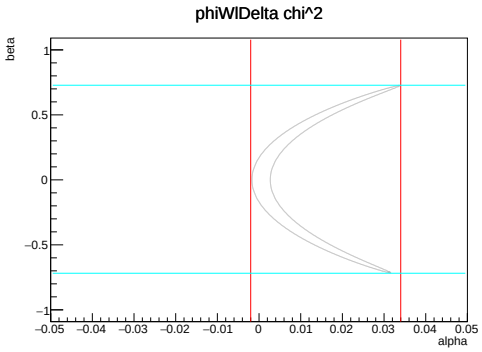

(e) χ^2 of ϕ_{Wl}

Figure D.101: χ^2 of tv_ttA-ta_ttA 1 Dimensional Angular Distribution

tv_ttA-ta_ttA σ excluded

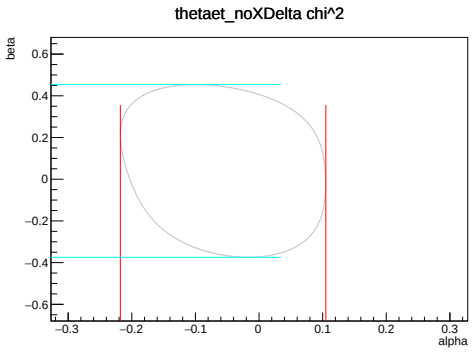

(a) χ^2 of θ_{et}

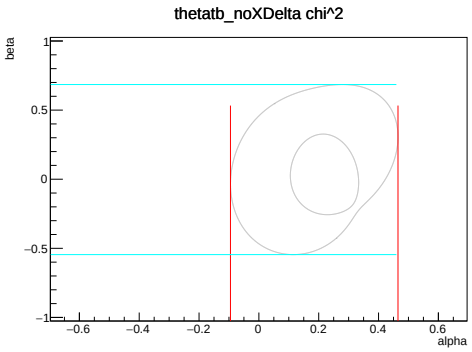

(b) χ^2 of θ_{tb}

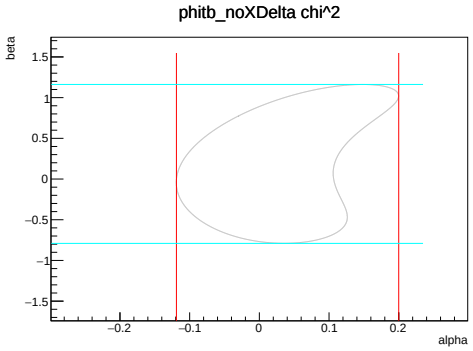

(c) χ^2 of ϕ_{tb}

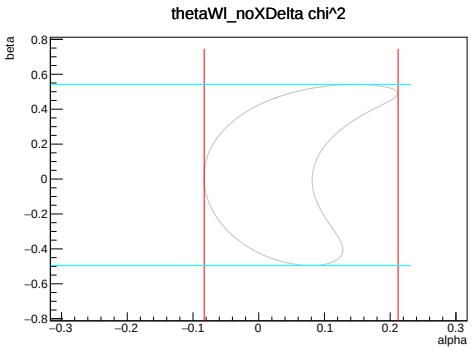

(d) χ^2 of θ_{Wl}

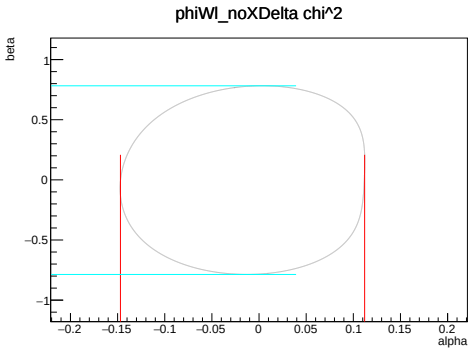

(e) χ^2 of ϕ_{Wl}

Figure D.102: χ^2 of tv_ttA-ta_ttA 1 Dimensional Angular Distribution

tv_ttA-vr_ttZ σ included

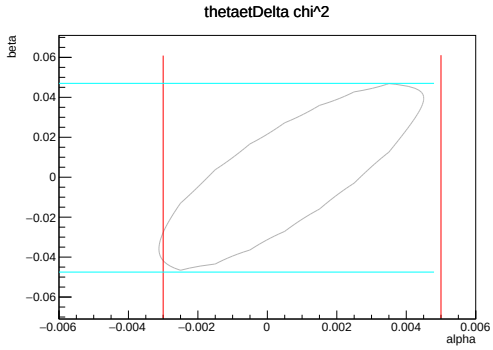

(a) χ^2 of θ_{et}

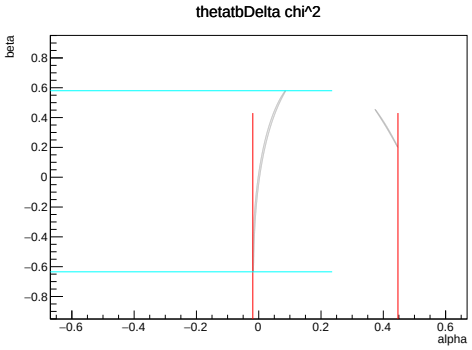

(b) χ^2 of θ_{tb}

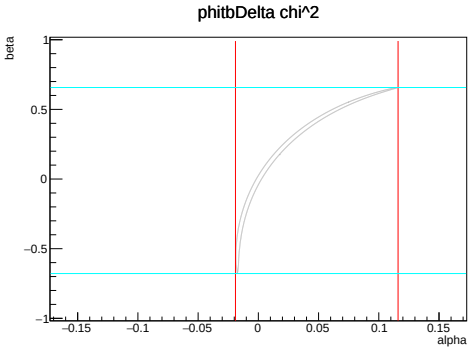

(c) χ^2 of ϕ_{tb}

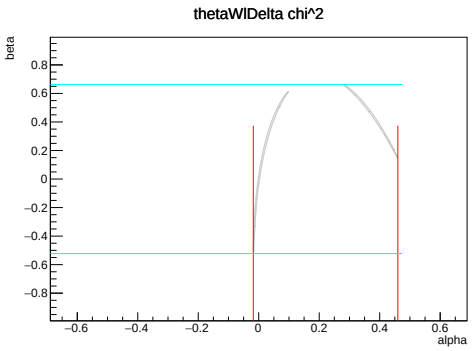

(d) χ^2 of θ_{Wl}

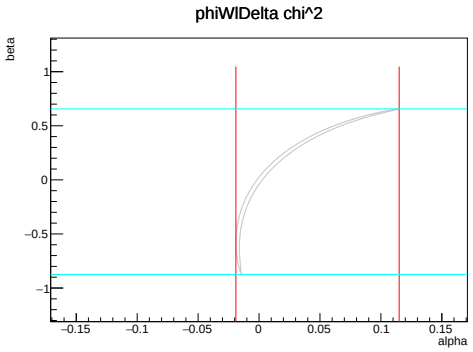

(e) χ^2 of ϕ_{Wl}

Figure D.103: χ^2 of tv_ttA-vr_ttZ 1 Dimensional Angular Distribution

tv_ttA-vr_ttZ σ excluded

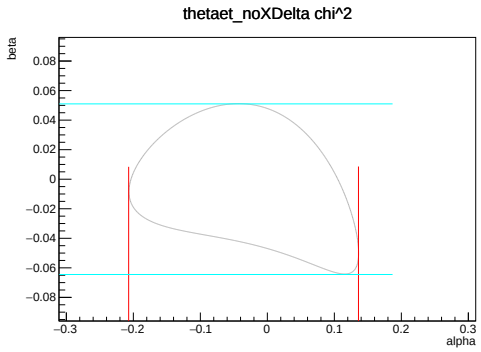

(a) χ^2 of θ_{et}

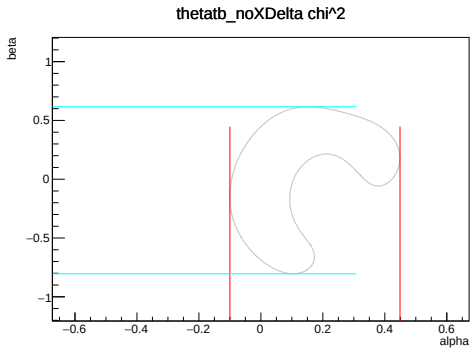

(b) χ^2 of θ_{tb}

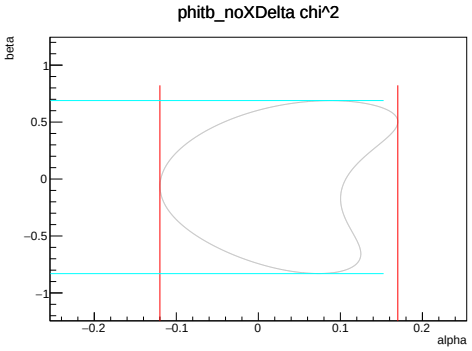

(c) χ^2 of ϕ_{tb}

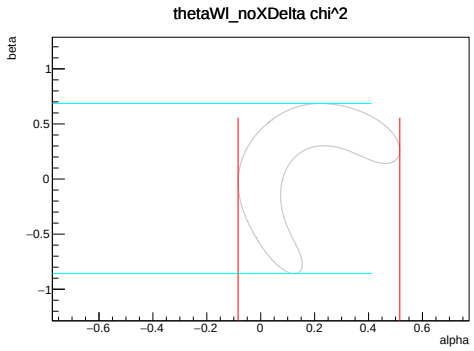

(d) χ^2 of θ_{Wl}

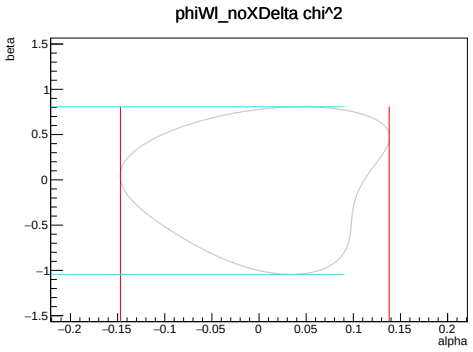

(e) χ^2 of ϕ_{Wl}

Figure D.104: χ^2 of tv_ttA-vr_ttZ 1 Dimensional Angular Distribution

vl_tbW_Re-ta_ttA σ included

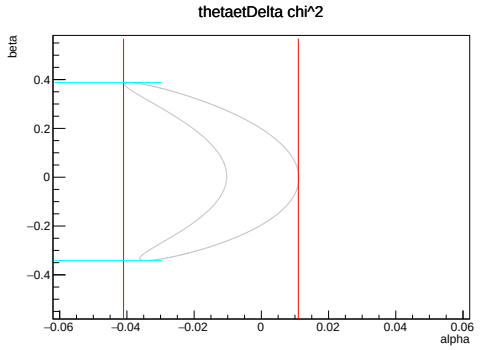

(a) χ^2 of θ_{et}

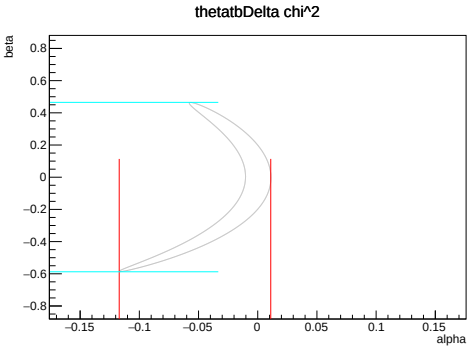

(b) χ^2 of θ_{tb}

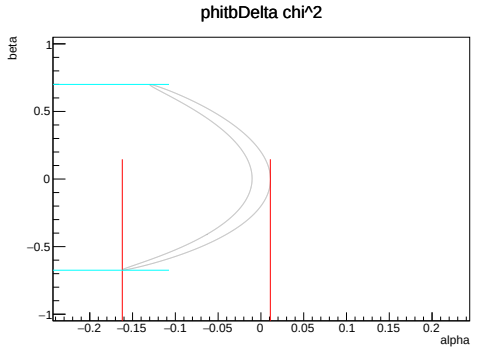

(c) χ^2 of ϕ_{tb}

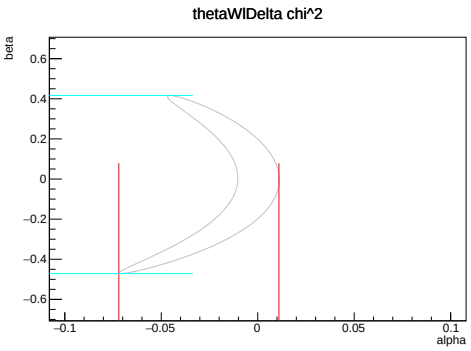

(d) χ^2 of θ_{Wl}

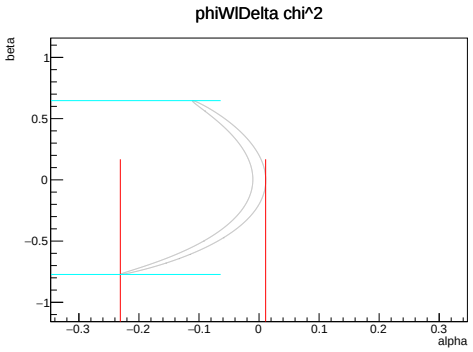

(e) χ^2 of ϕ_{Wl}

Figure D.105: χ^2 of vl_tbW_Re-ta_ttA 1 Dimensional Angular Distribution

vl_tbW_Re-ta_ttA σ excluded

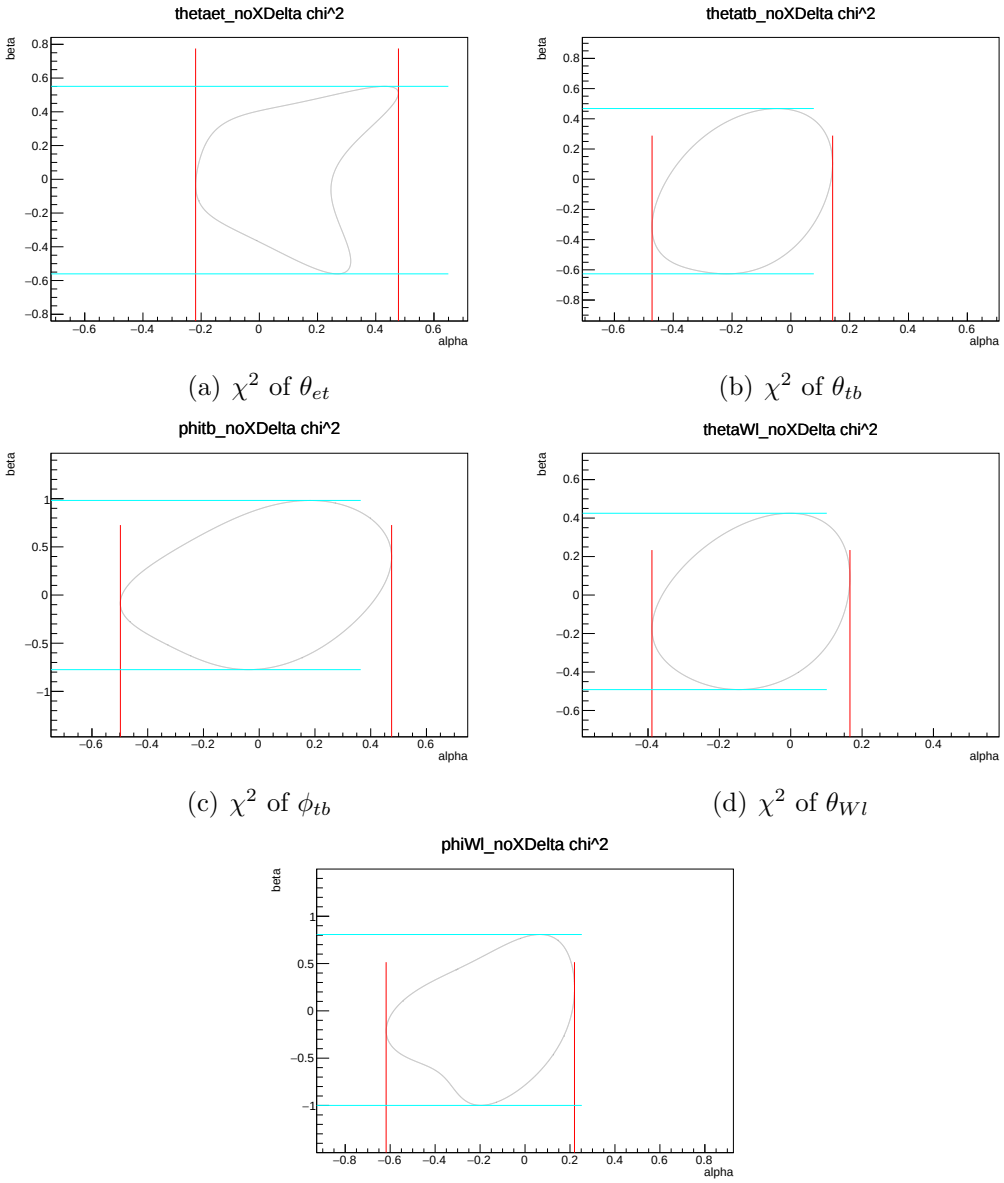

(a) χ^2 of θ_{et}

(b) χ^2 of θ_{tb}

(c) χ^2 of ϕ_{tb}

(d) χ^2 of θ_{Wl}

(e) χ^2 of ϕ_{Wl}

Figure D.106: χ^2 of vl_tbW_Re-ta_ttA 1 Dimensional Angular Distribution

vl_tbW_Re-tl_tbW_Re σ included

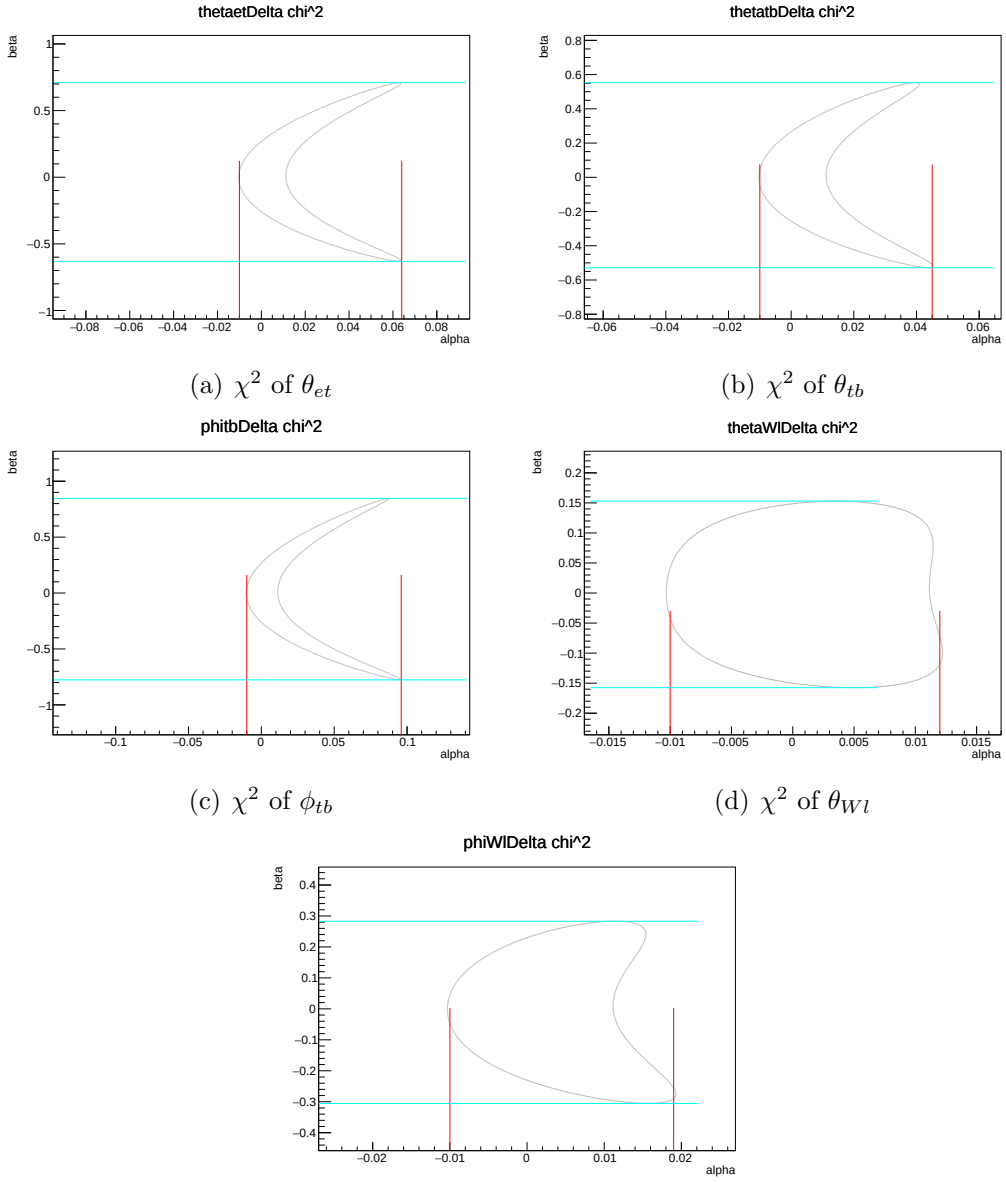

(a) χ^2 of θ_{et}

(b) χ^2 of θ_{tb}

(c) χ^2 of ϕ_{tb}

(d) χ^2 of θ_{Wl}

(e) χ^2 of ϕ_{Wl}

Figure D.107: χ^2 of vl_tbW_Re-tl_tbW_Re 1 Dimensional Angular Distribution

vl_tbW_Re-tl_tbW_Re σ excluded

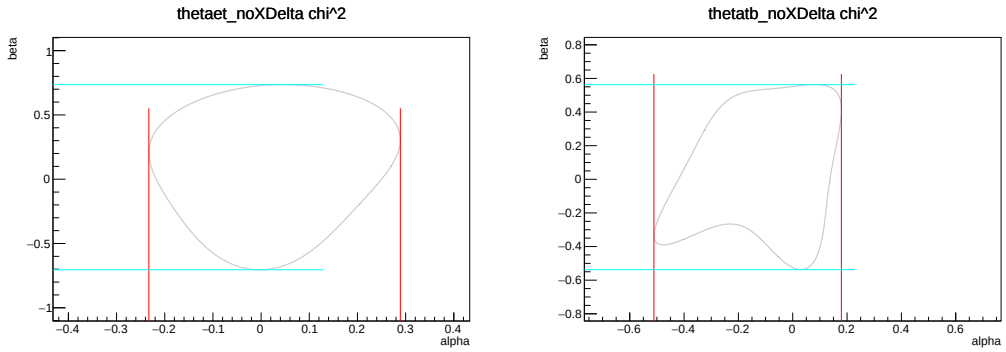

(a) χ^2 of θ_{et}

(b) χ^2 of θ_{tb}

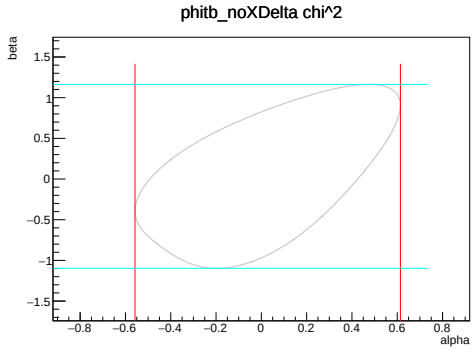

(c) χ^2 of ϕ_{tb}

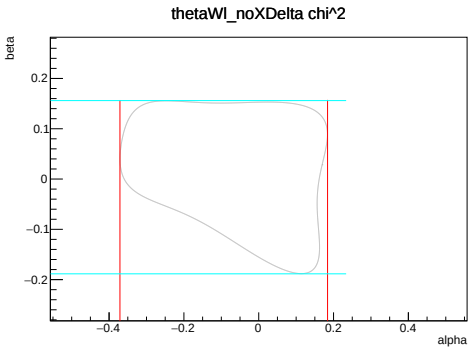

(d) χ^2 of θ_{Wl}

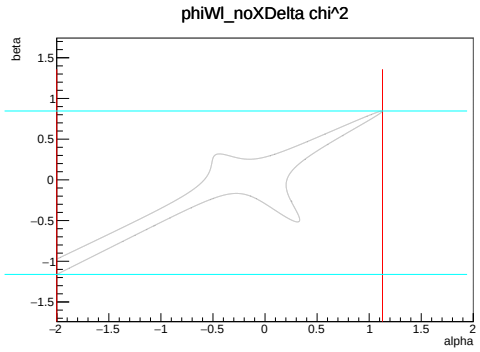

(e) χ^2 of ϕ_{Wl}

Figure D.108: χ^2 of vl_tbW_Re-tl_tbW_Re 1 Dimensional Angular Distribution

vl_tbW_Re-tr_tbW_Re σ included

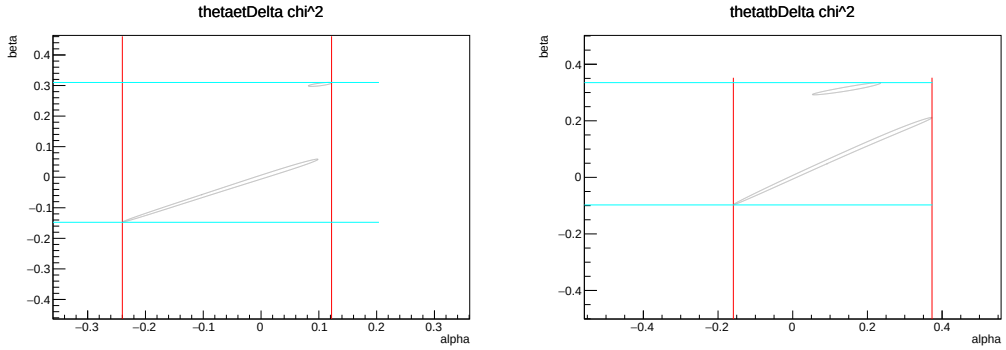

(a) χ^2 of θ_{et}

(b) χ^2 of θ_{tb}

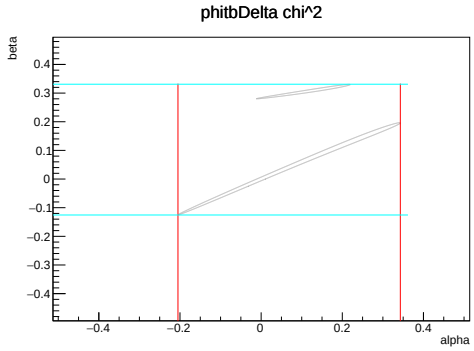

(c) χ^2 of ϕ_{tb}

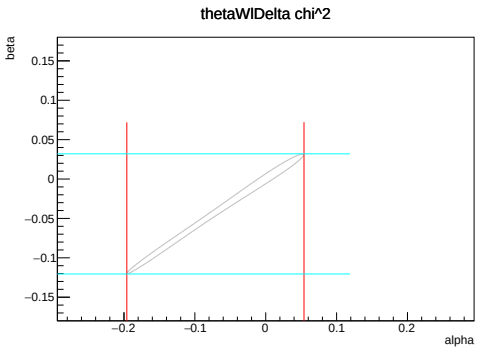

(d) χ^2 of θ_{Wl}

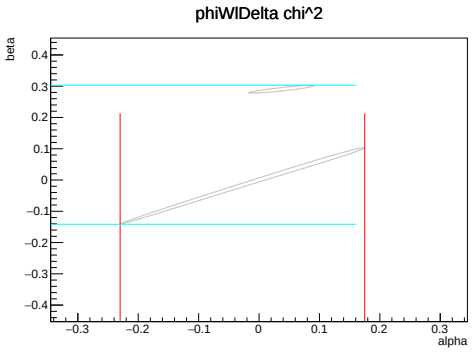

(e) χ^2 of ϕ_{Wl}

Figure D.109: χ^2 of vl_tbW_Re-tr_tbW_Re 1 Dimensional Angular Distribution

vl_tbW_Re-tr_tbW_Re σ excluded

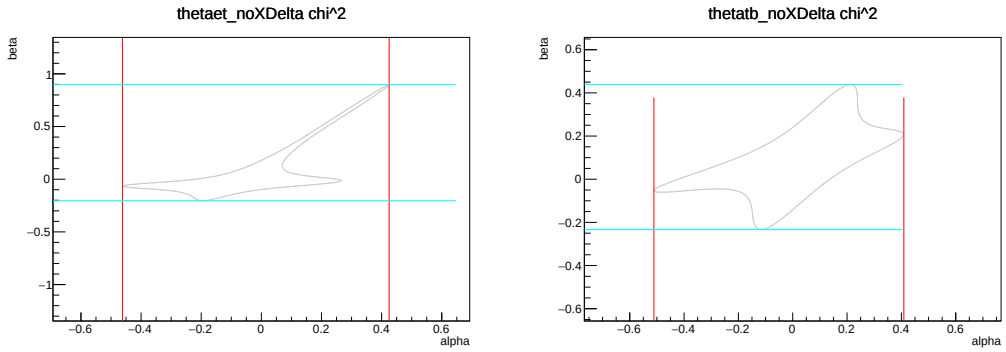

(a) χ^2 of θ_{et}

(b) χ^2 of θ_{tb}

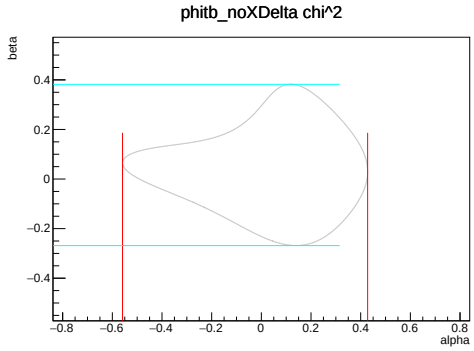

(c) χ^2 of ϕ_{tb}

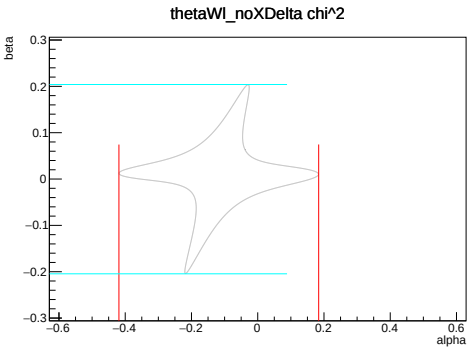

(d) χ^2 of θ_{Wl}

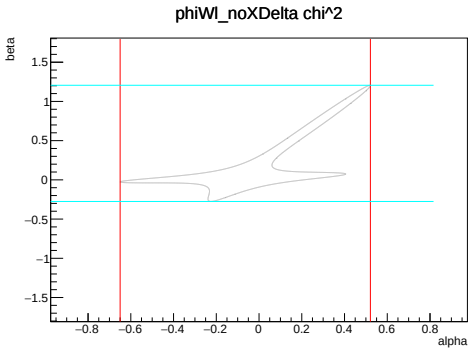

(e) χ^2 of ϕ_{Wl}

Figure D.110: χ^2 of vl_tbW_Re-tr_tbW_Re 1 Dimensional Angular Distribution

vl_tbW_Re-tv_ttA σ included

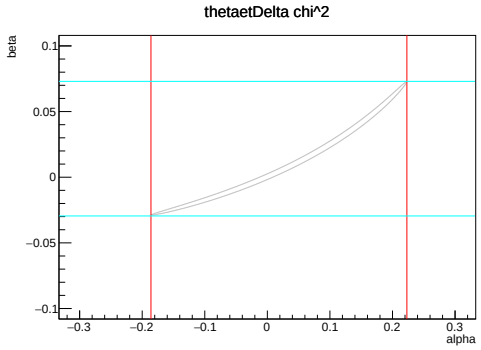

(a) χ^2 of θ_{et}

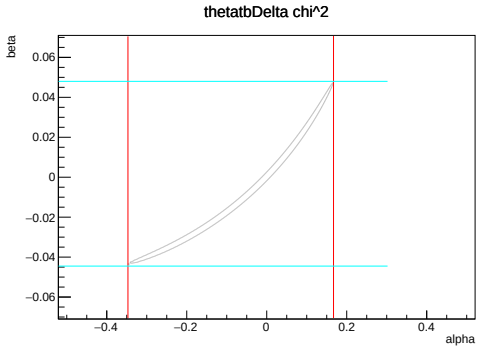

(b) χ^2 of θ_{tb}

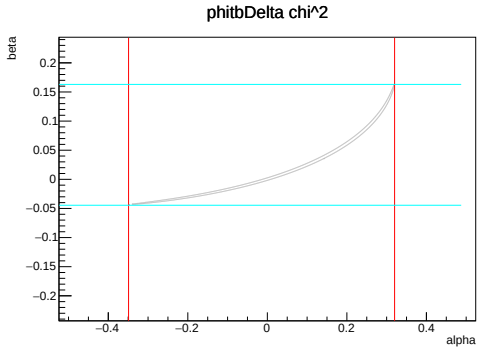

(c) χ^2 of ϕ_{tb}

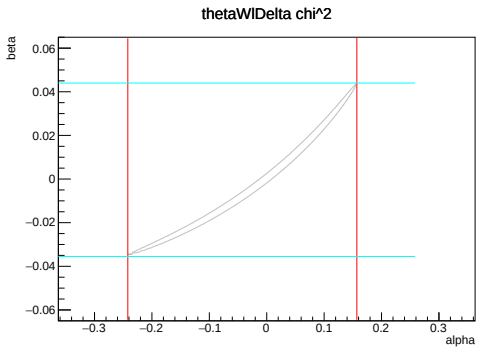

(d) χ^2 of θ_{Wl}

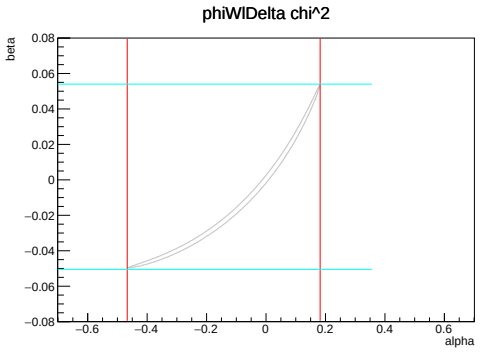

(e) χ^2 of ϕ_{Wl}

Figure D.111: χ^2 of vl_tbW_Re-tv_ttA 1 Dimensional Angular Distribution

vl_tbW_Re-tv_ttA σ excluded

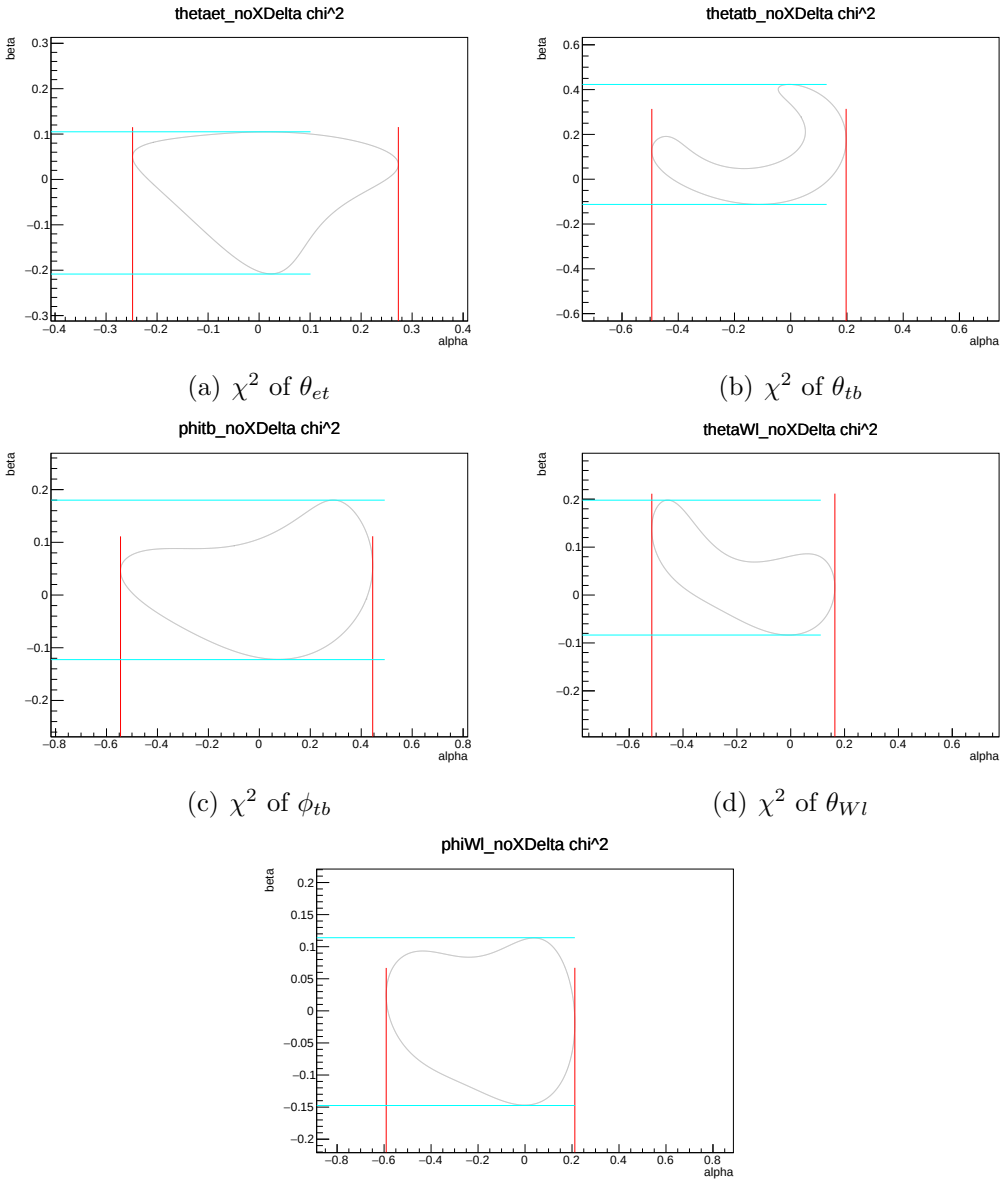

(a) χ^2 of θ_{et}

(b) χ^2 of θ_{tb}

(c) χ^2 of ϕ_{tb}

(d) χ^2 of θ_{Wl}

(e) χ^2 of ϕ_{Wl}

Figure D.112: χ^2 of vl_tbW_Re-tv_ttA 1 Dimensional Angular Distribution

vl_tbW_Re-vr_tbW_Re σ included

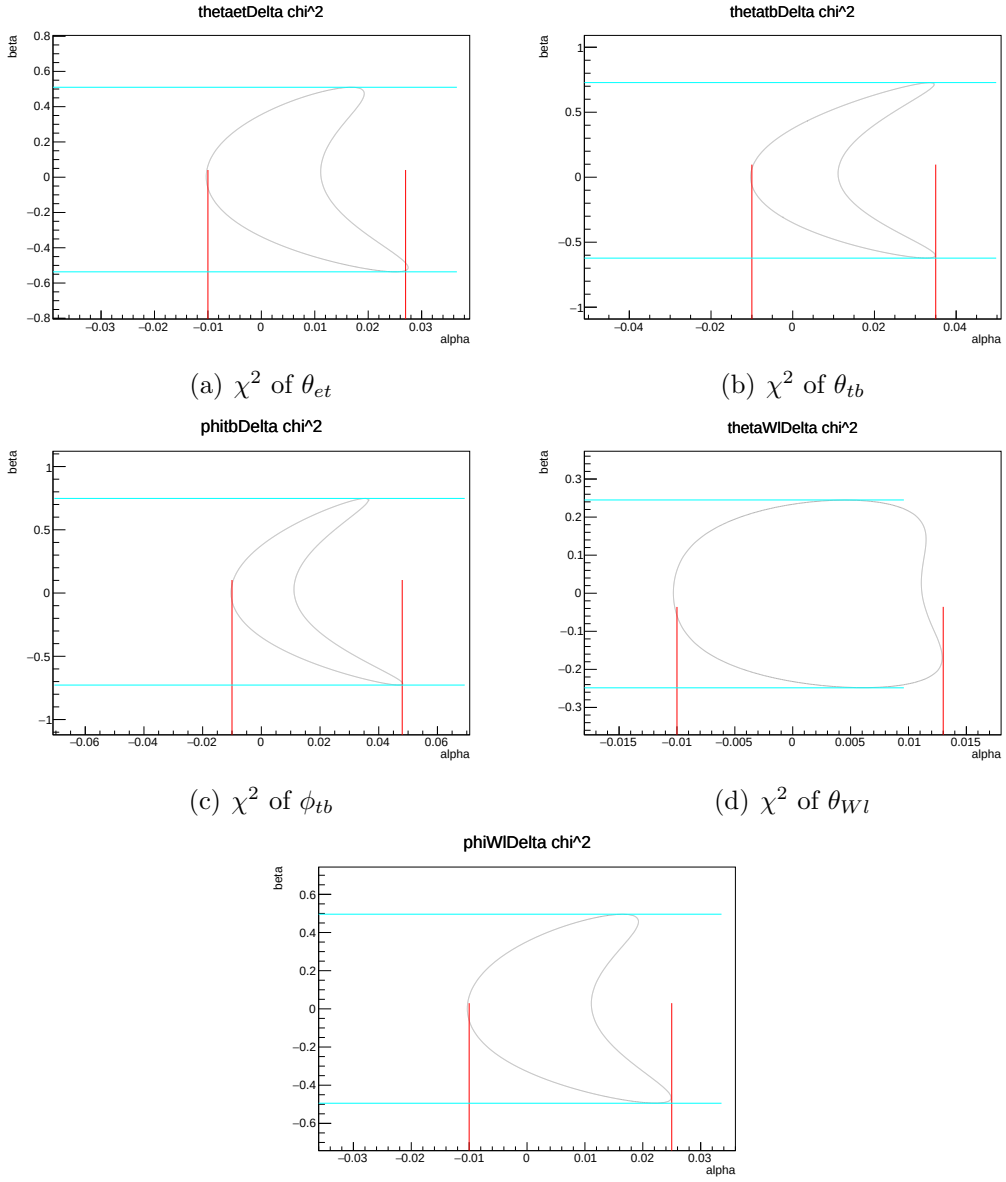

(a) χ^2 of θ_{et}

(b) χ^2 of θ_{tb}

(c) χ^2 of ϕ_{tb}

(d) χ^2 of θ_{Wl}

(e) χ^2 of ϕ_{Wl}

Figure D.113: χ^2 of vl_tbW_Re-vr_tbW_Re 1 Dimensional Angular Distribution

vl_tbW_Re-vr_tbW_Re σ excluded

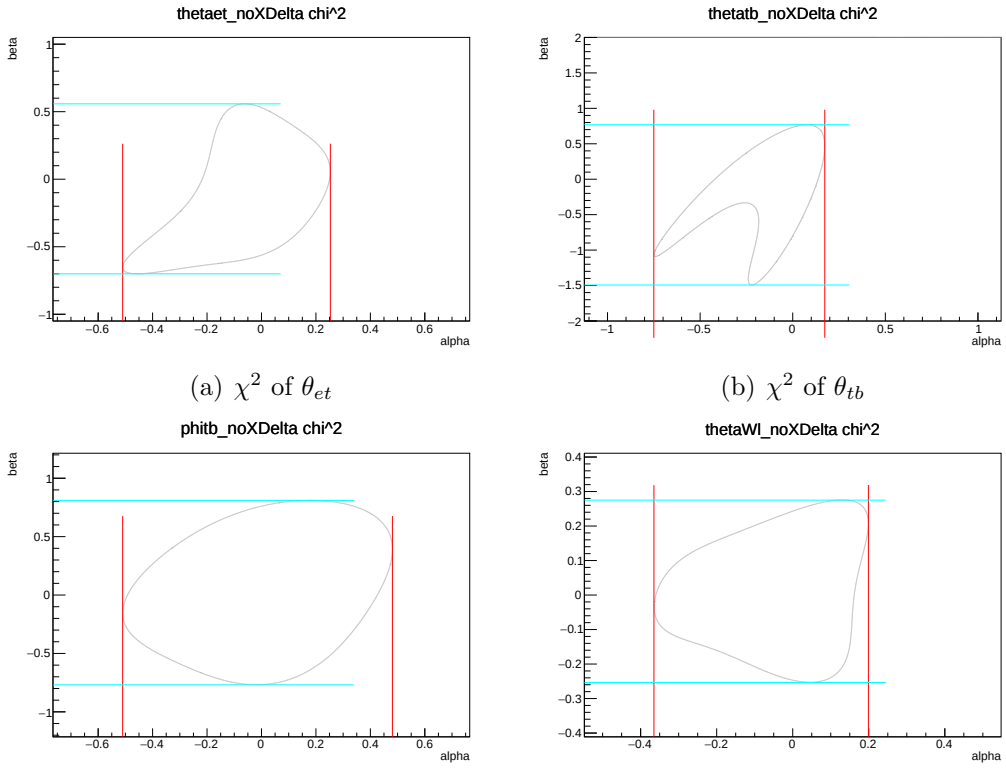

(a) χ^2 of θ_{et}

(b) χ^2 of θ_{tb}

(c) χ^2 of ϕ_{tb}

(d) χ^2 of θ_{Wl}

(e) χ^2 of ϕ_{Wl}

Figure D.114: χ^2 of vl_tbW_Re-vr_tbW_Re 1 Dimensional Angular Distribution

vl_tbW_Re-vr_ttZ σ included

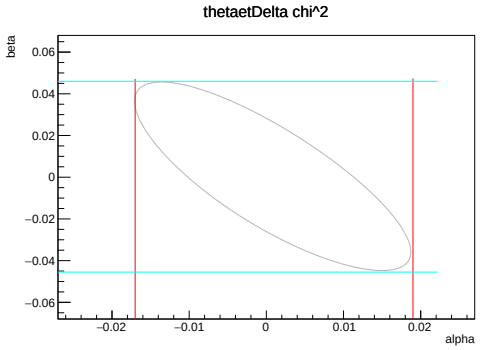

(a) χ^2 of θ_{et}

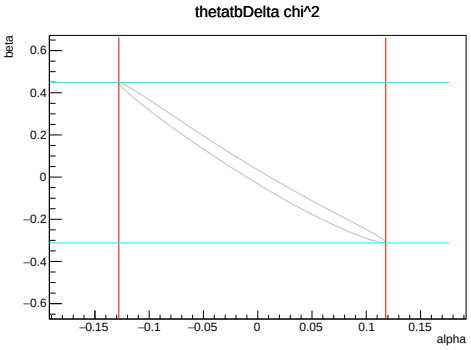

(b) χ^2 of θ_{tb}

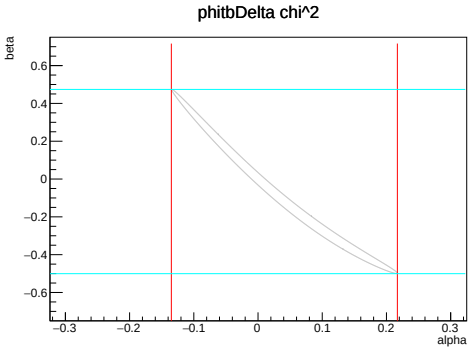

(c) χ^2 of ϕ_{tb}

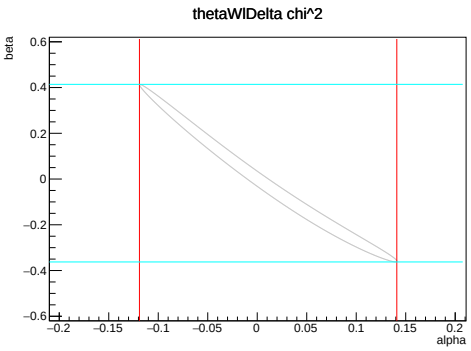

(d) χ^2 of θ_{Wl}

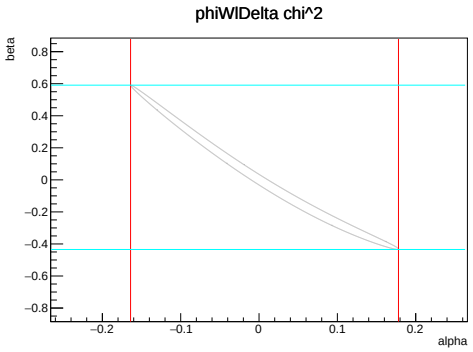

(e) χ^2 of ϕ_{Wl}

Figure D.115: χ^2 of vl_tbW_Re-vr_ttZ 1 Dimensional Angular Distribution

vl_tbW_Re-vr_ttZ σ excluded

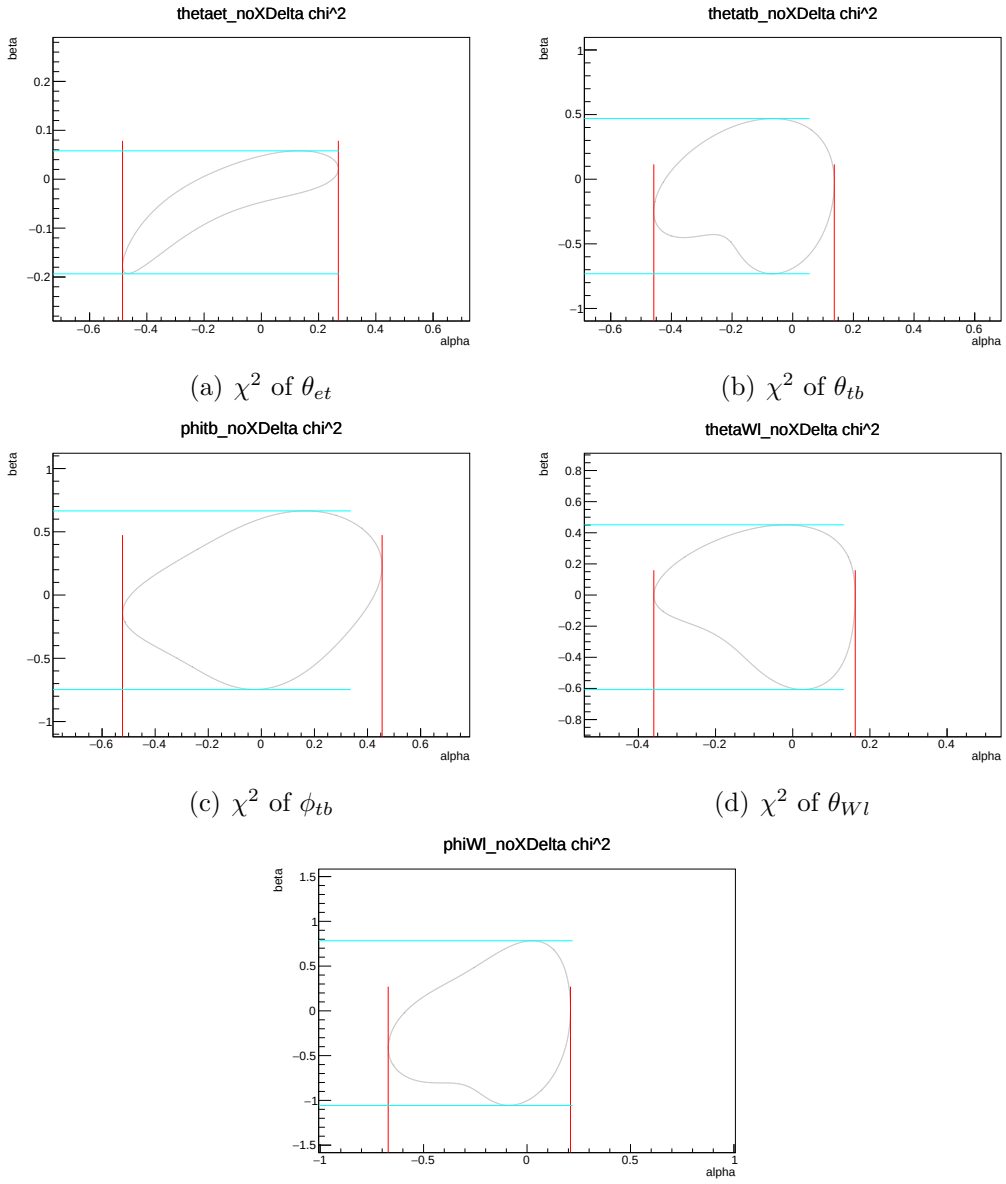

(a) χ^2 of θ_{et}

(b) χ^2 of θ_{tb}

(c) χ^2 of ϕ_{tb}

(d) χ^2 of θ_{Wl}

(e) χ^2 of ϕ_{Wl}

Figure D.116: χ^2 of vl_tbW_Re-vr_ttZ 1 Dimensional Angular Distribution

vr_tbW_Re-ta_ttA σ included

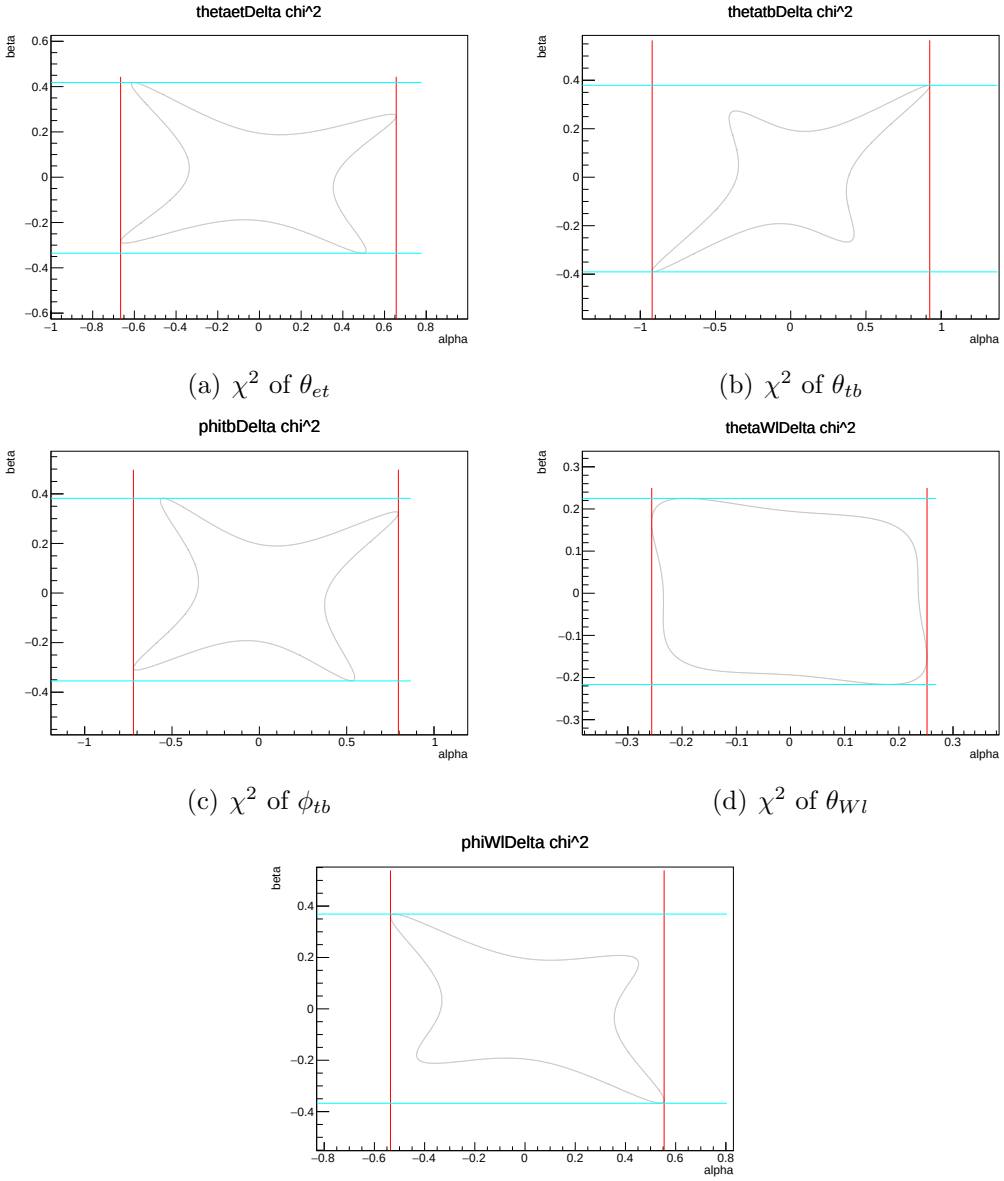

(a) χ^2 of θ_{et}

(b) χ^2 of θ_{tb}

(c) χ^2 of ϕ_{tb}

(d) χ^2 of θ_{Wl}

(e) χ^2 of ϕ_{Wl}

Figure D.117: χ^2 of vr_tbW_Re-ta_ttA 1 Dimensional Angular Distribution

vr_tbW_Re-ta_ttA σ excluded

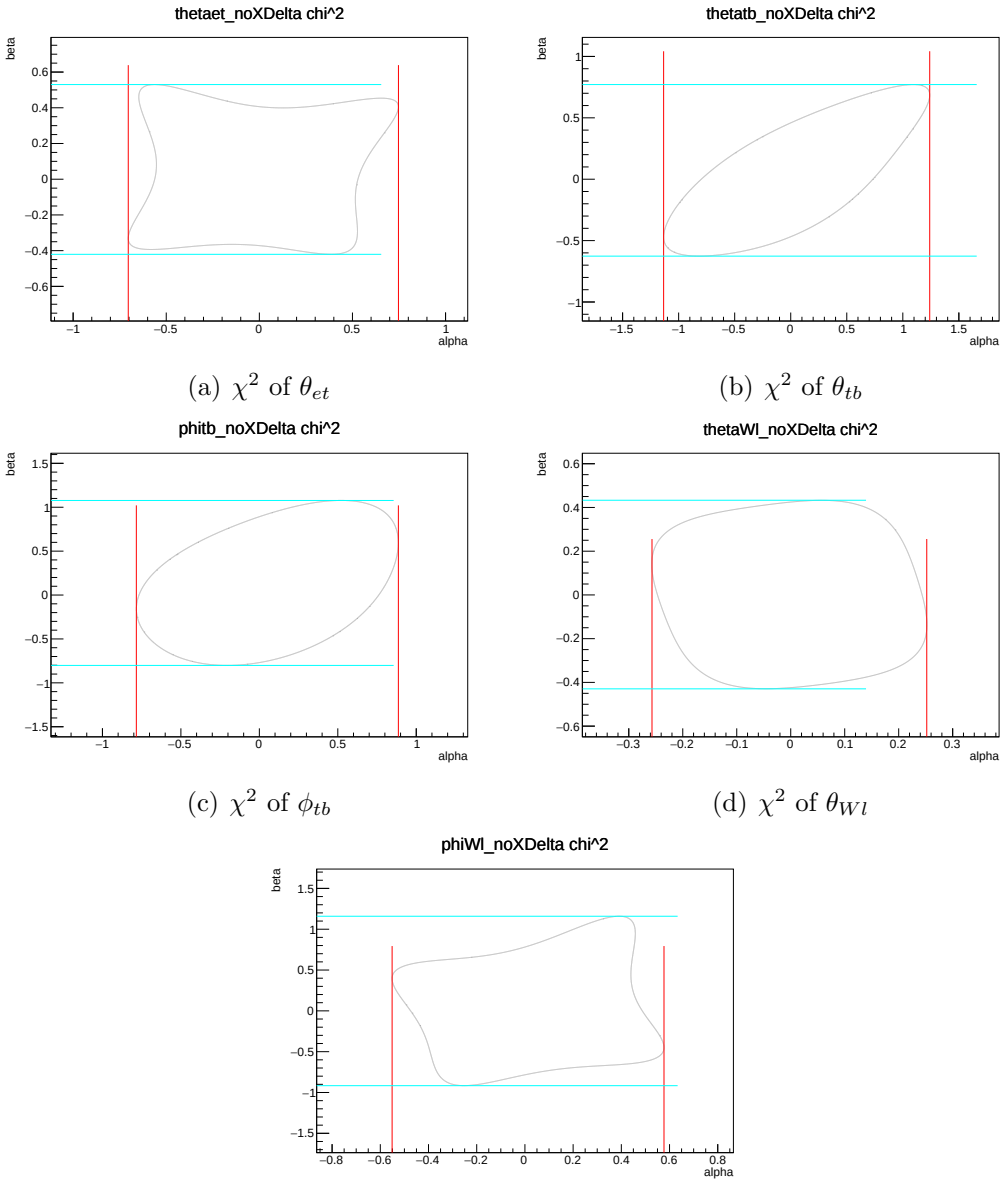

(a) χ^2 of θ_{et}

(b) χ^2 of θ_{tb}

(c) χ^2 of ϕ_{tb}

(d) χ^2 of θ_{Wl}

(e) χ^2 of ϕ_{Wl}

Figure D.118: χ^2 of vr_tbW_Re-ta_ttA 1 Dimensional Angular Distribution

vr_tbW_Re-tl_tbW_Re σ included

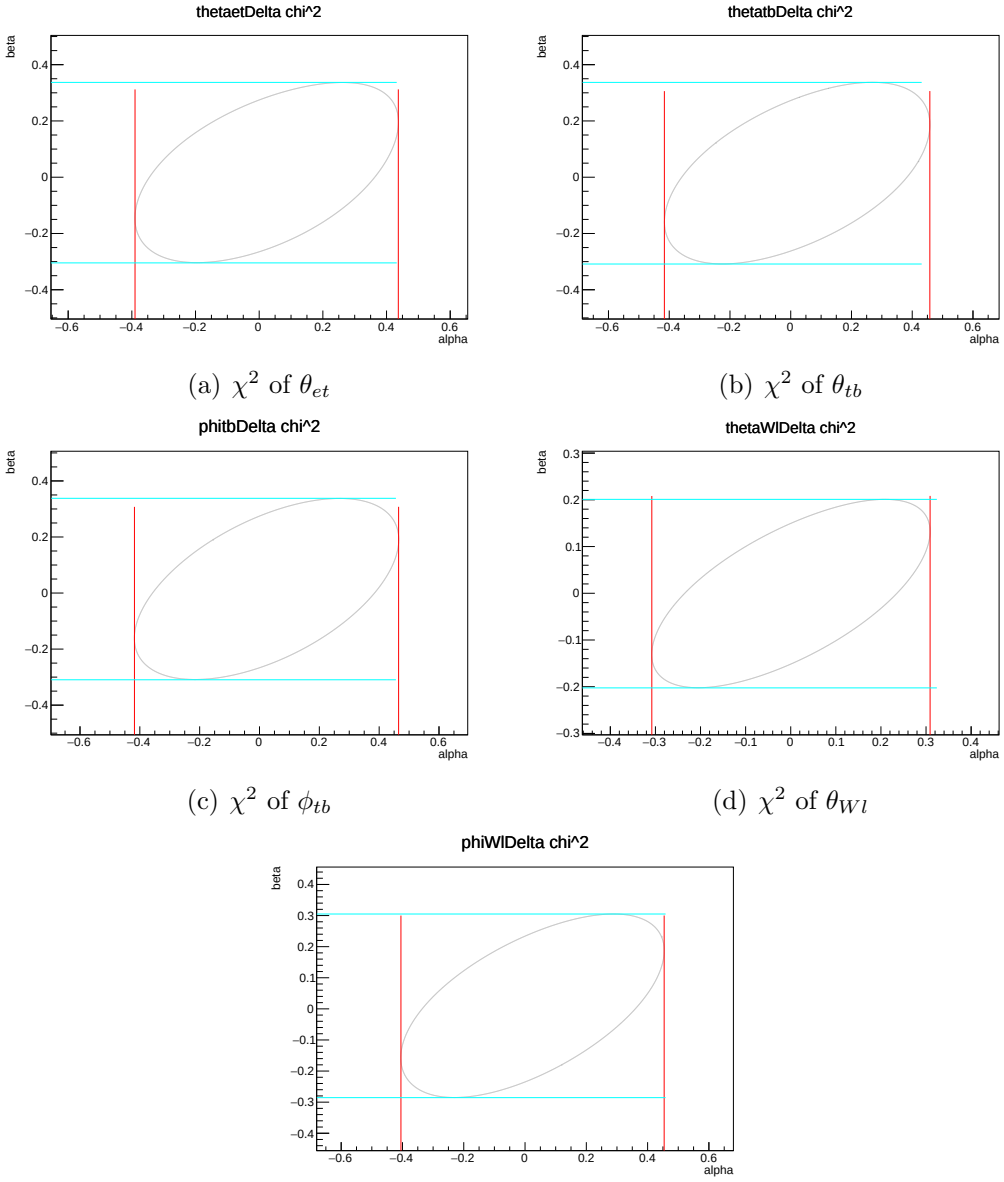

(a) χ^2 of θ_{et}

(b) χ^2 of θ_{tb}

(c) χ^2 of ϕ_{tb}

(d) χ^2 of θ_{Wl}

(e) χ^2 of ϕ_{Wl}

Figure D.119: χ^2 of vr_tbW_Re-tl_tbW_Re 1 Dimensional Angular Distribution

vr_tbW_Re-tl_tbW_Re σ excluded

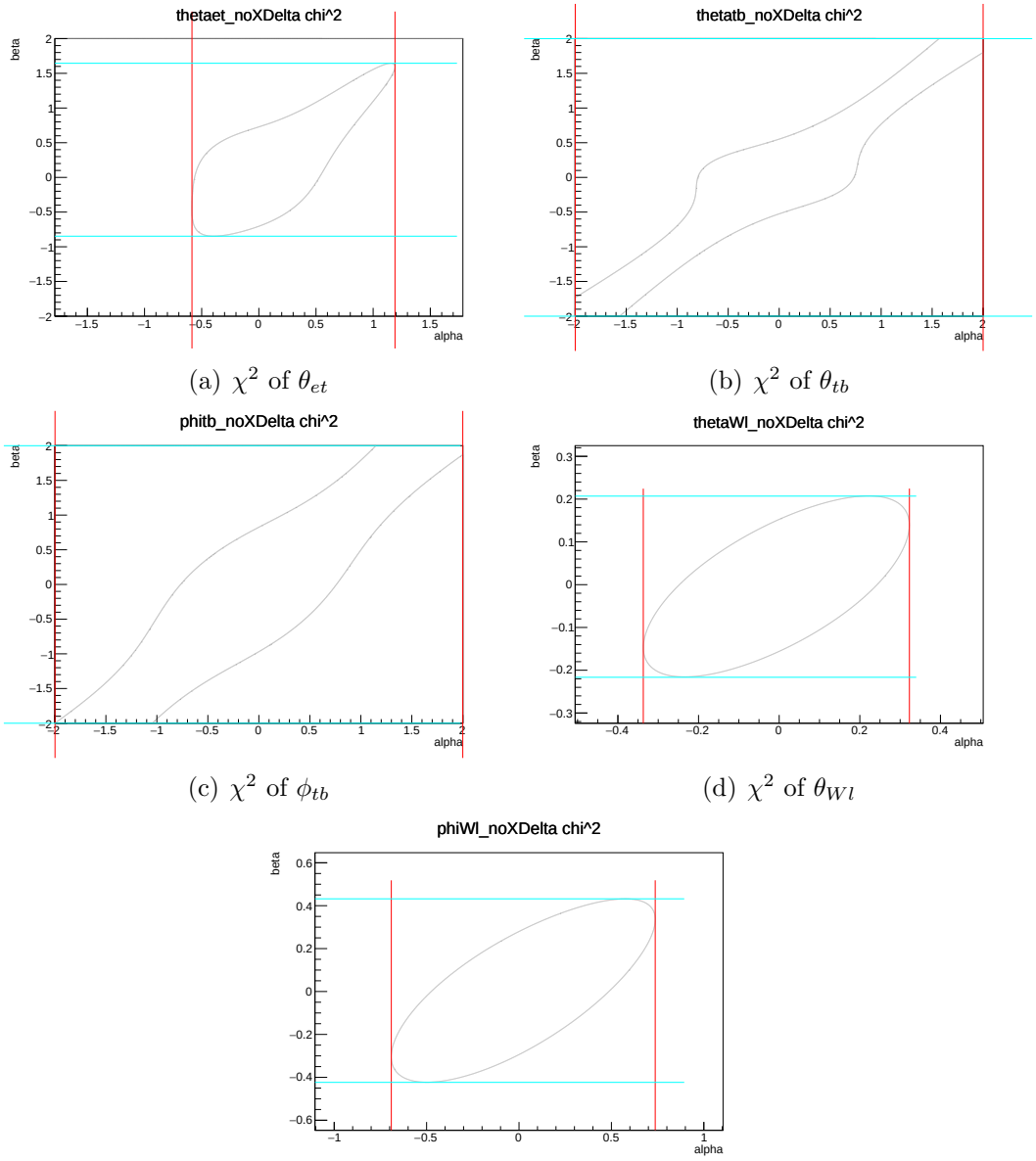

(a) χ^2 of θ_{et}

(b) χ^2 of θ_{tb}

(c) χ^2 of ϕ_{tb}

(d) χ^2 of θ_{Wl}

(e) χ^2 of ϕ_{Wl}

Figure D.120: χ^2 of vr_tbW_Re-tl_tbW_Re 1 Dimensional Angular Distribution

vr_tbW_Re-tr_tbW_Re σ included

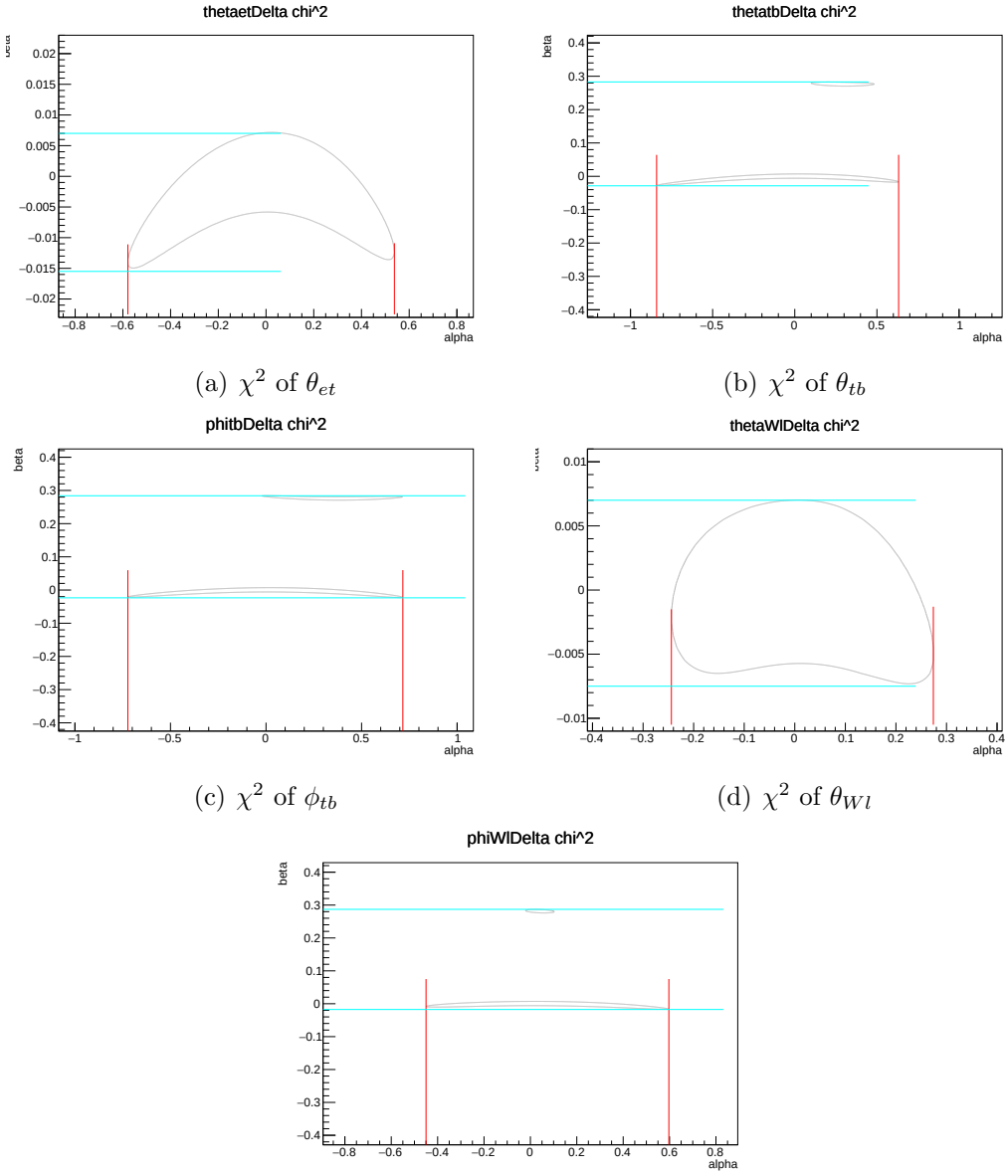

(a) χ^2 of θ_{et}

(b) χ^2 of θ_{tb}

(c) χ^2 of ϕ_{tb}

(d) χ^2 of θ_{Wl}

(e) χ^2 of ϕ_{Wl}

Figure D.121: χ^2 of vr_tbW_Re-tr_tbW_Re 1 Dimensional Angular Distribution

vr_tbW_Re-tr_tbW_Re σ excluded

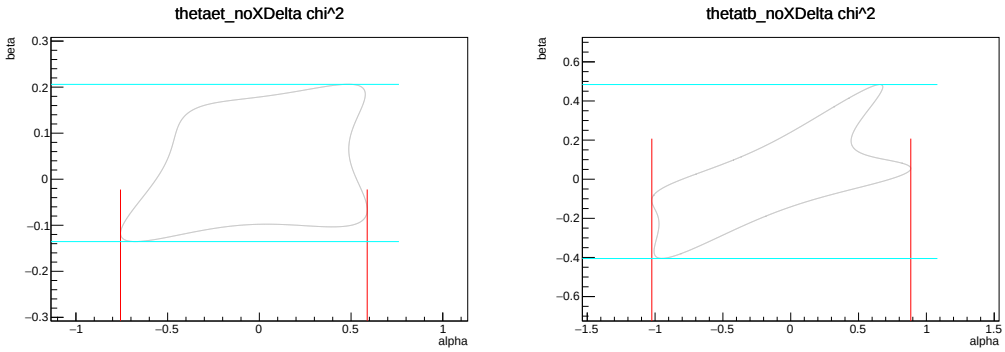

(a) χ^2 of θ_{et}

(b) χ^2 of θ_{tb}

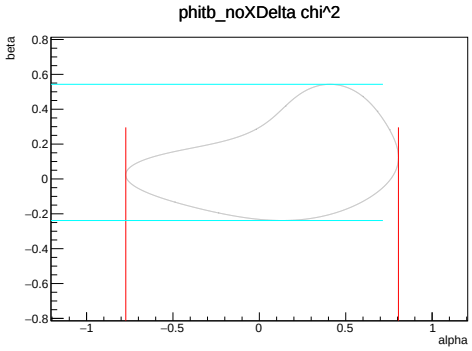

(c) χ^2 of ϕ_{tb}

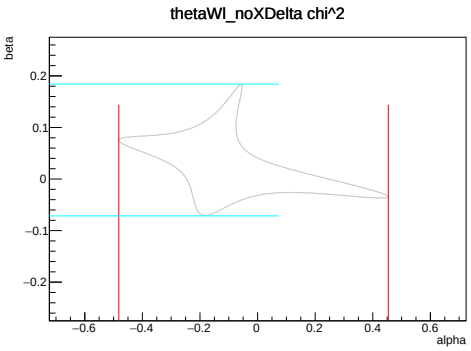

(d) χ^2 of θ_{Wl}

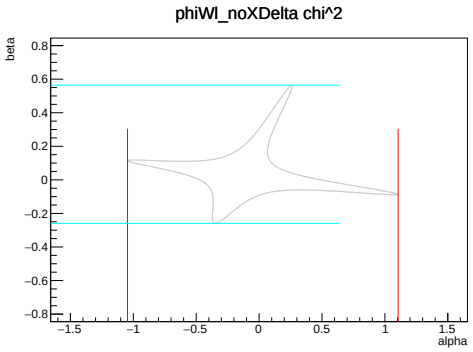

(e) χ^2 of ϕ_{Wl}

Figure D.122: χ^2 of vr_tbW_Re-tr_tbW_Re 1 Dimensional Angular Distribution

vr_tbW_Re-tv_ttA σ included

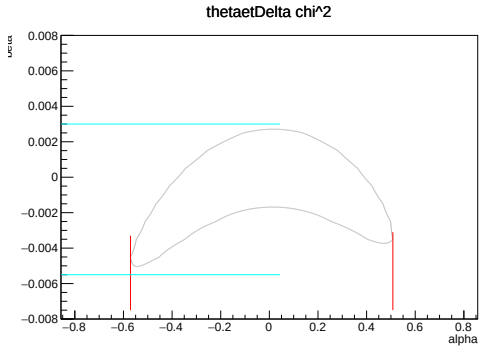

(a) χ^2 of θ_{et}

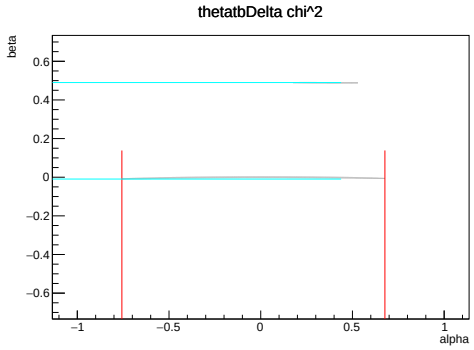

(b) χ^2 of θ_{tb}

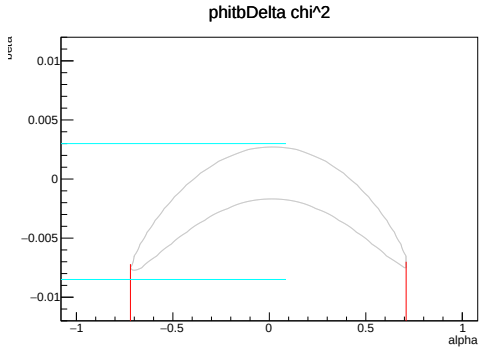

(c) χ^2 of ϕ_{tb}

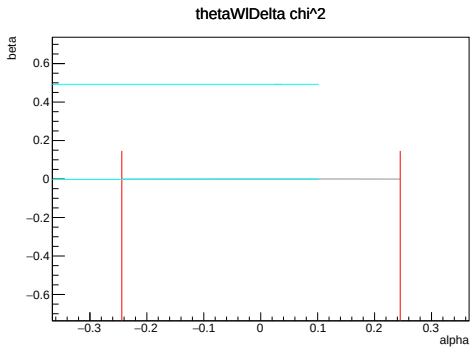

(d) χ^2 of θ_{Wl}

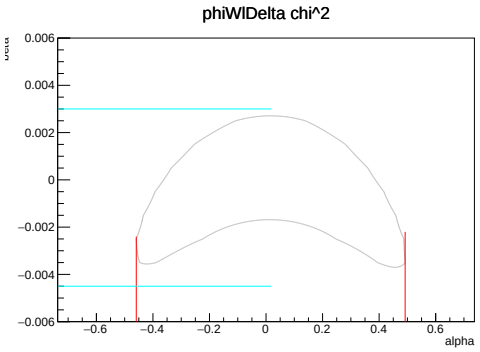

(e) χ^2 of ϕ_{Wl}

Figure D.123: χ^2 of vr_tbW_Re-tv_ttA 1 Dimensional Angular Distribution

vr_tbW_Re-tv_ttA σ excluded

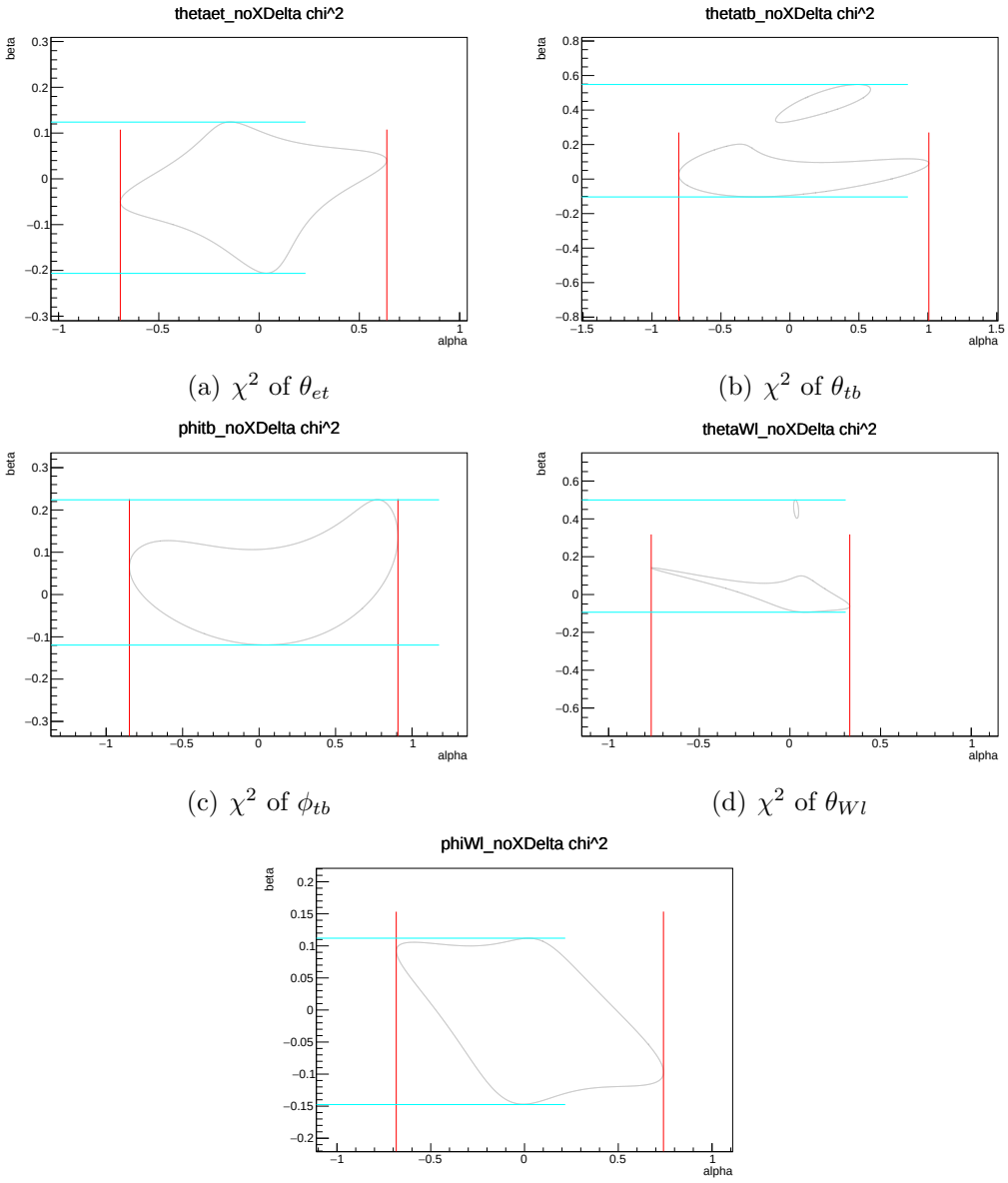

(a) χ^2 of θ_{et}

(b) χ^2 of θ_{tb}

(c) χ^2 of ϕ_{tb}

(d) χ^2 of θ_{Wl}

(e) χ^2 of ϕ_{Wl}

Figure D.124: χ^2 of vr_tbW_Re-tv_ttA 1 Dimensional Angular Distribution

vr_tbW_Re-vr_ttZ σ included

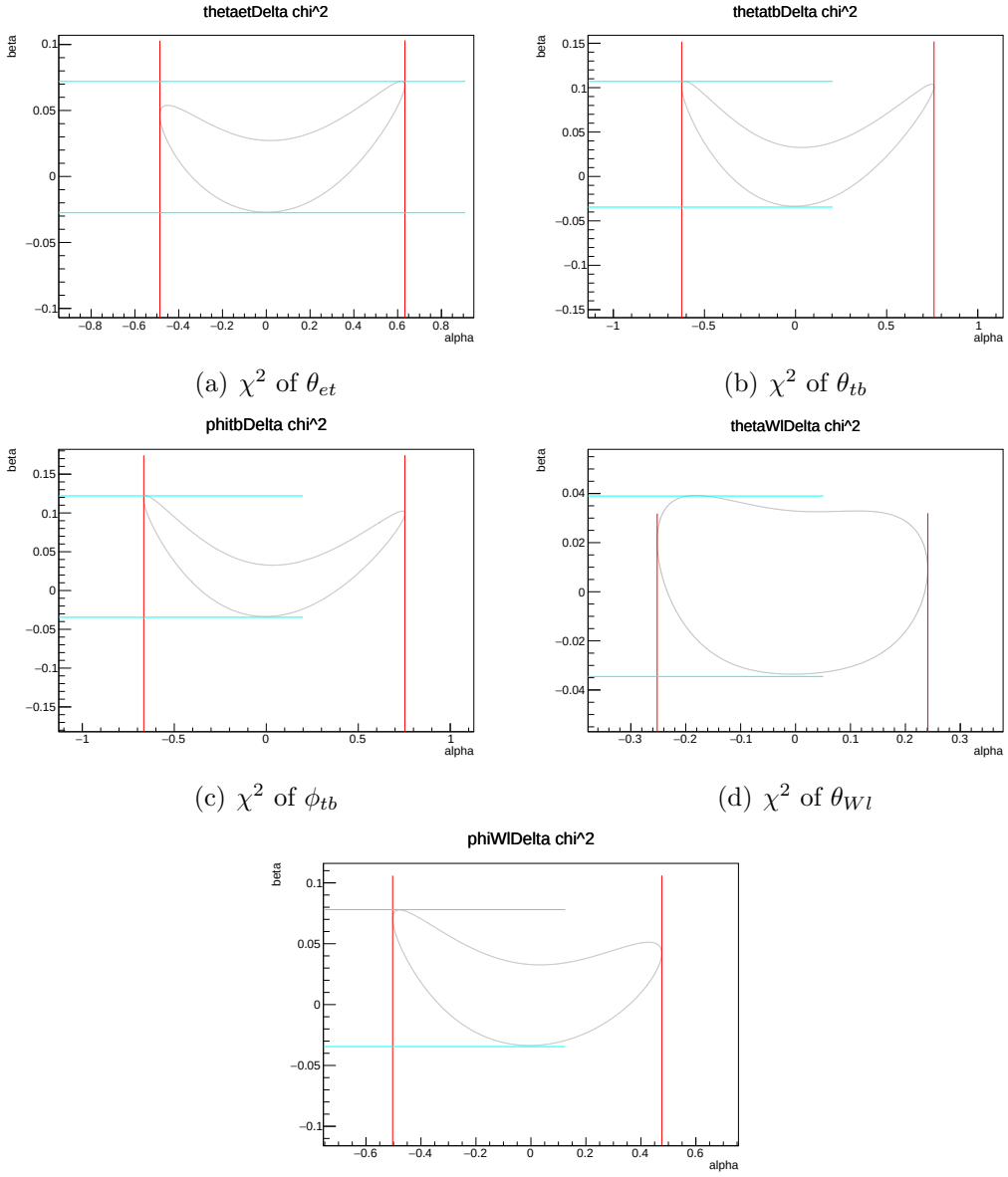

(a) χ^2 of θ_{et}

(b) χ^2 of θ_{tb}

(c) χ^2 of ϕ_{tb}

(d) χ^2 of θ_{Wl}

(e) χ^2 of ϕ_{Wl}

Figure D.125: χ^2 of vr_tbW_Re-vr_ttZ 1 Dimensional Angular Distribution

vr_tbW_Re-vr_ttZ σ excluded

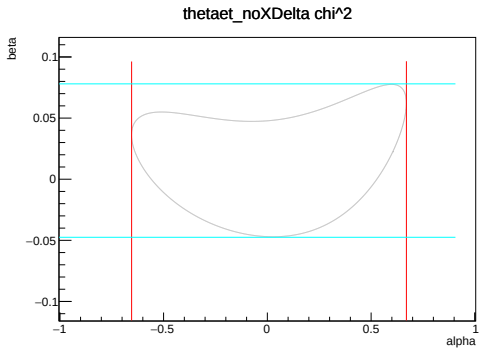

(a) χ^2 of θ_{et}

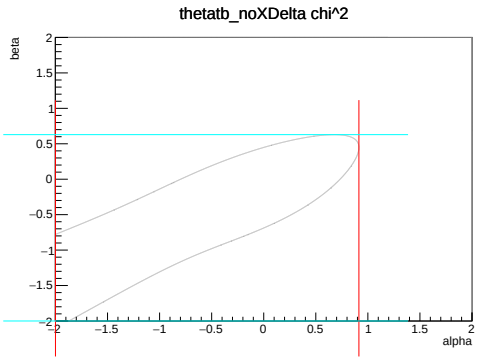

(b) χ^2 of θ_{tb}

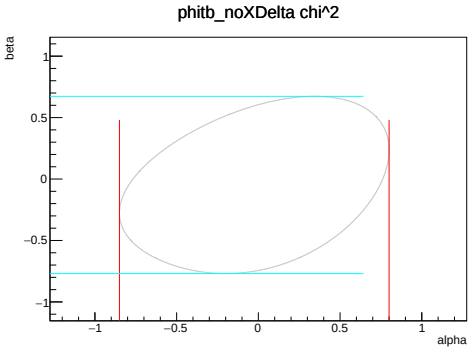

(c) χ^2 of ϕ_{tb}

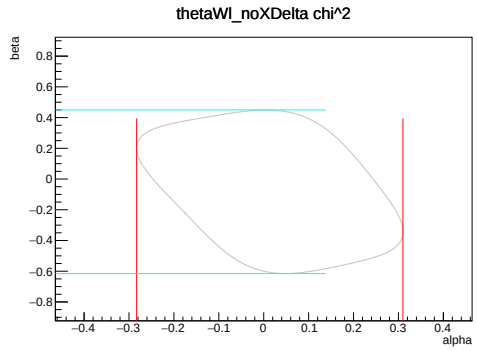

(d) χ^2 of θ_{Wl}

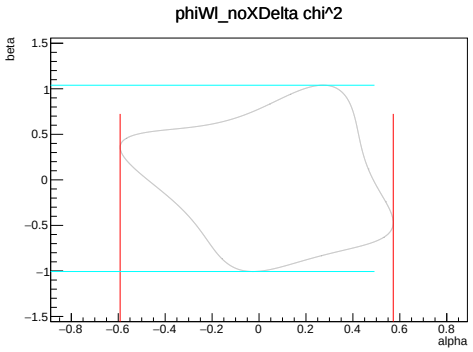

(e) χ^2 of ϕ_{Wl}

Figure D.126: χ^2 of vr_tbW_Re-vr_ttZ 1 Dimensional Angular Distribution

References

[1] Wikipedia contributors, "Timeline of particle physics — Wikipedia, the free encyclopedia," 2022.

[2] Wikipedia contributors, "Standard model — Wikipedia, the free encyclopedia," 2023.

[3] Wikipedia contributors, "Weak hypercharge — Wikipedia, the free encyclopedia," 2023.

[4] D. d'Enterria, P. Skands, S. Alekhin, A. Banfi, S. Bethke, J. Bluemlein, K. Chetyrkin, D. d'Enterria, G. Dissertori, X. Tormo, A. Hoang, M. Klasen, T. Klijnsma, S. Kluth, J. Kneur, B. Kniehl, D. Kolodrubetz, J. Kühn, P. Mackenzie, and I. Stewart, "High-precision α_s measurements from lhc to fcc-ee," 12 2015.

[5] A. Ceccucci, Z. Ligeti, and Y. Sakai, "Ckm quark-mixing matrix." https://pdg.lbl.gov/2020/reviews/rpp2020-rev-ckm-matrix.pdf, March 2020.

[6] M. Thomson, *Modern Particle Physics*. Cambridge University Press, 1st ed., 2013.

[7] A. Cohen, *Theoretical Concepts in Particle Physics*. Princeton University Press, 2nd ed., 2013.

[8] J. Aguilar-Saavedra, "A minimal set of top anomalous couplings," *Nuclear Physics B*, vol. 812, pp. 181–204, 2001.

[9] The FCC Collaboration and others, "FCC-ee: The Lepton Collider: Future Circular Collider Conceptual Design Report Volume 2," tech. rep., CERN, 2019.

[10] R. Chehab, E. Cortina Gil, C. Deaconu, and et al., "Idea: A detector concept for future leptonic colliders," *Nuclear Instruments and Methods in Physics Research Section A: Accelerators, Spectrometers, Detectors and Associated Equipment*, vol. 617, no. 1-3, pp. 149–155, 2010.

[11] A. Abada, E. Cortina Gil, A. De Roeck, Z. Liu, J. López-Pavón, K. Meier, T. Mori, P. Musella, K. Sasaki, U. Soldevila, N. T. Tran, T. Wang, and M. Xu, "IDEA: A Detector for Electron Ion Collisions at the LHC," 2021.

[12] J. de Favereau, C. Delaere, P. Demin, A. Giammanco, V. Lemaître, A. Mertens, M. Selvaggi, and M. Vidal Marono, "DELPHES 3: a modular framework for fast simulation of a generic collider experiment," *JHEP*, vol. 02, p. 057, 2014.

[13] A. Buckley, J. Butterworth, and et al., "The FCC Software Ecosystem: Preparing for an Era of High-Precision Physics," 2021.

[14] T. Sjostrand *et al.*, "Pythia 8.2." http://home.thep.lu.se/ torbjorn/Pythia.html, 2015.

[15] J. Alwall, R. Frederix, S. Frixione, V. Hirschi, F. Maltoni, O. Mattelaer, H. Shao, T. Stelzer, P. Torrielli, and M. Zaro, "MadGraph5_aMC@NLO brief user manual." https://launchpad.net/mg5amcnlo, 2014.

[16] A. Pukhov and et al., "CompHEP - a package for evaluation of Feynman diagrams and integration over multi-particle phase space. User's manual for version 3.3," tech. rep., Moscow State U., 1999.

[17] E. Boos and et al., "CompHEP 4.4: Automatic computations from Lagrangians to events," *Nucl. Instrum. Meth. A*, vol. 534, pp. 250–259, 2004.

[18] J. M. Torndal, "A study of top anomalous couplings at a future e^+e^- collider." https://www.nbi.dk/ beck/julie.pdf, 2021. Master's thesis, Niels Bohr Institute, University of Copenhagen.

[19] W. Kilian, T. Ohl, and J. Reuter, "WHIZARD: Simulating multi-particle processes at lhc and ilc." https://whizard.event-generator.org/, 2016.

[20] E. Boos, M. Dubinin, A. Pukhov, M. Sachwitz, and H. J. Schreiber, "Single top production in e+ e-, e gamma, and gamma gamma collisions at linear colliders," *Phys. Rev.*, vol. D64, p. 037701, 2001.

[21] G. Roland, *Phenomenological study of anomalous $t\bar{t}$ production at FCC-ee*. Bachelor's thesis, University of Copenhagen, June 2021.

[22] R. Atkin, "Review of jet reconstruction algorithms," *J. Phys. Conf. Ser.*, vol. 645, no. 1, p. 012008, 2015.

[23] M. Cacciari, G. P. Salam, and G. Soyez, "FastJet User Manual," *Eur. Phys. J. C*, vol. 72, p. 1896, 2012.

[24] G. P. Salam, G. Soyez, and J. Thaler, eds., *Jet Algorithms and Jet Substructure: Physical Principles and Recent Advances*. Springer, 2019.

[25] J. Hansen, *Triple Gauge-boson Couplings in W pair Production via e+e- Annihilation*. PhD thesis, Copenhagen U., 1996.

[26] R. L. Workman *et al.*, "Review of Particle Physics," *PTEP*, vol. 2022, p. 083C01, 2022.

[27] A. Valassi, "ROC curves, AUC's and alternatives in HEP event selection and in other domains." Inter-Experimental LHC Machine Learning WG - 26th January 2018, 2018.

[28] M. Shapiro, "Lecture 12: Qcd and $e^+e^- \to$ hadrons continued." https://www-atlas.lbl.gov/ shapiro/Physics226/lecture12.pdf, October 2016.

[29] V. Blobel, *Least Squares Methods*. World Scientific, 2006.

[30] J. B. Hansen and J. M. Torndal, "Abcfit++." https://github.com/Torndal/ABCfitplusplus/, 2021.

[31] F. James, "The interpretation of errors," 2004.